# ULTRA HIGH ENERGY COSMIC RAY ENERGY SPECTRUM AND COMPOSITION USING HYBRID ANALYSIS WITH TELESCOPE ARRAY

by

Monica Gene Allen

A dissertation submitted to the faculty of
The University of Utah
in partial fulfillment of the requirements for the degree of

Doctor of Philosophy

in

Physics

Department of Physics and Astronomy

The University of Utah

December 2012

***The Graduate School***
THE UNIVERSITY OF UTAH

## STATEMENT OF DISSERTATION APPROVAL

The dissertation of Monica Allen
has been approved by the following supervisory committee members:

| | |
|---|---|
| Wayne Springer , Chair | October 15, 2012<br>Date Approved |
| Charles Jui , Member | October 15, 2012<br>Date Approved |
| John N. Matthews , Member | October 15, 2012<br>Date Approved |
| Stephan LeBohec , Member | October 15, 2012<br>Date Approved |
| Brian Saam , Member | October 15, 2012<br>Date Approved |
| Cynthia Furse , Member | October 15, 2012<br>Date Approved |

and by David Kieda, Chair of the Department of

Physics and Astronomy

Charles A. Wight,
Dean of The Graduate School

# ABSTRACT

Cosmic radiation was discovered in 1912. This year, the $100^{th}$ anniversary of the discovery, marks not only the major progress that has been made in understanding these particles, but also the remaining questions about them. Questions about their sources, acceleration mechanisms, propagation and composition are still unanswered. There are only two experiments currently running that have the ability to study cosmic rays in the Ultra High Energy ($E > 10^{18.0}$ eV) regime.

The Telescope Array studies Ultra High Energy Cosmic Rays (UHECRs) using a hybrid detector. Fluorescence telescopes measure the longitudinal development of the extensive air shower generated by a primary cosmic ray particle, while scintillator detectors measure the lateral distribution of secondary particles that hit the ground. The Middle Drum (MD) fluorescence telescope consists of 14 refurbished telescopes from the High Resolution Fly's Eye (HiRes) experiment, providing a direct link back to the HiRes experiment and data. The surface array is comprised of 507 Scintillator Detectors (SD) of a similar design as was used by the Akeno Giant Air Shower Array (AGASA), providing a link to that experiment as well. Studying TA hybrid events (events observed by both the FD and SD), makes the analysis presented in this work the lynchpin that connects the HiRes experiment to the AGASA experiment. This uniquely allows for a direct comparison between the two detection types and allows us to answer questions about the differences in the energy spectrum measurements shown by the two previous experiments.

Furthermore, the hybrid analysis improves the geometrical reconstruction of the showers significantly. This provides a more accurate measurement of the energy of the primary particle and makes it possible to make an accurate prediction regarding the chemical composition of the cosmic ray particle. Historically, only the HiRes experiment and the Pierre Auger Observatory (PAO) have made significant composition measurements of UHECRs, and they report conflicting measurements. The hybrid composition measurement done in this work can be directly compared to the hybrid PAO result.

For Addie.

# CONTENTS

**ABSTRACT** . . . . . **iii**

**LIST OF FIGURES** . . . . . **vii**

**LIST OF TABLES** . . . . . **xvii**

**ACKNOWLEDGMENTS** . . . . . **xviii**

**CHAPTERS**

**1. INTRODUCTION** . . . . . **1**

1.1 Discovery of Cosmic Radiation . . . . . 1
1.2 Flux of Cosmic Ray Particles . . . . . 2
1.3 Extensive Air Showers . . . . . 2
1.3.1 Muonic Component . . . . . 2
1.3.2 Hadronic Component . . . . . 5
1.3.3 Electromagnetic Cascade . . . . . 5
1.4 Cosmic Ray Physics . . . . . 6
1.4.1 Energy Spectrum . . . . . 7
1.4.2 Anisotropy . . . . . 9
1.4.3 Composition . . . . . 9
1.5 Ultra-High Energy Cosmic Ray Detection . . . . . 10

**2. RECENT RESULTS OF ULTRA HIGH ENERGY COSMIC RAY RESEARCH** . . . . . **13**

2.1 Fly's Eye . . . . . 13
2.2 Akeno Giant Air Shower Array . . . . . 15
2.3 HiRes-MIA . . . . . 17
2.4 High Resolution Fly's Eye . . . . . 23
2.5 Pierre Auger Observatory . . . . . 28
2.6 Telescope Array . . . . . 28

**3. TELESCOPE ARRAY EXPERIMENT DESCRIPTION** . . . . . **36**

3.1 Surface Detectors . . . . . 38
3.1.1 Description and Deployment . . . . . 38
3.1.2 Read-out Electronics . . . . . 44
3.1.3 Trigger . . . . . 44
3.1.4 Scintillator Detector Calibration . . . . . 44
3.2 Middle Drum Fluorescence Detector . . . . . 51
3.2.1 Middle Drum Fluorescence Detector Trigger . . . . . 52
3.2.2 Middle Drum Detector Electronics . . . . . 57
3.3 Middle Drum Calibration . . . . . 59

3.3.1 Photometric Calibration . . . 59
3.3.2 Atmospheric Calibration and Monitoring . . . 63
3.3.2.1 Atmospheric Profile . . . 63
3.3.2.2 Aerosols . . . 65
3.3.2.3 Weather Monitoring . . . 69
3.3.3 Fluorescence Yield . . . 70

**4. SIMULATIONS . . . 74**

4.1 Hybrid Monte Carlo Program . . . 74
4.1.1 SD Monte Carlo Programs . . . 78
4.1.2 Middle Drum Monte Carlo Programs . . . 83
4.2 Monte Carlo Event Set . . . 88
4.2.1 Energy Scale Correction . . . 89
4.2.2 Resolutions . . . 89
4.2.3 Data/Monte Carlo Comparisons . . . 95

**5. EVENT RECONSTRUCTION . . . 111**

5.1 Data Format . . . 111
5.2 SD Reconstruction . . . 113
5.3 MD Reconstruction . . . 122
5.4 Hybrid Reconstruction . . . 127
5.5 Energy Reconstruction . . . 131

**6. DATA AND ENERGY SPECTRUM RESULTS . . . 134**

6.1 Middle Drum Hybrid Event Selection . . . 134
6.2 Middle Drum Hybrid Aperture and Exposure Calculations . . . 135
6.2.1 Reconstruction Bias Correction . . . 140
6.2.2 Ratio Correction . . . 140
6.3 Result . . . 144
6.3.1 Comparison with other Telescope Array Analyses . . . 144

**7. COMPOSITION RESULT . . . 154**

7.1 Introduction . . . 154
7.2 $X_{max}$ Studies . . . 154
7.3 Iron Monte Carlo Set . . . 158
7.4 Composition Results . . . 159

**8. SUMMARY . . . 179**

**APPENDIX: TOP ELEVEN HIGHEST ENERGY EVENTS . . . 182**

**REFERENCES . . . 207**

# LIST OF FIGURES


1.1 Flux of cosmic ray particles: the energy spectrum of cosmic ray particles measured by various experiments on a log-log plot. . . . . 3

1.2 Extensive Air Shower (EAS): A diagram showing the EAS development. . . . . 4

1.3 The Heitler model for the branching of the Electromagnetic (EM) component of an EAS: this diagram shows how pair production and Bremsstrahlung radiation work together in the development of the EM cascade. . . . . 6

1.4 Fluorescence Detection (FD): this is a schematic of the Telescope Array fluorescence telescope observation of a cosmic ray induced air shower. . . . . 12

2.1 Fly's Eye (FE) event display: the telescopes were positioned to view the entire sky in a dome-like shape. . . . . 14

2.2 Fly's Eye I (FEI) monocular energy spectrum: shown is the energy spectrum as seen by FEI in monocular mode as well as the fit. . . . . 16

2.3 The Fly's Eye stereo energy spectrum: shown is the energy spectrum as seen by FEI and FEII in stereo mode. . . . . 17

2.4 The Fly's Eye composition measurement, using the $X_{max}$ technique: The data shows a transition from heavy to light particles. . . . . 18

2.5 The stereo Fly's Eye energy spectrum: shown is a simultaneous two-component fit using a mixed composition of proton and iron nuclei. . . . . 19

2.6 AGASA energy spectrum: shown is the flux of UHECRs measured by the AGASA experiment. . . . . 20

2.7 An event display from the HiRes Prototype fluorescence telescope: shown are the 14 telescopes arranged as they view the sky. . . . . 21

2.8 An overview of the placement of the MIchigan Muon Array (MIA): it is shown relative to the HiRes site. . . . . 22

2.9 HiRes-MIA energy spectrum compared to the Fly's Eye stereo energy spectrum: good agreement is shown here and indicates that the HiRes Prototype and FE had the same energy scale. . . . . 24

2.10 HiRes-MIA and HiRes composition measurement: shown is the $<X_{max}>$ value as a function of energy. . . . . 25

2.11 HiRes event display: shown is a typical HiRes-2 event which traverses three telescope cameras. . . . . 26

2.12 HiRes energy spectra: shown is the flux of UHECRs measured by the HiRes-1 and HiRes-2 experiments in comparison with the AGASA energy spectrum. . . 27

2.13 The PAO energy spectrum overlaid with the HiRes spectrum: the flux of cosmic ray particles is plotted as a function of energy. . . . . 29

2.14 PAO composition measurement: the average $X_{max}$ value is plotted as a function of energy along with several "rails" that represent different shower models for light and heavy particles for comparison. . . . . 30

2.15 Cosmic ray event observed by the multiple detector elements of the Telescope Array experiment: shown is the event display of the Surface Detector (SD) of an event observed on October 26, 2008 in stereo hybrid mode. . . . . 31

2.16 Cosmic ray event observed by the multiple detector elements of the Telescope Array experiment: shown is the event display of the Middle Drum Fluorescence Detector (MDFD) of an event observed on October 26, 2008 in stereo hybrid mode. . . . . 32

2.17 Cosmic ray event observed by the multiple detector elements of the Telescope Array experiment: shown is the event display of the Black Rock Mesa Fluorescence Detector (BRMFD) of an event observed on October 26, 2008 in stereo hybrid mode. . . . . 33

2.18 Cosmic ray event observed by the multiple detector elements of the Telescope Array experiment: shown is an event observed on October 26, 2008 in stereo hybrid mode. Shown is the event display of the Long Ridge Fluorescence Detector (LRFD). . . . . 34

3.1 The layout of the Telescope Array experiment: the different components of the experiment are indicated on this map. . . . . 37

3.2 A typical Surface Detector (SD) event: the SD counters which viewed a signal for this event are shown. . . . . 39

3.3 The SD construction facility at the University of Tokyo's Akeno Observatory in Akeno, Japan: in the photo, we are preparing the wavelength shifting fibers to be attached to PMTs. . . . . 40

3.4 A schematic of internal components of a TA Surface Detector (SD) viewed from above (top) and from the side (bottom). . . . . 41

3.5 Placement of the wavelength shifting fibers in the grooves in the scintillating plastic in a SD: each fiber was individually placed by hand and taped at the two ends. . . . . 42

3.6 Diagram of external view of a Surface Detector (SD): the external components are labeled. . . . . 43

3.7 Image of field deployment of a Surface Detector (SD) via helicopter: one helicopter brought the SD itself, while a second helicopter ferried a crew from site to site to receive the SD, align it, and turn it on. . . . . 45

3.8 Shown is a schematic of the SD data acquisition system. . . . . 46

3.9 These are the FADC traces from the upper and lower layers of scintillator in one Surface Detector (SD) counter. . . . . 47

3.10 The results of a GEANT4 simulation of mean energy deposition of vertical muon versus kinetic energy: a 300 MeV muon has minimum ionization energy. 48

3.11 Minimum ionizing, 300 MeV vertical muon simulation: The Most Probable Value (MPV) of energy deposited is 2.05 MeV for one VEM unit. . . . . 49

3.12 1-MIP peak for determining detector gains in FADC counts/MeV in (a) the upper scintillator layer and (b) the lower scintillator layer of a Surface Detector (SD). . . . . 50

3.13 Middle Drum Fluorescence Detector (MDFD): 14 telescopes view the southern night sky 3° to 31° in elevation. . . . . 52

3.14 Location of the Middle Drum (MD) detector at the northern end of the SD array: it is located ∼10 km from the nearest SD counter. . . . . 53

3.15 A pair of telescopes at the Middle Drum Fluorescence Detector (MDFD): in the photo, the telescope on the right views 3°-17° above the horizon, while the one on the left views 17°-31° above the horizon. . . . . 54

3.16 Photos of MD telescope PMT Camera: they are shown with the filter closed (top) and open (bottom). . . . . 55

3.17 Examples of trigger conditions and triggering logic flow: triggering conditions are typically three tubes, two of which must be adjacent from two subclusters. 56

3.18 This is a schematic of Middle Drum (MD) telescope electronics. . . . . 58

3.19 This is a photograph of the close up view of the Roving Xenon Flasher (RXF). 60

3.20 A photograph of the Roving Xenon Flasher (RXF) positioned at the center of the mirror where it illuminates the PMTs in the camera: the UVLED has been removed from its position at the center of the mirror to make space for the RXF. . . . . 61

3.21 This is the charge distribution of one PMT over many RXF flashes. . . . . 62

3.22 Ultra Violet Light Emitting Diode (UVLED): Each of the 14 telescopes at the Middle Drum (MD) site is instrumented with a UVLED at the center of the mirror as shown. . . . . 64

3.23 RXF and UVLED data: shown is the variation of the number of photoelectrons per QDC produced over time. . . . . 65

3.24 UVLED data: shown is the variation of the number of photoelectrons per QDC produced versus temperature in the two types of PMTs (Photonis and EMI). . . . . 66

3.25 Number of photoelectrons produced by the RXF and UVLED, shown corrected for temperature variation. . . . . 67

3.26 The TA average atmospheric pressure profile measured from Radiosonde is plotted (dotted line) with the US 1976 atmospheric pressure model (solid line). 67

3.27 This photograph shows the monostatic LIDAR facility located at the Black Rock Mesa Fluorescence Detector (BRMFD). . . . . 68

3.28 The measured Vertical Aerosol Optical Depth (VAOD) at Telescope Array: each entry in the histogram corresponds to a measurement of the VAOD performed using the monostatic LIDAR system. . . . . 68

3.29 The nitrogen fluorescence spectrum as measured by the FLASH collaboration: the spectrum calculated by Bunner is shown as a black line for reference. . . . . 71

3.30 Shown are the measurements of the nitrogen fluorescence yield done by several experiments. . . . . 72

4.1 Schematic showing the dethinning process: weighted particles created from the thinning process in CORSIKA are used to re-insert the missing particles. . 76

4.2 The mean and RMS of energy deposited per SD counter plotted as a function of distance from the shower core for an un-thinned CORSIKA shower compared with a thinned shower (top) and a dethinned shower (bottom). . . . . 77

4.3 The Monte Carlo (MC) generated energy distribution: it comes from the HiRes measurement. . . . . 79

4.4 The Monte Carlo (MC) generated distribution of the position where the shower core crosses the SD plane: it is thrown in a circle centered at the CLF, with a radius of 25 km. . . . . 80

4.5 The Monte Carlo (MC) generated zenith angle distribution: it is a $\sin(\theta)\cos(\theta)$ distribution from 0° - 60°. . . . . 81

4.6 The Monte Carlo (MC) generated azimuthal angle distribution: it is a flat distribution from 0°-360°. . . . . 82

4.7 Data-MC comparison for timing offset between MD and SD: plotted is the difference between the calculated time that the shower core crosses the SD plane as calculated by the MD and the SD for the data set ($t_{MD} - t_{SD}$). . . . . 84

4.8 The Longtin phase function of the fraction of scattered light plotted as a function of scattering angle. . . . . 87

4.9 The Surface Detector (SD) trigger aperture: shown is the aperture from the CORSIKA energy compared with the energy scaled to the Fluorescence Detector (FD) reconstructed energy. . . . . 90

4.10 Schematic of the MD detector relative to the shower core: shown are the important geometric parameters, the in-plane angle ($\psi$), and the impact parameter ($R_P$). . . . . 92

4.11 Resolutions for Middle Drum hybrid geometry reconstructed parameters compared to the MD monocular reconstruction: shown are the in-plane angle ($\psi$), (top), impact parameter ($R_P$), (middle), and zenith angle ($\theta$) (bottom). . . . . 93

4.12 Resolutions for Middle Drum hybrid reconstructed energy compared to the MD monocular reconstruction: shown are events broken up into energy ranges: $10^{18} < \mathrm{E} < 10^{18.5}$ eV (top), $10^{18.5} < \mathrm{E} < 10^{19.0}$ eV (middle), and $\mathrm{E} > 10^{19.0}$ eV (bottom). . . . . 94

4.13 Data-MC comparison: the Middle Drum hybrid in-plane angle ($\psi$) is the angle of the shower track in the shower detector plane. . . . . 96

4.14 Data-MC comparison: the Middle Drum hybrid impact parameter ($R_P$) is the distance of closest approach of the shower to the Middle Drum detector. . . . . 97

4.15 Data-MC comparison: the Middle Drum hybrid zenith angle ($\theta$) is the angle of the shower from the zenith. . . . . 98

4.16 Data-MC comparison: the Middle Drum hybrid azimuthal angle ($\phi$) is the angle of the shower from East. . . . . 99

4.17 Data-MC comparison: the Middle Drum hybrid in-plane angle ($\psi$) is shown in three energy ranges: top to bottom, $10^{18.0} < \mathrm{E} < 10^{18.5}$ eV, $10^{18.5} < \mathrm{E} < 10^{19.0}$ eV, and $\mathrm{E} > 10^{19.0}$ eV, respectively, to show the evolution of this parameter with energy. . . . . 100

4.18 Data-MC comparison: the Middle Drum hybrid impact parameter ($R_P$) is shown in three energy ranges: top to bottom, $10^{18.0} < \mathrm{E} < 10^{18.5}$ eV, $10^{18.5} < \mathrm{E} < 10^{19.0}$ eV, and $\mathrm{E} > 10^{19.0}$ eV, respectively, to show the evolution of this parameter with energy. . . . . 101

4.19 Data-MC comparison: the Middle Drum hybrid zenith angle ($\theta$) is shown in three energy ranges: top to bottom, $10^{18.0} < \mathrm{E} < 10^{18.5}$ eV, $10^{18.5} < \mathrm{E} < 10^{19.0}$ eV, and $\mathrm{E} > 10^{19.0}$ eV, respectively, to show the evolution of this parameter with energy. . . . . 102

4.20 Data-MC comparison: the Middle Drum hybrid azimuthal angle ($\phi$) is shown in three energy ranges: top to bottom, $10^{18.0} < \mathrm{E} < 10^{18.5}$ eV, $10^{18.5} < \mathrm{E} < 10^{19.0}$ eV, and $\mathrm{E} > 10^{19.0}$ eV, respectively, to show the evolution of this parameter with energy. . . . . 103

4.21 Data-MC comparison: the Middle Drum hybrid location of the east-west ("X") coordinate of the shower core is calculated with respect to the Central Laser Facility (CLF). . . . . 104

4.22 Data-MC comparison: the Middle Drum hybrid location of the north-south ("Y") coordinate of the shower core is calculated with respect to the Central Laser Facility (CLF). . . . . 105

4.23 Data-MC comparison: Middle Drum hybrid calculated location of the east-west ("X") coordinate of the shower core with respect to the Central Laser Facility (CLF), is shown in three energy ranges: top to bottom, $10^{18.0} < \mathrm{E} < 10^{18.5}$ eV, $10^{18.5} < \mathrm{E} < 10^{19.0}$ eV, and $\mathrm{E} > 10^{19.0}$ eV, respectively, to show the evolution of this parameter with energy. . . . . 106

4.24 Data-MC comparison: Middle Drum hybrid calculated location of the north-south ("Y") coordinate of the shower core with respect to the Central Laser Facility (CLF) is shown in three energy ranges: top to bottom, $10^{18.0} < \mathrm{E} < 10^{18.5}$ eV, $10^{18.5} < \mathrm{E} < 10^{19.0}$ eV, and $\mathrm{E} > 10^{19.0}$ eV, respectively, to show the evolution of this parameter with energy. . . . . 107

4.25 Data-MC comparison: Middle Drum hybrid number of photoelectrons is shown per degree of track length. . . . . 109

4.26 Data-MC comparison: Middle Drum hybrid number of photoelectrons per degree of track length is shown in three energy ranges: top to bottom, $10^{18.0}$ < E < $10^{18.5}$ eV, $10^{18.5}$ < E < $10^{19.0}$ eV, and E > $10^{19.0}$ eV, respectively, to show the evolution of this parameter with energy. . . . . 110

5.1 FADC signal waveforms are shown from the upper (above) and lower (below) layers of scintillator in detector 408 for event 2009/09/19 08:45:52 UTC. . . . . 114

5.2 A schematic of the shower front is shown as it hits the SD array. . . . . 115

5.3 SD event display: the Center Of Gravity (COG) core position is shown where the arrow crosses the line for event 2009/09/19 08:45:52. . . . . 116

5.4 The SD timing fit shown for event 2009/09/19 08:45:52: the time of counter hit is plotted as a function of distance along the projection of the shower axis on the ground. . . . . 118

5.5 The fit to the Lateral Distribution Function (LDF): the pulse height (VEM/$m^2$) is plotted as a function of the lateral distance from the shower axis for event 2009/09/19 08:45:52. . . . . 120

5.6 SD event display: the Center Of Gravity (COG) core position is shown where the red arrow crosses the (red) line, and the arrow points in the initial direction calculated using the COG. The black arrow shows the result of the timing fit for the shower core (where the black arrow crosses the black line). This is the event display for event 2009/09/19 08:45:52. . . . . 121

5.7 The SD energy table: the S800 value (in log scale) is plotted as a function of the secant of the zenith angle. The energy for the SD events is found using this table with the calculated values for S800 and zenith angle. . . . . 122

5.8 Middle Drum event display for event 2009/09/19 08:45:52: it shows the Shower Detector Plane (SDP) fit to the PMTs. . . . . 125

5.9 MD timing vs. angle plot for event 2009/09/19 08:45:52: the time of the PMTs is plotted as a function of their elevation angle within the Shower Detector Plane (SDP). . . . . 126

5.10 Diagram indicating the geometry of the shower within the SDP and parameter names: the diagram shows how the PMT trigger time is related to a given pointing angle within the SDP. . . . . 128

5.11 Timing vs angle plot for event 2009/09/19 08:45:52, observed by the PMTs at the Middle Drum fluorescence detector site: the angle of the observed signal along the SDP is plotted with respect to the time information of the signal. . . 129

5.12 Timing vs angle plot for event 2009/09/19 08:45:52: it is extended using information from Surface Detectors. . . . . 130

5.13 The profile plot for hybrid event 2009/09/19 08:45:52: the signal size is plotted as a function of slant depth in the shower. . . . . 132

6.1 Middle Drum hybrid on-time: the solid line indicates an integration of all hours when there is no sun and no moon. . . . . 137

6.2 Middle Drum hybrid aperture for simulated showers initiated by a proton primary: It ramps up with energy and flattens out at about $10^{8.5}$ $m^2$ steradians. 139

6.3 Mean energy reconstruction bias as a function of energy: above $10^{18.0}$ eV, the hybrid energy resolution is very good. . . . . 141

6.4 Shown is the aperture from the CORSIKA energy compared with the Fluorescence Detector (FD) energy. . . . . 142

6.5 The Middle Drum hybrid aperture: shown are the apertures from the proton Monte Carlo (MC) set using no correction, the ratio correction to the aperture, and a new MC set with the trigger efficiency folded in. . . . . 143

6.6 The raw energy distribution of events passing all quality cuts observed in hybrid mode by the Middle Drum telescope site: the events are binned in energy and total 349 that were used for the MD hybrid spectrum. . . . . 146

6.7 Middle Drum hybrid energy spectrum: shown is the differential flux of ultra high energy cosmic rays versus energy. . . . . 147

6.8 A scatter plot showing the an event-by-event comparison of data events reconstructed by the Middle Drum hybrid Nerling analysis (X-axis), and the Middle Drum monocular Hillas analysis (Y-axis). . . . . 149

6.9 A histogram of the log ratio of the energies of events reconstructed by the Middle Drum monocular Hillas analysis versus the Middle Drum hybrid analysis: the width in this histogram is dominated by the resolution in the MD monocular reconstruction. . . . . 150

6.10 The Middle Drum hybrid energy spectrum (closed circles) compared with the spectrum measured by the Middle Drum detector in monocular mode, using the Hillas reconstruction (open circles), as well as the spectra measured by the HiRes-1 (open squares) and HiRes-2 (open triangles) detectors. . . . . 151

6.11 The Middle Drum hybrid spectrum (closed circles) compared with the spectrum measured by the surface array (open squares): the MD monocular spectrum is shown for reference. . . . . 152

7.1 HiRes stereo composition result: the $<X_{max}>$ value as a function of energy is plotted (filled circles) with several "rails" which represent different shower models for proton (top) and iron (bottom) showers. . . . . 156

7.2 HiRes stereo composition result: the $X_{max}$ distribution width, $\sigma$, is plotted as a function of energy. . . . . 157

7.3 PAO hybrid composition result: the $<X_{max}>$ value as a function of energy is plotted with several "rails" which represent different shower models for proton (top) and iron (bottom) showers. . . . . 158

7.4 PAO hybrid composition result: the $X_{max}$ distribution width, RMS, is plotted as a function of energy. . . . . 159

7.5 Resolution plots are shown for the iron Monte Carlo (MC) geometry and energy resolutions. . . . . 160

7.6 Data/iron MC comparison: shown is the comparison for the Middle Drum hybrid impact parameter ($R_P$). . . . . 161

7.7 Data/iron MC comparison: Middle Drum hybrid impact parameter ($R_P$) is shown in three energy ranges: top to bottom, $10^{18.0} < \mathrm{E} < 10^{18.5}$ eV, $10^{18.5} < \mathrm{E} < 10^{19.0}$ eV, and $\mathrm{E} > 10^{19.0}$ eV, respectively, to show the evolution of this parameter with energy. . . . . 162

7.8 Data/iron MC comparison: shown is the comparison for the Middle Drum hybrid zenith angle ($\theta$). . . . . 163

7.9 Data/iron MC comparison: Middle Drum hybrid zenith angle ($\Theta$) is shown in three energy ranges: top to bottom, $10^{18.0} < \mathrm{E} < 10^{18.5}$ eV, $10^{18.5} < \mathrm{E} < 10^{19.0}$ eV, and $\mathrm{E} > 10^{19.0}$ eV, respectively, to show the evolution of this parameter with energy. . . . . 164

7.10 The distribution of the shower maximum for (a) the proton Monte Carlo set, and (b) the iron Monte Carlo set, are shown, each fit to a gaussian. . . . . 165

7.11 The MD hybrid $X_{max}$ resolution for the Monte Carlo sets: shown is the difference between the reconstructed $X_{max}$ values and the thrown $X_{max}$ values for (a) proton, and (b) iron induced showers, fit to a gaussian. . . . . 167

7.12 Middle Drum hybrid $X_{max}$ distribution scatter plot: the $<X_{max}>$ values are plotted as a function of energy. . . . . 168

7.13 The data/MC comparisons of the shower maximum ($X_{max}$): the distribution of measurements is shown for the data (black points with error bars) with (a) the proton Monte Carlo (MC), and (b), the iron MC (histograms). . . . . 169

7.14 The data/MC comparison of the shower maximum ($X_{max}$) is plotted broken up into 3 energy ranges: top to bottom, $10^{18.0} < \mathrm{E} < 10^{18.5}$ eV, $10^{18.5} < \mathrm{E} < 10^{19.0}$ eV, and $\mathrm{E} > 10^{19.0}$ eV, respectively, to show the evolution $X_{max}$ with energy. . . . . 170

7.15 Middle Drum hybrid composition result: the $<X_{max}>$ values for each data event are plotted as a function of energy overlaid with the proton and iron "rails". . . . . 171

7.16 The $X_{max}$ distributions from the data (black points), proton MC (dotted histogram), and iron MC (solid histogram): energy range = $18.0 \leq Log_{10}(E) < 18.2$ eV. . . . . 173

7.17 The $X_{max}$ distributions from the data (black points), proton MC (dotted histogram), and iron MC (solid histogram): energy range = $18.2 \leq Log_{10}(E) < 18.4$ eV. . . . . 173

7.18 The $X_{max}$ distributions from the data (black points), proton MC (dotted histogram), and iron MC (solid histogram): energy range = $18.4 \leq Log_{10}(E) < 18.6$ eV. . . . . 174

7.19 The $X_{max}$ distributions from the data (black points), proton MC (dotted histogram), and iron MC (solid histogram): energy range = $18.6 \leq Log_{10}(E) < 18.8$ eV. . . . . 174

7.20 The $X_{max}$ distributions from the data (black points), proton MC (dotted histogram), and iron MC (solid histogram): energy range = $18.8 \leq Log_{10}(E) <$ 19.0 eV. . . . . 175

7.21 The $X_{max}$ distributions from the data (black points), proton MC (dotted histogram), and iron MC (solid histogram): energy range = $19.0 \leq Log_{10}(E) <$ 19.2 eV. . . . . 175

7.22 The $X_{max}$ distributions from the data (black points), proton MC (dotted histogram), and iron MC (solid histogram): energy range = $19.2 \leq Log_{10}(E) <$ 19.4 eV. . . . . 176

7.23 The $X_{max}$ distributions from the data (black points), proton MC (dotted histogram), and iron MC (solid histogram): energy range = $19.4 \leq Log_{10}(E) <$ 19.6 eV. . . . . 176

7.24 The $X_{max}$ distributions from the data (black points), proton MC (dotted histogram), and iron MC (solid histogram): energy range = $Log_{10}(E) > 19.6$ eV. All energy bins above $Log_{10}(E) = 19.6$ eV have been combined so that the two highest energy events are in one bin. . . . . 177

7.25 The K-S values for the data-proton MC comparisons are plotted with the K-S values for the data-iron MC comparisons. . . . . 178

A.1 A MD Hybrid event display: shown is the highest energy event in the data set. 183

A.2 The highest energy event in the Middle Drum hybrid data set: it was recorded on 08/12/2010 at 7:30:33 UTC. Shown are (a) the Middle Drum event display, and (b) the Surface Detector event display. . . . . 184

A.2 Continuation of the highest energy event in the Middle Drum hybrid data set: shown are (c) the timing vs. angle plot for the geometry reconstruction, and (d) the plot of the shower profile (signal as a function of atmospheric depth). . 186

A.3 The second highest energy event in the Middle Drum hybrid data set: it was recorded on 10/08/2008 at 7:53:14 UTC. . . . . 187

A.3 Continuation of the second highest energy event in the Middle Drum hybrid data set. . . . . 188

A.4 The third highest energy event in the Middle Drum hybrid data set: it was recorded on 09/19/2009 at 8:45:52 UTC. . . . . 189

A.4 Continuation of the third highest energy event in the Middle Drum hybrid data set. . . . . 190

A.5 The fourth highest energy event in the Middle Drum hybrid data set: it was recorded on 09/29/2008 at 7:44:10 UTC. . . . . 191

A.5 Continuation of the fourth highest energy event in the Middle Drum hybrid data set. . . . . 192

A.6 The fifth highest energy event in the Middle Drum hybrid data set: it was recorded on 9/28/2008 at 5:43:03 UTC. . . . . 193

A.6 Continuation of the fifth highest energy event in the Middle Drum hybrid data set. . . . . 194

A.7 The sixth highest energy event in the Middle Drum hybrid data set: it was recorded on 4/01/2011 at 3:37:34 UTC. . . . . 195
A.7 Continuation of the sixth highest energy event in the Middle Drum hybrid data set. . . . . 196
A.8 The seventh highest energy event in the Middle Drum hybrid data set: it was recorded on 6/05/2011 at 8:38:01 UTC. . . . . 197
A.8 Continuation of the seventh highest energy event in the Middle Drum hybrid data set. . . . . 198
A.9 The eighth highest energy event in the Middle Drum hybrid data set: it was recorded on 12/07/2008 at 12:08:08 UTC. . . . . 199
A.9 Continuation of the eighth highest energy event in the Middle Drum hybrid data set. . . . . 200
A.10 The ninth highest energy event in the Middle Drum hybrid data set: it was recorded on 11/16/2009 at 9:10:14 UTC. . . . . 201
A.10 Continuation of the ninth highest energy event in the Middle Drum hybrid data set. . . . . 202
A.11 The tenth highest energy event in the Middle Drum hybrid data set: it was recorded on 5/05/2011 at 5:52:14 UTC. . . . . 203
A.11 Continuation of the tenth highest energy event in the Middle Drum hybrid data set. . . . . 204
A.12 The eleventh highest energy event in the Middle Drum hybrid data set: it was recorded on 8/21/2009 at 9:41:41 UTC. . . . . 205
A.12 Continuation of the eleventh highest energy event in the Middle Drum hybrid data set. . . . . 206

# LIST OF TABLES

3.1 This is a summary of WEAT (weather) codes. . . . . 70

6.1 A table of allowed WEAT code combinations: events that occur during times when these criteria are not met are cut from the data set. . . . . 135

6.2 Aperture calculation for showers initiated by proton primary particles: the number of events thrown and reconstructed are given for each energy bin, as well as the calculated aperture. . . . . 138

6.3 The number of data events per energy bin, after cuts, used in the spectrum calculation are given. . . . . 145

6.4 A summary of the results of a $\chi^2$ test performed to compare four analyses with the Middle Drum hybrid analysis is given. . . . . 153

7.1 The composition parameters are given for the data, proton MC, and iron MC. 171

7.2 A summary of the K-S tests performed to compare the MD hybrid data to the proton and iron Monte Carlo sets for the $X_{max}$ parameter is given. . . . . 177

# ACKNOWLEDGMENTS

I wish to thank the members of the Telescope Array Collaboration for helping me discover a fascinating research topic in cosmic rays. I especially appreciate the help I got from my committee. In particular, I want to thank Wayne Springer, who took me on as a graduate student and provided me with encouragement that helped keep me motivated in the final stages of my graduate work; John Matthews, who hired me before I started graduate school and has been an endless source of support, interesting work, and meaningful advice; and Charlie Jui, who took responsibility for me when I needed help finishing my dissertation and preparing for my defense. He spent countless hours helping me, and I learned more from him than any other single person in graduate school.

Other members of the TA collaboration who provided immeasurable help include Dmitri Ivanov, who was instrumental in my transition from hardware work into analysis work. He also was a tireless source of help with my analysis; Tareq Abu-Zayyad who has always been available with complete, well-explained answers to any questions I have for him; Doug Rodriguez, who taught me everything I needed to know to get started where he left off; and Stan Thomas, who has been a wonderful source of fascinating insights into not only the cosmic ray experiment, but also any topic that we have ever broached.

My list of friends who kept me sane during my graduate school years is too long to note here. However, they are all loved, and I couldn't have finished without their help and support.

My family has always valued education, and for this, I feel I can give them full credit for my decision to go to graduate school. My brother, Dave, has been a fantastic source of levity and insight. My sister has given me so much good advice about navigating graduate school that I would have been lost without her. And I must thank my parents for instilling in me a desire to learn, and for supporting me whole-heartedly throughout this entire endeavor. I definitely could not have finished if it weren't for their love and encouragement.

Finally, I want to thank Zayd Ma for being an incredible support system. I couldn't think of anyone who would be better to have by my side these past few years. He went through this experience with me, and every step of the way was able to take time to help

me with my work. In particular, his insightful questions helped me to understand how little I know, and kept me motivated to keep learning. I am so grateful that he is in my life.

# CHAPTER 1

# INTRODUCTION

## 1.1 Discovery of Cosmic Radiation

Victor Hess received the Nobel prize in 1936 for the "discovery of cosmic radiation." His work focused on the source of ionizing radiation, discovered by Elster, Geitel, and separately, Wilson, in 1901 [45]. Initially, Hess was making radiation measurements but was hampered by the ionizing radiation background. He hoped to reduce the background by performing his experiments at higher altitudes. Hess used balloons to study the flux of ionizing radiation with increasing altitude. He placed electroscopes in hot air balloons and flew them to altitudes up to 5300 m above seal level. He expected to confirm the common wisdom at the time: ionizing radiation was terrestrial in origin; in that case, he should have observed that the amount of radiation decreases with altitude. Instead, his results showed that the flux increases with altitude, and concluded that a significant part of the background is extra-terrestrial in origin [25] (1912).

At roughly the same time (1911) another group, led by Domenico Pacini in Italy, performed a series underwater experiments - the first of its kind. He submerged an electroscope under the sea and measured the discharge of particles there as well as on the surface. He discovered that the flux of ionizing radiation was significantly lower (20%) at a depth of 3 m than at the surface, in effect, decreasing with underwater depth. This result led him to the same conclusion as Hess: the ubiquitous ionizing "background" radiation is mostly extra-terrestrial.

One of the most notable aspects of cosmic radiation is that the flux ranges in energy from $\sim 10^9$ eV up to $\sim 10^{20}$ eV. Cosmic ray particles at the high end of the spectrum have energies more than five orders of magnitude higher than anything seen or produced on Earth. Therefore, they allow us to study elementary particle physics in an energy regime unattainable in the laboratory. Even today, the Large Hadron Collider (LHC) at Cern collides protons accelerated to $\sim 10^{13}$ eV, which is still much lower than energies seen in some cosmic ray particles. A head-on collision between two $10^{13}$ eV protons moving in

opposite directions has the same center of mass energy, $\sqrt{s}$, as a proton with $\sim 10^{16}$ eV colliding with a stationary Nitrogen nucleus.

## 1.2 Flux of Cosmic Ray Particles

Figure 1.1 shows the compilation of cosmic ray flux data from 11 different experiments in the field [23]. These experiments span more than 11 orders of magnitude in energy and 32 orders of magnitude in flux. On a log vs log plot, the fall of the flux is approximately linear. For every order of magnitude increase in energy, the flux decreases by $\sim$3 orders of magnitude with slight changes in spectral index. This power law relationship holds over nearly the entire range in the figure. The work in this dissertation is focused on particles in the Ultra High Energy (UHE) range, which refers to energies, E $\geq 10^{17}$ eV, where the flux has fallen to less than 1 particle/km$^2$/year.

## 1.3 Extensive Air Showers

In the lower energy ranges, direct detection using satellites and balloons are used to detect and study cosmic rays at the top of the atmosphere. However, due to the steeply falling flux of cosmic ray particles in the in the UHE regime, these techniques are unfeasible. Experiments must make use of indirect detection techniques. Predominantly, Ultra High Energy Cosmic Rays (UHERCRs) have been studied using Extensive Air Showers (EAS) created when these particles interact with the atmosphere.

The initial interaction between a cosmic ray particle and the atmosphere is hadronic and produces secondary particles of many different types, mostly mesons. Figure 1.2 shows the three major components of the EAS: the hadronic component, the electromagnetic cascade, and the muonic component [23]. The most abundant secondary particle from hadronic collisions is the pion. Pions are produced with roughly equal charge distributions. The charged pions will either go on to produce more hadronic collisions, generating more pions, or decay weakly into muons and neutrinos, generating the muonic component of the EAS. The neutral pions decay electromagnetically to generate the electromagnetic cascade.

### 1.3.1 Muonic Component

Charged pions from any hadronic collision decay into muons and neutrinos nearly 100% of the time ($\pi^{\pm} \longrightarrow \mu^{\pm} + \nu$ ). The mean lifetime of a charged pion is relatively long ($2.6 \times 10^{-8}$ s) because the decay is via the weak interaction. Most of the muonic component of the shower is generated through these decays which occur mostly in the upper atmosphere,

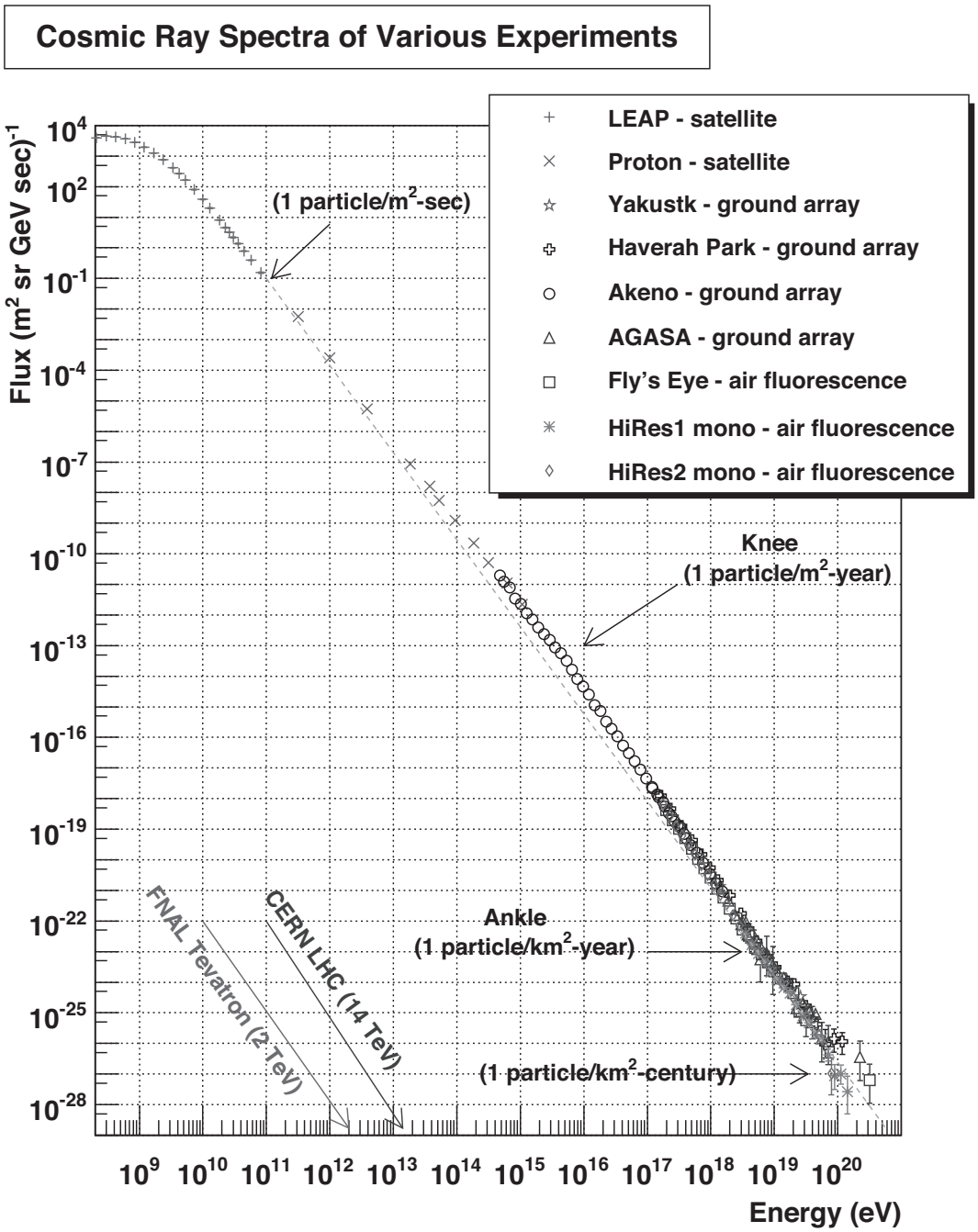


**Figure 1.1**. Flux of cosmic ray particles: the energy spectrum of cosmic ray particles measured by various experiments on a log-log plot. The spectrum is relatively featureless and follows a simple power law, $E^{-3}$ (dashed line). There is a slight kink near $10^{16}$ eV which is a known spectral feature, called the "knee."

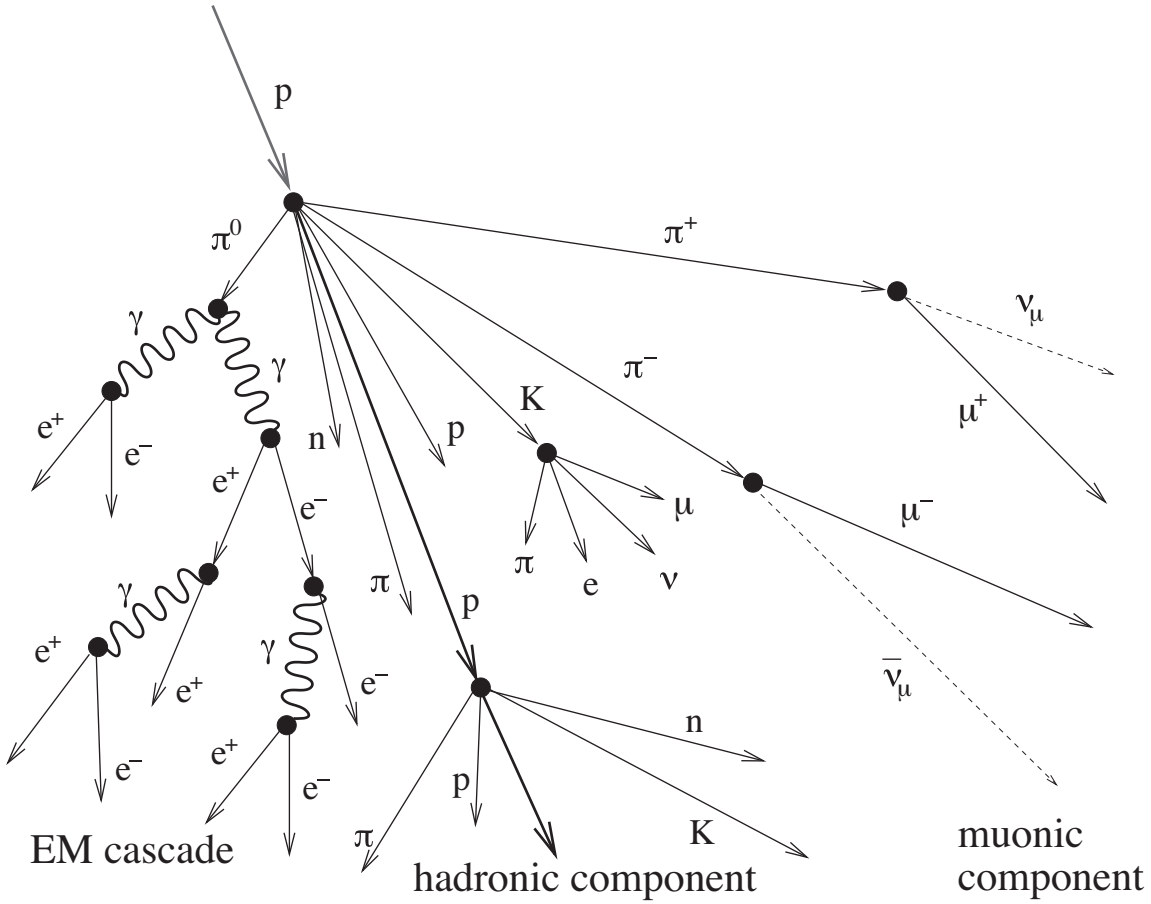


**Figure 1.2**. Extensive Air Shower (EAS): A diagram showing the EAS development. Its 3 major components are the electromagnetic cascade, the hadronic component, and the muonic component.

where the air density is such that the charged pions have more of a chance to decay before colliding. Secondary muons and neutrinos undergo hard collisions only very rarely in the atmosphere.

### 1.3.2 Hadronic Component

As the shower progresses, collisions between charged pions and other long-lived hadrons with nuclei in the atmosphere become more abundant. Most of these collisions result in the same fractional abundance of secondary particles, though the total number of particles will change with energy. Typically, the secondary particles are in the form of pions (∼60%), kaons (∼15%), and nucleons (∼10%). The pions are produced in roughly equal numbers so that 1/3 of the pions, the $\pi^0$ third, will generate part of the electromagnetic portion of the shower. Therefore, roughly 20% of the energy in any hadronic interaction is transferred immediately to the electromagnetic part of the shower. Due to these interactions, the electromagnetic portion of the shower becomes dominant after only a few generations of collisions, while a small hadronic shower is maintained.

### 1.3.3 Electromagnetic Cascade

The electromagnetic part of the shower becomes important due to the fact that it is not only the largest part of the shower, but it is also the component by which the shower is detected. At 8.4 $\times 10^{-17}$ s, the decay time of a $\pi^0$ is much shorter than that of its charged partners, because this decay is purely electromagnetic. So it will essentially never interact before it decays. The primary decay of the $\pi^0$ particle is into two photons ($\pi^0 \longrightarrow \gamma + \gamma$). Each photon produced initiates its own electromagnetic cascade. The mechanisms involved in this cascade are (1) pair production and (2) Bremsstrahlung. Pair production is the result of an interaction between a high energy photon ($\geq$10 MeV) and a charged nucleus ($\gamma + A \longrightarrow e^- + e^+ + A$). The radiation length, or $X_0$, for pair production from a photon is 7/9 of the mean free path of a photon. Bremsstrahlung radiation is the result of an electron or positron scattering off of a heavy nucleus and emitting a photon ($e^{\pm} \longrightarrow e^{\pm} + \gamma$). The radiation length for Bremsstrahlung radiation of electrons is proportional to the exponential rate of energy loss. In air, at standard temperature and pressure, it is 36.5 g/cm$^2$, and is approximately equal to the radiation length for pair production.

Figure 1.3 gives an idea of how pair production and Bremsstrahlung processes work in tandem to grow the size of the electromagnetic shower at each radiation length (recall that

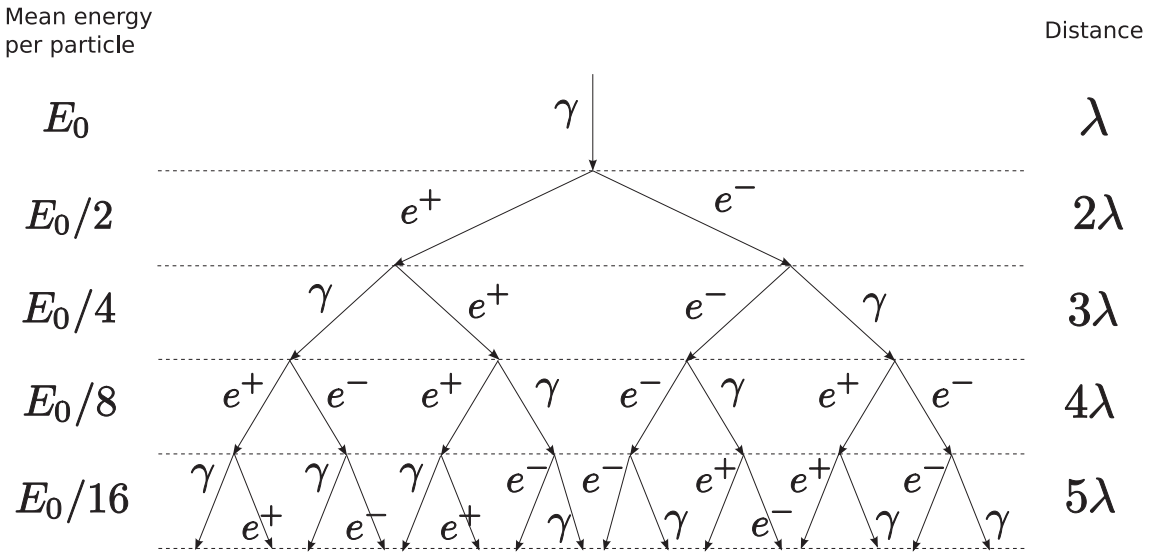


**Figure 1.3**. The Heitler model for the branching of the Electromagnetic (EM) component of an EAS: this diagram shows how pair production and Bremsstrahlung radiation work together in the development of the EM cascade. At each radiation length, $\lambda$, the number of particles in the EM cascade doubles, and the amount of energy per particle is cut in half. Once the amount of energy per particle is no longer high enough to continue these processes, the shower reaches a maximum, and begins to decrease in size.

these lengths are roughly equivalent in the two processes) [23]. At each radiation length level, the number of particles is doubled, and the average energy per particle is halved.

As the energy of each photon decreases, pair production becomes less and less likely, and Compton scattering becomes dominant ($\gamma + A \longrightarrow \gamma + e^- + A^+$). When this occurs, the shower no longer increases in size. Similarly, at sufficiently low energies, electrons interact with the atmosphere through ionization rather than through Bremsstrahlung and lose energy without generating more particles. Beyond this point, the shower begins to decay exponentially in size (number of particles). The point at which the shower size reaches a maximum is referred to as the shower maximum. The slant depth of this point is denoted $X_{max}$.

## 1.4 Cosmic Ray Physics

Cosmic ray particles in the UHE regime are not well understood. Detectors must have a large aperture and exposure time to generate enough statistics for study, and the indirect detection of the particles leads to systematic uncertainties in the measurement. Because of these difficulties, many of the physical questions about UHECRs have not been answered.

The basic questions are "What are these particles?", "How are they accelerated?", "What are their sources?", and "How do they get here?" Experiments endeavor to answer these questions through studies of energy spectrum, anisotropy, and composition.

### 1.4.1 Energy Spectrum

The primary focus of this dissertation is to measure the energy spectrum of UHECRs. Recall that a power law describes the flux of UHECRs. Deviations from the power law, or features in the cosmic ray spectrum, give clues about possible acceleration mechanisms, propagation losses, and the composition of the particles. Recent energy spectrum results will be discussed in detail in Chapter 2. While the absolute energy scale differs moderately from experiment to experiment, the major structures can be found in all recent spectrum measurements. The features of note in the UHE spectrum are (a) the "ankle," a dip in the spectrum at $3.5 - 4.5 \times 10^{18}$ eV [2], and (b) the GZK cut off at $6 \times 10^{19}$ eV. The observation of the GZK cut-off is the most important recent result in the UHE regime. The cut-off refers to the prediction by Greisen, and independently, Zatsepin and Kuz'min which show that a proton with high enough energy ($\sim 6 \times 10^{19}$ eV) will interact with the Cosmic Microwave Background (CMB), which has average energy of 0.235 meV [22, 46].

The highest energy cosmic ray particles of galactic origin are expected to be composed mostly of iron. This is due to the abundance of iron within the galaxy and its high atomic number. As the heaviest, stable element created by stellar fusion, iron is more easily confined within the galactic magnetic field than lighter particles. Furthermore, one of the leading candidate cosmic ray acceleration mechanisms, Fermi Shock Acceleration, accelerates particles at a rate proportional to Z. This acceleration mechanism refers to the interactions of particles with shock fronts, such as those from supernovae explosions in interstellar space. In this type of interaction, the macroscopic kinetic energy from the shock front can be transferred to a charged particle. As described by Gaisser [21], each collision between an particle and a shock front results in an increase in energy which is proportional to the initial energy of the particle ($\Delta E = \xi E_0$). After a given number of collisions, the number of particles above a particular energy, E that remain within the acceleration region is given by equation 1.1, and the exponent is written out in equation 1.2.

$$N \propto \frac{1}{P_{esc}} \left( \frac{E}{E_0} \right)^{-\gamma} \tag{1.1}$$

$$\gamma = \frac{ln\left(\frac{1}{1-P_{esc}}\right)}{ln(1+\xi)} \tag{1.2}$$

Here, $P_{esc}$ represents the probability that a particle will escape from the acceleration region, and $\xi$ is the amount by which the energy of the particle will be increased with each collision. Note that the Fermi Shock Acceleration naturally results in a universal power law, with index =2. Although the index is not quite right, the ability to obtain this power law with no further assumptions is the major reason that it is considered one of the best acceleration models in the field.

For extragalactic cosmic ray particles, the acceleration mechanisms may be the same, but the physical observational result on Earth is likely different. Although iron nuclei are accelerated more readily in shock acceleration, particles in the UHE regime are expected to be light, proton-like for extragalactic flux. Two major reasons for this are containment, and nuclear spallation. An iron nucleus is more likely to be confined to its source galaxy because of its high atomic number. Also, due to the large distances, it will interact before being observed on Earth. Interactions with CMB photons can result in nuclear spallation. As the iron nucleus interacts, it ejects nucleons; with enough space, it will be reduced to a fraction of its original number of nucleons. The transition from galactic to extragalactic particles (expected to be from heavy to light) is one of the most compelling topics of the physics in the UHE regime.

As observed, the GZK cut-off is directly related to the composition of cosmic ray particles in the UHE regime because it is the consequence of interactions between the CMB and protons. Proton dominance at the highest energies is consistent with the attenuation of nuclei in propagating to Earth. Equation 1.3 shows this inelastic collision which results in the photo-production of the $\Delta^+$ resonance.

$$\begin{aligned} p + \gamma_{CMB} \longrightarrow \Delta^+(1232MeV) &\longrightarrow p + \pi^0 \\ &\longrightarrow n + \pi^+ \left(\longrightarrow\ p + \nu + \pi^+\right) \end{aligned} \tag{1.3}$$

This interaction results in a suppression of the observed flux of cosmic ray protons at energies $\geq 6 \times 10^{19}$ eV. It also implies a pile-up just below the GZK energy threshold from the super-GZK particles being degraded in energy in these interactions. Noting that the energy spectrum does indeed show a suppression at the anticipated GZK energy threshold, as well as a pile-up just below, a good argument can be made that the highest energy particles in the spectrum are protons.

### 1.4.2 Anisotropy

Anisotropy refers to study of the incident directions of cosmic ray particles and their correlations with possible sources. As noted in the previous section, the cosmic ray particles in the UHE regime are thought to be of extragalactic origin, though their sources remain unknown. We look for these sources via small scale anisotropy as well as large scale anisotropy. The idea of small scale anisotropy is to determine the direction from which cosmic ray particles originate, and to search for possible sources in their vicinity. Unfortunately, any charged particle traveling through intergalactic space will be subject to bending from magnetic fields, both inter- and intra-galactic. The galactic field has has a strength on the order of $\sim$1 microgauss, while the extragalactic field is on the order of $\sim$10 nanogauss [39]. While this does complicate studies, particles with energies, E $> 10^{19}$ eV are expected to experience deflections of only a few degrees over a scale of $\sim$100 Mpc (redshift $z \approx 0.025$). This distance is also the expected attenuation length for the GZK interaction. Experiments search for large scale anisotropy by looking for correlations with the matter distribution or a dipole structure with respect to the galactic or super-galactic plane, or centers. Using this type of search one can at least localize the origin of the UHECRs, if not pinpoint the actual sources.

### 1.4.3 Composition

The secondary goal of this dissertation is to perform a preliminary composition study. Due to indirect detection of UHECRs, determining particle type cannot be done on an event-by-event basis. Instead, a distribution of events is used in comparison with simulated distributions to look for trends. Primarily, experiments have studied the parameter of the shower that describes the atmospheric depth of the shower maximum, or $X_{max}$, to infer information about particle type. In all showers, for a given species, the higher the energy of the primary particle, the deeper the penetration of the shower. This means that as a function of energy, the $X_{max}$ parameter increases logarithmically. However, showers generated by light particles and heavy particles behave differently, and this behavior is exploited while making composition measurements.

Light cosmic ray primary particles, such as protons, have smaller cross sections. This allows them to penetrate relatively far into the atmosphere before their first interaction. The shower will therefore take longer to develop, resulting in an average $X_{max}$ value that is relatively large. Heavy particles, such as iron nuclei, will interact almost immediately in

the atmosphere, due to their large cross section. In addition, the first interaction of a heavy particle will result in more secondary particles. Because the energy of the primary particle is spread across more particles and interacts early, the shower develops sooner, resulting in a smaller average $X_{max}$. Comparisons between distributions of simulated light primaries with simulated heavy primaries show that while the average values of $X_{max}$ differ, the distributions of many events overlap. In fact, shower-to-shower fluctuations are comparable in magnitude to the difference between proton and iron nuclei generated showers. In the next chapter, recent $X_{max}$-based composition results in the UHE regime will be discussed. My composition study and results will be shown in Chapter 7.

## 1.5 Ultra-High Energy Cosmic Ray Detection

The detection of UHECRs relies on the EAS generated by the high energy particles as they reach the atmosphere. There are two major methods for detecting these showers: surface detection and fluorescence detection.

Surface detectors have been around the longest and are the most common method for studying high energy particle EAS. Bruno Rossi (1934) and Pierre Auger (who discovered EAS [13], 1939) were early pioneers of this observational technique. Surface detectors take advantage of the sheer number of particles generated in high energy cosmic ray EAS, and how widely (up to ∼10 km) they are distributed. These detectors are usually made using scintillators or water tanks for detecting charged particles.

One advantage of scintillation or water detectors is that the size of the array can be changed depending on the energy range of the cosmic ray particles being studied. The energy threshold is dependent on the detector spacing. For example, by spacing the detectors farther and farther apart, and requiring a coincidence signal, only large showers, generated by particles with high energies will be detected. And in doing so, the overall size of the detector is made larger, for the same cost.

In water tanks, charged particles generate Cherenkov light. This light is collected using one or several Photo-Multiplier Tubes (PMT) inside the tank. Scintillation detectors are usually constructed out of organic plastics that produce luminescence when the charged particles interact with the plastic and deposit energy. This light can then be directed to a PMT via wavelength shifting fibers, or collected directly from the scintillator by attaching the PMT. The Telescope Array scintillation detectors were used in this study, and will therefore be discussed in detail in Chapter 3.

Figure 1.4 shows a schematic of a fluorescence telescope observing a UHECR shower [38]. The fluorescence technique for studying UHECR was first successfully used by the University of Utah Cosmic Ray group. Fluorescence telescopes are used in a number of UHECR experiments to measure the longitudinal profile of an EAS generated by UHECR. These telescopes make use of the fact that as an EAS develops, it produces ultraviolet light through interactions with the nitrogen in the atmosphere. Because this light is generated isotropically, a small fraction of it will be in the direction of the telescope. The telescope consists of a mirror that focuses the light from the shower onto PMT pixels placed at the focal plane. Because the light is detected as the shower propagates, the longitudinal development of the shower can be measured. The fluorescence technique is also used in the Telescope Array experiment, and will therefore be discussed in detail in Chapter 3.

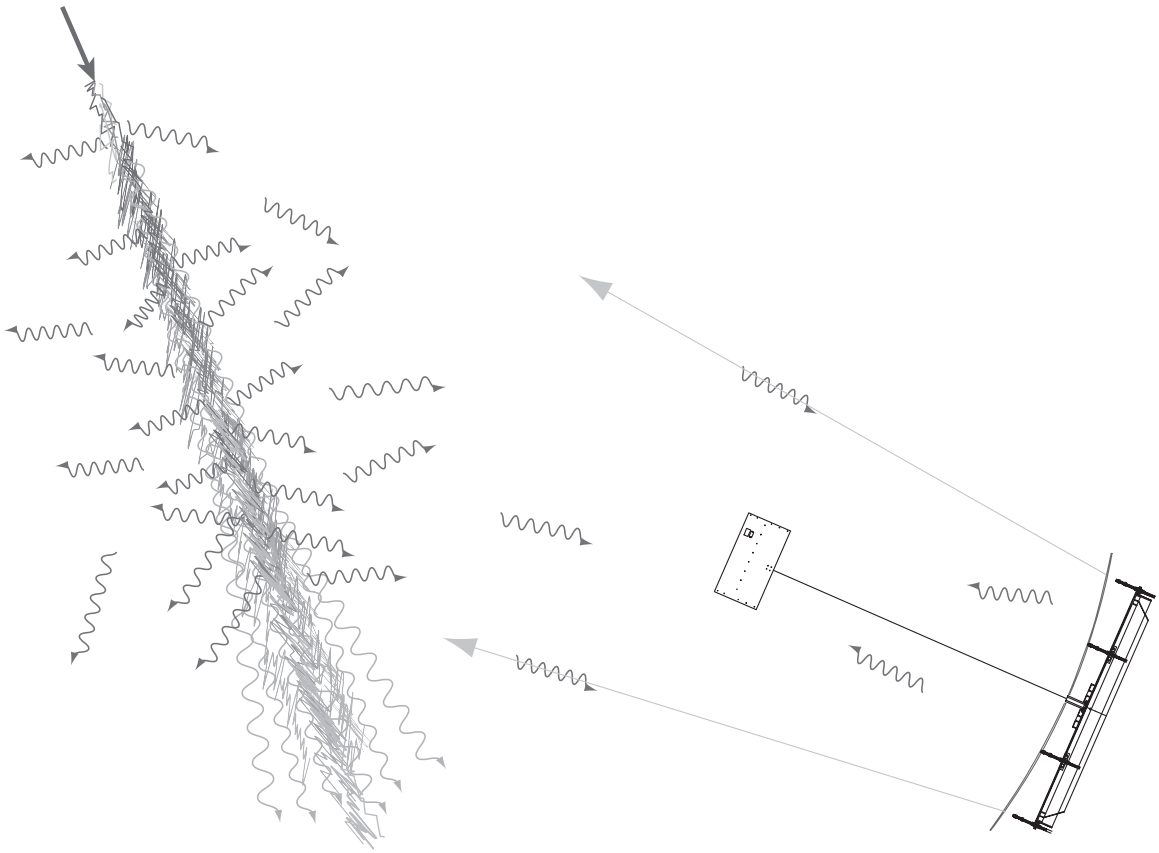

**Figure 1.4**. Fluorescence Detection (FD): this is a schematic of the Telescope Array fluorescence telescope observation of a cosmic ray induced air shower. The cosmic ray enters the atmosphere (upper left) and collides. This generates an extensive air shower containing billions of secondary particles. The charged particles in the shower excite the nitrogen in the atmosphere which in turn emits UV light as they de-excite. Some of this light is gathered by the telescope mirrors and focused onto the cameras (lower right).

# CHAPTER 2

# RECENT RESULTS OF ULTRA HIGH ENERGY COSMIC RAY RESEARCH

The primary focus of this dissertation is to study the energy spectrum of Ultra High Energy Cosmic Rays (UHECRs) using hybrid Telescope Array Middle Drum (MD) data and secondarily to make an initial composition measurement using the same hybrid data set. Historically, only a handful of experiments have had the capability of measuring cosmic rays in the UHE regime (i.e. $E > 10^{17}$ eV). A brief summary of the past results is given in this chapter to bring this work into proper scientific context. Relevant energy spectrum measurements have been made by the Fly's Eye, Akeno Giant Air Shower Array (AGASA), as well as the High Resolution Fly's Eye (HiRes) experiments. For composition results, the Fly's Eye, HiRes-MIA, and HiRes stereo measurements will be discussed in comparison with that of the Pierre Auger Observatory (PAO).

## 2.1 Fly's Eye

The Fly's Eye experiment was built in Dugway, Utah by the cosmic ray physics group of the University of Utah. The Fly's Eye was the first experiment to extract physics measurements from the fluorescence technique. It was constructed after a successful prototype test in 1976 where Fly's Eye-style mirrors and cameras were used to detect cosmic ray air showers in coincidence with the Volcano Ranch ground array.

The Fly's Eye experiment consisted of two detectors. The Fly's Eye I (FEI) comprised 67 telescopes, arranged to view the full sky. Each telescope was instrumented with a camera consisting of 12 or 14 Photo-Multiplier Tube (PMT) pixels, which viewed a 5° cone of the sky. FEI operated between 1981-1993, initially in monocular mode. In 1986, a second site, Fly's Eye II (FEII) was added to provide stereoscopic observation with 36 additional telescopes located 3.4 km from FEI. The FEII telescopes viewed half of the sky, in the direction of FEI. A typical event from the Fly's Eye is shown in Figure 2.1 [17].

The energy spectrum measured by the Fly's Eye experiment in monocular mode is shown

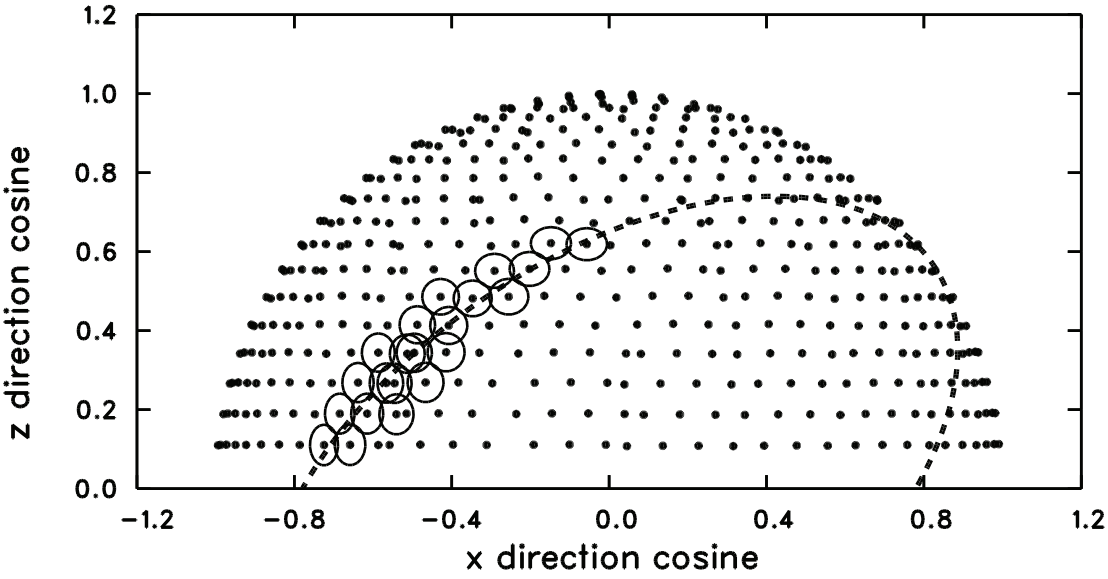


**Figure 2.1**. Fly's Eye (FE) event display: the telescopes were positioned to view the entire sky in a dome-like shape. The dots represent the pointing direction of the PMTs. The circles indicate signals from a cosmic ray event as it passes through the line of sight. The dashed line represents the Shower Detector Plane (SDP), or the intersection of the plane of the event through the center of the detector, generating a "great circle". Reproduced by permission of the AAS.

in Figure 2.2 [16]. The FEI monocular spectrum contained the first convincing super-GZK event which was reconstructed with an energy of $3 \times 10^{20}$ eV. While the statistics of the monocular spectrum were relatively high, the energy resolution (∼30-35%) was not good enough to see any detailed structure. The stereo spectrum from the joint FEI and FEII is shown in Figure 2.3 [16]. Note that using events that were reconstructed in stereo mode improved the energy resolution sufficiently (∼20-25%) to resolve the structure of the "ankle" structure, visible in Figure 2.4.

The composition measurement made using the Fly's Eye stereo data is shown in Figure 2.4 [16]. The result of $X_{max}$ measurements are shown as compared with model simulations of proton and iron. The elongation rate of the data (i.e., d$<X_{max}>$/dlogE) was inconsistent with that expected from a single component. The FE group concluded that a transition from heavy primary particles to light primary particles occurs between $10^{18} - 10^{19}$ eV. Figures 2.4 and 2.5 each show a two-component fit to the Fly's Eye stereo spectrum (diamonds), while the dashed lines represent the two single-power index spectra for protons and iron nuclei. The energy spectra of iron and proton, (spectral indices and normalizations), were used as the free parameters in the fit, and the observed stereo spectrum was simultaneously fit with $<X_{max}>$ vs. log(E) using the two components (i.e., a mixed composition of proton and iron nuclei, shown with the diamonds in both figures). The two figures together give a picture consistent with that expected from the transition from a heavy (iron) galactic flux for E $< 10^{18}$ eV to a light, (proton) extragalactic flux above $10^{19}$ eV [16].

## 2.2 Akeno Giant Air Shower Array

The Akeno Giant Air Shower Array (AGASA) was built in Akeno, Japan, by a consortium led by the Institute for Cosmic Ray Research (ICRR) of the University of Tokyo. It consisted of a large surface array of surface scintillator detectors built to study the sources of UHECRs. The array covered an area of 100 km$^2$ and consisted of 111 scintillator detectors, along with 27 muon detectors. The AGASA experiment operated from 1990 to 2006.

The AGASA energy spectrum is shown in Figure 2.6 [41]. The dashed curve on the plot represents the spectrum that is calculated using a model of the Universe in which the extragalactic sources are uniformly distributed. The important point to note is that the AGASA results supported a spectrum that extends beyond $10^{20}$ eV, implying that the expected flux suppression from the GZK effect [22] was missing, and some new physics beyond the standard model would be needed to explain this.

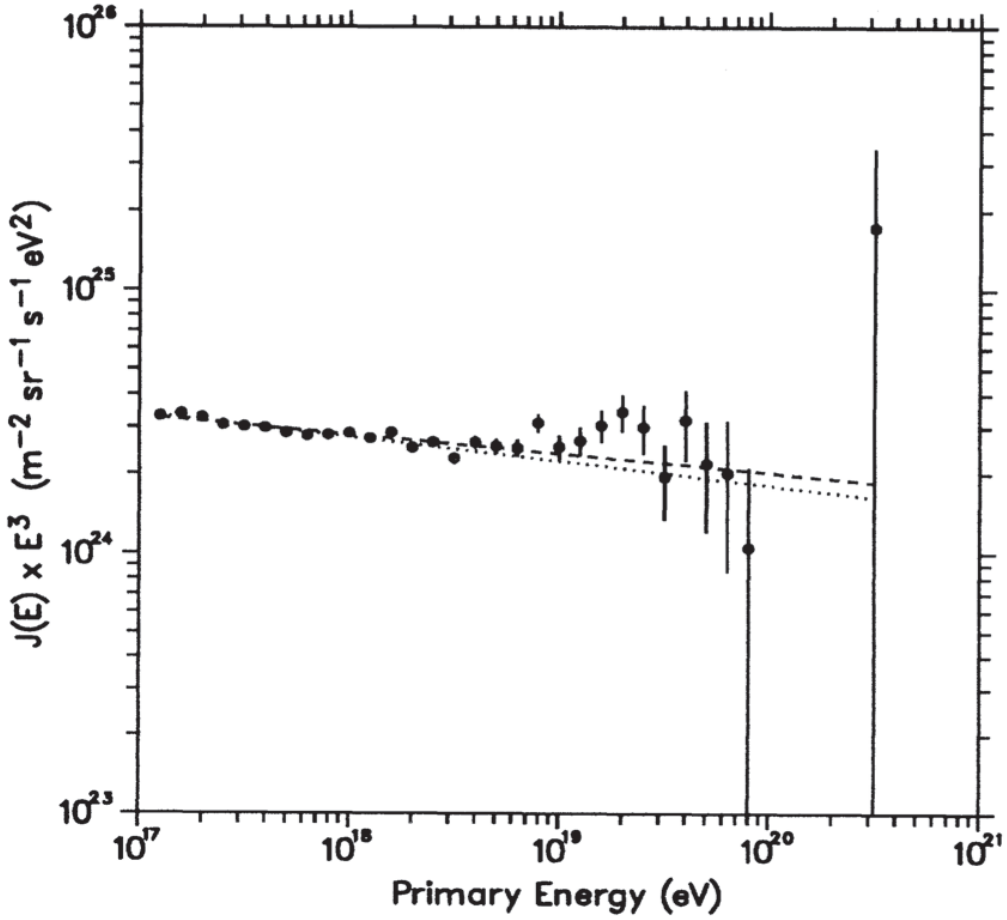


**Figure 2.2**. Fly's Eye I (FEI) monocular energy spectrum: shown is the energy spectrum as seen by FEI in monocular mode as well as the fit. The resolution was ∼30-35% which is not sufficient to see any detailed structure. The highest energy cosmic ray event ever recorded is shown in this spectrum with an energy of $3.2 \times 10^{20}$ eV. Copyright (1993) by the American Physical Society $http://prl.org/abstract/PRL/v71/i21/p3401\_1$.

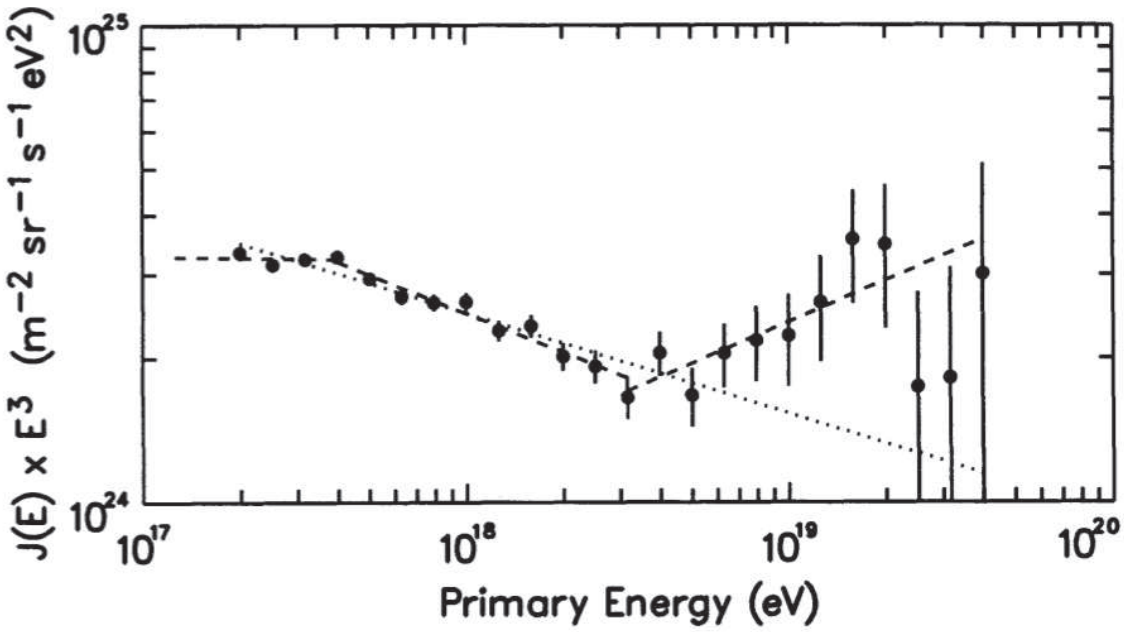


**Figure 2.3**. The Fly's Eye stereo energy spectrum: shown is the energy spectrum as seen by FEI and FEII in stereo mode. The improved energy resolution (∼20-25%) in stereo mode allows one to discern structure in the spectrum. A dip in the spectrum can be clearly seen near $\sim 10^{18.5}$ eV. This is known as the "ankle." Copyright (1993) by the American Physical Society $http://prl.aps.org/abstract/PRL/v71/i21/p3401\_1$.

## 2.3 HiRes-MIA

The High Resolution Fly's Eye (HiRes) Prototype detector was a follow-on to the Fly's Eye experiment. It was constructed to test the optical design of the proposed new HiRes experiment. It used the same fluorescence detection technique as the Fly's Eye experiment, but with larger mirrors and smaller pixels. Specifically, the 14 mirrors were 4 $m^2$ in area and imaged light onto 256 pixels, each of which viewed 1° of the sky. The telescopes used sample-and-hold electronics. The new hardware allowed HiRes to see showers three times farther than Fly's Eye and was ∼10 times more sensitive. The array of telescopes overlooked the MIchigan Muon Array (MIA), an array of 1024 buried muon detectors. MIA consisted of 16 patches of 64 scintillation counters and covered an active area of 2500 $m^2$ [9]. The 14 telescopes in the prototype were reused in the HiRes-1 experiment, and are the same telescopes used at the Middle Drum detector at Telescope Array. They will be described in detail in Chapter 3. Figure 2.7 shows an event display from the HiRes Prototype, and 2.8 shows where the MIA ground detector was located in reference to the HiRes sites. The 14 telescopes of the HiRes Prototype were positioned in a "tower" arrangement. As shown in

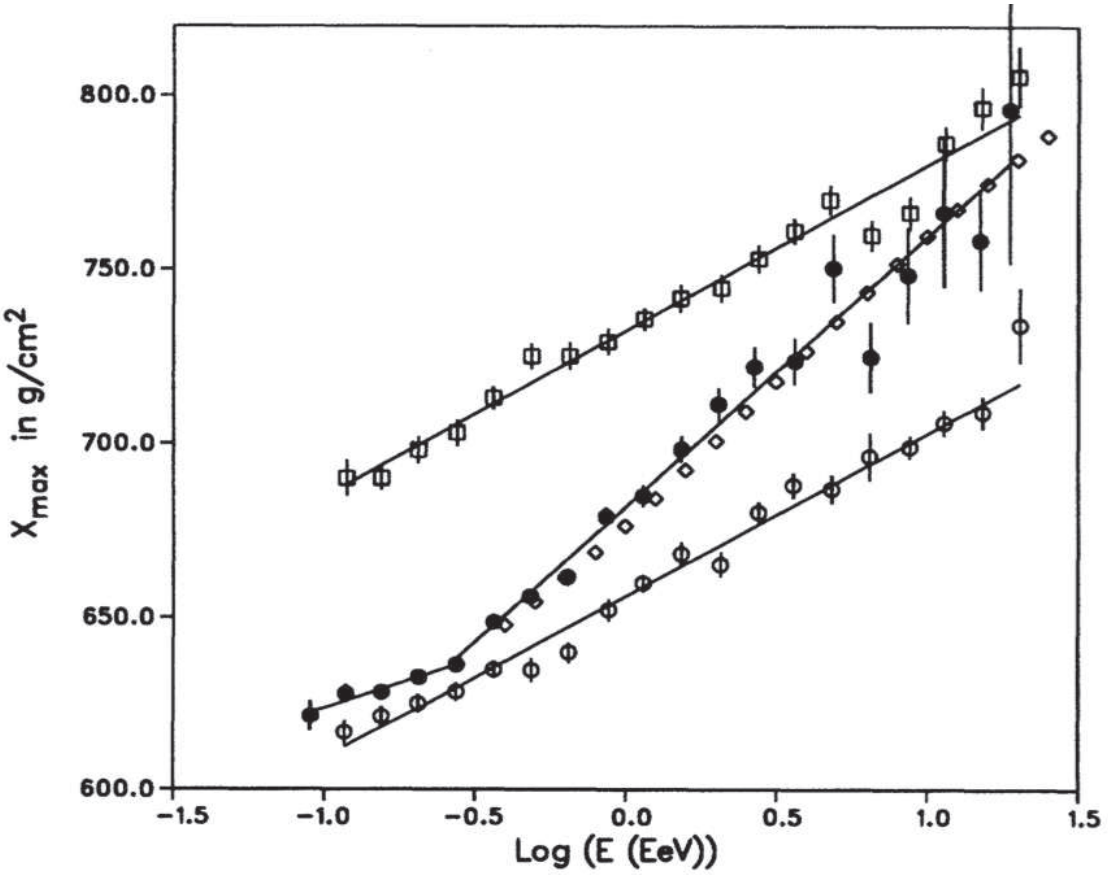


**Figure 2.4**. The Fly's Eye composition measurement, using the $X_{max}$ technique: The data shows a transition from heavy to light particles. The open squares represent the reconstruction of data from a proton model while the open circles represent an iron model. The data is shown as filled circles. The diamonds represent a simultaneous two-component fit using a mixed composition of proton and iron nuclei. Copyright (1993) by the American Physical Society $http://prl.aps.org/abstract/PRL/v71/i21/p3401\_1$.

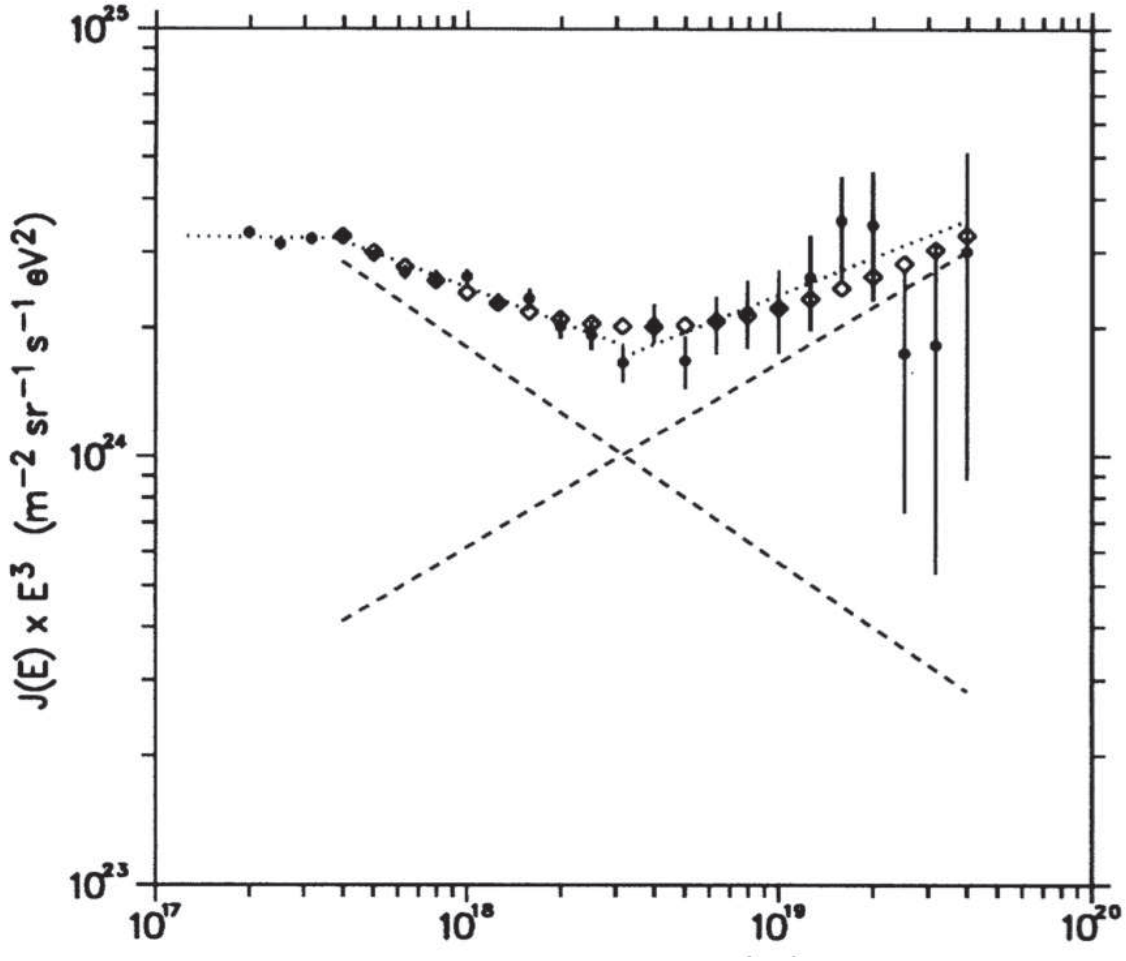


**Figure 2.5**. The stereo Fly's Eye energy spectrum: shown is a simultaneous two-component fit using a mixed composition of proton and iron nuclei (diamonds). The dashed lines are the two single-power index spectra for the protons and iron nuclei. Copyright (1993) by the American Physical Society $http://prl.aps.org/abstract/PRL/v71/i21/p3401\_1$.

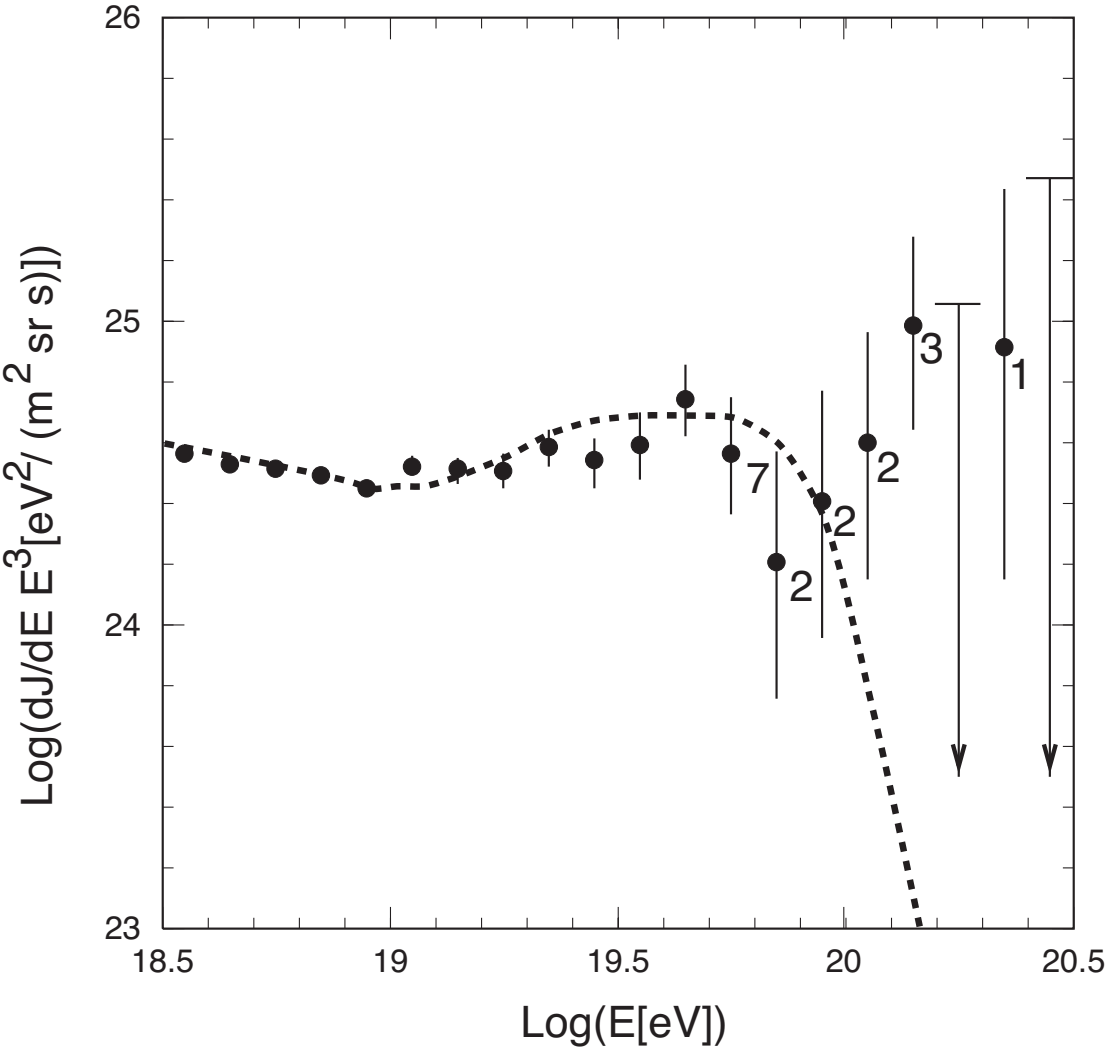


**Figure 2.6**. AGASA energy spectrum: shown is the flux of UHECRs measured by the AGASA experiment. The number of events in each of the highest energy bins is indicated on the plot. Note that arrows are plotted in bins with no events and represent a 90% confidence level on the upper limits in those bins. The three highest points indicate 6 super-GZK events, which imply a spectrum without a GZK suppression. Copyright (1998) by the American Physical Society $http://prl.aps.org/abstract/PRL/v81/i6/p1163\_1$.

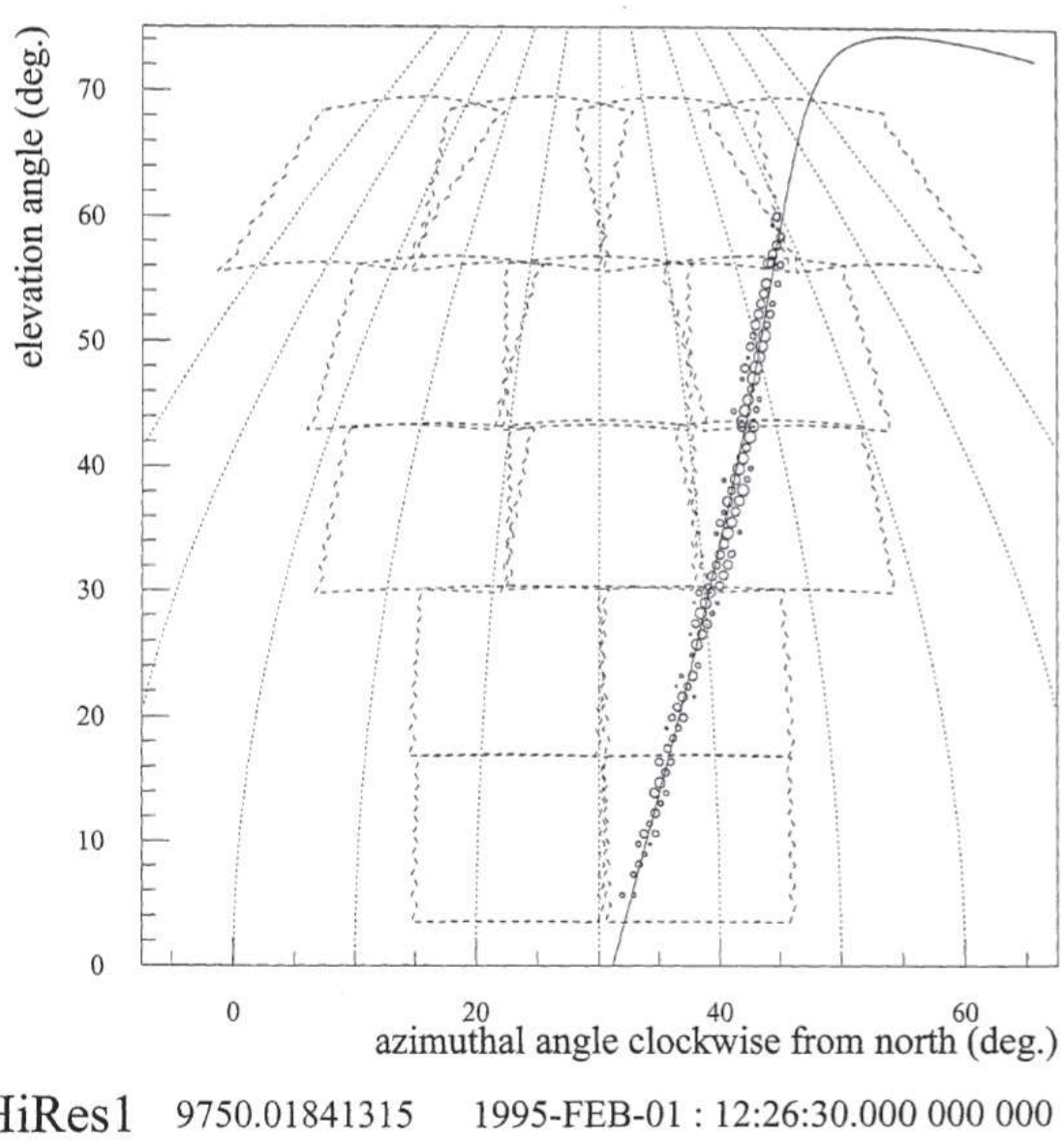


**Figure 2.7**. An event display from the HiRes Prototype fluorescence telescope: shown are the 14 telescopes arranged as they view the sky. Circles indicate signal from an EAS track. The line indicates the fit to the shower geometry.

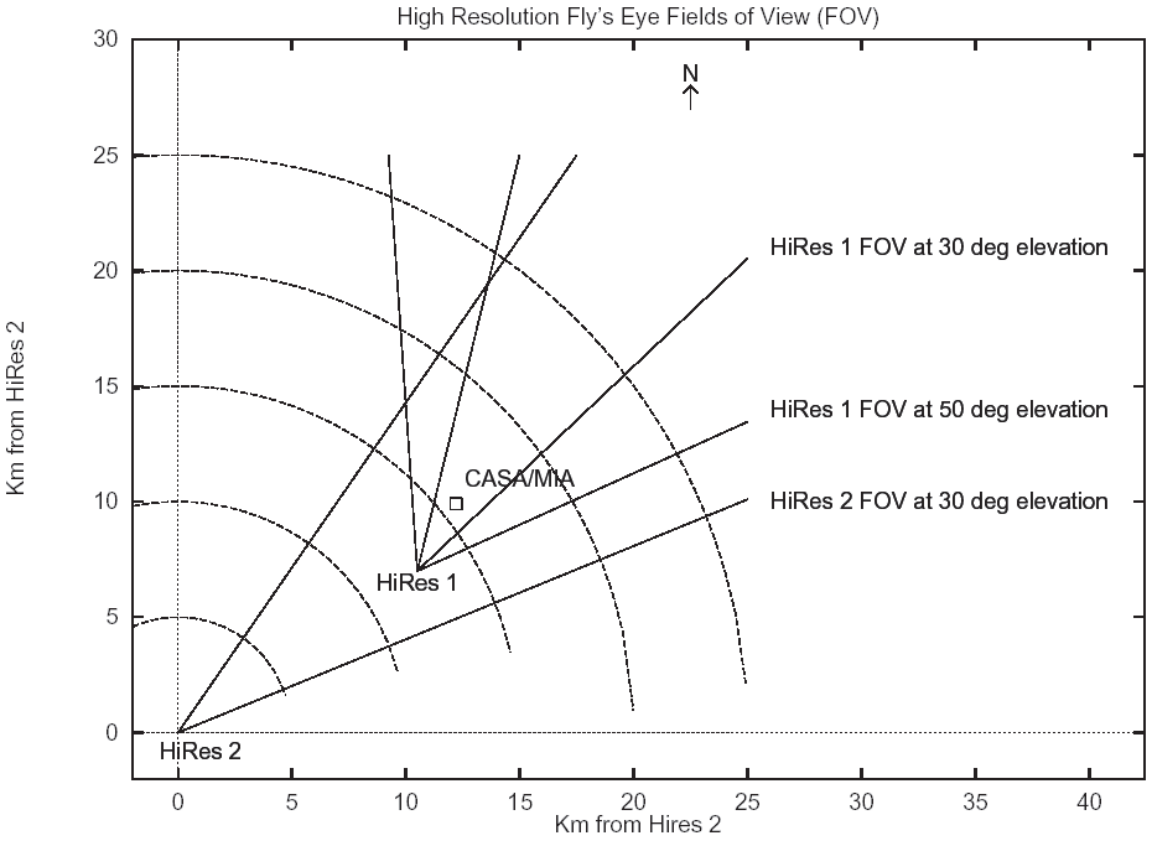


**Figure 2.8**. An overview of the placement of the MIchigan Muon Array (MIA): it is shown relative to the HiRes site. The HiRes prototype was built at the HiRes-1 site, overlooking the MIA array, ∼3 km to its north-east.

the figure, each row of telescopes was angled to view higher elevation angles. The overall detector was able to view up to 70° in elevation. The telescopes which view higher elevation angles have a lower energy threshold because the $X_{max}$ value for low energy events occurs earlier in the shower development, and is visible higher up in the sky. The HiRes Prototype was operational from 1992 through 1996.

The energy spectrum measured by the HiRes Prototype with the MIA ground array in hybrid mode is shown in Figure 2.9 [9]. The Fly's Eye stereo spectrum is included for reference, and the two spectra are in good agreement, which also indicates that the HiRes Protoype and the FE stereo had the same energy scale.

The first hybrid composition results were given in [3], and are shown in Figure 2.10. Data from the HiRes experiment are shown in the figure for reference and will be discussed in the next section. The HiRes-MIA results are shown in the range from $10^{17.0} - 10^{18.0}$ eV, covering only the lower range in energy of the composition results measured by Fly's Eye ($10^{17.0} - 10^{19.2}$ eV). While both results show a transition from heavy to light particles, the HiRes-MIA result shows the transition happening lower in energy by an order of magnitude than does the Fly's Eye result. The resolution in $X_{max}$ measured from the models that were used was 25 g/cm$^2$ [9], which is much smaller than that measured by Fly's Eye, ∼40 g/cm$^2$ [16].

## 2.4 High Resolution Fly's Eye

The High Resolution Fly's Eye (HiRes) experiment was built to expand the detector aperture from that of the Fly's Eye experiment by a factor of 10. The 14 telescopes from the HiRes Prototype were redistributed, and eight new telescopes were added, some with the addition of a newer revision of electronics (Rev. 4). Combined, these 22 telescopes comprised the HiRes-1 site. The HiRes-1 site began operation in the spring of 1997. Each of the 22 mirrors viewed 3° to 17° in elevation, and were situated in a "ring" to view nearly 360° in azimuth. The HiRes-2 site began operation in 2000. This site was instrumented with a new set of 42 telescopes which were built using a new flash ADC board. The site was also configured in a "ring" to view 360° in azimuth, but added a second set of mirrors that viewed 17° to 31° in elevation, allowing the detector to observe longer track lengths of showers. The two sites were ∼12 km apart and allowed for viewing showers in stereo, as did the original Fly's Eye. The HiRes experiment ran from the spring of 1997 through April 2006. A HiRes event display is shown in Figure 2.11 [23].

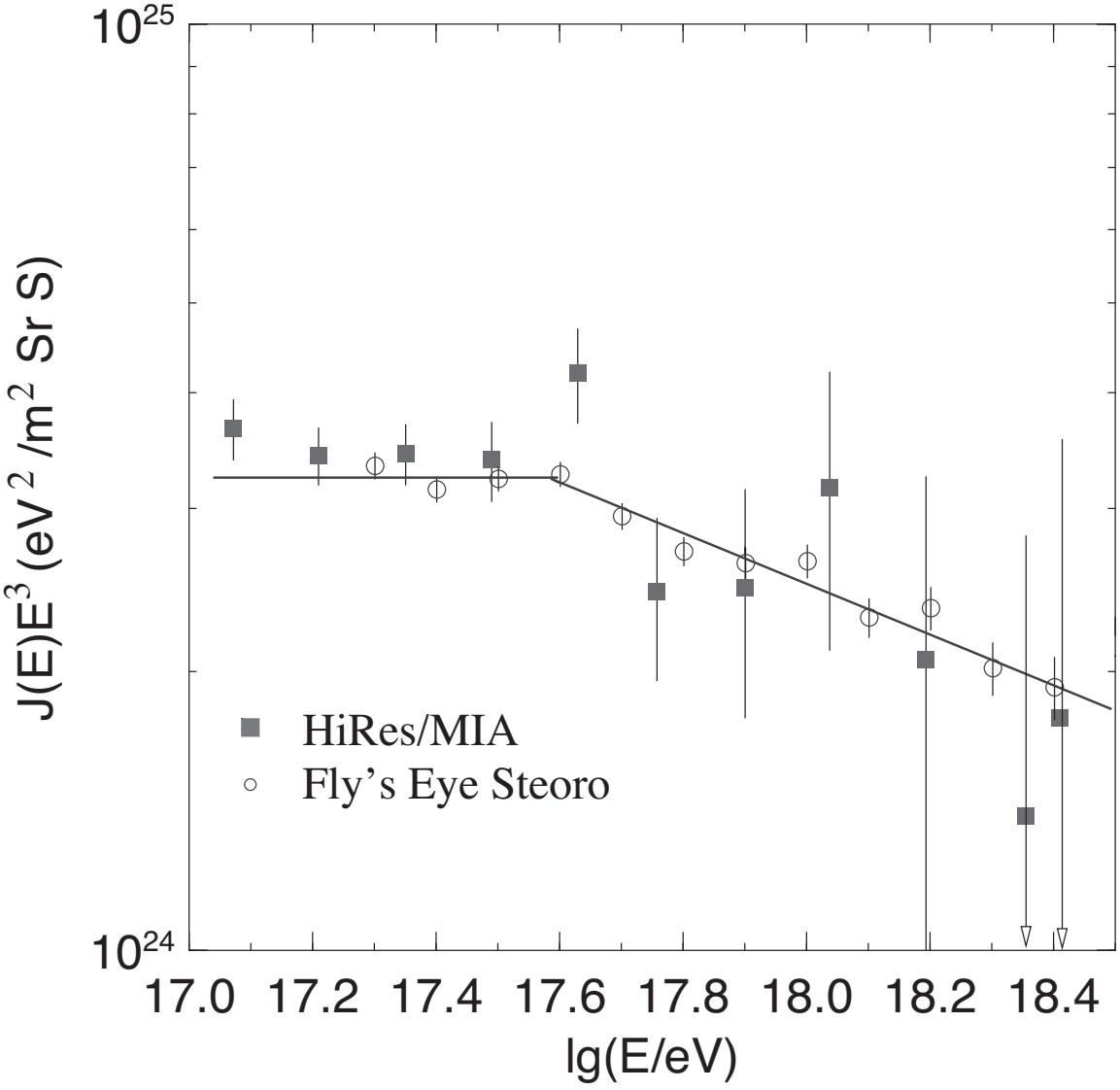


**Figure 2.9**. HiRes-MIA energy spectrum compared to the Fly's Eye stereo energy spectrum: good agreement is shown here and indicates that the HiRes Prototype and FE had the same energy scale. The squares represent the HiRes/MIA spectrum while the open circles are the Fly's Eye stereo points. Reproduced by permission of the AAS.

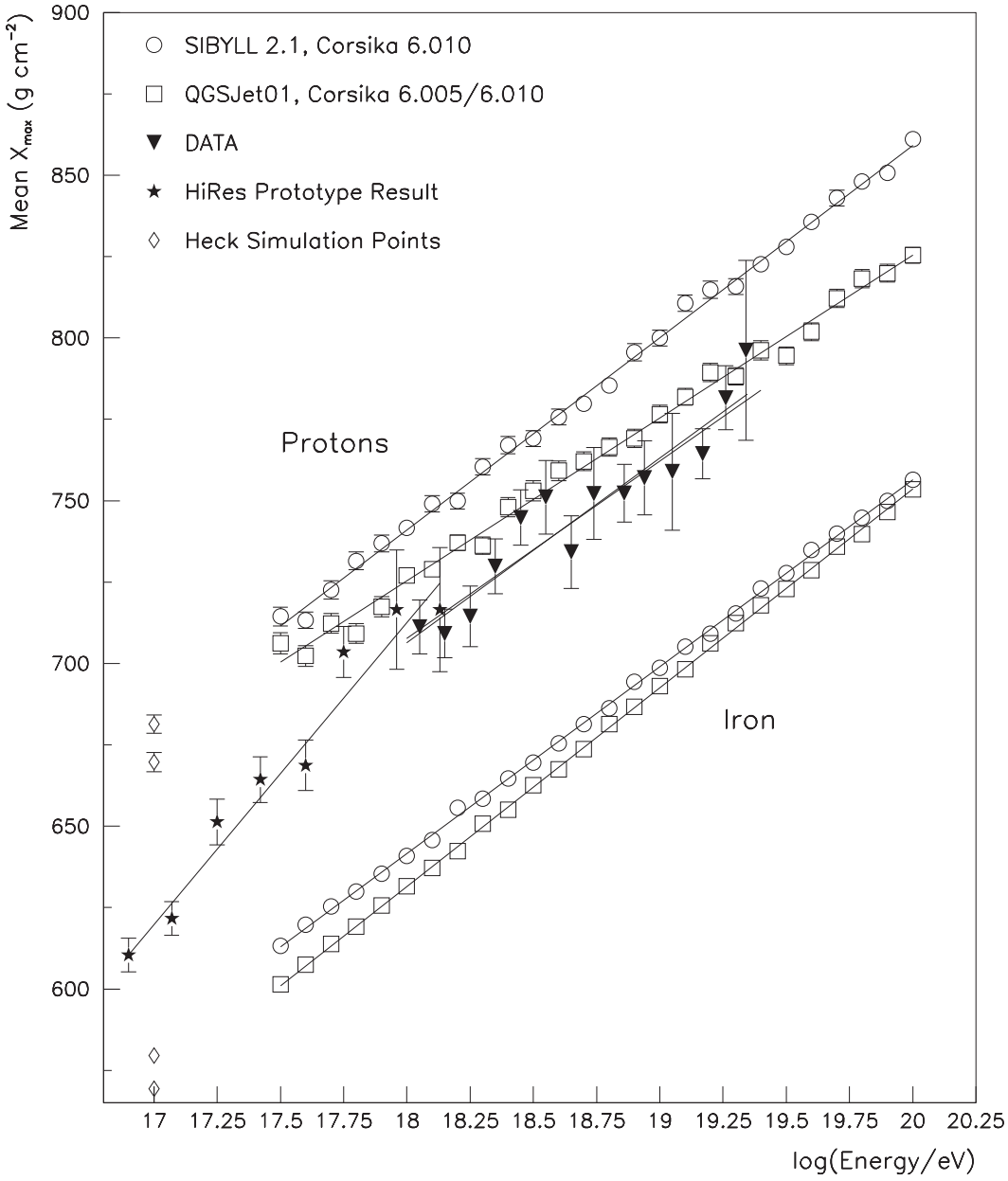


**Figure 2.10**. HiRes-MIA and HiRes composition measurement: shown is the $<X_{max}>$ value as a function of energy. The stars represent the HiRes-MIA measurement, and the triangles represent the HiRes stereo measurement. These results are compared with the reconstruction of the models of proton and iron showers. Measurements indicate a transition between $10^{17}$ and $10^{18}$ eV (HiRes-MIA) and a light-protonic composition above $10^{18}$ (HiRes stereo). Reproduced by permission of the AAS.

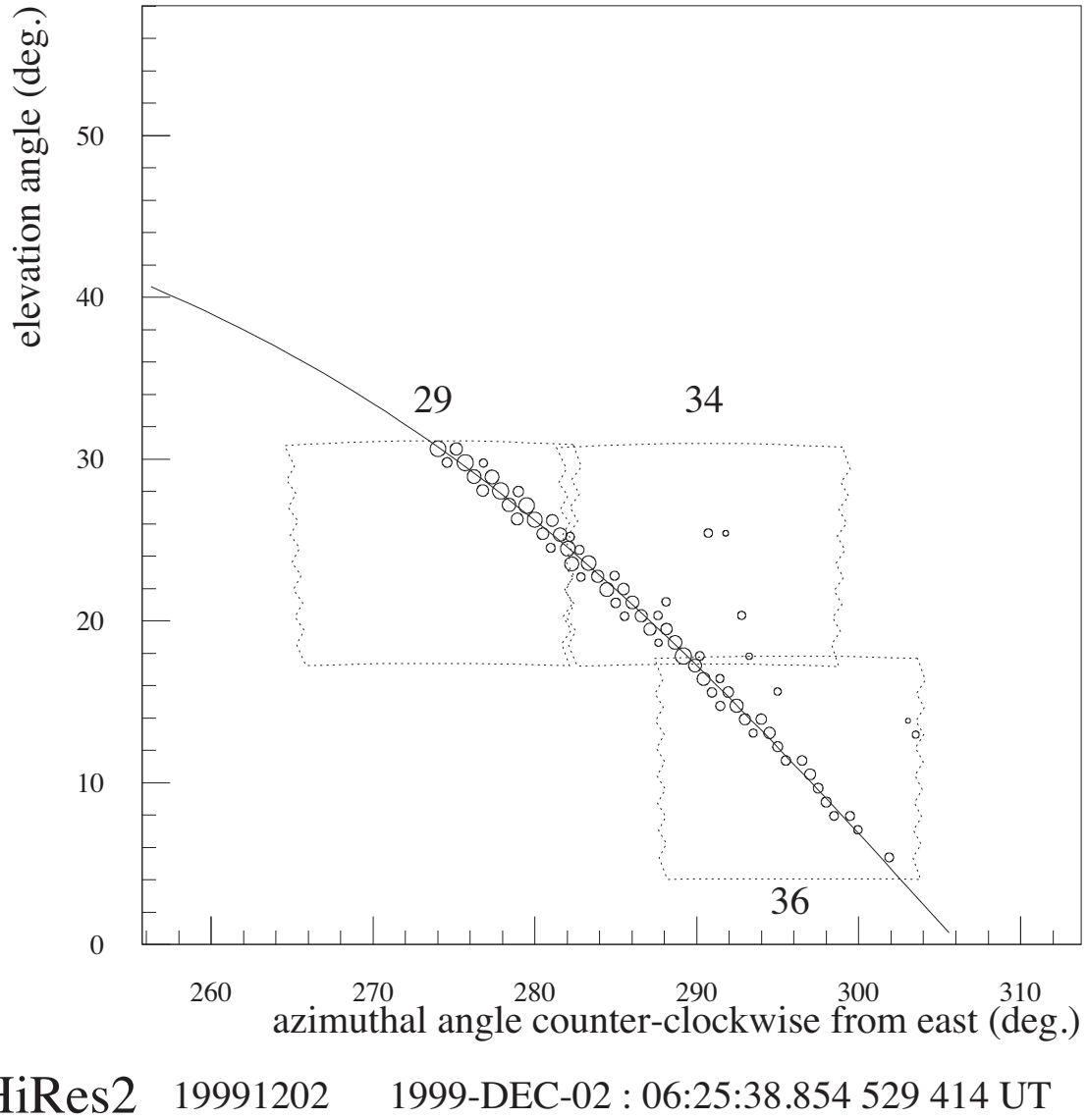


**Figure 2.11**. HiRes event display: shown is a typical HiRes-2 event which traverses three telescope cameras. The area of the open circles indicates the signal size observed by each PMT.

The HiRes monocular and energy spectra are shown in Figure 2.12 [4]. They are shown with the AGASA energy spectrum for reference. The HiRes measurement was the first observation of the predicted GZK suppression, which contradicted the AGASA observation of a continuing spectrum. The two experiments also differed in the normalization scale of the flux.

The HiRes stereo composition measurement was also shown in the previous section,

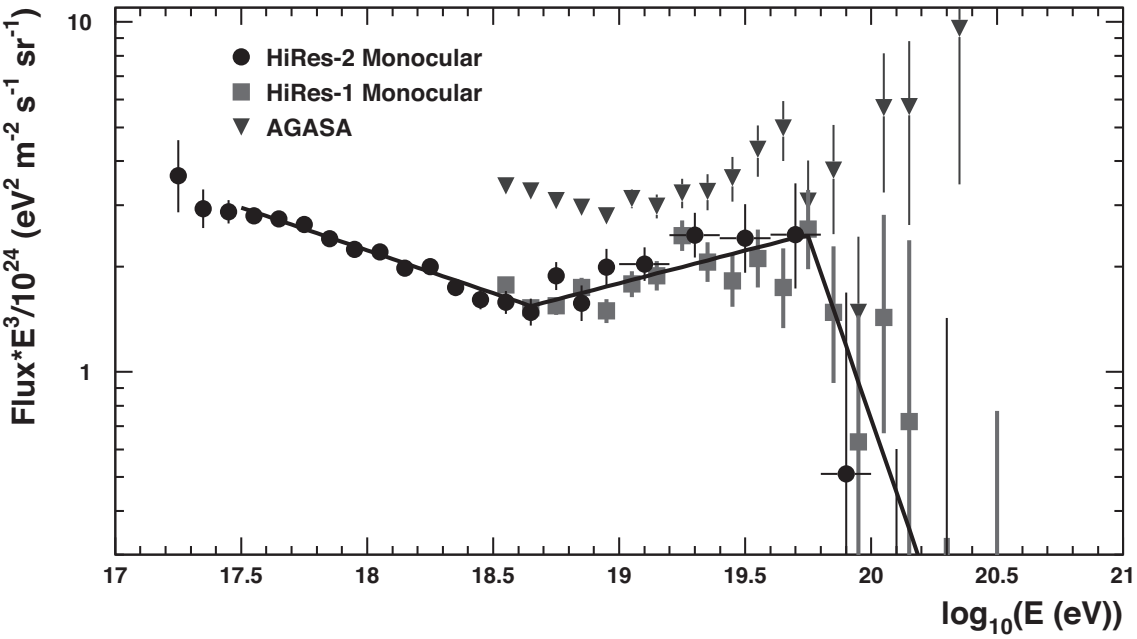


**Figure 2.12**. HiRes energy spectra: shown is the flux of UHECRs measured by the HiRes-1 and HiRes-2 experiments in comparison with the AGASA energy spectrum. The HiRes measurements include the first observation of the expected GZK suppression with more than $5\sigma$ significance. The AGASA spectrum has a higher normalization and lacks the suppression, indicating a continuing spectrum. Copyright (2007) by the American Physical Society $http://prl.aps.org/abstract/PRL/v100/i10/e101101$.

Figure 2.10 [3]. The average $X_{max}$ value is plotted versus energy along with proton and iron models. The data shows agreement with a proton-dominated composition at energies above $10^{18}$ eV.

## 2.5 Pierre Auger Observatory

The Pierre Auger Observatory, located near Malargue, Argentina, began data collection in 2004 with a partial detector and finished construction in 2008. It continues to operate at the writing of this dissertation. It was built to be the largest possible surface detector, and uses fluorescence telescopes for energy calibration. The array consists of 1600 water tanks which measure the Cherenkov light from charged particles that pass through the tanks, and four stations of fluorescence telescopes overlooking the surface array. The spectrum measurement from the PAO is shown in Figure 2.13 [7]. The spectrum is plotted with the HiRes spectrum for reference [2]. Both experiments observed the GZK suppression, though with an apparent energy scale difference of $\sim$22% [4, 7]. In the case of the PAO measurement, the GZK cut-off is also lower in energy.

Figure 2.14 shows an early hybrid composition measurement by the PAO, from 2007 [44]. The average $X_{max}$ value is plotted as a function of energy along with the results of simulations of proton and iron showers. The most notable feature here is that the data composition appears to be growing heavier as the energy increases beyond $\sim 2 \times 10^{18}$ eV. This is a departure from the measurements of the previous experiments, and will be discussed in more detail in Chapter 7.

## 2.6 Telescope Array

The Telescope Array experiment began data collection in 2007. It was built in part to resolve the controversy between the HiRes and AGASA spectral measurements. In particular, the question of the existence of the GZK cut-off was to be studied. Members from both experiments joined forces to form the new Telescope Array Collaboration and constructed a hybrid experiment employing both the fluorescence technique from Fly's Eye and HiRes, and a large area scintillation ground array like that of AGASA. A high-energy event viewed by all three fluorescence telescopes in conjunction with the surface detector is shown in Figures 2.15 - 2.18.

The details of the Telescope Array (TA) experiment will be described in detail in Chapter 3. However, to put the TA in context, it should be noted that the Middle Drum Fluorescence

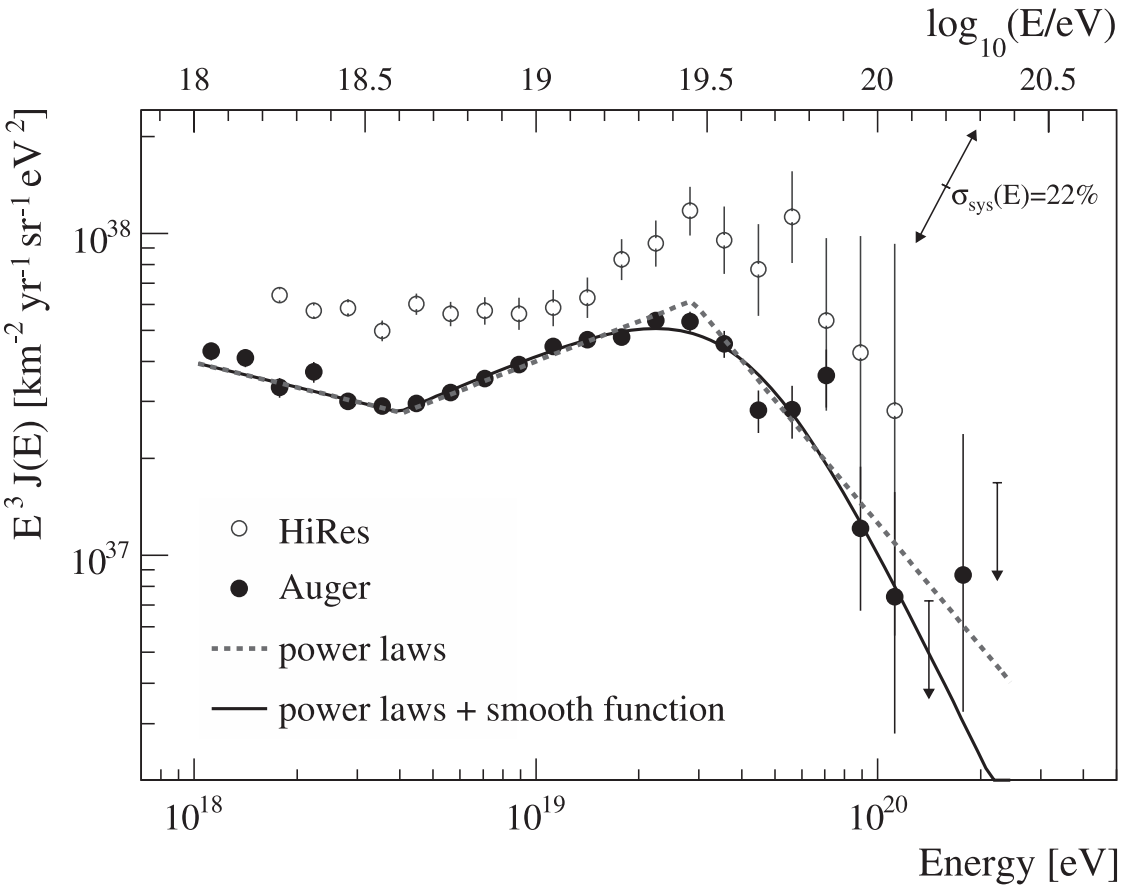


**Figure 2.13**. The PAO energy spectrum overlaid with the HiRes spectrum: the flux of cosmic ray particles is plotted as a function of energy. The HiRes stereo spectrum is plotted for reference. Both experiments observed a GZK suppression, with a 22% energy scale difference, as interpreted by the PAO collaboration. Copyright (2010), with permission from Elsevier.

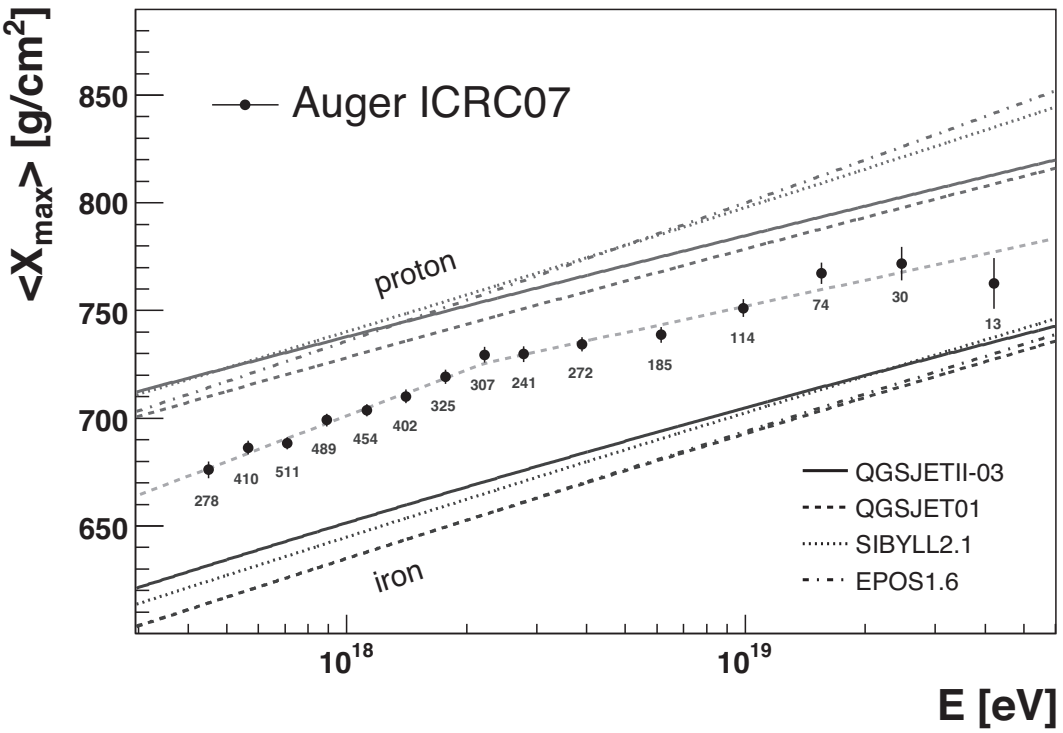


**Figure 2.14**. PAO composition measurement: the average $X_{max}$ value is plotted as a function of energy along with several "rails" that represent different shower models for light and heavy particles for comparison. The data approach the proton model as energy increases to $\sim 2 \times 10^{18}$ eV. Above that, the data approach the heavier models.

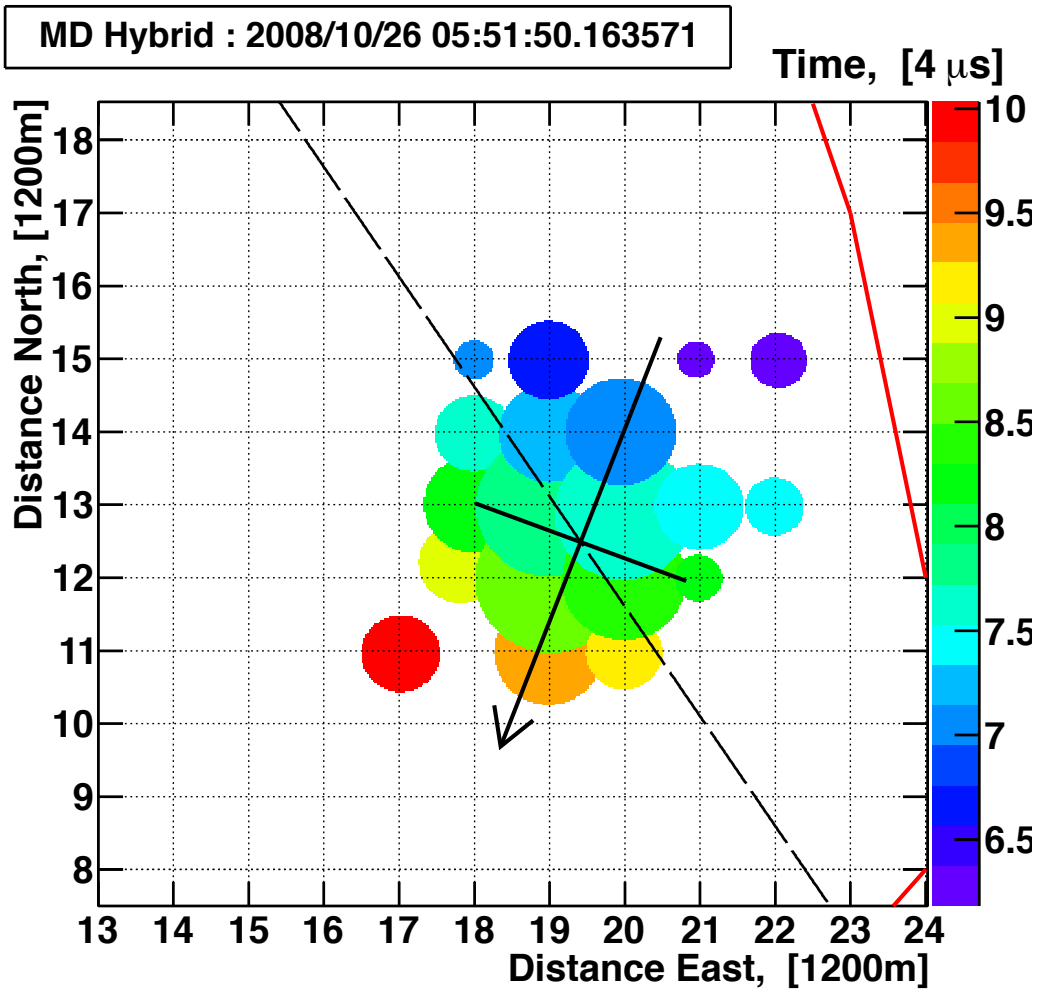


**Figure 2.15**. Cosmic ray event observed by the multiple detector elements of the Telescope Array experiment: shown is the event display of the Surface Detector (SD) of an event observed on October 26, 2008 in stereo hybrid mode.

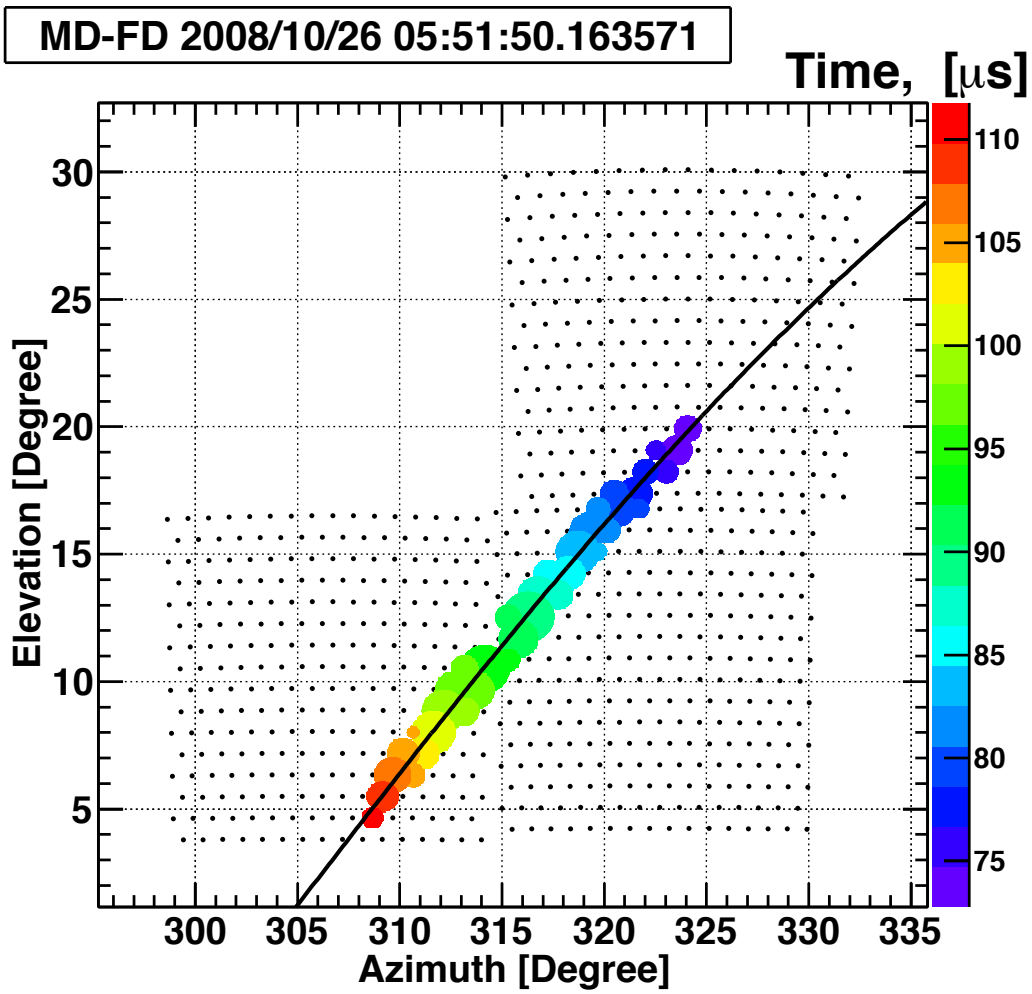


**Figure 2.16**. Cosmic ray event observed by the multiple detector elements of the Telescope Array experiment: shown is the event display of the Middle Drum Fluorescence Detector (MDFD) of an event observed on October 26, 2008 in stereo hybrid mode.

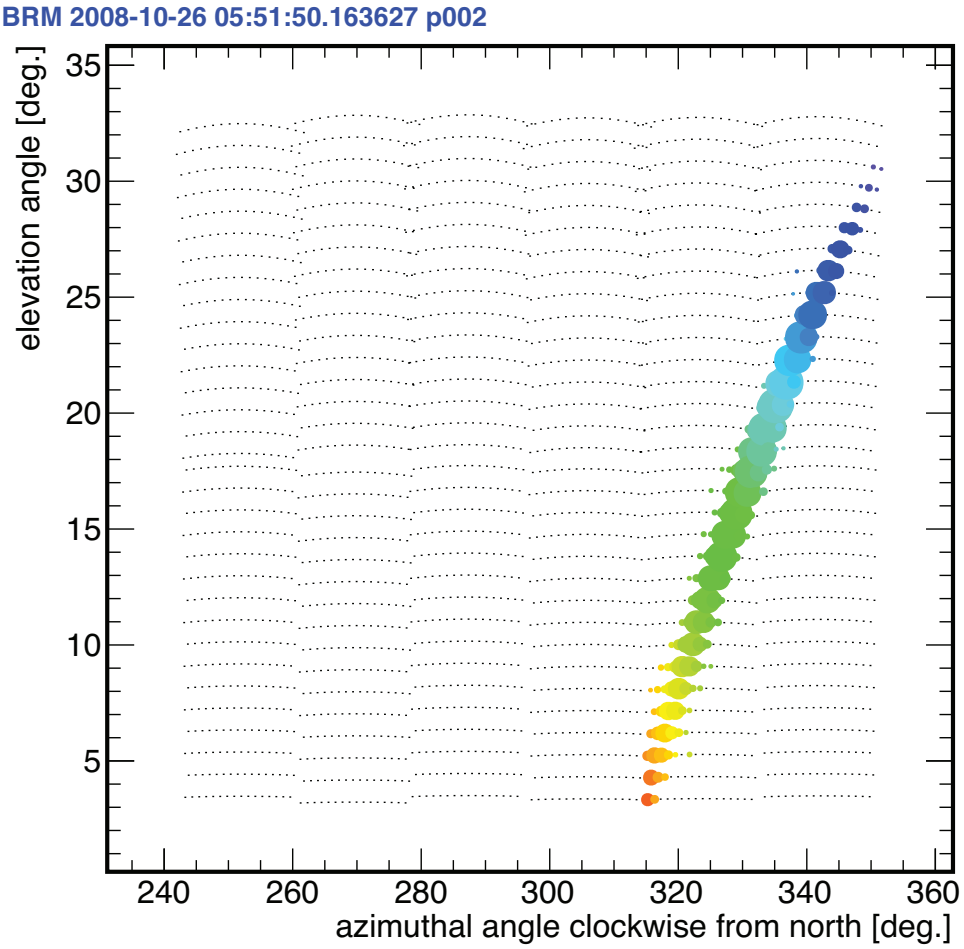


**Figure 2.17**. Cosmic ray event observed by the multiple detector elements of the Telescope Array experiment: shown is the event display of the Black Rock Mesa Fluorescence Detector (BRMFD) of an event observed on October 26, 2008 in stereo hybrid mode.

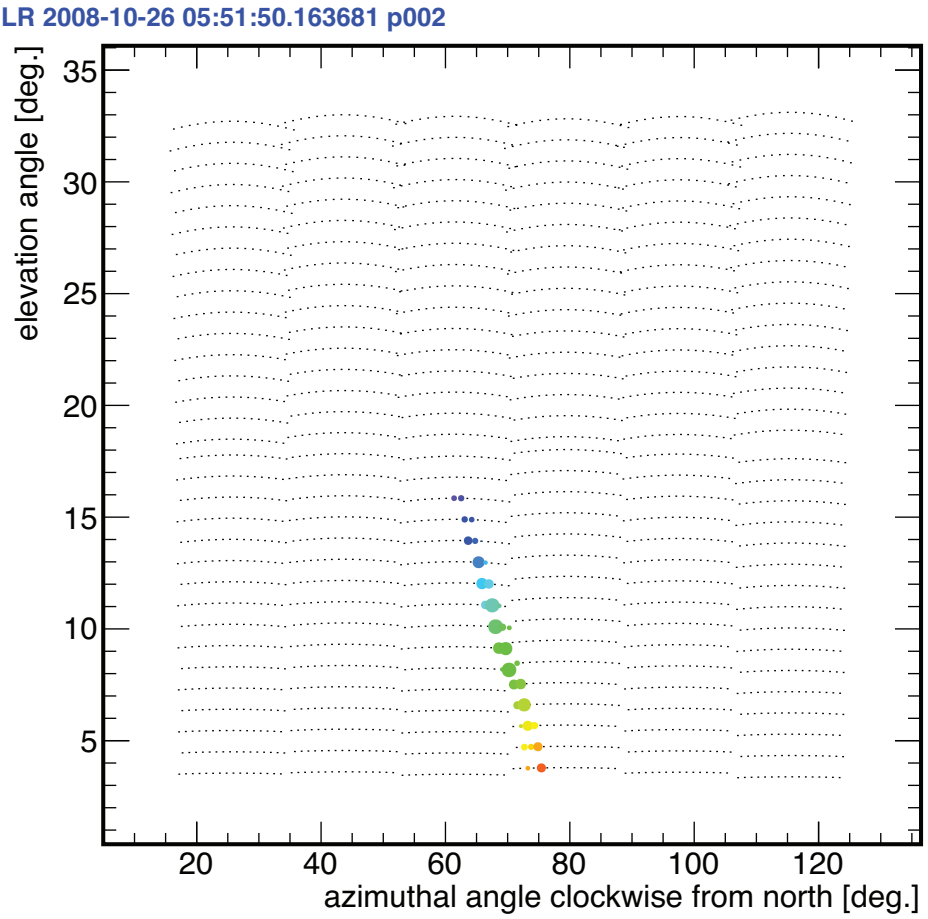


**Figure 2.18**. Cosmic ray event observed by the multiple detector elements of the Telescope Array experiment: shown is an event observed on October 26, 2008 in stereo hybrid mode. Shown is the event display of the Long Ridge Fluorescence Detector (LRFD).

Detector (MDFD), located in the northernmost part of the Telescope Array, uses the exact same equipment that was used for the HiRes-MIA prototype, and later at the HiRes-1 site. While a major goal of the Telescope Array is to resolve energy spectrum discrepancies, the goal of this dissertation is to create a link between the Telescope Array experiment back to the HiRes experiment. Specifically, this analysis links the MDFD to the surface array by studying events in hybrid mode. An analysis comparing the MDFD monocular data directly to the HiRes data was performed by D. Rodriguez in [38], and the analysis in this dissertation completes the connection to the rest of the experiment.

A second goal for this hybrid analysis emerged after the TA was commissioned, once the PAO released their composition measurements. These measurements were obtained from fluorescence detectors operated in hybrid mode with the surface array, while HiRes composition measurement used stereoscopic reconstruction, so a direct comparison has potential complications. Using TA in hybrid mode would address directly the differences in shower reconstruction. Furthermore, the TA link to HiRes makes it particularly useful for resolving this discrepancy. The PAO and TA are the only two operating experiments of their kind with the capability of studying UHECRs. Therefore, a hybrid composition study using the MDFD for comparison is not only appropriate, but also essential.

# CHAPTER 3

# TELESCOPE ARRAY EXPERIMENT DESCRIPTION

The Telescope Array experiment is located near Delta, Utah, about 250 km southwest of Salt Lake City, Utah. It is a hybrid experiment that incorporates two of the main types of detectors (fluorescence telescopes and a scintillation counter array) for studying Ultra High Energy Cosmic Rays (UHECR). As we have discussed in an earlier chapter, the minuscule flux of cosmic ray particles at energies above $10^{18}$ eV and above makes direct detection of these particles impractical.

Both types of TA detectors use the Earth's atmosphere itself as part of a calorimeter. As a cosmic ray enters the atmosphere, it collides with a nucleus (mostly nitrogen or oxygen) and initiates a hadronic shower that gradually transforms into an electromagnetic cascade. This is generated from the electromagnetic decays of neutral pions and other $I_z = 0$ (isospin) mesons. This phenomenon, known as an Extensive Air Shower (EAS), has been described in Section 1.3.

Figure 3.1 shows the distribution of 507 scintillation counters that comprise the TA surface detector (SD). The locations of the counters, shown by the filled black circles, are laid out on a 1.2 km square grid. The SD counters sample the lateral distribution of the remnant of the air showers at ground level (∼4600 ft above sea level). The SD array is operational 24 hours a day, every day. The detection efficiency of the SD array rises quickly above $\sim 10^{18}$ eV and becomes fully efficient above $\sim 10^{19}$ eV. The aperture for the highest energy cosmic rays is about 1500 km$^2$ steradians.

Indicated by the triangles in Figure 3.1 are the three fluorescence detector sites located at the periphery of the SD array. The two southern sites each consist of 12 telescopes built by the TA collaborators from Japan. The northern most fluorescence detection site, located at Middle Drum (MD), was constructed with 14 refurbished telescopes from the HiRes-1 site of the previous High-Resolution Fly's Eye (HiRes) experiment. The re-use of these telescopes provides a direct connection between TA and HiRes: the energy scale of the

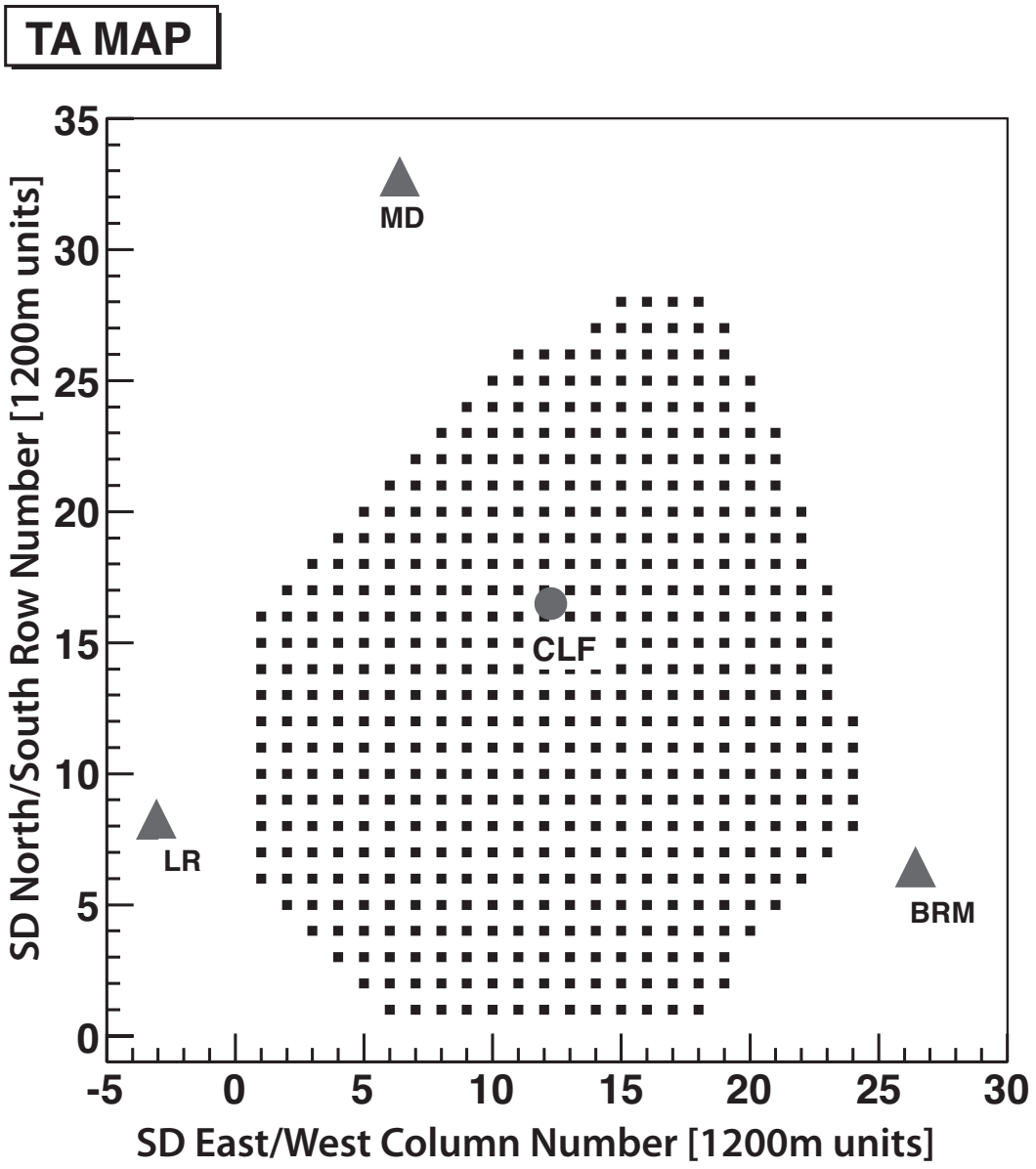


**Figure 3.1**. The layout of the Telescope Array experiment: the different components of the experiment are indicated on this map. The filled black squares indicate the locations of the scintillation counters that comprise the Surface Detector (SD). The triangles mark the three fluorescence detector sites at the periphery of the SD array. The Central Laser Facility, shown by the circle, is placed equidistant from the three fluorescence detection sites to provide atmospheric monitoring and cross-calibration.

HiRes experiment can be directly transferred to TA. This transfer of the energy scale is one of the major goals of this dissertation. The fluorescence telescopes image the luminescence (usually referred to as fluorescence) light emitted by nitrogen in the wake of the passage of charged shower particles. The fluorescence detector is therefore capable of measuring the shower size as a function of slant depth, which allows this technique to give a statistical measure of the chemical composition of the primary cosmic rays. The Telescope Array is the second largest detector of UHECRs in the world, and has the largest aperture for measuring the highest energy particles from the northern sky.

## 3.1 Surface Detectors

The Surface Detector (SD) array at the Telescope Array experiment consists of 507 scintillator counters. The individual counters are arranged in a square grid pattern with 1.2 $km^2$ unit-cell spacing. The 1.2 km grid spacing and the scintillation collection area (3 $m^2$) are optimized for the measurement of cosmic ray showers with primary energy, $E \geq 10^{19}$ eV. The arrival direction of each shower is reconstructed from the timing information collected from each counter. The energy of the primary cosmic ray is inferred from the particle flux sampled by the counters.

Figure 3.2 shows an event display of a typical SD event. The SD counters lie at the intersection points on the grid. The circle sizes are proportional to the signal size, while the color represents the timing.

### 3.1.1 Description and Deployment

While my primary contribution to the experiment involved my work with the Middle Drum detector, I also worked on the construction and testing of replacement scinitillator counters in the SD array, as well as the deployment of the counters in the field. Figure 3.3 shows the facility in Akeno, Japan where I worked with a team on the assembly of the scintillator detectors. The detectors were then shipped to the Cosmic Ray Center in Delta, Utah, where I helped to install the solar panels, batteries, and electronics. The final testing of the detectors was performed there, at the Cosmic Ray Center, before deploying the SD counters into the field.

Figure 3.4 shows the interior of an SD counter [28]. Each SD counter houses two layers of plastic scintillator. Each layer contains 2-1.5 $m^2$ pieces of plastic, 1.2 cm thick. The scintillator plastic is comprised of polyvinyl toluene (CIMS-G2, CI Kogyo Ltd) [20]. The plastic is shielded by Tyvek sheeting to help ensure maximum light capture.

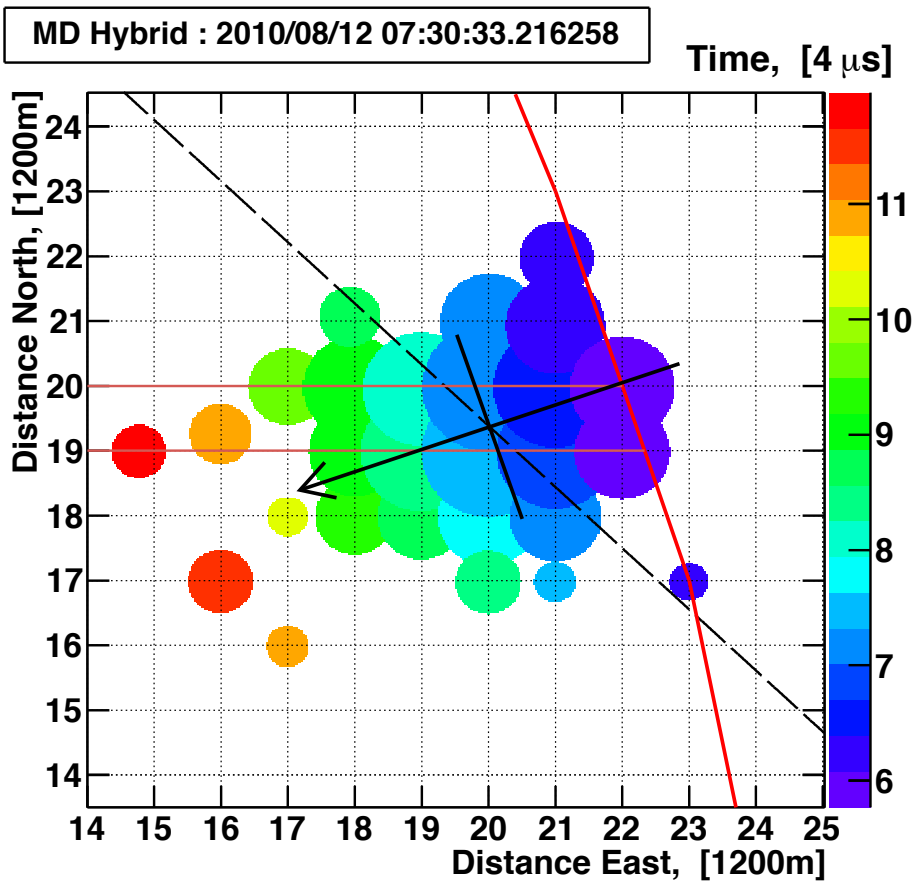


**Figure 3.2**. A typical Surface Detector (SD) event: the SD counters which viewed a signal for this event are shown. SD counters are located at the intersection points of the grid. Circle size is proportional to signal size, and circle color represents the trigger timing of each detector. The arrow represents the reconstructed direction of the shower, and the point where the arrow crosses the solid black line represents the reconstructed shower core position on the ground. The red line represents the SD array boundary.

**Figure 3.3**. The SD construction facility at the University of Tokyo's Akeno Observatory in Akeno, Japan: in the photo, we are preparing the wavelength shifting fibers to be attached to PMTs.

The light from passing particles in the scintillator are collected by wavelength shifting fibers (Y-11(200)M, Kuraray Co., Ltd) [20]. Figure 3.5 shows how the fibers are placed in grooves in the plastic. All the light from each layer are concentrated separately into a single Photo Multiplier Tube (PMT) (9124SA, Electron Tubes Limited, now ET Enterprises, Ltd.) [20].

Figure 3.6 shows the external view of a Surface Detector [28]. Each detector consists of a metal support frame, a wireless communications antenna, a GPS receiver, a battery and electronics box, a solar panel and a steel roof. The steel roof shields a stainless steel box which contains the plastic scintillators plastic, wavelength shifting fibers, and PMTs.

Each SD contains a deep-cycle 12 V battery that is charged during daylight hours by the solar panel. The GPS receiver is used to synchronize the clocks on each of the SDs, so that triggers can be matched in time. The directional wireless antenna transmits data using a 2.4 GHz wireless radio. The data are transferred using a wireless local area network with a customized networking protocol. This protocol is based on IEEE 802.11b and transfers data at a rate of 11 MB/s.

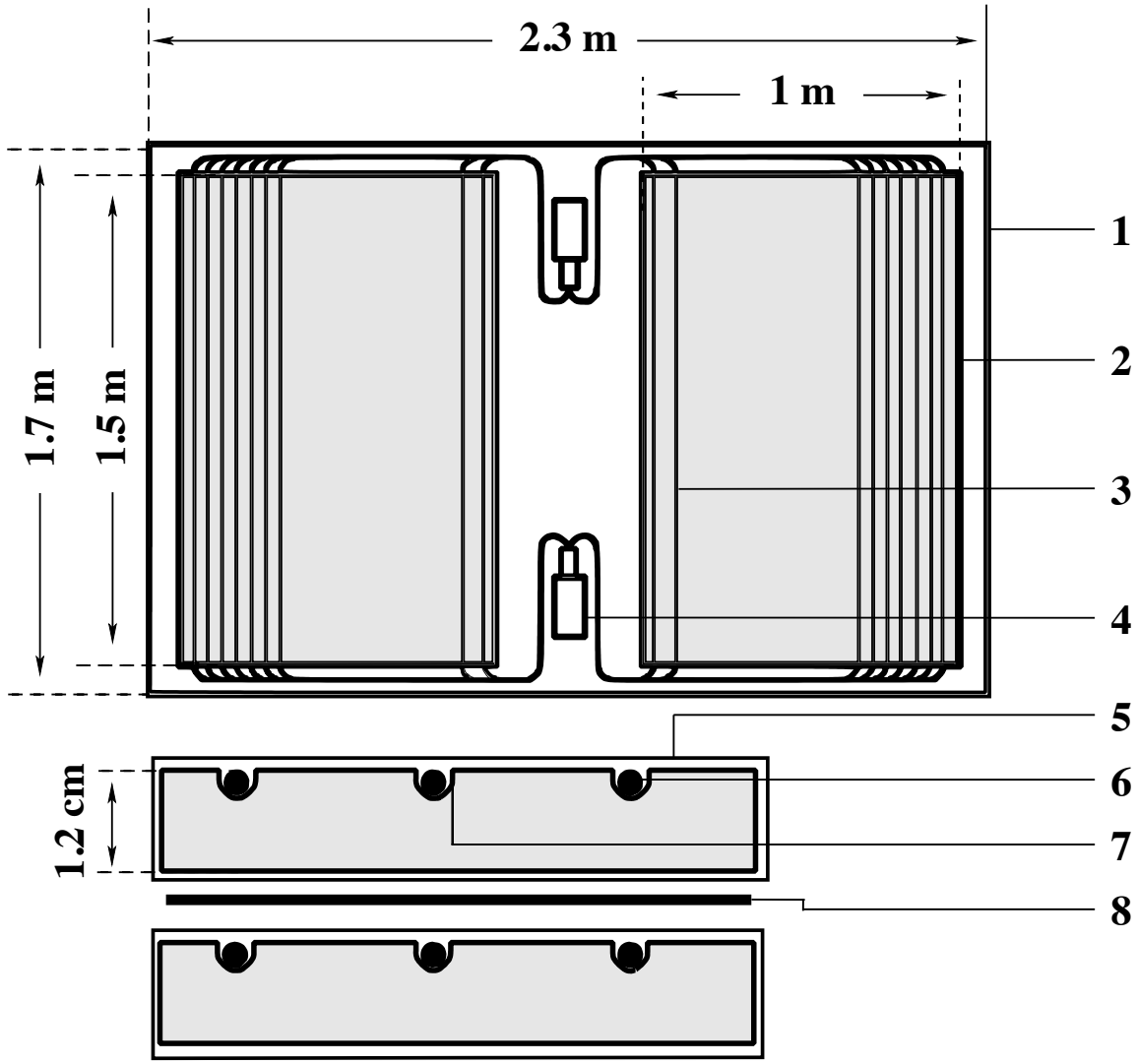


**Figure 3.4**. A schematic of internal components of a TA Surface Detector (SD) viewed from above (top) and from the side (bottom). Shown components include the stainless steel container (1), plastic scintillator panels (2), wavelength shifting fibers (3), photomultiplier tube (4), Tyvek sheet (5), wavelength shifting fibers (side-view) (6), grooves in scintillator for the fibers (7), and a stainless steel separator plate between the two layers (8).

**Figure 3.5**. Placement of the wavelength shifting fibers in the grooves in the scintillating plastic in a SD: each fiber was individually placed by hand and taped at the two ends. Optical fibers from each layer are glued into bundles (four bundles per layer: two for each end of each piece of plastic). These are then mated with the PMTs, one per scintillator layer.

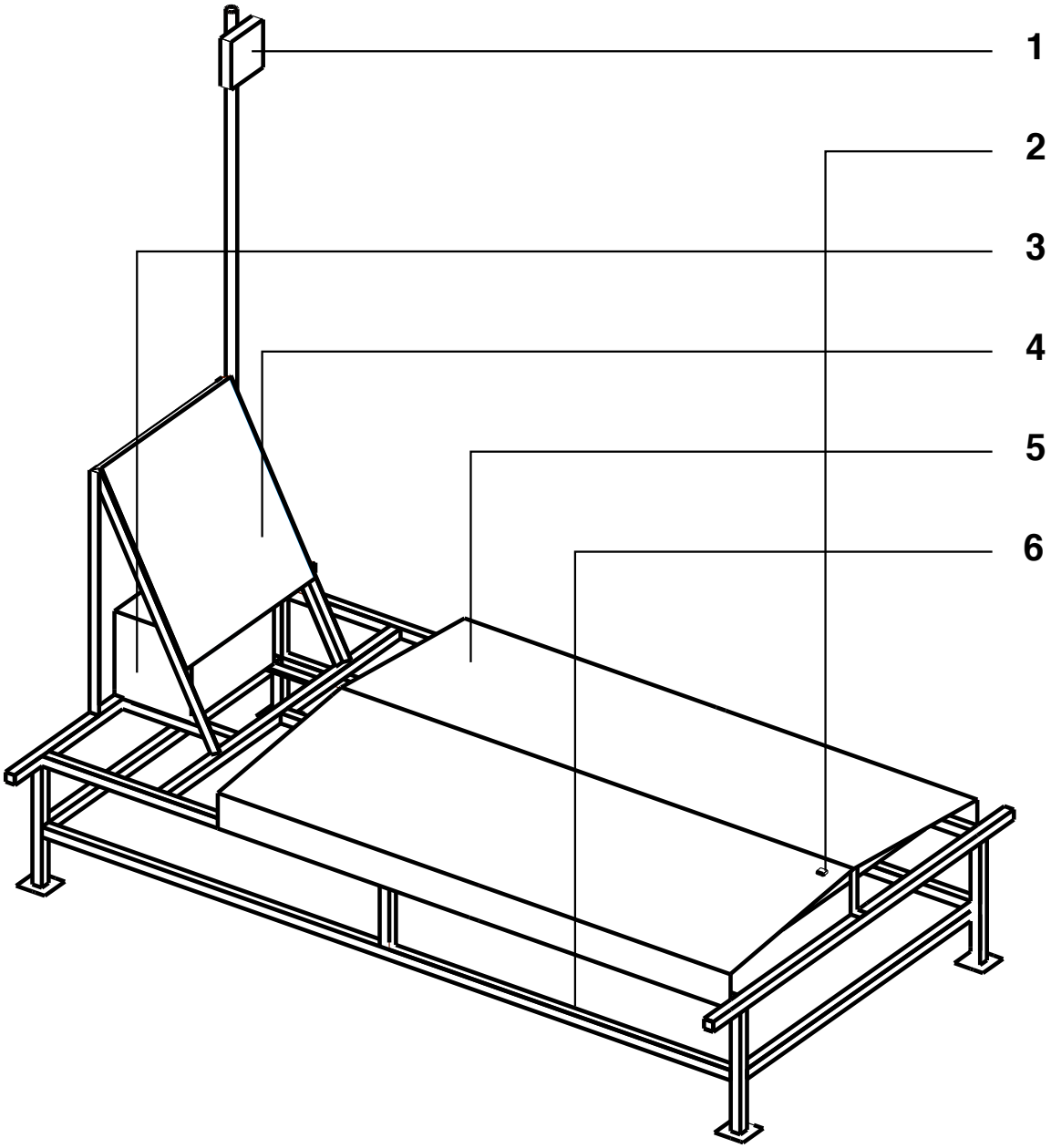


**Figure 3.6**. Diagram of external view of a Surface Detector: the external components are labeled. These include a wireless communications antenna (1), GPS receiver (2), electronics box (3), solar panel (4), steel shielding (5), and the metal support frame (6). The light tight box containing the scintillator panels, the optical fibers and the PMTs is hidden under the steel shielding.

Figure 3.7 shows one SD during deployment. Each of the 507 counters weighs approximately a half ton and was carried by trailer to a staging area, from where it was transported via helicopter to its designated position in the array. The majority of the detectors (485) were deployed in early 2007. I participated in the deployment of remaining detectors in December 2007. After final testing, the SD array became fully operational in May 2008, and the first analysis datfa was taken on May 11, 2008.

### 3.1.2 Read-out Electronics

Figure 3.8 shows the Data Acquisition System (DAQ) for the SDs. The signals from each of the PMTs are amplified and then digitized by a Flash Analog to Digital Converter (FADC), operating at 50 MHz. Figure 3.9 shows the paired FADC traces from the upper and lower layers [28]. The saved portion of the digitized signal extends over 128 FADC time (20 ns) bins.

### 3.1.3 Trigger

While the FADC digitizes the analog input from the PMTs continuously at 50 MHz, those pulses which exceed 0.3 MIPs (Minimum Ionizing Particle, described in Section 3.1.4) in integrated area are stored in memory, along with the time of the pulse (registered via a GPS clock). The integrated signal of 0.3 MIPs corresponds to 15 FADC counts above the pedestal in each layer (shown in Figure 3.9).

Trigger computers at the communication towers poll each SD counter at one second intervals. The time of pulses greater than 3 MIPs are reported to the towers and this information is used to form an event trigger. An event trigger occurs when three adjacent SDs see a signal greater than 3 MIPs within an 8 $\mu$s window. When an event trigger does occur, the signals from all of the detectors in the array with signal greater than 0.3 MIPs within the coincidence window are then transferred from the individual counters to the central data acquisition system via the wireless network.

### 3.1.4 Scintillator Detector Calibration

The SDs are calibrated using muons from cosmic ray showers. Simulations using GEometry ANd Tracking (GEANT4) software [12] of a muon traveling vertically downward through a layer of scintillator are used to determine the amount of energy deposited from these muons. Figure 3.10 shows the mean energy deposited in the scintillator as a function of the kinetic energy of the muon. The minimum energy deposited is measured at 300 MeV.

**Figure 3.7**. Image of field deployment of a Surface Detector (SD) via helicopter: one helicopter brought the SD itself, while a second helicopter ferried a crew from site to site to receive the SD, align it, and turn it on.

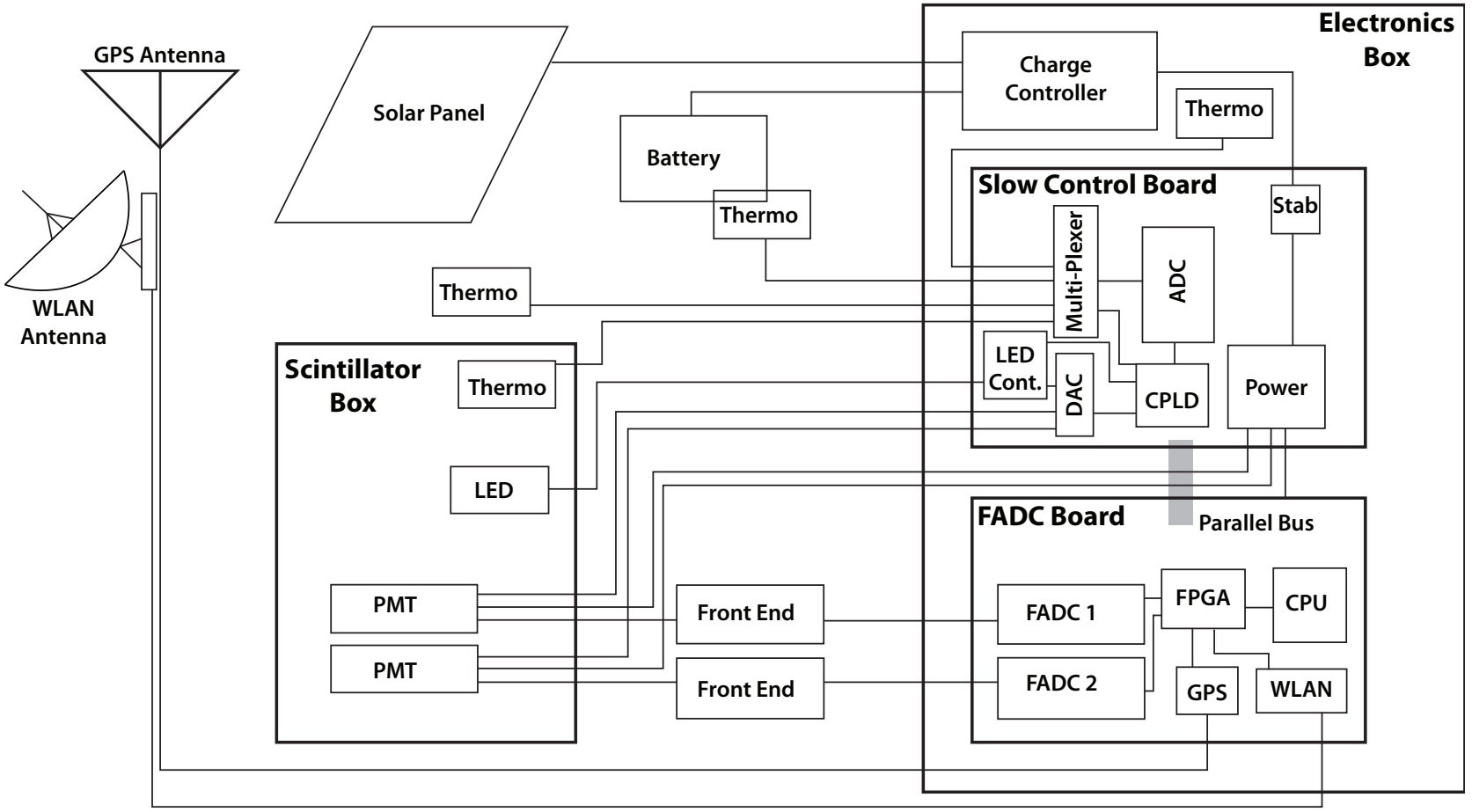


**Figure 3.8**. Shown is a schematic of the SD data acquisition system. The important components include the scintillator box which is controlled by the slow-control board, and sends signal to the FADC board, the solar panel and battery that provide power, and the GPS and WLAN antenna that allow the detector to communicate with the rest of the array.

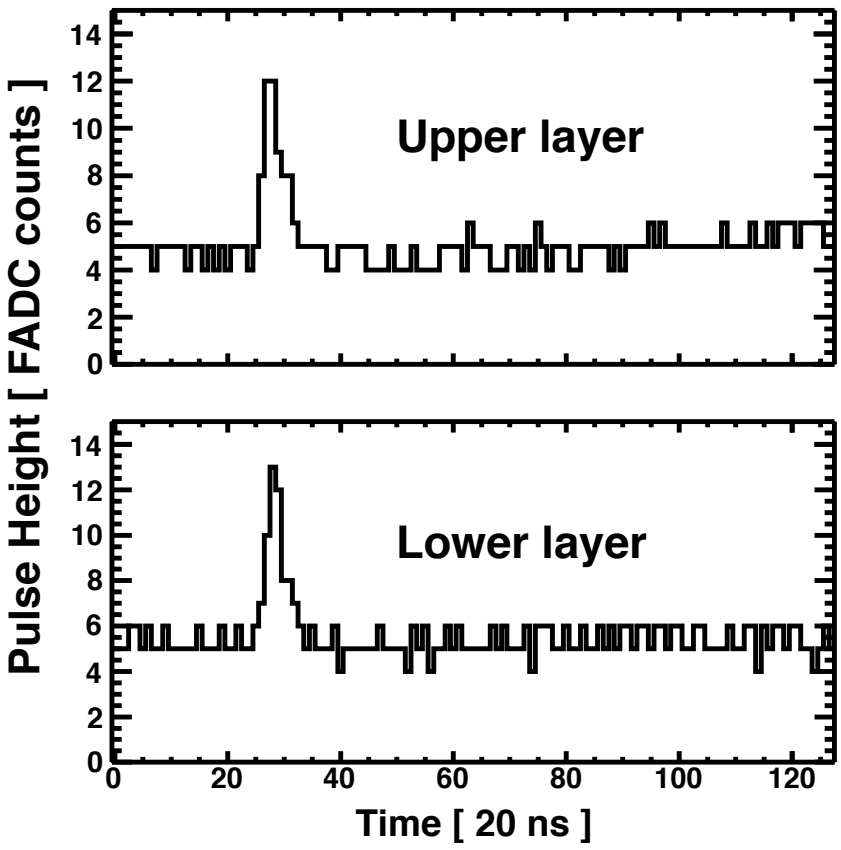


**Figure 3.9**. These are the FADC traces from the upper and lower layers of scintillator in one Surface Detector (SD) counter.

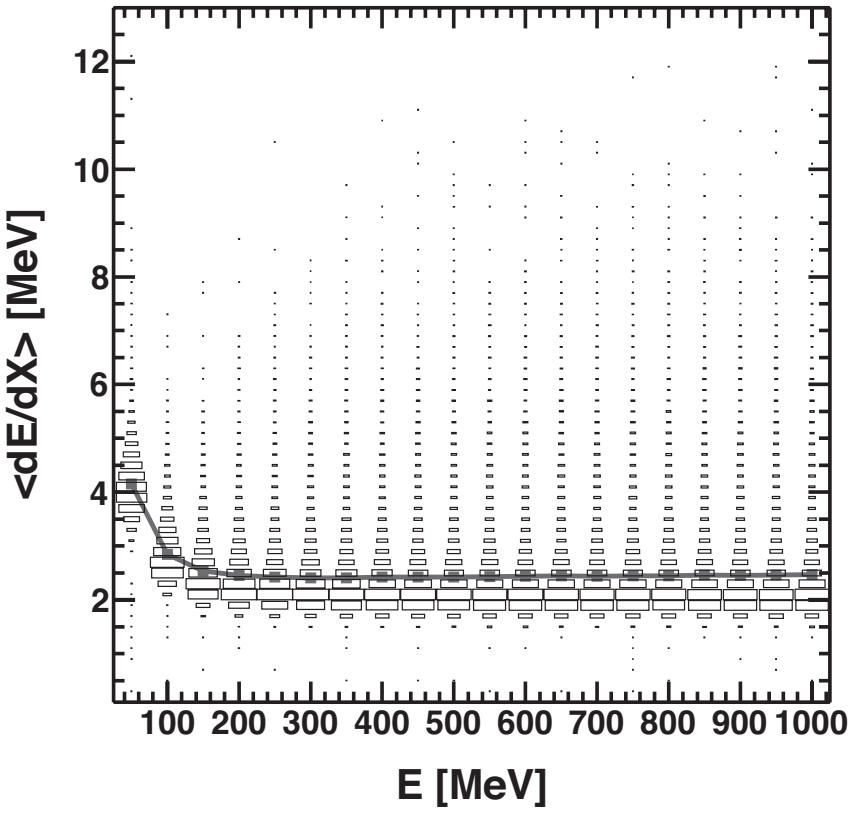


**Figure 3.10**. The results of a GEANT4 simulation of mean energy deposition of vertical muon versus kinetic energy: a 300 MeV muon has minimum ionization energy.

This is called the minimum ionizing energy and corresponds to the muon as a Minimum Ionizing Particle (MIP). Figure 3.11 shows a plot of the energy deposited by a 300 MeV vertical muon as simulated in GEANT4 [28]. The data are fit to a Landau probability function, in the form of equation 3.1.

$$P(x) = \frac{1}{\pi} \int_0^\infty e^{-t \ln t - xt} sin(\pi t) dt \tag{3.1}$$

Here, the probability at a given value, $x$ is defined by the integral. The Most Probable Value (MPV) of the energy deposition is the fitted peak to the data at 2.05 MeV. This value is then taken as the energy deposited by a Vertical Equivalent Muon (VEM).

From the data, a histogram is generated from the FADC signal of every particle that triggers both layers of scintillator. The peak of this histogram is fit in the same way as the simulated data, and is used to calibrate each detector. Figures 3.12a and 3.12b show the Landau fit for the upper and lower layers, respectively, of a typical cosmic ray event [28]. The shape of the histogram is scaled to the VEM, representing a MIP.

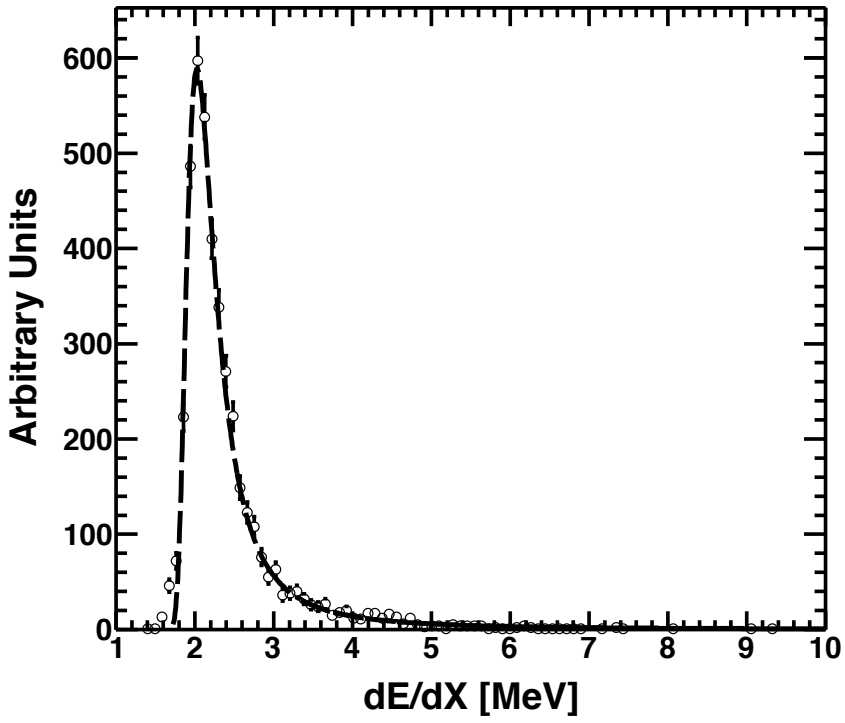


**Figure 3.11**. Minimum ionizing, 300 MeV vertical muon simulation: The Most Probable Value (MPV) of energy deposited is 2.05 MeV for one VEM unit.

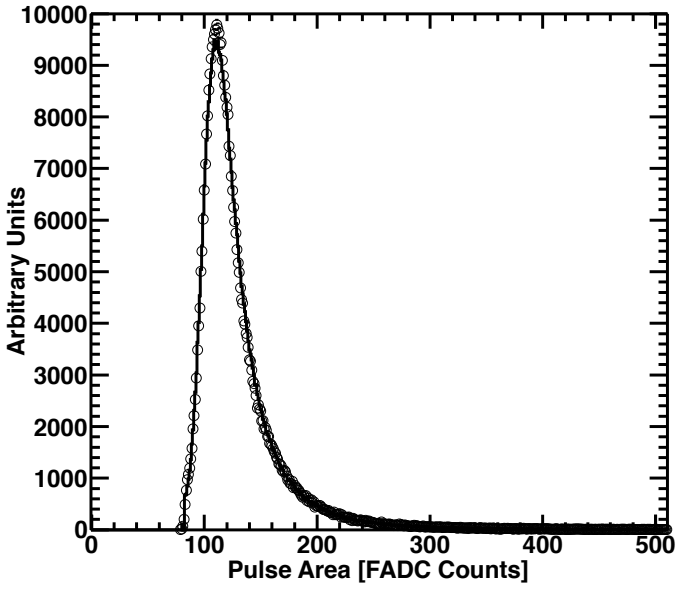


(a)

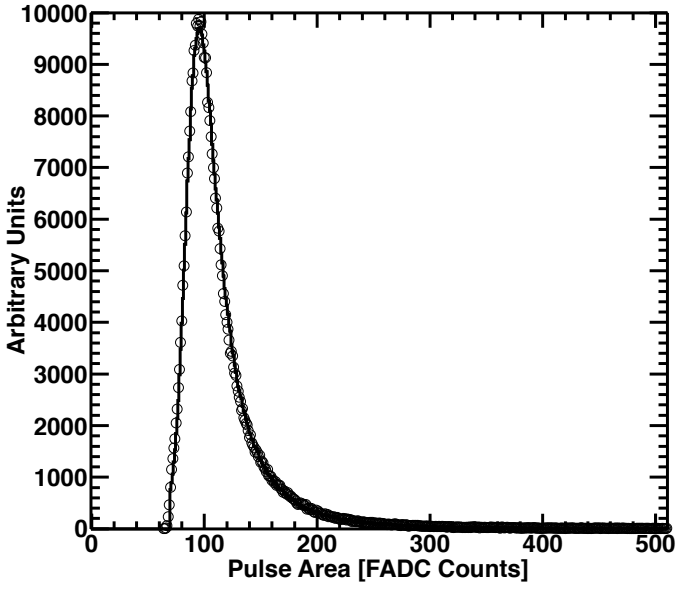


(b)

**Figure 3.12**. 1-MIP peak for determining detector gains in FADC counts/MeV in (a) the upper scintillator layer and (b) the lower scintillator layer of a Surface Detector (SD).

## 3.2 Middle Drum Fluorescence Detector

Figure 3.13 shows the Middle Drum (MD) fluorescence detector. It is a unique component of the Telescope Array experiment, because the telescopes deployed at this site were previously used by the High-Resolution Fly's Eye (HiRes) experiment at the HiRes-1 site. In particular, the first observation of the Greisen-Zatsepin-Kuz'min (GZK) cut-off by the HiRes collaboration relied on the statistical power of the HiRes-1 monocular data set [4]. These 14 refurbished telescopes are a common element of both HiRes and TA. Data collected at the MD site provides a direct link between the two experiments.

By using the exact same equipment, simulation, and analysis programs, we have made a measurement of the cosmic ray spectrum using the MD site alone. The agreement between the HiRes-1 and MD monocular spectra forges the link in the energy scale between the HiRes measurement and the hybrid analysis described in this dissertation [10]. The MD hybrid analysis in turn bridges the energy scale of the MD monocular spectrum to that of the SD spectrum and the rest of TA.

Figure 3.14 shows the northern portion of the Telescope Array, and the position of MD with respect to it. The MD detector consists of 14 telescopes and is located $\sim$10 km from the nearest SD at the northern end of the array, and 21 km northwest of the Central Laser Facility. Each of the 14 telescopes consists of a 5.1 $m^2$ spherical mirror which images the luminous air shower onto a camera comprised of a cluster of 256 PMTs [38].

Each telescope mirror is composed of four glass mirror segments arranged in a cloverleaf shape. The segments are individually adjustable, and have been aligned to focus light onto the camera at their common focal plane. Due to the obscuration of the cluster and stand directly in front of the mirror, the total effective collection area of the mirror is 3.72 $m^2$. Seven of the 14 telescopes view $3^\circ - 17^\circ$ in elevation, while the remainder view $17^\circ - 31^\circ$. Figure 3.15 shows a pair telescopes in the MD detector, demonstrating the total viewing ability of $3^\circ - 31^\circ$ in elevation above the horizon. In azimuth, all 14 mirrors used in conjunction can see $112^\circ$ between southwest and southeast (see Figure 3.14).

Figure 3.16a shows a photo of the camera of a fluorescence telescope at the MD site. The fluorescence light from an EAS passes through a UV band-pass filter before reaching the PMTs in order to remove most starshine and man made light and thus improve the signal to noise ratio. Figure 3.16b shows an open cluster box, revealing the 256 hexagonally close-packed PMTs. Each PMT is optimized to collect UV light and is provided with its own high voltage setting to provide uniform gain.

**Figure 3.13**. Middle Drum Fluorescence Detector (MDFD): 14 telescopes view the southern night sky 3° to 31° in elevation.

There are two types of PMTs inherited from the HiRes experiment that are used in the MD detector: the EMI 9974KAFL can be found in cameras 1-6 (cameras are numbered from the west end of the building, viewing the southeastern part of the sky) and Philips (now Photonis) XP3062/FL are in cameras 7-14. The bi-alkali photocathodes in these PMTs give excellent quantum efficiency in the UV range. The high voltage of each PMT is individually adjusted in order to achieve the greatest uniformity in the tube gains, which are typically about $10^5$. The charge collected from each PMT is sampled by the Charge to Digital Converter (QDC) and the pulse is integrated if trigger conditions are met.

### 3.2.1 Middle Drum Fluorescence Detector Trigger

Figure 3.17 shows a diagram of the logic flow of the triggering system at the MD detector. Each PMT is individually monitored and the threshold (200 - 1240 mV) is continuously modified to keep the tube trigger rate, or "count rate" at 200 Hz. As described in the

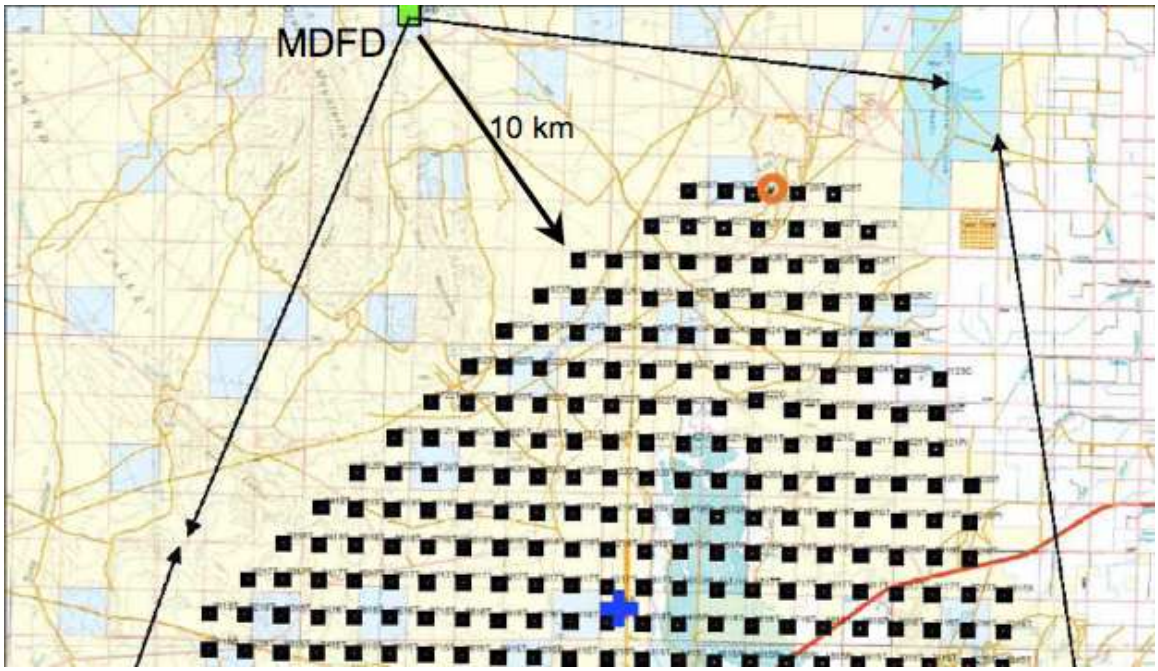


**Figure 3.14**. Location of the Middle Drum detector at the northern end of the SD array: it is located ∼10 km from the nearest SD counter. The cross near the bottom of the picture represents the Central Laser Facility (CLF), which is located equidistant from all three fluorescence detector stations, at the center of the array.

**Figure 3.15**. A pair of telescopes at the Middle Drum Fluorescence Detector (MDFD): in the photo, the telescope on the right views 3°-17° above the horizon, while the one on the left views 17°-31° above the horizon. Thus, the pair view 28° in elevation and the seven pairs of telescopes view 112° in azimuth.

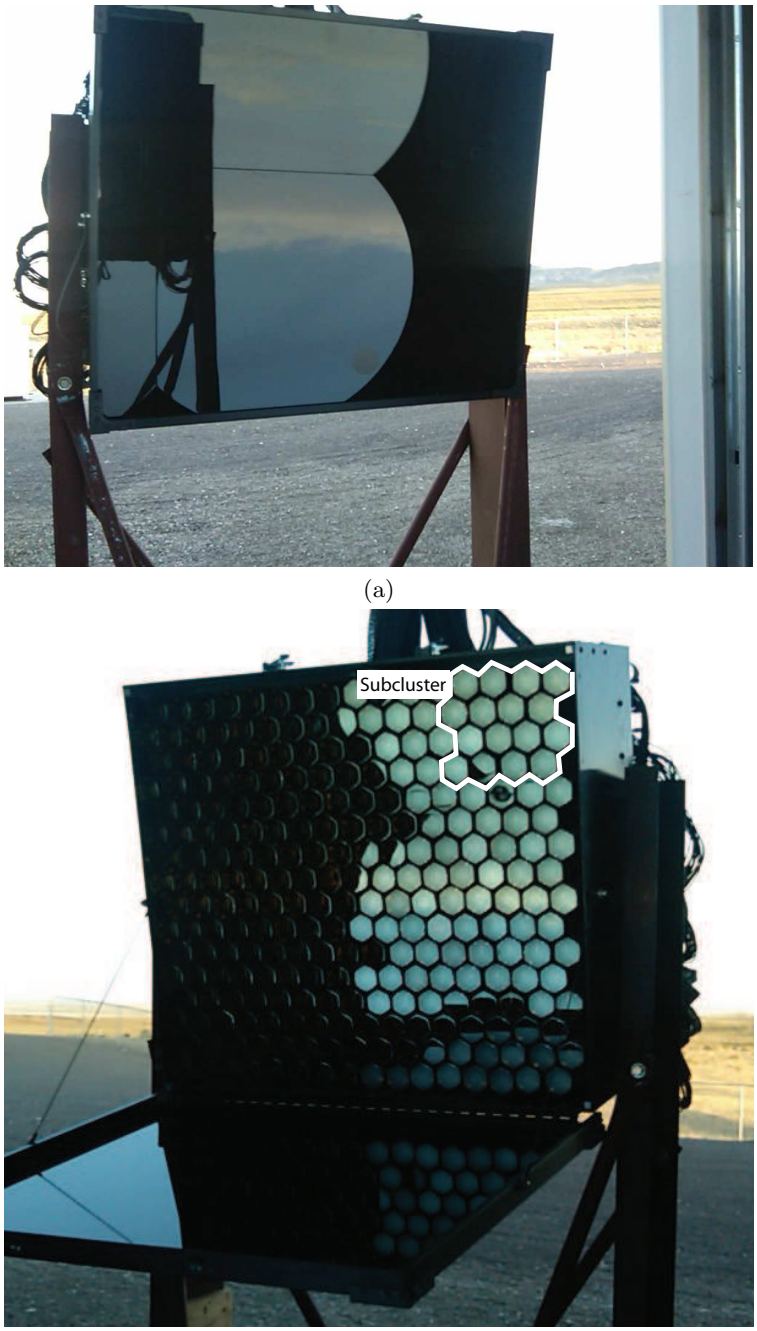


(a)

(b)

**Figure 3.16**. Photos of MD telescope PMT Camera: they are shown with the filter closed (top) and open (bottom). (a) One can see the image of the cloverleaf mirror and the camera itself reflected from the UV band-pass filter covering the PMTs. (b) The UV filter has been opened to reveal the 256 PMTs (pixels) housed within. A subcluster of 16 PMTs has been highlighted for reference.

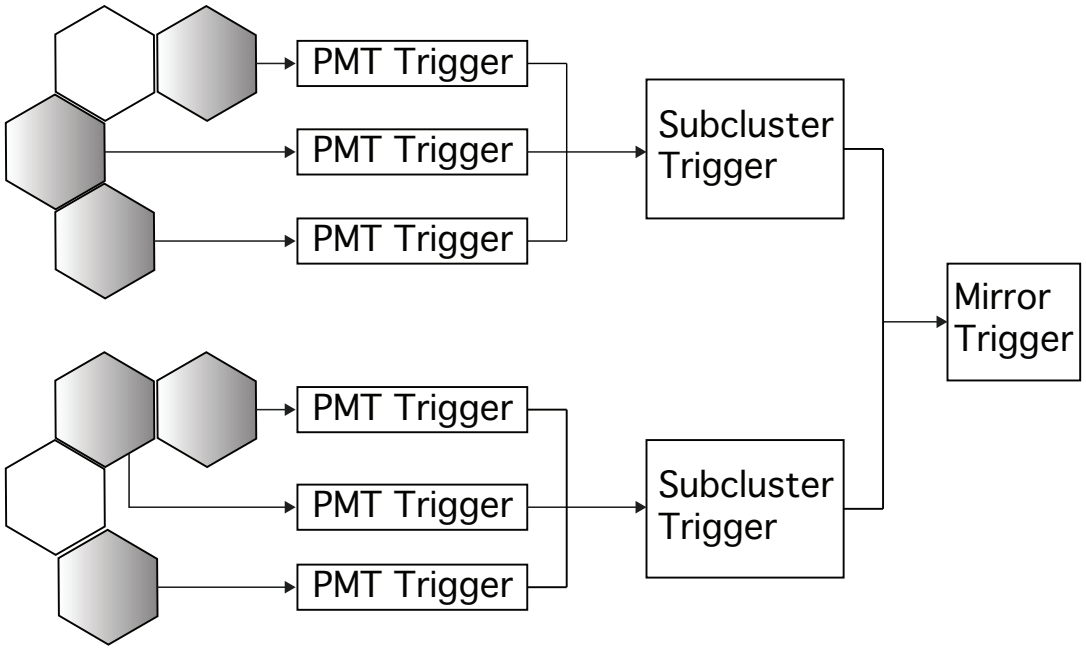


**Figure 3.17**. Examples of trigger conditions and triggering logic flow: triggering conditions are typically three tubes, two of which must be adjacent from two subclusters.

previous section, a single tube trigger is saved for 25 $\mu$s. A "subcluster" (cluster of 16 PMTs within one camera, shown in Figure 3.16b) trigger occurs when at least three tubes, with two adjacent, all trigger within a 25 $\mu$s window. All possible combinations of this trigger condition are stored in memory ($64k \times 4$) static RAM on an "OMmatidial" Board (OMB), and when any of the conditions are met, the subcluster trigger becomes true.

Each subcluster trigger is transmitted to a "mirror trigger" board. When two subclusters trigger within a 25 $\mu$s window, a "telescope" level trigger occurs. A set of trigger conditions are also stored for the telescope level pattern on the trigger board. A telescope level trigger initiates (i) an additional 25 $\mu$s holdoff time to allow for data collected by tubes which triggered after the early triggered tubes, and (ii) a signal to neighboring telescopes, known as the "nearest neighbor trigger." The latter reduces the requirements for a telescope level trigger in the neighboring telescopes to a single subcluster. The reduced neighbor trigger allows small pieces of the shower crossing only one subcluster on the edge of a telescope to be captured that otherwise might be missed.

During MD data-taking, the individual trigger rate of a telescope is about 1.2 - 2 Hz, which includes a steady 1 Hz rate of UVLED flashes (see Section 3.3.1). The actual trigger rate is determined by the count rate target of 200 Hz, which optimizes our sensitivity without overwhelming the bandwidth of the Data AcQuisition (DAQ) system.

### 3.2.2 Middle Drum Detector Electronics

Figure 3.18 shows a schematic of the electronic DAQ system for each telescope in the Middle Drum detector [38]. A pre-amplifier is attached to each PMT which converts the PMT current output to a voltage signal. The latter is then sent to the read-out electronics rack through twisted pair ribbon cables. The signal is split into a single-threshold discriminator and a delay line. If the signal in the discriminator exceeds threshold (set between 200 - 1240 mV), the signal in the delay line is stored in a capacitor and integrated for 5.6 $\mu$s. Then the Time to Digital Converter (TDC) for this channel receives an individual start signal. The digitized tube signals are held for 25 $\mu$s. During this time, if a telescope level trigger occurs, all the PMT signals that are being held are converted to a digital signal through a 12-bit Analog to Digital Converter (ADC). The "cluster" of 256 PMTs is organized into sixteen subclusters. All the PMTs from a subcluster view a contiguous $\sim 4^\circ \times 4^\circ$ piece of the sky, and all the signals are processed by a single subcluster OMB. When a telescope trigger occurs, a "common STOP" is sent to all the TDCs. All the DC

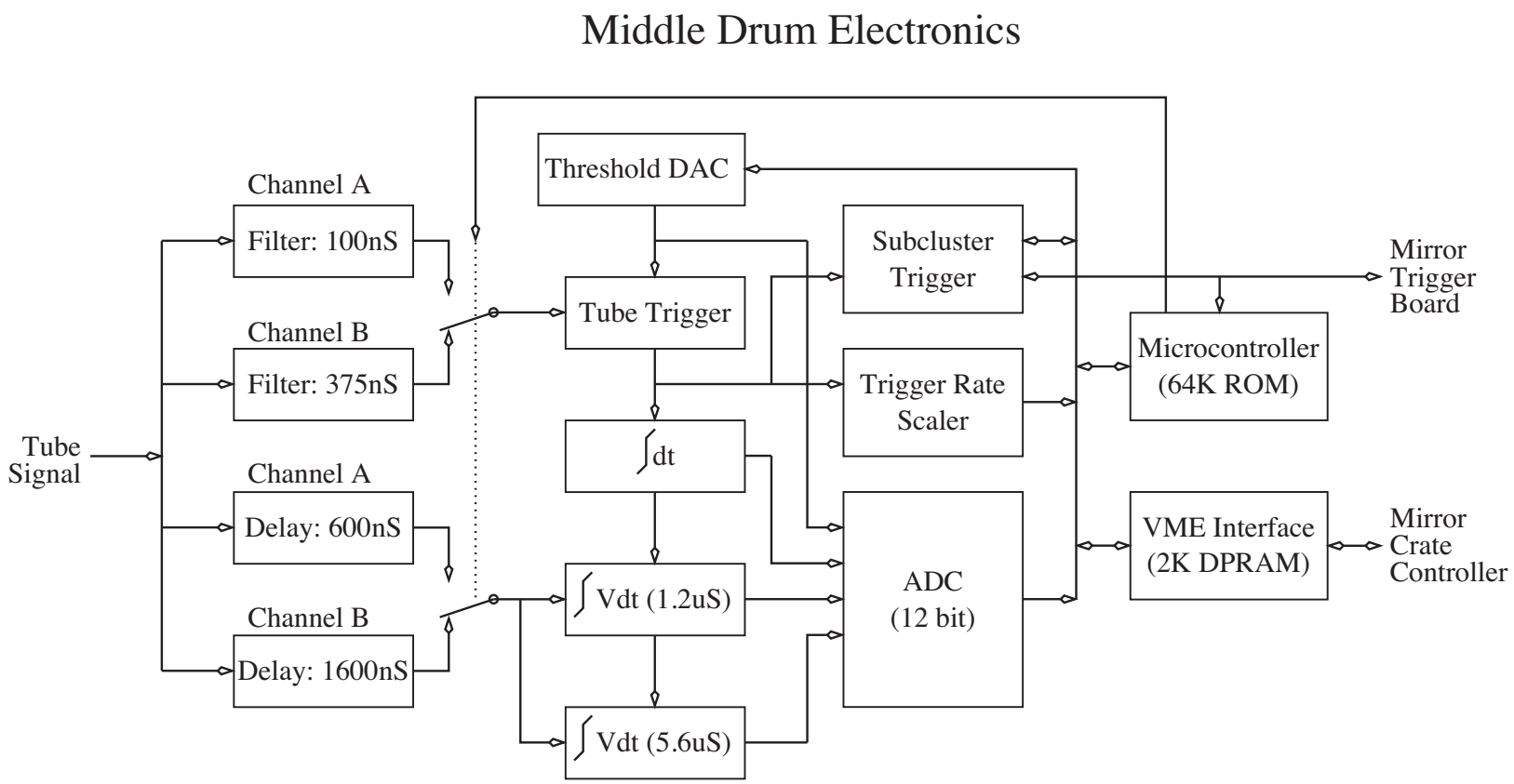


**Figure 3.18**. This is a schematic of Middle Drum (MD) telescope electronics. The tube signal can be sent to "Channel A" or "Channel B" where it is split between a discriminator and a delay line. Note that the switches for the tube trigger and integrator are set for the signal to use "Channel B" for our current use ("Channel A" was used in a previous experiment). The PMT signal is split between a discriminator (filter) and a delay line (1600 ns), and integrated for 5.6 $\mu$s, before it is read by the Analog to Digital Converter (ADC).

channels and TDC channels in a subcluster are digitized using a single ADC chip (Maxim, MAX162). On average, 0.8 photoelectrons per QDC count is measured. Each TDC count is approximately 14 ns. Each telescope has a "dead time" of 2 ms while the event data is read out.

## 3.3 Middle Drum Calibration

The energy measurement of the primary cosmic rays from the air shower depends upon several important calculations. These include (a) the conversion of the digitized QDC signal to the number of photons; (b) the transmission of the fluorescence photons from the shower to the detector; and (c) the conversion of the observed number of photons at the shower to the number of charged particles in the shower (mostly $e^+$ and $e^-$), i.e., the fluorescence yield.

### 3.3.1 Photometric Calibration

For the MD detector, the photometric calibration, i.e., the conversion between the number of photons captured by a PMT and the digitized QDC value relies primarily on the Roving Xenon Flasher (RXF). The flasher uses a xenon flash lamp, optical filters and a teflon diffuser to provide a uniform light source to all the PMTs. When performing an RXF calibration run, the flasher is used to illuminate the camera of each telescope. It is placed at the center of each mirror (always the same distance from the camera, $\sim$2 m). Figures 3.19 and 3.20 show the RXF close up, and in its position at the center of a mirror, illuminating a camera, respectively. The RXF illuminates a camera for $\sim$1 $\mu$s pulses of light, and is fired at 1.5 Hz for about 500 shots. The RXF is particularly useful for calibration purposes due to its stability. The number of photons produced per flash varies only slightly from pulse to pulse ($\sim$0.3%) [29]. RXF calibrations are performed about once or twice each month.

From the RXF data, each of the individual PMTs is calibrated using photo-statistics. The number of photoelectrons sampled by the PMT represents a Poisson distribution. However, after the dynodes have amplified the signal, the number of electrons sampled represents a Poisson distribution broadened by a "noise" factor. Therefore, Poisson statistics may be used, after accounting for this factor.

Using Poisson statistics, the average number of photoelectrons produced in a PMT may be estimated using the width of the measured charge distribution of that PMT after a significant number of measurements (i.e., flashes of the RXF). Equations 3.2 and 3.3 relate the average number of photoelectrons to the mean, $\mu$, and standard deviation, $\sigma$,

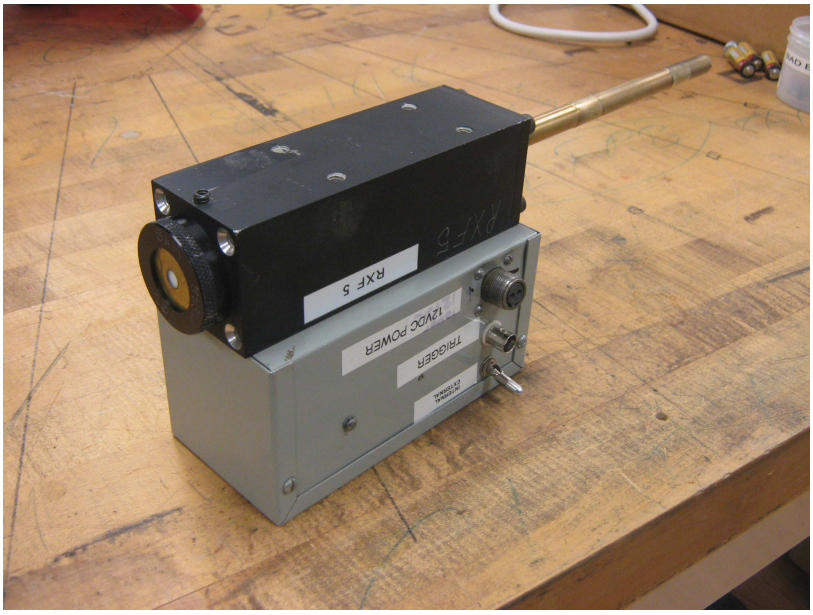


**Figure 3.19**. This is a photograph of the close up view of the Roving Xenon Flasher (RXF). Shown is the long post for mounting the RXF on each mirror, the black box which contains the flash lamp, and the grey box containing the power source.

of the charge distribution using the gain of the PMT. Figure 3.21 shows a typical charge distribution of a PMT.

$$\mu_{QDC} = G \times pe \tag{3.2}$$

$$\sigma_{QDC} = G \times \alpha\sqrt{pe} \tag{3.3}$$

In these equations, $\mu_{QDC}$ and $\sigma_{QDC}$ represent the mean and standard deviation of the charge distribution of the PMT, while $pe$ represents the average number of photoelectrons, G represents the gain of the PMT, and $\alpha$ is the excess noise factor in the PMT. Since the average number of photoelectrons, or $pe$, is not known, it is estimated using equation 3.4.

$$N_{pe} = \frac{(n-3)}{(n-1)}\alpha^2\frac{\mu_{QDC}^2}{\sigma_{QDC}^2} - \frac{\alpha^2}{n}\,,\ n > 3 \tag{3.4}$$

Here, $N_{pe}$ represents an estimate of $pe$, $n$ represents the number of measurements, while $\mu_{QDC}$ and $\sigma_{QDC}$ are the mean and standard deviation of the charge distribution. Equation 3.5 gives the expression of the statistical uncertainty for this estimate.

$$\sigma_{N_{pe}}^2 = \frac{2}{(n-5)}(pe)^2\left[1 + 2(n-2)\left(\frac{\alpha^2}{n\cdot pe}\right) + (n-2)\left(\frac{\alpha^2}{n\cdot pe}\right)^2\right],\ n > 5 \tag{3.5}$$

**Figure 3.20**. A photograph of the Roving Xenon Flasher (RXF) positioned at the center of the mirror where it illuminates the PMTs in the camera: the UVLED has been removed from its position at the center of the mirror to make space for the RXF.

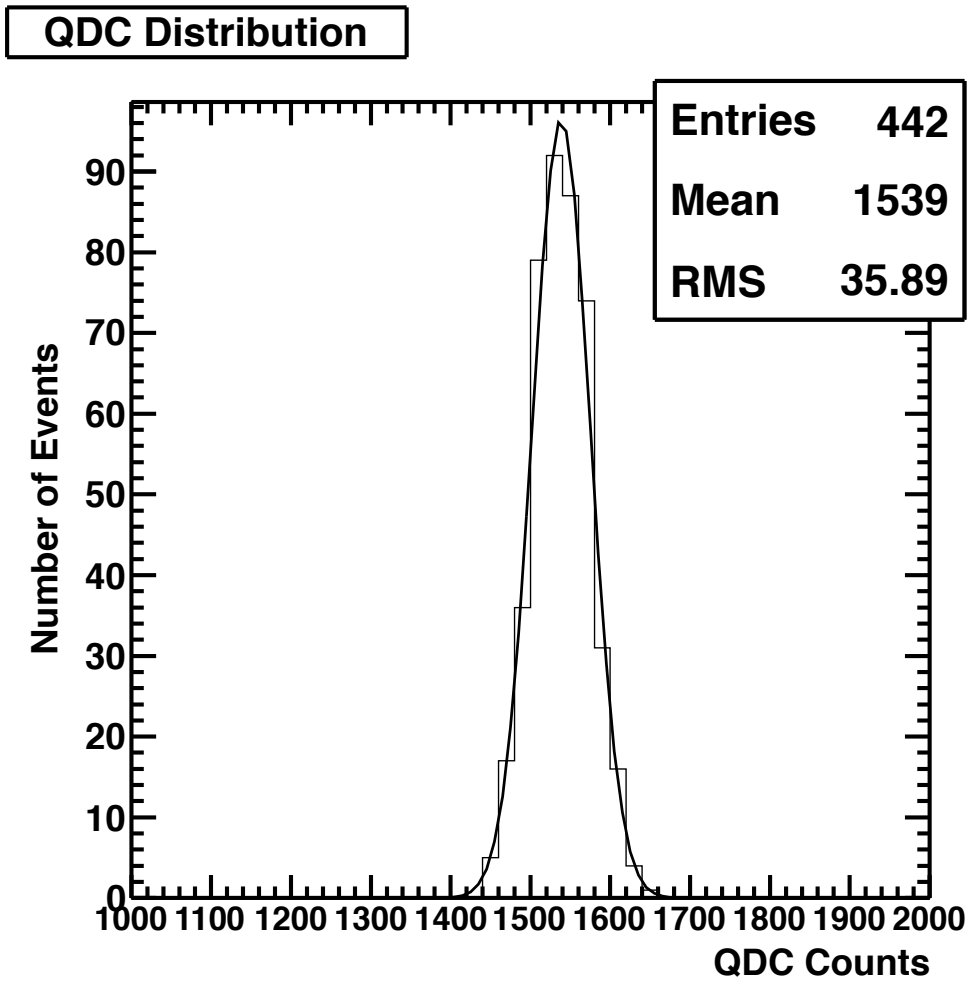


**Figure 3.21**. This is the charge distribution of one PMT over many RXF flashes. The mean and RMS of this measurement is used to estimate the number of photoelectrons.

In the limit of large $n$, these formulas can be reduced to the form of equations 3.6 and 3.7. Therefore, only the mean and standard deviation of the charge distribution over many measurements is needed to measure the average number of photoelectrons.

$$N_{pe} \approx \alpha^2 \frac{\mu_{QDC}^2}{\sigma_{QDC}^2}, \; n \gg 3 \tag{3.6}$$

$$\sigma_{N_{pe}}^2 \approx \frac{2}{(n-5)} (pe)^2, \; n \gg 5 \tag{3.7}$$

In addition to the RXF, a temperature controlled Ultra Violet Light Emitting Diode (UVLED) is placed at the center of each mirror, as shown in Figure 3.22. (In Figure 3.20, the UVLED is removed to allow the insertion of the RXF.) The UVLED flashers are used nightly to calibrate the PMTs. Each camera is illuminated by its own UVLED. As in the

case of the RXF, a teflon diffuser is used to ensure uniform coverage of the PMTs in the camera. Black cups are placed around the UVLED source to prevent strong light from hitting a neighboring mirror or camera. Before, during, and after every run, the UVLEDs flash light at 355 nm uniformly across all the PMTs in the cluster. During data collection, the UVLED fires at 1 Hz. The consistent measurements performed by the UVLEDs allows us to track the PMT gain virtually in real time.

The output of each UVLED is well understood as a function of temperature. We also control and monitor the temperature of each UVLED individually. Figure 3.23 shows the variation of the gain, or number of photoelectrons per QDC produced over time. Figure 3.24 shows how the output of both the Photonis and EMI PMTs is correlated with temperature. The clear understanding of this variation is accounted for in the calibration process. Figure 3.25 shows how the gain is stabilized after this correction.

### 3.3.2 Atmospheric Calibration and Monitoring

An understanding of the atmosphere is important for analyzing both how the showers develop from the primary particle interaction as well as how the light from the shower propagates to the detector where it is collected. Atmospheric modeling for the fluorescence telescopes relies on (a) atmospheric density profile, and (b) aerosol concentration and distribution.

#### 3.3.2.1 Atmospheric Profile

The amount of light generated at a particular position in an EAS depends directly on the number of particles at that point in the shower. The particles in the shower are generated as a function of the density of the atmosphere. Therefore, an accurate understanding of the density gives a more accurate calculation of the number of particles at any given point in the shower. Early versions of this analysis depended upon the US 1976 atmospheric profile [33], but for a more accurate atmospheric density profile measurement, this analysis uses radiosonde data from the National Weather Service site near Delta, Utah. As shown in Figure 3.26, the atmospheric profile includes information about pressure at varying heights above sea level. The US 1976 atmosphere is included on the plot for reference. As shown, the radiosonde measurements only reach to 30 km in height. At that point, the value of the radiosonde measurement is used as a starting point, and the US 1976 atmospheric profile is used to extrapolate rest of the atmospheric profile, so that there is no problem with discontinuity.

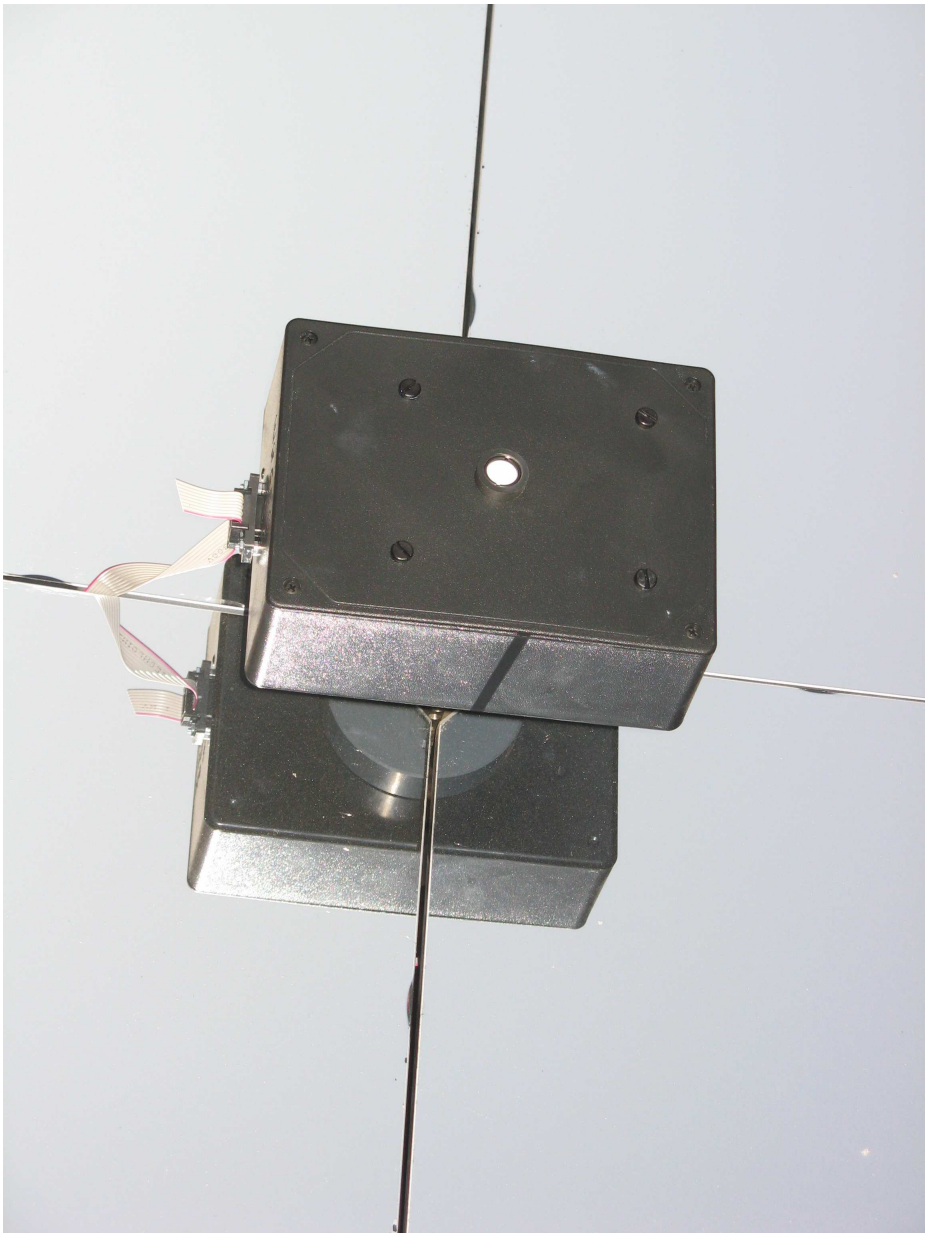

**Figure 3.22**. Ultra Violet Light Emitting Diode (UVLED): Each of the 14 telescopes at the Middle Drum (MD) site is instrumented with a UVLED at the center of the mirror as shown. These flashers are used to illuminate the PMTs before, during, and after data collection each night for calibration.

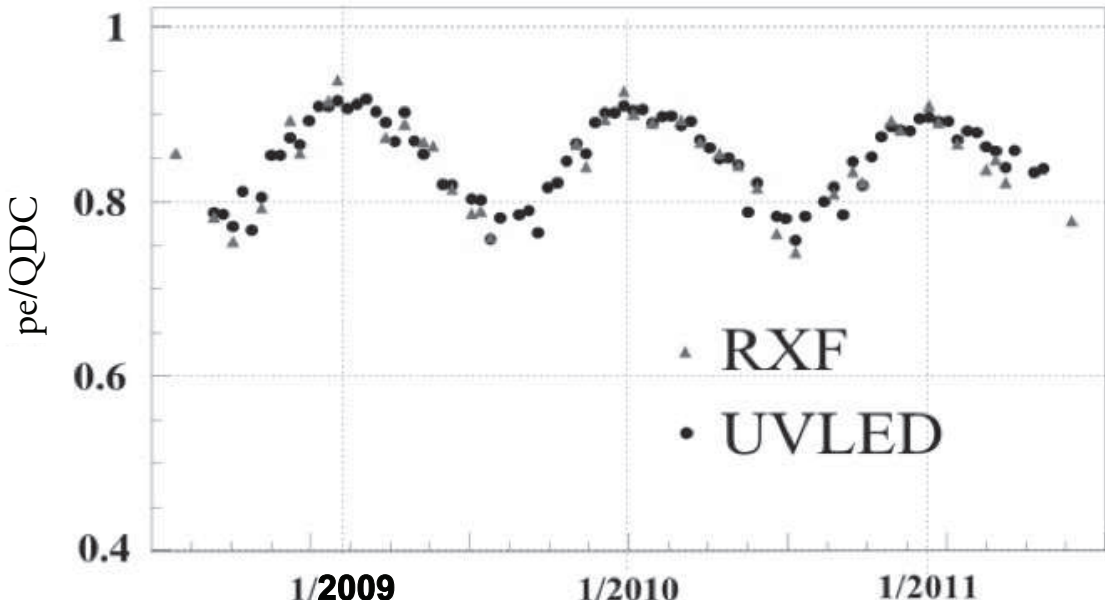


**Figure 3.23**. RXF and UVLED data: shown is the variation of the number of photo-electrons per QDC produced over time. The seasonal variation with temperature is clearly visible.

#### 3.3.2.2 Aerosols

Rayleigh scattering (described in Section 4.1.2) of the light from air showers is relatively constant, varying by only a few percent with the atmospheric profile; however, aerosol scattering can vary drastically from night to night. The LIght Detection And Ranging (LIDAR) technique is used to determine the total load and vertical distribution of aerosols. The total load is specified in terms of the Vertical Aerosol Optical Depth (VAOD). The transmission factor of aerosols as a particle passes through the atmosphere is defined by equation 3.8.

$$T_{aerosol} = e^{-\tau} \tag{3.8}$$

Here, $\tau$ represents the "aerosol optical depth", or opacity of the atmosphere. The VAOD is calculated as $\tau$ once $T_{aerosol}$ is integrated over the entire height of the atmosphere.

Both monostatic and bi-static LIDAR are used to study the Telescope Array atmosphere. Figure 3.27 shows the monostatic LIDAR facility, which is located at the Black Rock Mesa (BRM) fluorescence detector. This facility houses an energy tripled neodymium-doped yttrium aluminum garnet (Nd: YAG) laser operating at 355 nm. Figure 3.28 shows the measured VAOD at the Telescope Array [43]. The median value is 0.035.

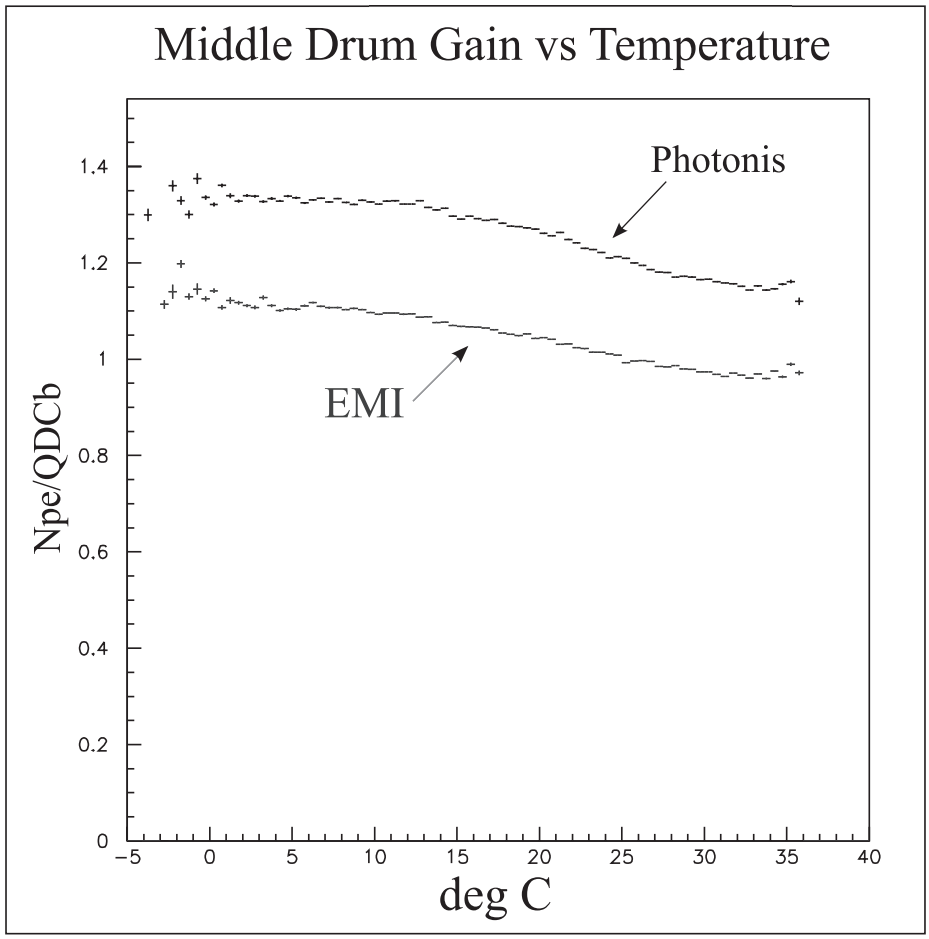


**Figure 3.24**. UVLED data: shown is the variation of the number of photoelectrons per QDC produced versus temperature in the two types of PMTs (Photonis and EMI). Both types of PMTs show a temperature dependence.

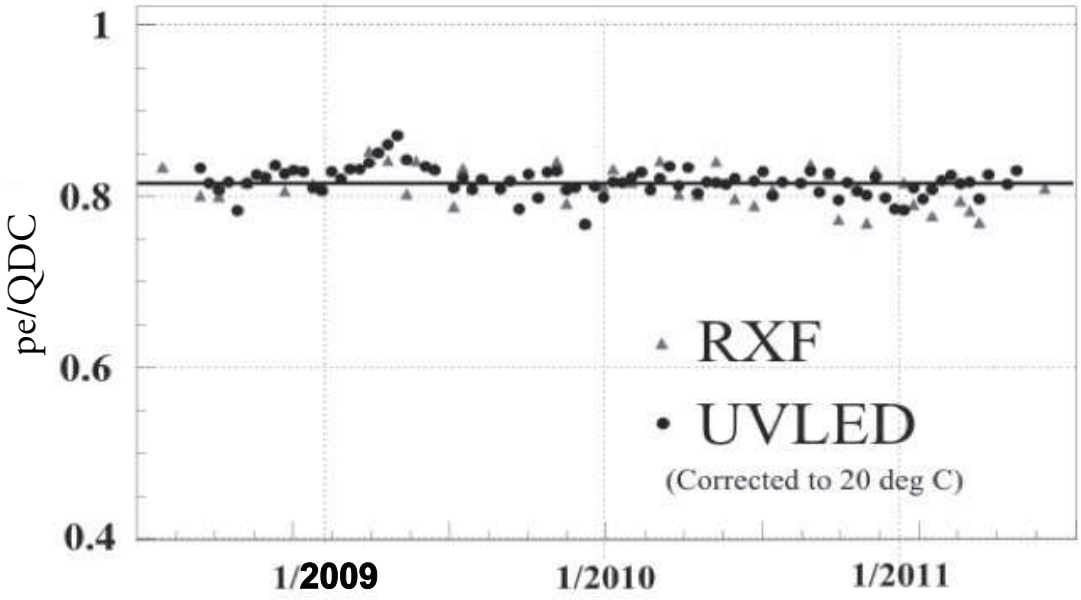


**Figure 3.25**. Number of photoelectrons produced by the RXF and UVLED, shown corrected for temperature variation. Here the temperature dependence has been removed, and the gain is stabilized after the correction.

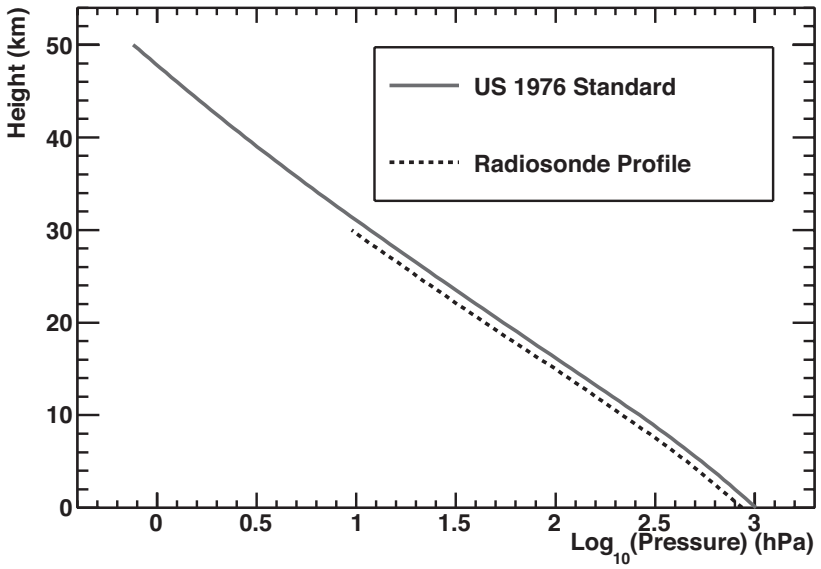


**Figure 3.26**. The TA average atmospheric pressure profile measured from Radiosonde is plotted (dotted line) with the US 1976 atmospheric pressure model (solid line). For this analysis, the Radiosonde model is used up to 30 km, at which point, the value at that height is used as a starting point for an extrapolation using the US 1976 model.

**Figure 3.27**. This photograph shows the monostatic LIDAR facility located at the Black Rock Mesa Fluorescence Detector (BRMFD). It houses a Nd: YAG laser used for measuring the Vertical Aerosol Optical Depth (VAOD).

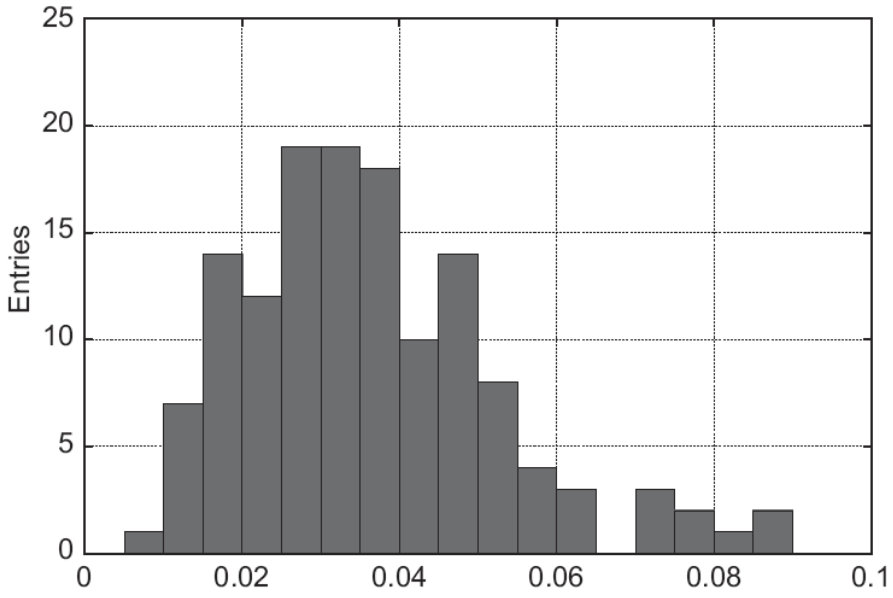


**Figure 3.28**. The measured Vertical Aerosol Optical Depth (VAOD) at Telescope Array: each entry in the histogram corresponds to a measurement of the VAOD performed using the monostatic LIDAR system. This system collects data each night that the detector is operational. Copyright (2010), with permission from Elsevier.

For this analysis, a mean value of 0.04 (one significant digit) for the VAOD was used. The effect of the VAOD value on the overall energy scale was studied and is documented in [38]. Using a range of VAOD values between 0.02 - 0.04, the estimated maximum uncertainty in the energy measurement due to the VAOD value was determined to be ∼3%.

The Central Laser Facility (CLF) is also used for atmospheric calibration. The CLF is located in the geometric center of the Telescope Array, equidistant from all three fluorescence detector stations (approximately 21 km away from each). This facility is also instrumented with a 355 nm energy tripled YAG laser, which fires vertically into the sky every 30 minutes during detector operations. One of the uses of the vertical laser at the CLF is for monitoring aerosol content in the air, via bi-static LIDAR. Each fluorescence detector measures the light from the laser and can therefore determine the effect of the atmosphere in propagating the light from the CLF to its location on the periphery of the array. By comparing the amount of light detected with the known amount of energy from the laser, the aerosol concentration can be determined by a reverse Monte Carlo process.

Furthermore, the three fluorescence telescopes can do a relative comparison of their energy reconstruction. This comparison allows for a cross-calibration of the energy reconstruction. Each telescope views the laser shots from the CLF through the same atmosphere, and therefore, assuming homogeneity over the area of the detector, the energy reconstructed without atmospheric calibration should be the same.

#### 3.3.2.3 Weather Monitoring

In order to make reliable calculations of the detector aperture, we must exclude data taken during periods of cloud cover in the field of view. For this purpose, weather monitoring is done by members of the collaboration on nightly shifts at the MD detector. Approximately every 40 minutes, a shift operator must go outside to observe and record the sky condition, with particular attention to clouds. A string of seven numbers, called a WEAT Code is used to describe the sky condition by the shift member. Table 3.1 gives a description of each number in the string. For example, a WEAT code for a perfectly clear night looks like "0000000," whereas on a totally overcast night is "1111411." This code is used to remove data taken during significant cloud cover, for which detector aperture calculations become unreliable. A list of allowed WEAT codes is included in Section 6.1, where the data selection process is described.

**Table 3.1**. This is a summary of WEAT (weather) codes. Listed are all the WEAT Codes used by operators when examining sky condition during MD detector operation.

| Place in string | Part of the sky | Possible Entries | Meaning of Entries |
|---|---|---|---|
| 1 | Northern Horizon | 0<br>1 | no clouds<br>clouds |
| 2 | Eastern Horizon | 0<br>1 | no clouds<br>clouds |
| 3 | Southern Horizon | 0<br>1 | no clouds<br>clouds |
| 4 | Western Horizon | 0<br>1 | no clouds<br>clouds |
| 5 | Overhead | 0<br>1<br>2<br>3<br>4 | No clouds overhead<br>up to 25% cloud cover<br>btw 25% and 50% cloud cover<br>btw 50% and 75% cloud cover<br>More than 75% cloud cover |
| 6 | Overhead Thickness | 0<br>1 | Can see stars through clouds<br>Cannot see stars |
| 7 | Haze | 0<br>1 | No haze<br>haze |

### 3.3.3 Fluorescence Yield

The fluorescence light generated from the shower is due to interactions of the charged particles of the shower with the atmosphere. Nitrogen molecules, excited by the charged particles in the atmosphere relax and emit characteristic ultraviolet light, mostly in the near UV range, 300-400 nm. The number of electrons in the shower is directly related to the amount of fluorescence light emitted. The fluorescence yield is the amount of light generated by a single ionizing particle. Equation 3.9 shows how the fluorescence yield is used to calculate the number of electrons at a particular point in an EAS, given the number of photons produced per unit length, per unit solid angle.

$$\frac{d^2N_\gamma}{dld\Omega} = \frac{YN_e}{4\pi} \tag{3.9}$$

Here, $N_\gamma$ is the number of photons generated from the number of electrons, $N_e$, at that point in the shower. Y is the fluorescence yield. The analysis described in this dissertation uses the FLASH differential spectrum, normalized to the overall fluorescence yield measured by Kakimoto et al [37, 30].

The wavelength spectrum of nitrogen fluorescence is shown in Figure 3.29. This measurement was performed by the FLuorescence in Air from SHowers (FLASH) experiment

[37]. This spectrum has primary peaks at ∼312 nm, ∼337 nm (the nitrogen laser line), ∼355 nm, and between 370 - 390 nm. In the figure, the Bunner spectrum is shown for reference [18]. The Middle Drum monocular analysis performed by D. Rodriguez, [38], used the Bunner spectrum. While the analysis for this work uses the FLASH spectrum, the analysis was also performed using the Bunner spectrum. There was no discernible difference in the result.

Most of the ionizing particles from EAS are electrons and positrons, of which more than 90% have energies below $10^9$ eV, and can be simulated by particle beams in an accelerator [15]. Figure 3.30 shows the overall fluorescence yield measured by several experiments using electrons of a wide variety of energies [38]. As the kinetic energy in the ionizing particle increases, the amount of energy deposited decreases, as there is less interaction between the moving particle and its surroundings. Eventually, the amount of energy deposited will reach a minimum, as the moving particle approaches the speed of light. Beyond this point,

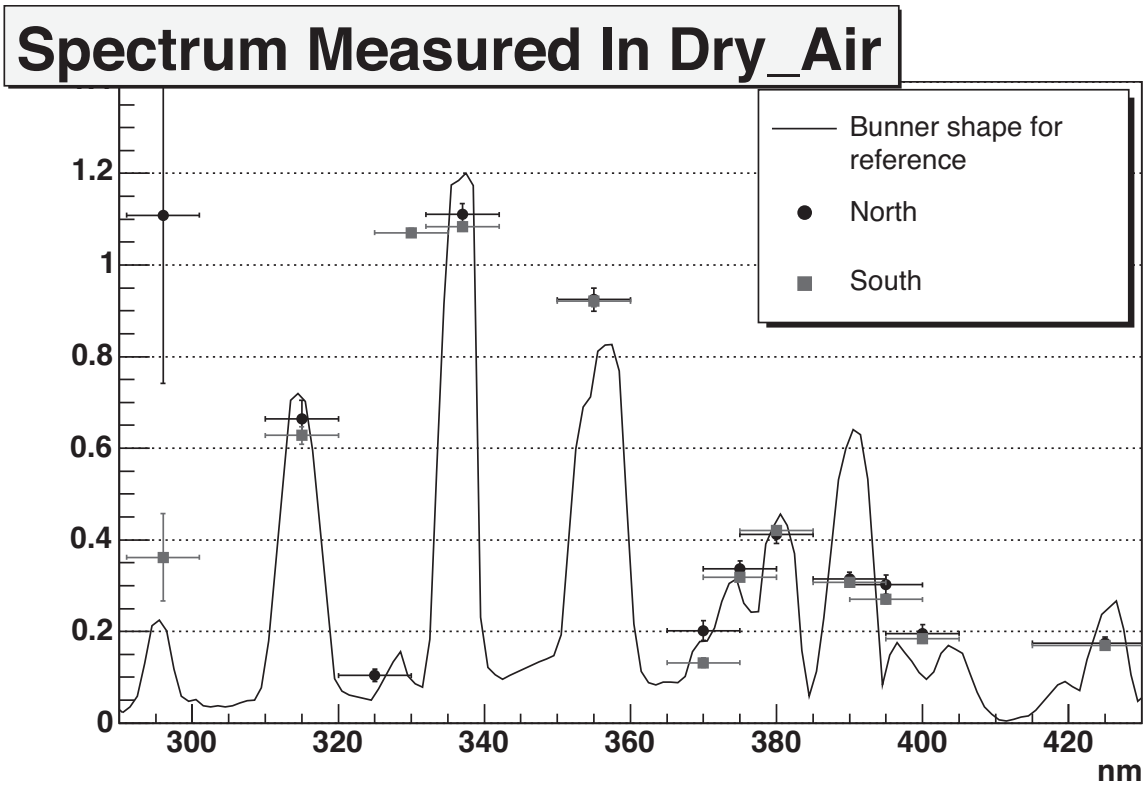


**Figure 3.29**. The nitrogen fluorescence spectrum as measured by the FLASH collaboration: the spectrum calculated by Bunner is shown as a black line for reference. This measurement done by the FLASH collaboration is used for the analysis in this dissertation.

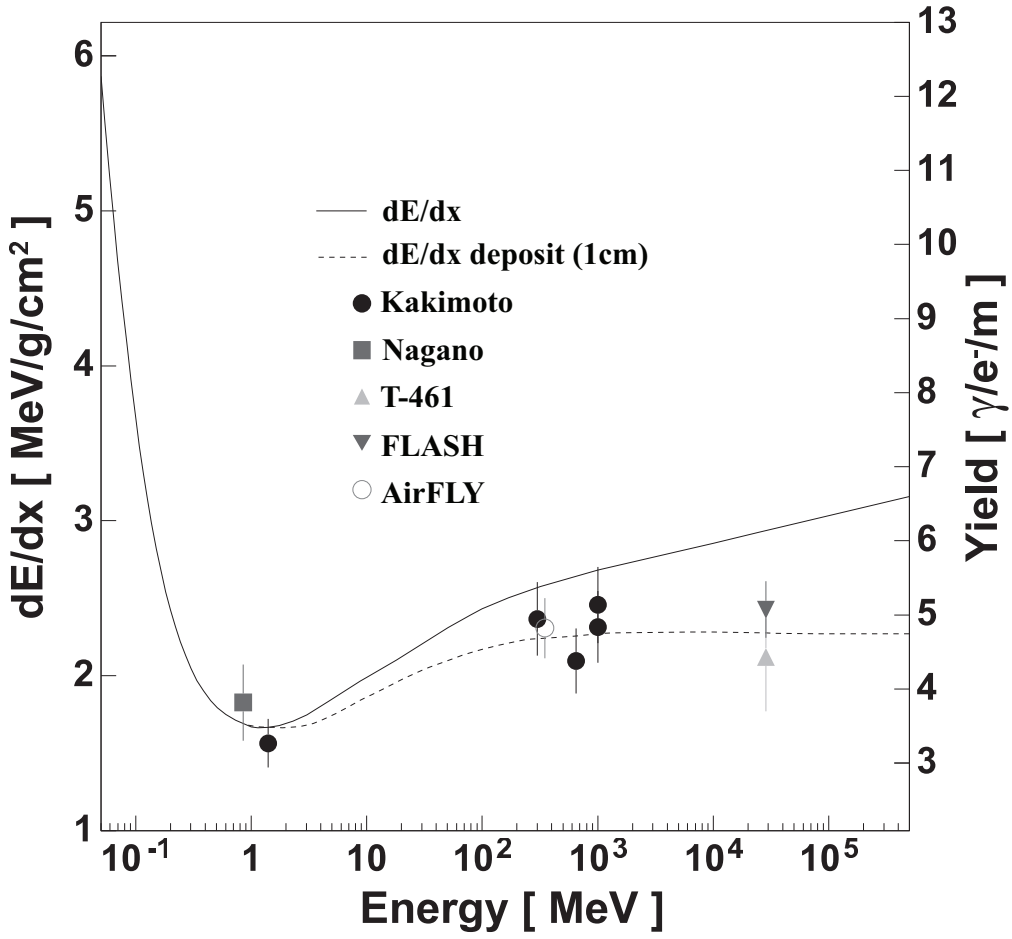


**Figure 3.30**. Shown are the measurements of the nitrogen fluorescence yield done by several experiments. As the ionizing particle reaches relativistic speeds, the amount of energy deposited reaches a minimum. Beyond this point, secondary ionizing particles, or $\delta$-rays contribute to the amount of energy deposited. The dotted line shows the amount of energy measured from deposition in 1 cm of atmosphere. The solid line gives the energy deposited from the particle with no limit on length scale, which allows for the energy absorbed from $\delta$-rays to be measured.

however, hard collisions between the moving particle and nearby particles will generate secondary moving ionizing particles, or $\delta$-rays. These $\delta$-rays then also deposit energy in the same manner as the primary particle. The increase in deposited energy above the minimum demonstrates this effect. The dotted line shows the amount of energy measured from the deposition of energy in only 1 cm of atmosphere. The solid line, however, shows the energy deposited in the atmosphere without limitation. This allows for the energy deposited by the $\delta$-rays to be measured as well.

In energy spectrum measurements, such as the measurement done for this dissertation, uncertainty in the fluorescence yield calculation represents a significant contribution to the uncertainty in the energy scale. It is important to note, however, that the same fluorescence yield was used by both the High Resolution Fly's Eye Experiment and by the Telescope Array experiment. Therefore, the fluorescence yield uncertainty is common for the two spectrum measurements. Similarly, the SD monocular energy spectrum measurement was made after setting its energy scale to the the Fluorescence Telescope, again making the energy scale uncertainty common to both results.

# CHAPTER 4

# SIMULATIONS

An accurate measurement of the hybrid energy spectrum depends on an accurate understanding of the aperture and exposure of the hybrid detector. The aperture of the detector is dependent upon the layout and efficiency of the detector as well as on the geometry and energy of the shower. The Surface Detector, for instance, is spaced such that events with energies, E $> 10^{19}$ eV are efficiently detected. As the energy increases, the efficiency and SD aperture become constant and the aperture becomes limited by physical boundaries. The fluorescence detector, on the other hand, is capable of efficiently detecting nearby showers at much lower energies than the Surface Detector. For example, for a shower with energy $10^{18}$ eV, the Middle Drum (MD) monocular aperture is $\sim$200 km$^2$ steradians, while the SD has an aperture of $\sim$20 km$^2$ steradians for the same shower energy [28]. The fluorescence detector aperture also increases with energy since energetic showers create more daughter particles, and thus more light that propagates to the detector.

The showers must be detected by both the SD and the fluorescence detector to be used in the hybrid analysis; therefore, the hybrid aperture is necessarily smaller than the aperture of either the SD or the fluorescence detector. Due to the complexities in understanding the union of the fluorescence detector and SD apertures, detailed simulations are the most reliable way to determine it.

## 4.1 Hybrid Monte Carlo Program

The Monte Carlo (MC) programs simulate both the cosmic ray showers as well as the detector response. The MC showers used for this hybrid analysis were generated initially using CORSIKA [24]. At high energies ($E > 80$ GeV), the QGSJET-II [36] hadronic model was used to simulate particle interactions within the shower. At lower energies ($E < 80$ GeV), the FLUKA [14] model was used. The electromagnetic component of the shower was treated using EGS4 [34] .

Due to the enormity and complexity of Extensive Air Showers (EAS) at Ultra High Energies (UHE) ($E \geq 10^{17}$ eV), tracking each daughter particle in the shower is not practical

with the computational power available. Storing these events also requires a huge amount of disk space (∼100 GB per $10^{19}$ eV event). To circumvent these problems, CORSIKA provides a "thinning" option. This option allows for faster computation by representing groups of secondary particles in proximity in phase space with a single weighted particle. A weighted particle is used if its energy is less than a preset energy, which is dependent on the level of thinning. For example, for a shower with initial energy $E_0$, a thinning level of $10^{-6}$ would correspond to an energy of $10^{-6} \times E_0$, below which the particles will be replaced with a single, weighted particle.

The thinning approximation reduces by orders of magnitude the time and disk space it takes to generate showers, and it can produce useful results for fluorescence detector simulations. However, depending on the level of thinning applied, the approximation becomes problematic for the SD MC, since the SD is dependent on the flux of particles that are at large lateral distances from the shower core, which is very sensitive to fluctuations. Therefore, the MC for this analysis and the analysis of the Telescope Array SD uses an innovative technique, pioneered by B. Stokes, called "dethinning" [40]. The major function of this process is to simulate more accurately the distribution of the particles on the ground by smearing each weighted particle using a gaussian distribution around its trajectory.

Figure 4.1 shows a schematic of how the dethinning is performed [28]. For each weighted particle created in the thinning process, the number of missing particles (determined by the weight of the original) are reinserted into the shower. First, a cone is created from an arbitrary vertex point along the weighted particle's path that ends in an oval on the ground. For each missing particle, a point on the ground within the oval is chosen using a gaussian distribution, and a new trajectory is created for that particle. The width of the cone is determined by the lateral distance of the weighted particle from the core axis of the shower. The cone angle for electromagnetic particles is $3\,^{\circ}/\mathrm{km}^2$ , and for hadrons and muons, it is $1\,^{\circ}/\mathrm{km}^2$. These values are used for dethinning showers with a thinning level of $10^{-6}$ and were calculated using a comparison with a library of unthinned showers. Each missing particle re-inserted into the shower is given an energy that is varied using a gaussian distribution with a mean at the energy of the original weighted particle and a standard deviation of 10% of that value. This process is described in detail in [40].

Figure 4.2a shows how the thinning process affects the amount of energy deposited per SD at certain distances from the shower core [28]. Shown in the figure is a comparison between an unthinned CORSIKA shower and the same shower with thinning level $10^{-6}$.

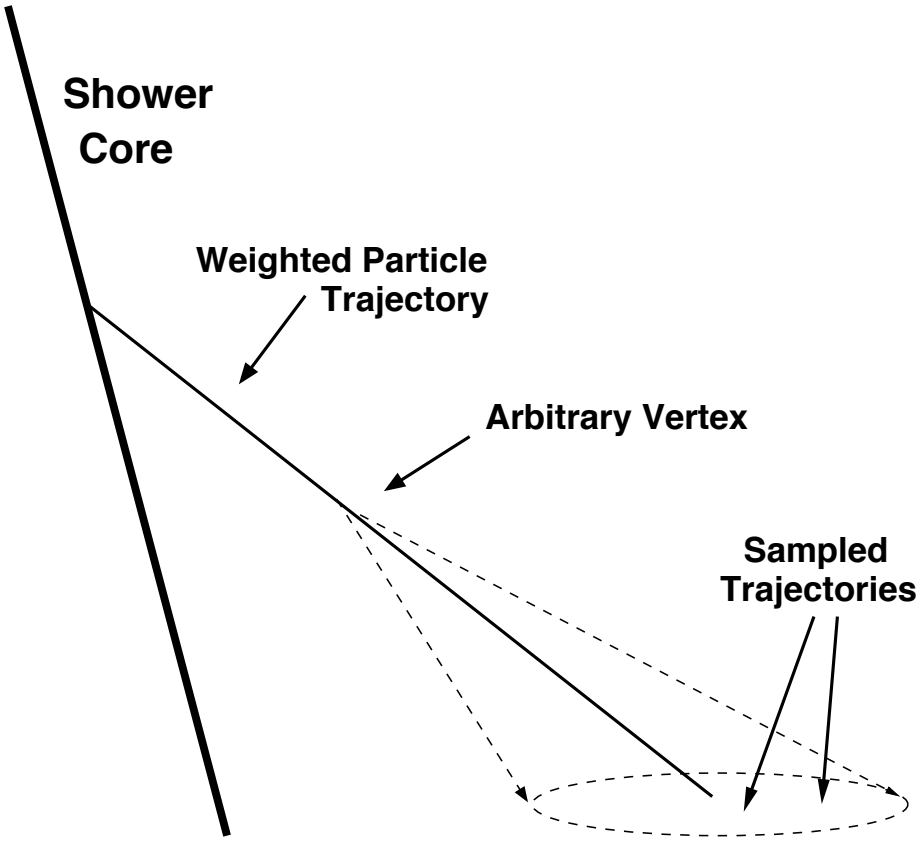


**Figure 4.1**. Schematic showing the dethinning process: weighted particles created from the thinning process in CORSIKA are used to re-insert the missing particles. The width of the cone is determined by the lateral distance of the weighted particle from the shower core. The energy of each missing particle is varied using a gaussian distribution with the mean equal to the energy of the original weighted particle, and $\sigma = 0.1$.

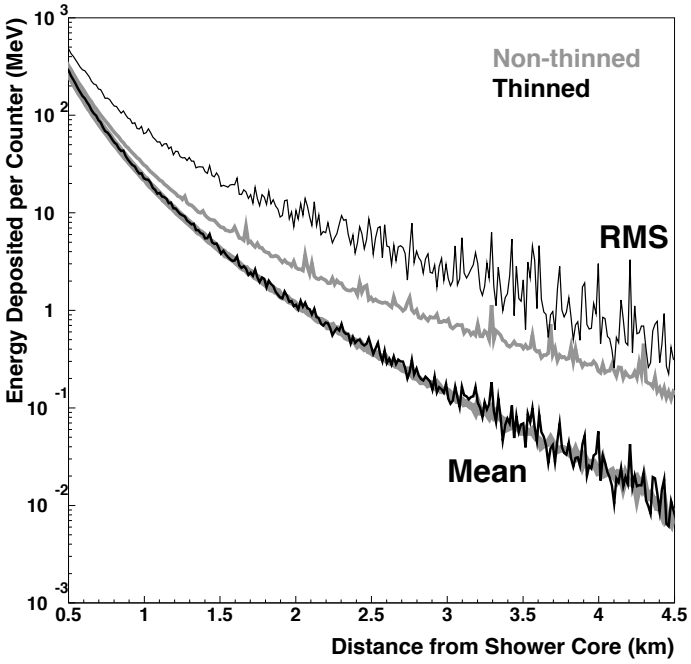


(a)

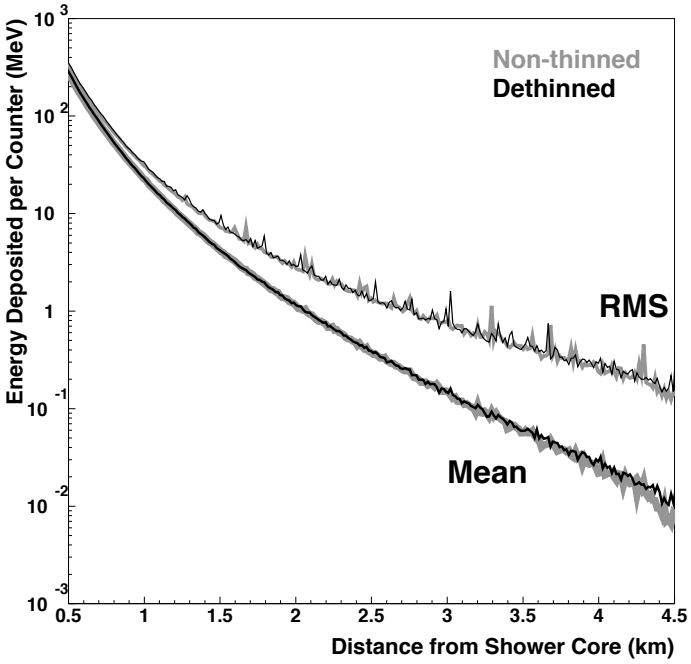


(b)

**Figure 4.2**. The mean and RMS of energy deposited per SD counter plotted as a function of distance from the shower core for an un-thinned CORSIKA shower compared with a thinned shower (top) and a dethinned shower (bottom). In (a), an un-thinned CORSIKA shower is compared to the same shower with a thinning level of $10^{-6}$, while in (b), the un-thinned shower is compared to the same shower after dethinning with much better agreement in both the mean and RMS values.

This plot demonstrates that the RMS in the energy is not reproduced accurately in the thinned shower. Both the mean and the RMS of the thinned shower have much greater fluctuations than the unthinned one. Figure 4.2b compares a dethinned shower with an unthinned shower [28]. The mean and RMS now much more accurately simulate the unthinned shower.

Over 16,000 dethinned proton showers ranging in energy from $10^{16.75}$ eV to $10^{20.55}$ eV with a variety of geometries were created and stored in a shower library [28]. This library was resampled thousands of times using random azimuthal and zenith angles, as well as timing to generate a set of over 150 million simulated events. It is generated using the HiRes piece-wise power law spectrum [4]. Figures 4.3 - 4.6 show the distributions of the parameters [28]. The following list summarizes the parameters of this main simulated data set.

- Composition: Proton Showers only. Previous experiments have shown that showers above $10^{18.0}$ eV are consistent with proton composition [5].
- Energy Slope, E: $E^{-3.25}$ for $E < 10^{18.65}$ eV; $E^{-2.81}$ for $10^{18.65}$ eV $\leq E < 10^{18.75}$ eV; $E^{-5.1}$ for $E \geq 10^{19.75}$ eV. This is the piece-wise power law that was a fit to the HiRes data [4]. See Figure 4.3.
- Surface Impact Position: Uniform, random distribution inside a circle of radius 25 km, centered at the CLF. See Figure 4.4.
- Zenith Angle, $\theta$: $\sin(\theta)\cos(\theta)$ distribution in $[0^\circ - 60^\circ]$ range. The $\sin(\theta)$ represents a spherically isotropic distribution from the sky, while the $\cos(\theta)$ represents the projection of the distribution on a flat target. See Figure 4.5.
- Azimuthal Angle, $\phi$: Flat distribution in $[0^\circ, 360^\circ]$ range. See Figure 4.6.

### 4.1.1 SD Monte Carlo Programs

The SD array samples the particle density from the EAS as it reaches the ground. Each SD makes a measurement of the number of particles which pass through the two layers of scintillating plastic. The data from each SD are the electronic signal generated from the energy deposited by the particles in the shower as well as the time of that signal. Therefore, the SD simulation must model the energy deposited by all the particles as well

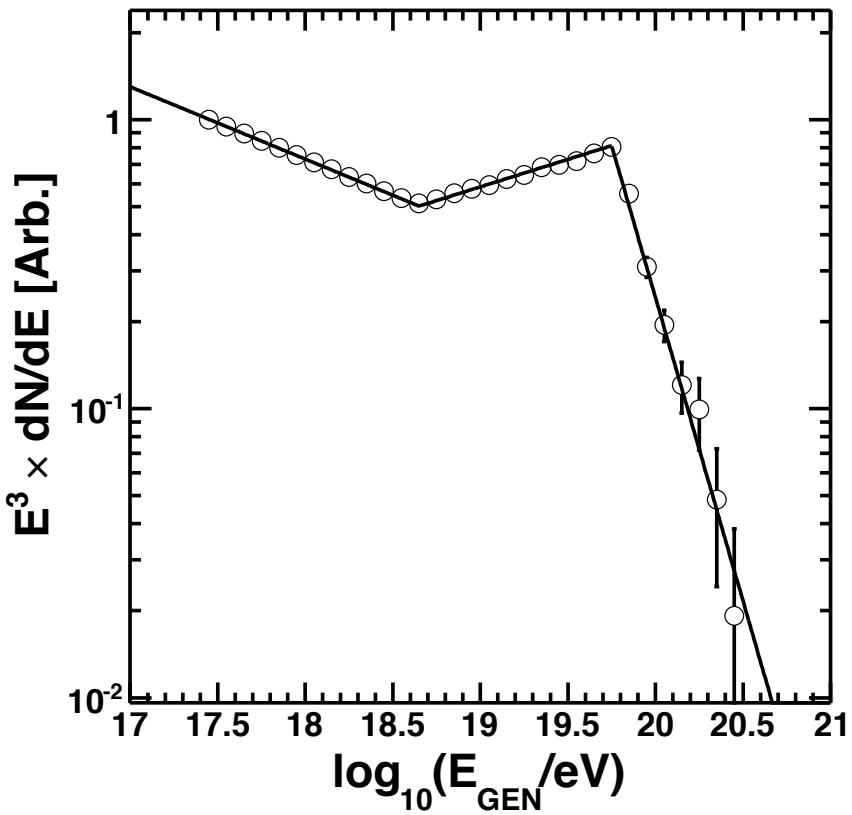


**Figure 4.3**. The Monte Carlo (MC) generated energy distribution: it comes from the HiRes measurement. The solid line represents the distribution, while the points represent samples from the distribution used to generate the Monte Carlo set.

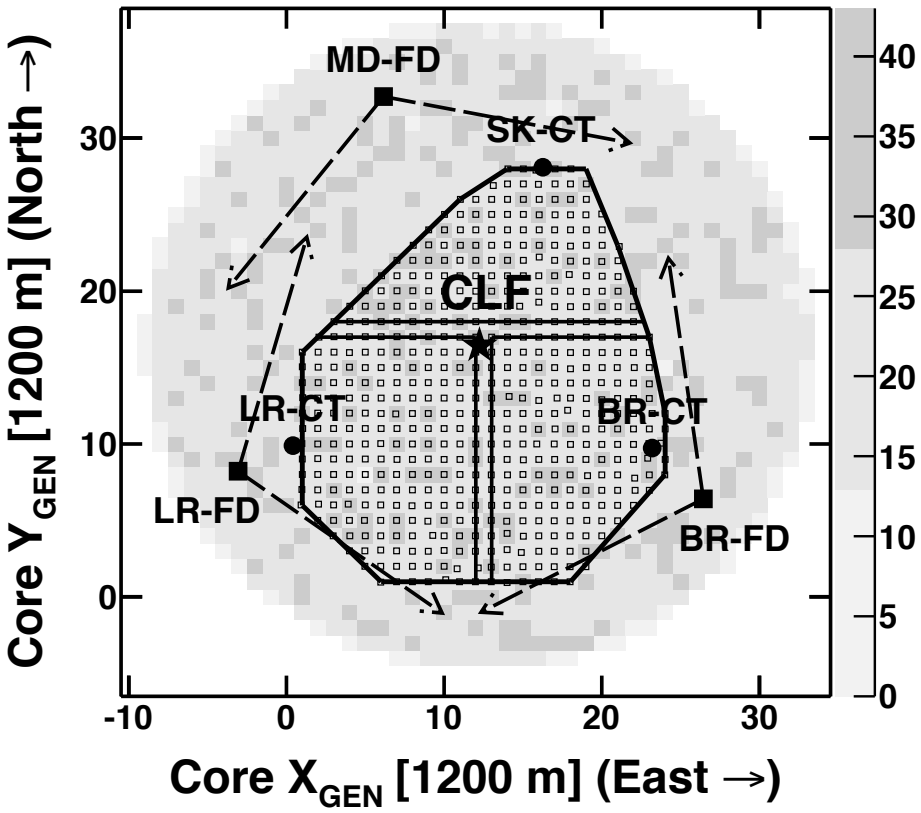


**Figure 4.4**. The Monte Carlo (MC) generated distribution of the position where the shower core crosses the SD plane: it is thrown in a circle centered at the CLF, with a radius of 25 km. The color represents the number of events thrown in each area.

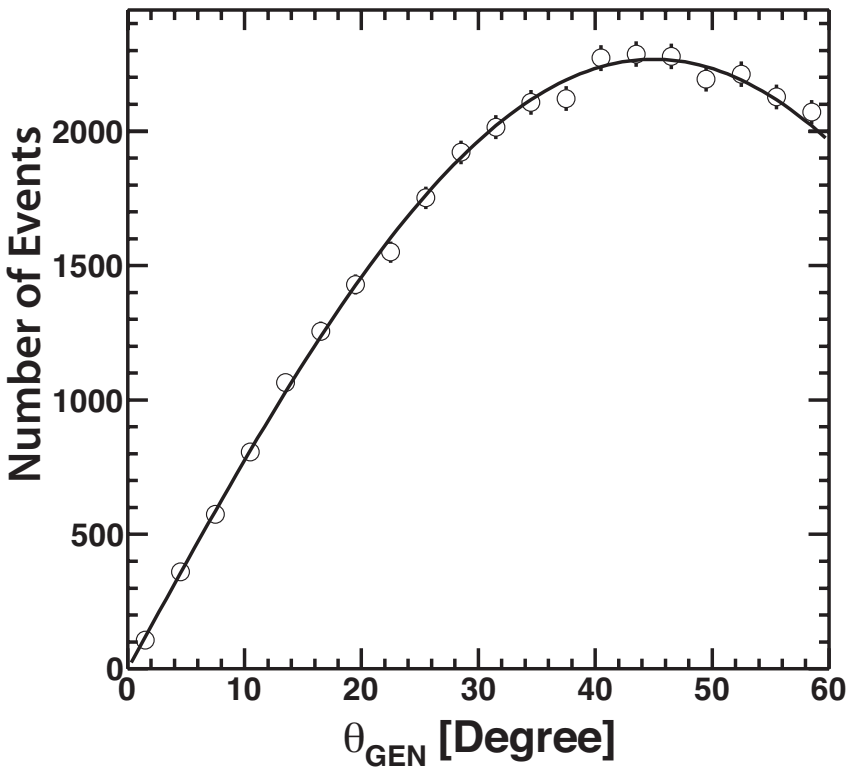


**Figure 4.5**. The Monte Carlo (MC) generated zenith angle distribution: it is a $\sin(\theta)\cos(\theta)$ distribution from 0° - 60°. The solid line represents the theoretical distribution for isotropic arrival, while the points represent samples from the distribution used to generate the Monte Carlo set.

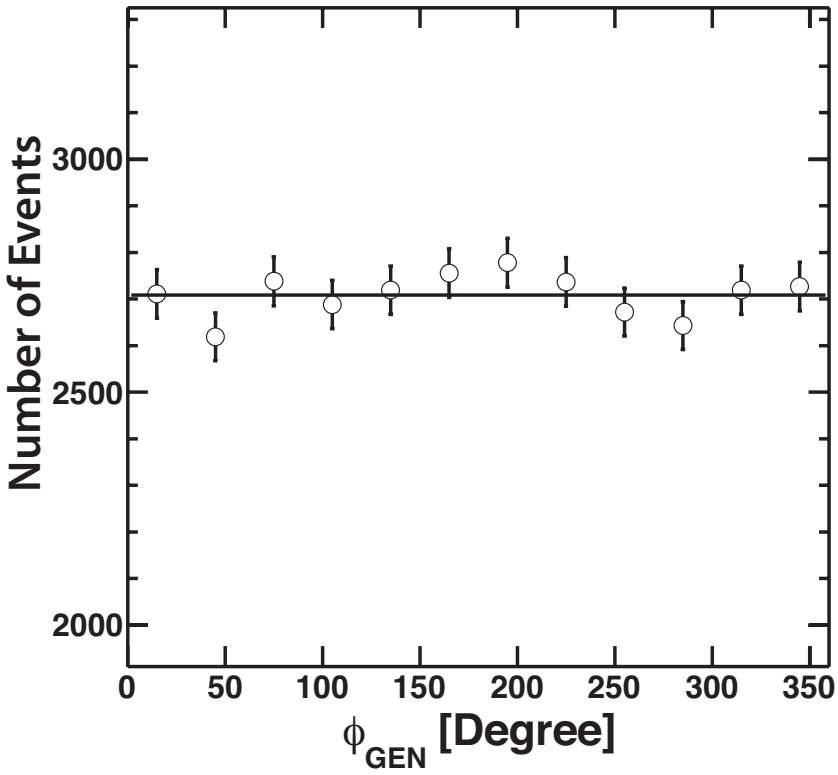


**Figure 4.6**. The Monte Carlo (MC) generated azimuthal angle distribution: it is a flat distribution from 0°-360°. The solid line represents the theoretical distribution for isotropic arrival, while the points represent samples from the distribution used to generate the Monte Carlo set.

as the detector response to the signal. A detailed account of the techniques used to simulate the SD response to EAS is given in [28].

The energy deposited by a particle in the detector is dependent on particle type, angle, interactions with materials in the detector, as well as the position of the particle in the detector (i.e., edge effects). For this detector Monte Carlo, a program based on the GEometry ANd Tracking (GEANT4) package [12] was used to simulate all of the detector instrumentation and the propagation of particles in and around the detector for calculating the energy deposited. Using this program, a library of two-dimensional histograms was created to give the energy deposited in the upper and lower layers of the SD for nine different particle types ($\gamma, e^{\pm}, \mu^{\pm}, p, n, \pi^{\pm}$) with a range of energies and zenith angles. For any given particle with any given energy and zenith angle within the ranges, the energy deposited can be sampled from the library.

Once the energy deposition from a particle is determined, the response of the electronics to this signal must be simulated. The pedestal and photoelectron fluctuations are accounted for to determine the number of FADC counts registered by the system. The time dependance of the energy deposition is recorded so that the counts can be binned in 20 ns time slices, just as they are in the real data. The signals are then recorded and analyzed using the same trigger logic and reconstruction programs as the real data [28].

The important features of the SD MC programs for this hybrid analysis are (1) the trigger efficiency vs. energy (2) the energy scale, and (3) the timing. The trigger efficiency and energy scale of the SD will be discussed in Section 4.2.1. The hybrid reconstruction depends on an accurate timing measurement to match the MD and SD events. The time that the shower core crosses the SD plane is calculated for both detectors and compared. Figure 4.7 shows the result of this comparison in the data and Monte Carlo. They agree.

### 4.1.2 Middle Drum Monte Carlo Programs

Once the simulated shower event list has been generated for the Surface Detector, the same list of generated events are passed to the Middle Drum detector Monte Carlo programs. The list is restricted to events that were randomly generated to occur during the MD detector on-time. Fluorescence detectors sample light propagating from the shower core as it develops. Therefore, the essential parts of the shower to simulate are (1) the longitudinal development of the shower, (2) the light production and propagation through the atmosphere (including dust and aerosols), and (3) optical (mirrors and filters) and

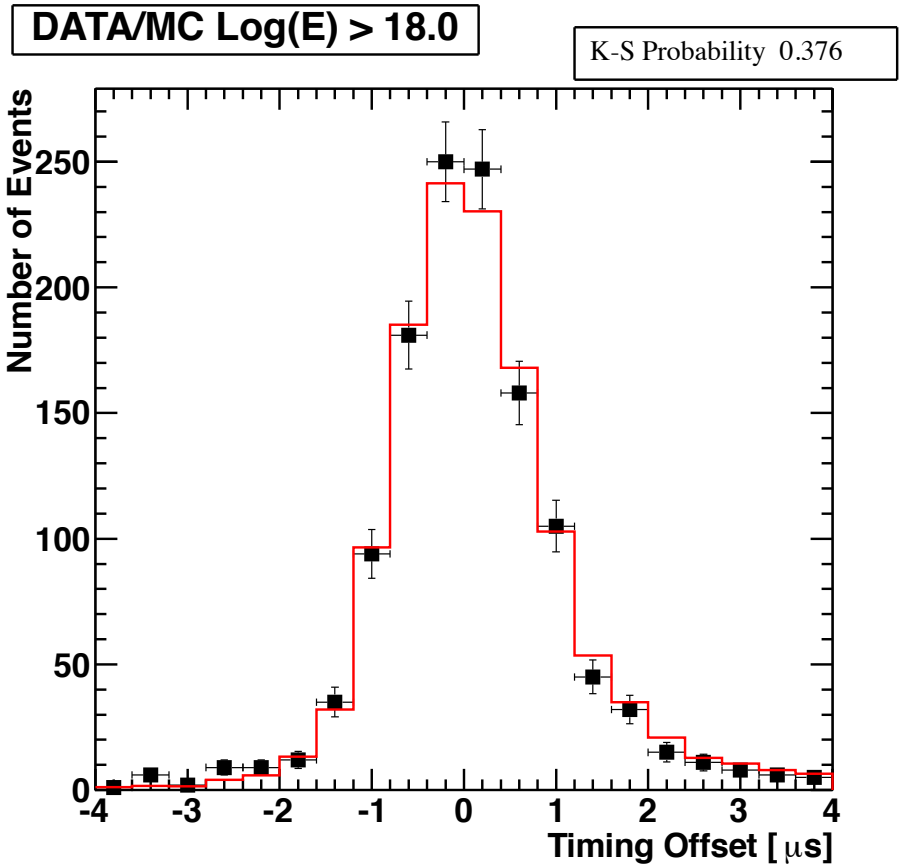


**Figure 4.7**. Data-MC comparison for timing offset between MD and SD: plotted is the difference between the calculated time that the shower core crosses the SD plane as calculated by the MD and the SD for the data set ($t_{MD} - t_{SD}$). The black points represent the data, while the MC is represented by the histogram, normalized in area to the data points.

electronic (PMTs and amplifiers) response.

The actual output of CORSIKA showers is too large (even at a thinning level of $10^{-7}$, it is ∼20 MB per $10^{19}$ eV event) to store even a small library of showers. Thus, for generating the longitudinal development of a shower for MD use, a fit to the Gaisser-Hillas function (equation 4.1) is performed and only the fit parameters ($N_{max}$, $x$, $X_0$, $X_{max}$, $\lambda$) are stored.

$$N_e\left(X\right) = N_{max} \times \left[\frac{X - X_0}{X_{max} - X_0}\right]^{\frac{X_{max}-X_0}{\lambda}} exp\left(\frac{X_{max} - X}{\lambda}\right) \tag{4.1}$$

Here, $N_e(X)$ is the number of charged particles at a given depth, $X$, and $N_{max}$ is the number of particles at the shower maximum, while $X_{max}$ is the atmospheric depth of the shower maximum. $X_0$ represents the atmospheric depth of the first interaction, and $\lambda$ is a scaling constant. When the MD MC is run, $N_e(x)$ is found from this equation and the stored parameters. Here, the atmospheric depth is measured in terms of the amount of material through which the shower has passed (g/cm$^2$).

The transmission of signal light from the shower to the MD detector is the product of three factors corresponding to (1) Rayleigh scattering ($T_R$), (2) aerosol scattering ($T_{Aer}$), and (3) ozone transmission ($T_{OZ}$). Rayleigh scattering refers to light scattering off of air molecules in the case where the wavelength ($\lambda$) of the light is much greater than the size of the molecules. Equation 4.2 describes the number of photons, $N_\gamma$, scattered per unit length ($dl$),

$$\frac{dN_\gamma}{dl} = -\rho\frac{N_\gamma}{x_R}\left(\frac{400}{\lambda}\right)^4 , \tag{4.2}$$

where $\rho$ is the density of the atmosphere (g/cm$^3$), $\lambda$ is the wavelength of the light (nm), and $x_R$ is the mean free path for photon scattering (for 400 nm, $x_R$ = 2970 g/cm$^2$). Equation 4.3 gives the angular distribution of the Rayleigh scattered light, while equation 4.4 shows the corresponding transmission factor for the light to propagate through a given path length in g/cm$^2$[39].

$$\frac{d^2N_\gamma}{dld\Omega} = \frac{dN_\gamma}{dl}\frac{3}{16\pi}\left(1 + cos^2\theta\right) \tag{4.3}$$

$$T_R = exp\left[-\frac{\Delta x}{x_R}\left(\frac{400}{\lambda}\right)^4\right] \tag{4.4}$$

In equation 4.3, $\Omega$ corresponds to solid angle, and $\theta$ is the scattering angle. In equation 4.4, $\Delta x$ represents the slant depth between the two points for which the transmission factor is calculated. Because the Earth and atmosphere are spherical, and the atmosphere is more dense closer to the Earth's surface, a numerical integral is used to calculate this slant depth.

Aerosol scattering refers to the scattering of light off particles with diameter greater than the wavelength of the incident light. While aerosol concentrations vary from night to night, their effect on the overall energy scale of reconstructed events is relatively small over the range of Vertical Aerosol Optical Depths (VAOD) seen in our experiment ($\sim$0.04 $\pm$ 0.02) (see Section 3.3.2.2). Recall that for this dissertation, we use a yearly average aerosol concentration of VAOD = 0.04.

Equation 4.5 gives the number of scattered photons due to aerosols, per unit length, as a function of height, $h$, above the ground.

$$\frac{dN_\gamma}{dl} = \frac{N_\gamma}{L_M(\lambda)} exp\left(-\frac{h}{H_M}\right) \tag{4.5}$$

Here, $L_M(\lambda)$ is the wavelength dependent horizontal extinction length, and $H_M$ represents the scale height. The horizontal extinction length for this analysis is based on the Elterman extinction model, which showed that aerosols are distributed exponentially above the surface of the Earth [19].

The angular distribution of the scattered light from aerosols is given in equation 4.6,

$$\frac{d^2N_\gamma}{dld\Omega} = \frac{dN_\gamma}{dl}\phi(\theta)\,, \tag{4.6}$$

where $\phi(\theta)$ is the scattering phase function at scattering angle $\theta$. Figure 4.8 shows the phase function used in this analysis. This result was taken from [32], which used a background desert aerosol model.

The transmission factor of light through aerosols is given in equation 4.7.

$$T_{Aer} = exp\left(\frac{-\Delta s}{L_M}\right) \tag{4.7}$$

In this equation, $\Delta$s is the numerical line integral of the normalized aerosol density (dimensionless) between two points. The values used in these equations are summarized in the following list [1].

- $L_M$: Horizontal extinction length, 25 km.
- $\lambda$: Wavelength of observed light, 334 nm.
- $H_M$: Scale height, 1.0 km.

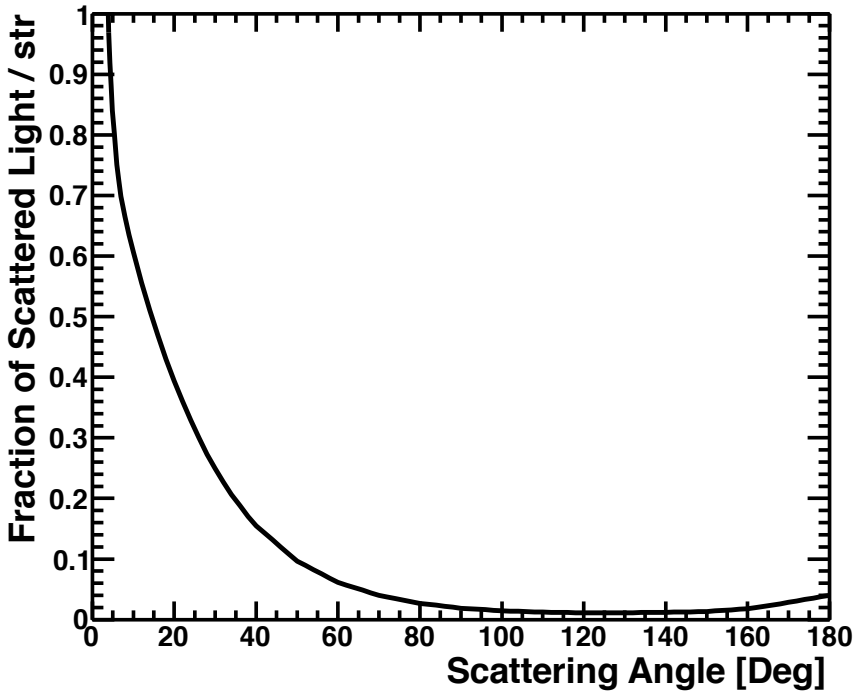


**Figure 4.8**. The Longtin phase function of the fraction of scattered light plotted as a function of scattering angle. It is used as the scattering phase function.

Ozone absorption refers to the attenuation of UV light due to ozone. The transmission factor of light through the ozone is given by equation 4.8.

$$T_{OZ} = exp\,(-\Delta x_{OZ} A_{OZ}) \tag{4.8}$$

Here, $\Delta x_{OZ}$ is the integrated slant depth and $A_{OZ}$ is the attenuation coefficient [11]. These effects are very small and the concentrations of ozone are only significant above 20 km in elevation.

Using the above equations, we track the amount of light produced in a segment of shower track and calculate the amount that reaches the telescope mirror. The light is then converted to photons per unit of solid angle (see Section 3.3.3). At this stage, the quantum efficiency of the PMTs is used to convert the photons to photoelectrons. For each photoelectron, the mirror reflectivity and UV transmission of the filter is applied to determine if the photoelectron actually contributes to a signal. For each contributing photoelectron, a ray-tracing program is used to track it through the detector. The ray-tracing is done after the quantum efficiency and filtering is applied to speed up the CPU processing time [11].

Finally, the detector electronics are simulated to create raw MC data that mimic the real data. The electronics are affected by noise; therefore the simulation requires an additional 25 $\mu$s window added to the beginning of the shower signal to account for the tube-level noise triggers, as well as 50 $\mu$s to be added to the end of the shower signal to account for the delay gate. The signal is then passed through the simulated PMT, preamplifier, and electronics to add the proper gains. Next, the signal is sent through a simulated low pass filter and the trigger and integration circuitry. Finally, the simulation program tests for trigger requirements, and if the trigger conditions are met, the time is saved and the signal is converted to tube QDCs and TDCs (see Section 3.2).

Raw MD and SD simulated data is then saved in the same format as real data so that they can both be reconstructed with exactly the same programs. Both the simulated and real data are reconstructed using the standard Surface Detector and standard Middle Drum reconstruction programs up through Pass 3, the Middle Drum detector shower plane fit. The reconstruction programs are described in more detail in Chapter 5. However, because the simulated showers are already determined to be hybrid showers, the time matching program described in Section 5.4 is not necessary for these events. Hybrid geometry and profile fitting is also done in the same way for both the data and MC for hybrid events (see Section 5.4).

## 4.2 Monte Carlo Event Set

The hybrid Monte Carlo event set uses protons as the primary particle in the shower because previous experiments have shown that for energies $E > 10^{18}$ eV, real data appears to be proton showers [5]. These details are described in Section 7.2. For the purpose of studying composition, a second Monte Carlo set was generated using iron nuclei as the primary cosmic ray. In Chapter 7, an analysis using an iron Monte Carlo set will be described.

### 4.2.1 Energy Scale Correction

A possible difference between the SD and Fluorescence Detector (FD) energy scales has long been the topic of speculation. Some have proposed such a difference as the resolution of the discrepancy between the published AGASA and HiRes spectra (see Section 2.4) [42], though this would not resolve the GZK problem. For TA, the SD reconstruction relies on inverse Monte Carlo techniques. The CORSIKA table used to determine the energies yielded a result that is 27% higher than the same data events reconstructed by the FDs [28]. In short, the CORSIKA MC produces too few particles at 800 m from the core if the FD energy scale is used.

This ratio of 1.27 ($E_{SD}/E_{FD}$) would, in fact, account for the difference in normalization between AGASA SD and HiRes FD. For the hybrid analysis, however, this difference makes it incorrect to use the same CORSIKA generated shower to represent simultaneously a true shower for both the FD and SD response. In particular, Figure 4.9 shows greater acceptance at lower energies once the scaling is made. Because FD energies are calorimetric and based on well-understood electromagnetic physics, this is the more trustworthy measurement and consequently is the one which we use in TA. Therefore, the SD events have been scaled down in energy by 27%. Two methods were used to overcome the problem of the shift in the SD trigger efficiency turn-on: a ratio correction to the aperture, and an energy scale correction to the Monte Carlo. The ratio correction is described in Section 6.2.2, but the energy scaled Monte Carlo is described here.

The energy scaled MC showers were thrown for the SD simulations, and then they were modified by reducing the initial thrown energies by a factor of 1/1.27. The energy modified showers were then thrown for the MD fluorescence detector simulation. This method addresses the energy scale difference in a more direct way than does the simple ratio correction. This energy scaled MC Set is used to generate the final hybrid energy

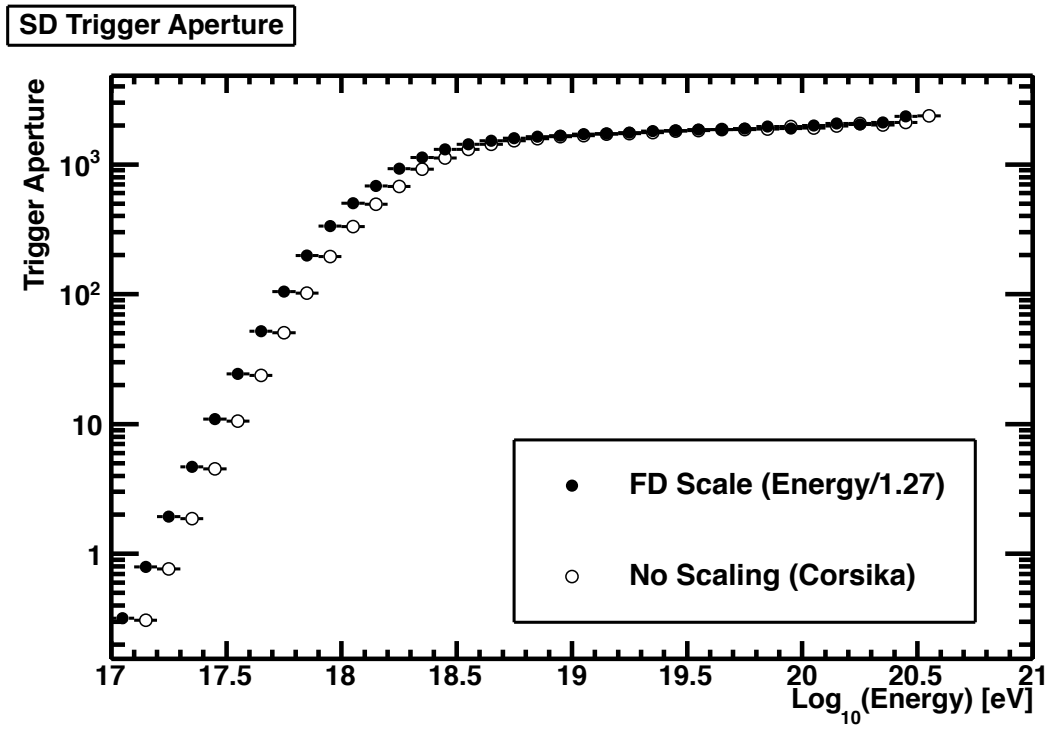


**Figure 4.9**. The Surface Detector (SD) trigger aperture: shown is the aperture from the CORSIKA energy compared with the energy scaled to the Fluorescence Detector (FD) reconstructed energy. The increase in aperture in the lower bins is expected because scaling to the FD energy reduces the energy by 27% with respect to the CORSIKA energy prediction.

spectrum shown in Chapter 6, Section 6.3.

### 4.2.2 Resolutions

An important objective for the Monte Carlo simulations is determining how well the reconstruction programs perform. Since the thrown Monte Carlo values are known, a direct comparison can be made to the reconstructed values. By comparing the reconstructed value of a parameter to the thrown value, the resolution of the reconstruction is determined. The resolution can then be used to make quality cuts on the data in order to improve the reconstruction resolution. By scrutinizing the different parameters of events that do not reconstruct well, a subset of events having poor reconstruction can be removed leaving higher quality events in the final analysis (see Section 6.1). These same cuts are then applied to the data.

The major motivation for performing a hybrid analysis is that adding the constraint of the surface core location improves the geometric reconstruction resolution. This in turn improves the energy resolution. The resolution plots shown in this section demonstrate this point when compared with the monocular result [38].

Figure 4.10 describes the geometry of the shower core axis. The parameters shown define the geometry of the shower and are very important in determining aperture. The shower core axis can be modeled as a straight line from the point of first interaction to the point on the surface at the center of the SD distribution of particles. This line can be constrained using three parameters:

- The in-plane angle ($\psi$): represents the angle the shower track makes with the ground in the shower-detector plane.
- The impact parameter ($R_P$): represents the distance of closest approach to the Middle Drum detector. For some geometries, this can be below the Earth's surface.
- The timing ($T_{Rp}$): represents the time at $R_P$, when the shower makes its closest approach to the MD detector.

In the hybrid analysis, the SD data and MD data are used to constrain these parameters, as shown in Section 5.4. In Figure 4.11a, the reconstructed values of the in-plane angle ($\psi$), impact parameter ($R_P$), and zenith angle ($\theta$) are compared with the MC thrown values. The width of these resolutions of MC events are used to place an uncertainty on the reconstructed values of the data events. The plots show that the in-plane angle and zenith

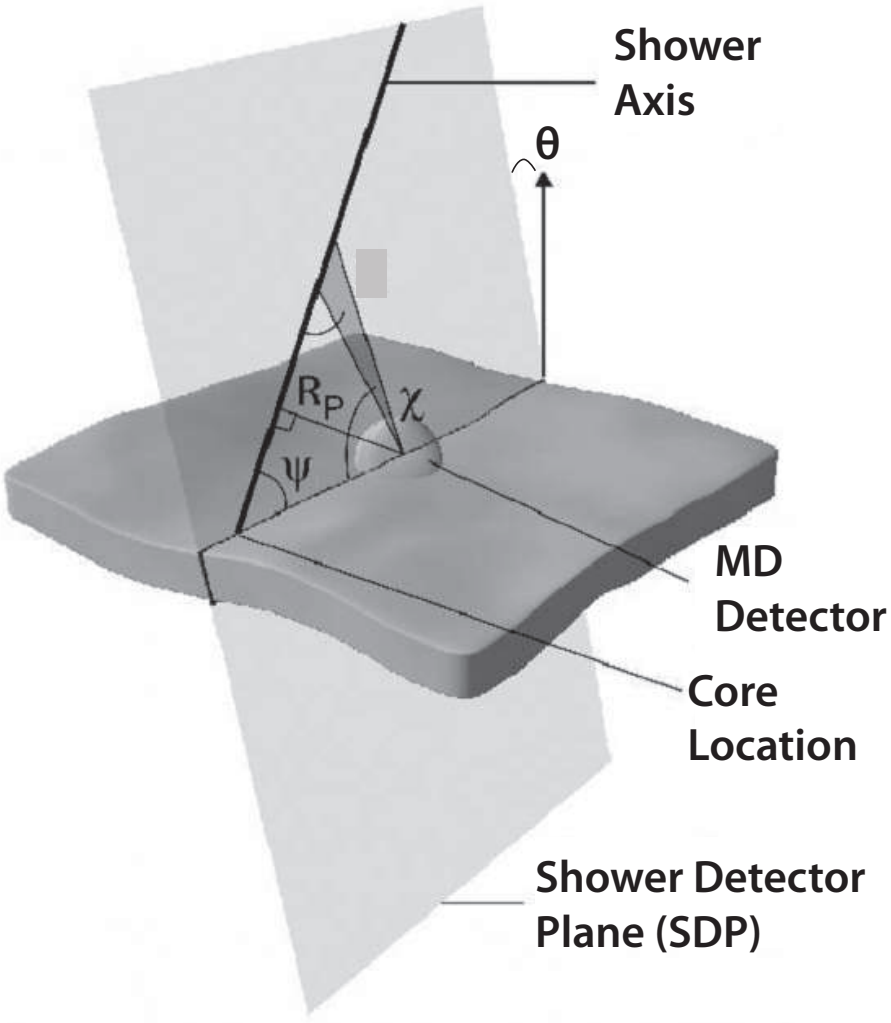


**Figure 4.10**. Schematic of the MD detector relative to the shower core: shown are the important geometric parameters, the in-plane angle ($\psi$), and the impact parameter ($R_P$). These values combined with the zenith angle ($\theta$) describe the geometry of the core of and EAS.

angle have hybrid resolutions of ∼0.5°, and the impact parameter has a 0.4% resolution. Figure 4.11b shows the MD monocular reconstruction resolutions for comparison. The MD hybrid resolutions show significant improvement over the MD monocular reconstruction.

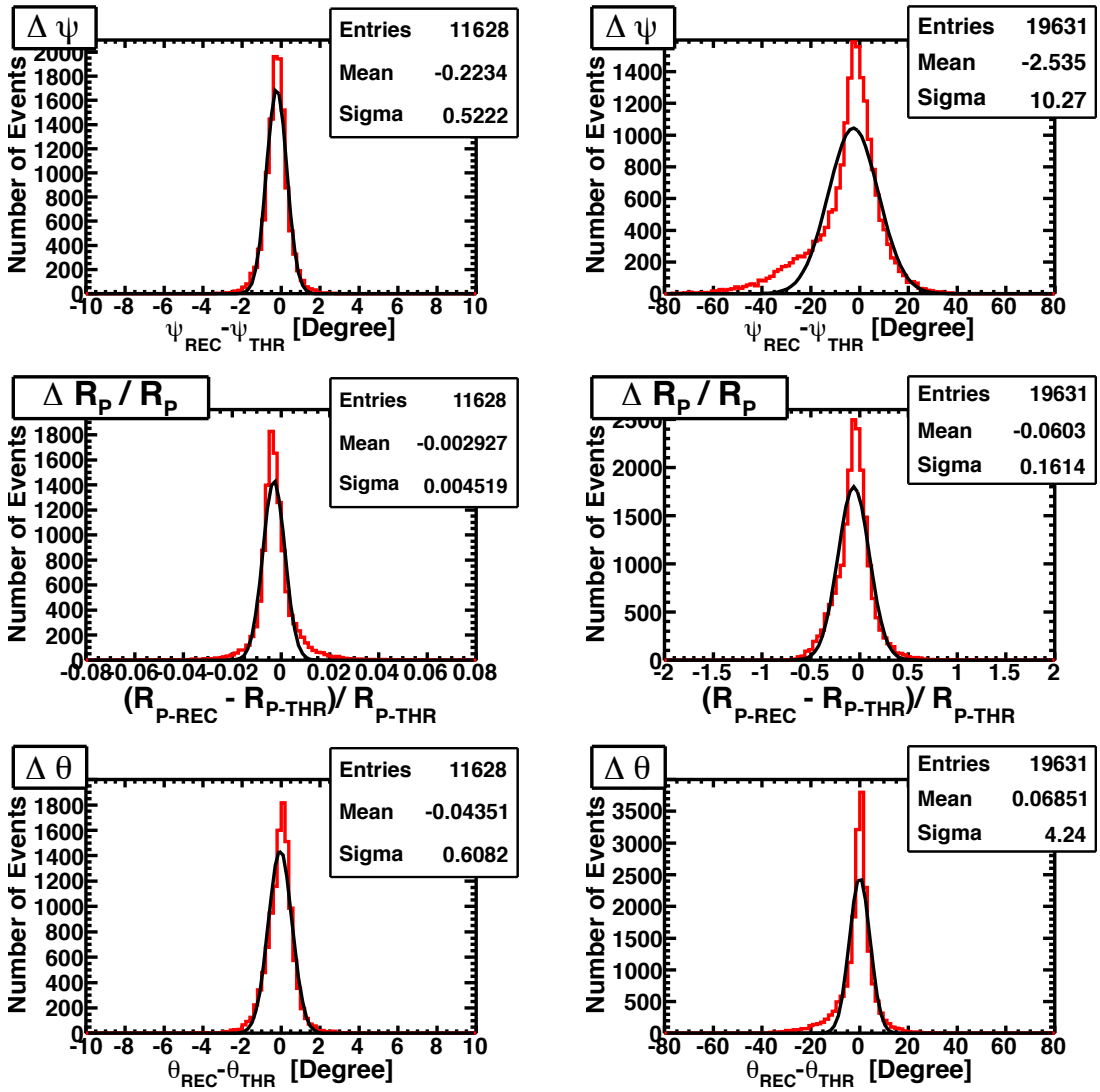


(a) MD hybrid geometry resolutions

(b) MD monocular geometry resolutions

**Figure 4.11**. Resolutions for Middle Drum hybrid geometry parameters compared to the MD monocular reconstruction: shown are the in-plane angle ($\psi$), (top), impact parameter ($R_P$), (middle), and zenith angle ($\theta$) (bottom). The (red) histogram shows the difference between the reconstructed and thrown values for each event, or in the case of the impact parameter, the normalized difference. The black line is a gaussian fit to the histogram. Note that the horizontal scale is changed in the (b) monocular case, and significant improvement in the (a) hybrid reconstructed parameters is shown.

Figure 4.12a shows the energy resolution for the MD hybrid reconstruction in three energy ranges. The improved angular resolution over the MD monocular result, shown in Figure 4.11a, directly contributes to the improvement in the energy resolution for the hybrid reconstruction. The resolution in energy starts at about 10% and improves with energy. This is more than a factor of two improvement over the MD monocular reconstruction, shown in Figure 4.12b. These improvements show the strength of the extra constraint of SD information.

### 4.2.3 Data/Monte Carlo Comparisons

In Section 4.2.2, we used the MC to show that the analysis programs (described in Chapter 5) give accurate reconstruction of the events. MC simulations are also used to calculate the aperture of the TA detector which is then folded in with running time of each detector element to calculate the exposure. These calculations will be shown in Chapter 6. However, the MC must provide a faithful representation of distributions in the data in order that we may trust the aperture calculation, and hence the measured flux. We validate the fidelity of the simulation by making a series of comparisons between the data and the Monte Carlo simulated data for a number of parameter distributions, in particular, of those variables directly connected to the aperture. Here we compare the distributions from accepted events of both the data and MC, having been processed using the same analysis programs and subjected to the same selection cuts.

In figures 4.13 - 4.16 the in-plane angle ($\psi$), impact parameter ($R_P$), zenith angle ($\theta$) and azimuthal angle ($\phi$) from MC are compared with the real data distributions, respectively. The azimuthal angle represents the angle of the shower with respect to East. In addition, for each comparison, a Kolmogorov-Smirnov (K-S) test is performed to compare the data and the MC distributions. This test is appropriate for the small size of the data sample. For a K-S test, values between 0.2 and 1 indicate reasonable agreement. The agreement between data and MC for these parameters in these comparisons is very good, which gives me confidence in my aperture calculation.

Figure 4.17 shows the Data/MC comparisons for the in-plane angle ($\psi$) for showers in three energy ranges. This comparison shows whether we are simulating the evolution of this parameter reliably with energy. Middle Drum hybrid is optimized in the region of $10^{18.5}$ eV to $10^{19.0}$ eV and therefore, the most accurate reconstructions of showers are found in this energy range. It is important to note, however, that the agreement between data and

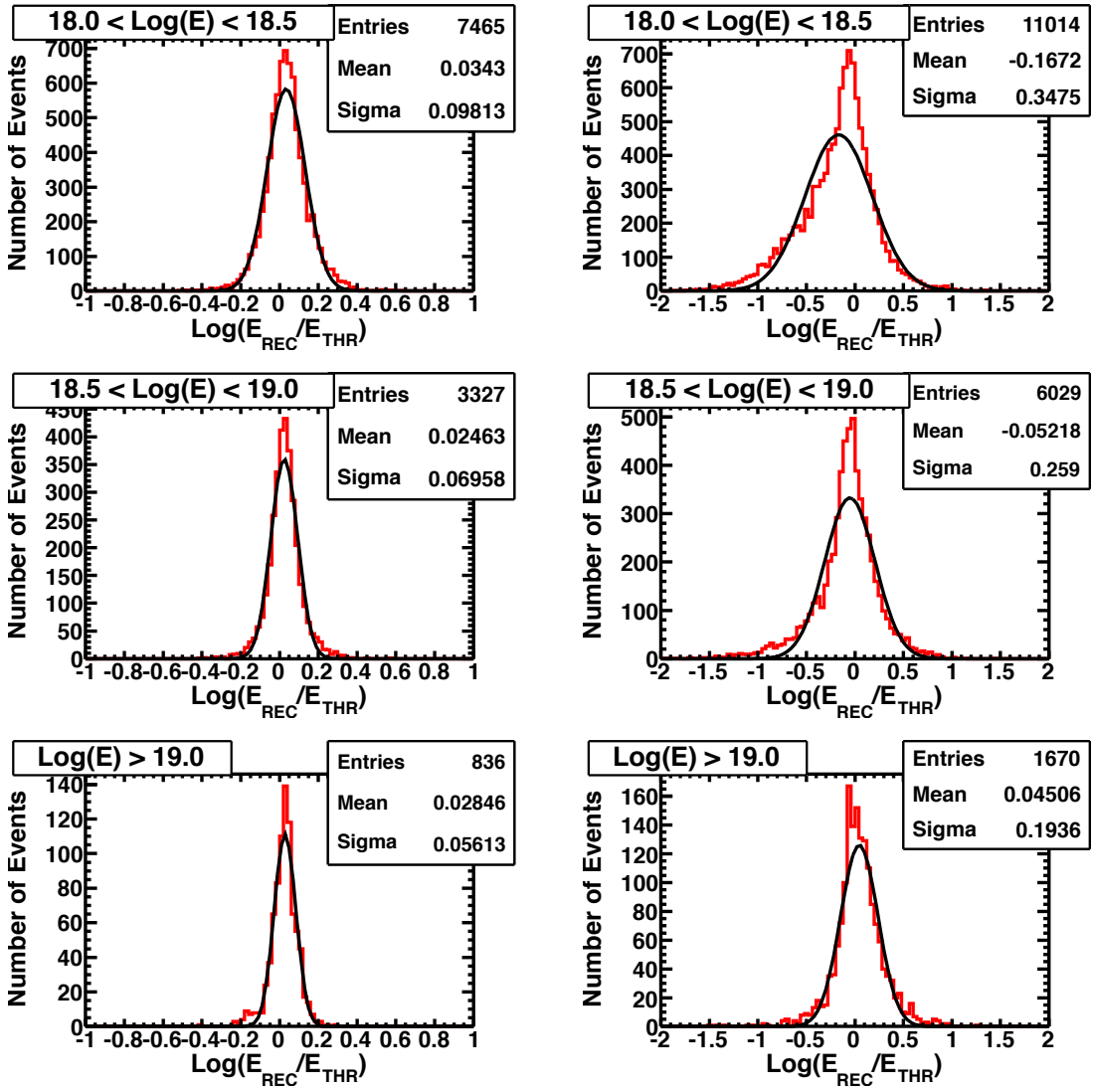


(a) MD hybrid energy resolution

(b) MD monocular energy resolution

**Figure 4.12**. Resolutions for Middle Drum hybrid reconstructed energy compared to the MD monocular reconstruction: shown are events broken up into energy ranges: $10^{18}$ < E < $10^{18.5}$ eV (top), $10^{18.5}$ < E < $10^{19.0}$ eV (middle), and E > $10^{19.0}$ eV (bottom). In each case, the histogram (red) shows the log of the ratio of the reconstructed and thrown energy for each event. The black line is a gaussian fit to the histogram. The energy resolutions (10%, 7%, and 6%) for the (a) hybrid reconstruction represent more than a factor of two improvement over the (b) monocular reconstruction (34%, 26% and 19%). Note that the horizontal scale is changed in the monocular case.

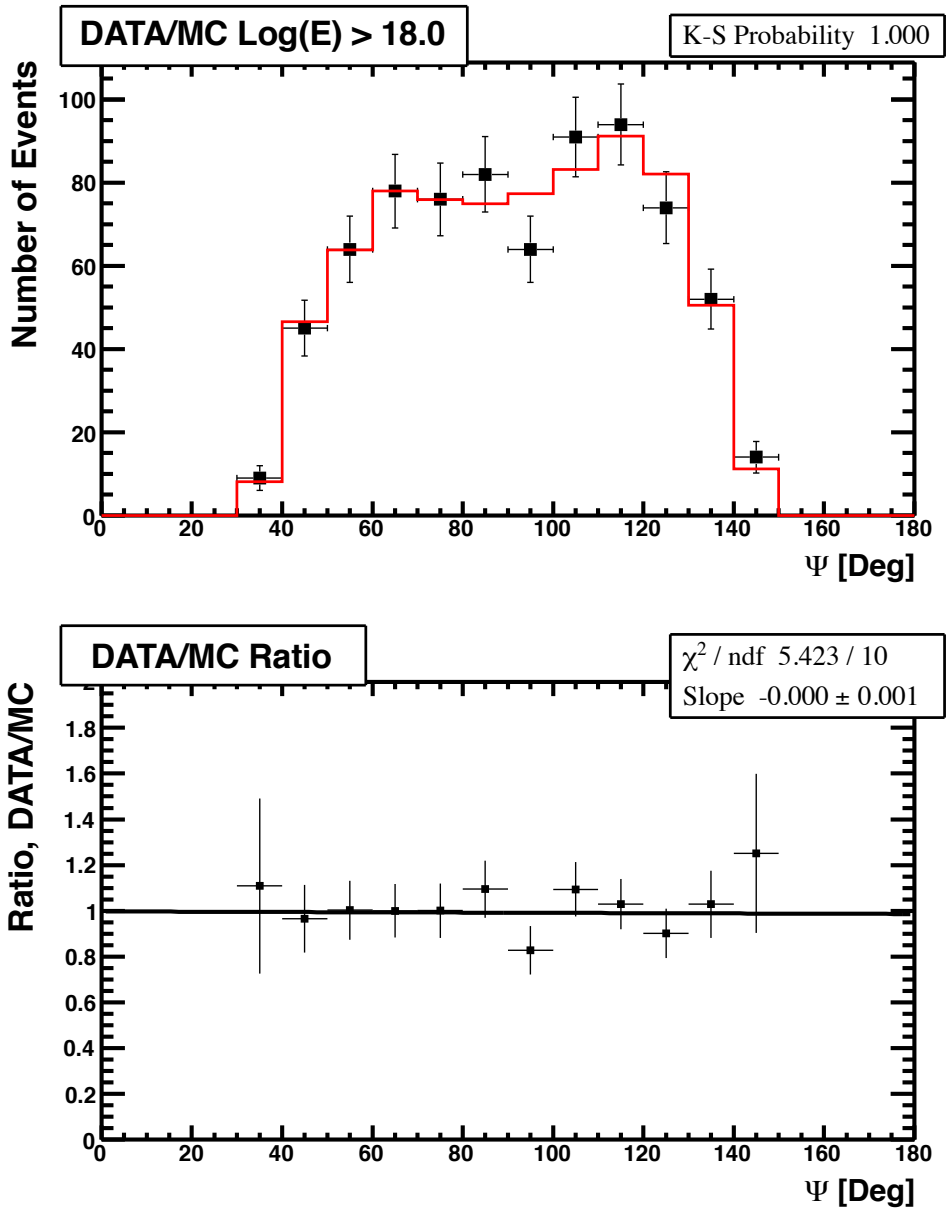


**Figure 4.13**. Data-MC comparison: the Middle Drum hybrid in-plane angle ($\psi$), is the angle of the shower track in the shower detector plane. Above: the distribution of measurements is shown for the data (black points with error bars) and MC (red histogram). The MC has been normalized to the area of the data in this plot. Below: the ratio of the data to the MC. The line is a linear fit to the points. It is flat with a ratio of 1 within uncertainties, indicating very good agreement.

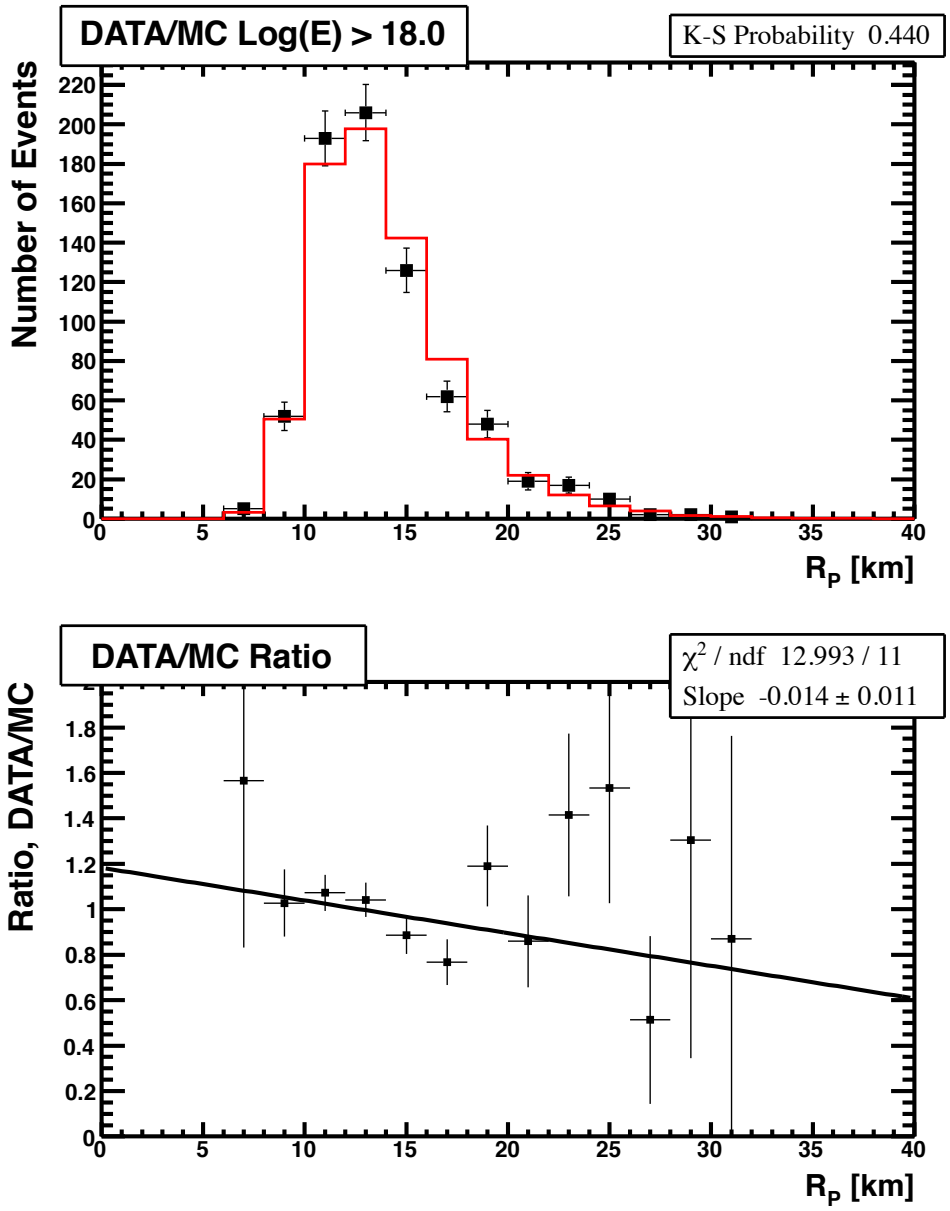


**Figure 4.14**. Data-MC comparison: the Middle Drum hybrid impact parameter, ($R_P$), is the distance of closest approach of the shower to the Middle Drum detector. Above: the distribution of measurements is shown for the data (black points with error bars) and MC (red histogram). The MC has been normalized to the area of the data in this plot. Below: the ratio of the data to the MC. The line is a linear fit to the points. It is flat with a ratio of 1 at just over 1 $\sigma$, indicating good agreement.

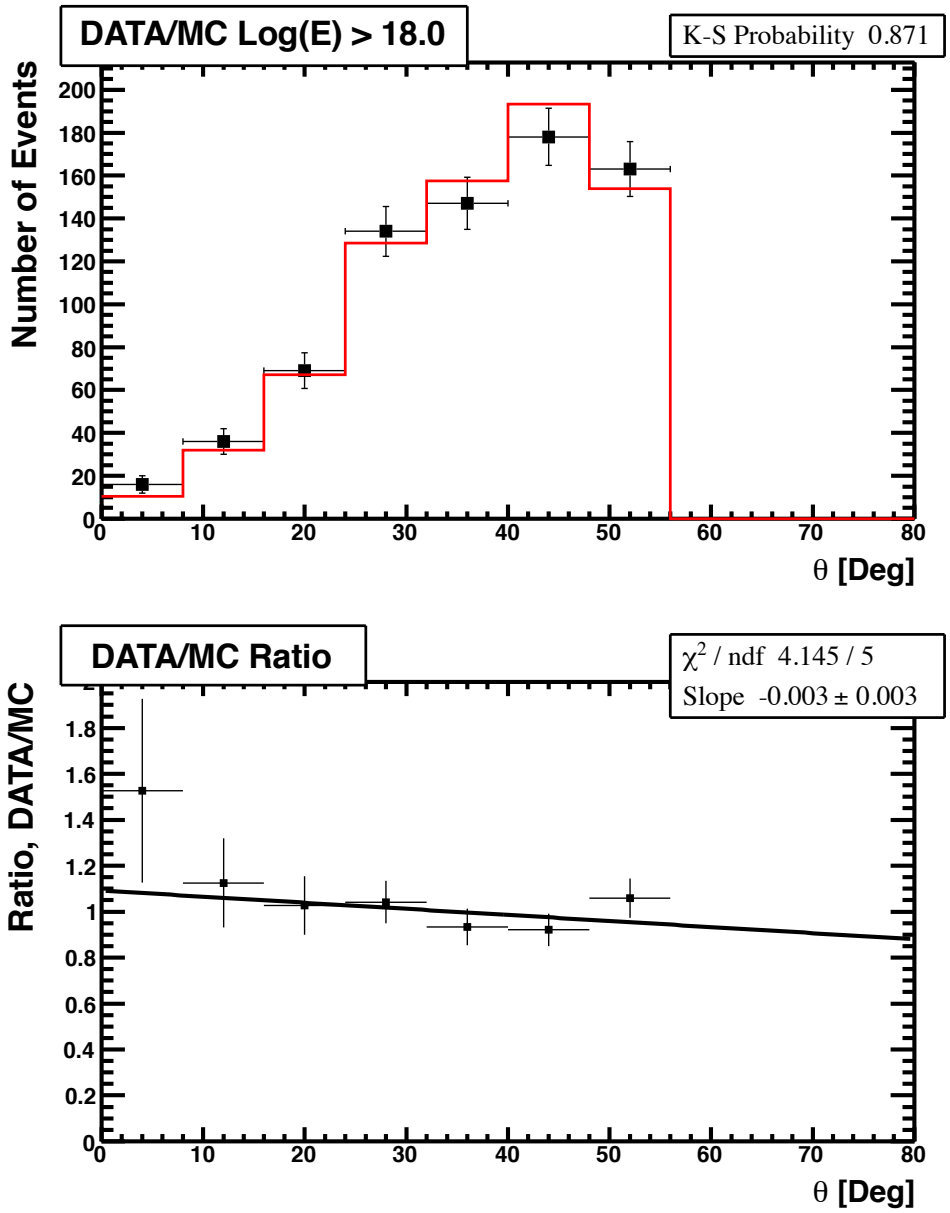


**Figure 4.15**. Data-MC comparison: the Middle Drum hybrid zenith angle ($\theta$) is the angle of the shower from the zenith. Above: the distribution of measurements is shown for the data (black points with error bars) and MC (red histogram). The MC has been normalized to the area of the data in this plot. Below: the ratio of the data to the MC. The line is a linear fit to the points. It is flat with a ratio of 1 within uncertainties, indicating very good agreement.

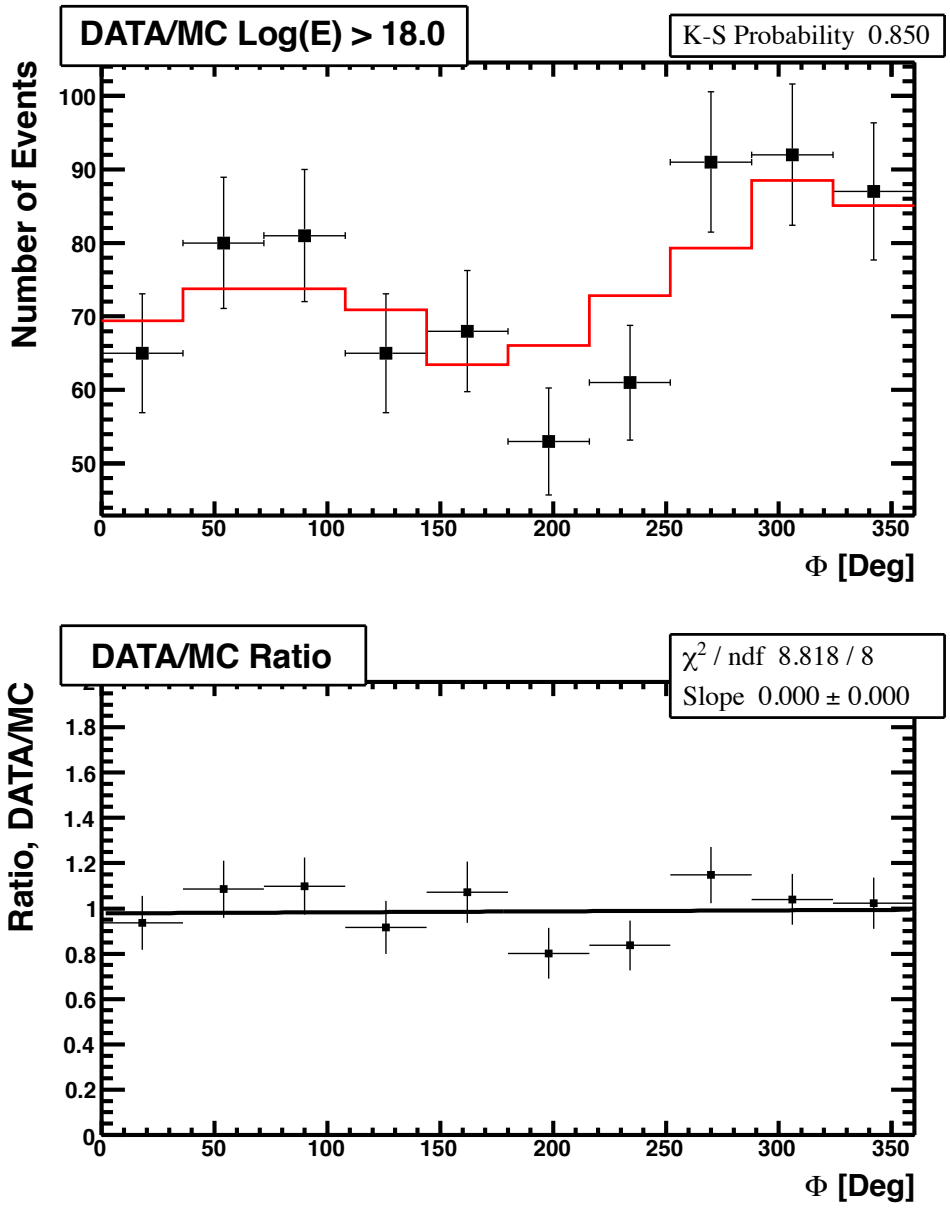


**Figure 4.16**. Data-MC comparison: the Middle Drum hybrid azimuthal angle ($\phi$) is the angle of the shower from East. Above: the distribution of measurements is shown for the data (black points with error bars) and MC (red histogram). The MC has been normalized to the area of the data in this plot. Below: the ratio of the data to the MC. The line is a linear fit to the points. It is flat with a ratio of 1 within uncertainties, indicating very good agreement.

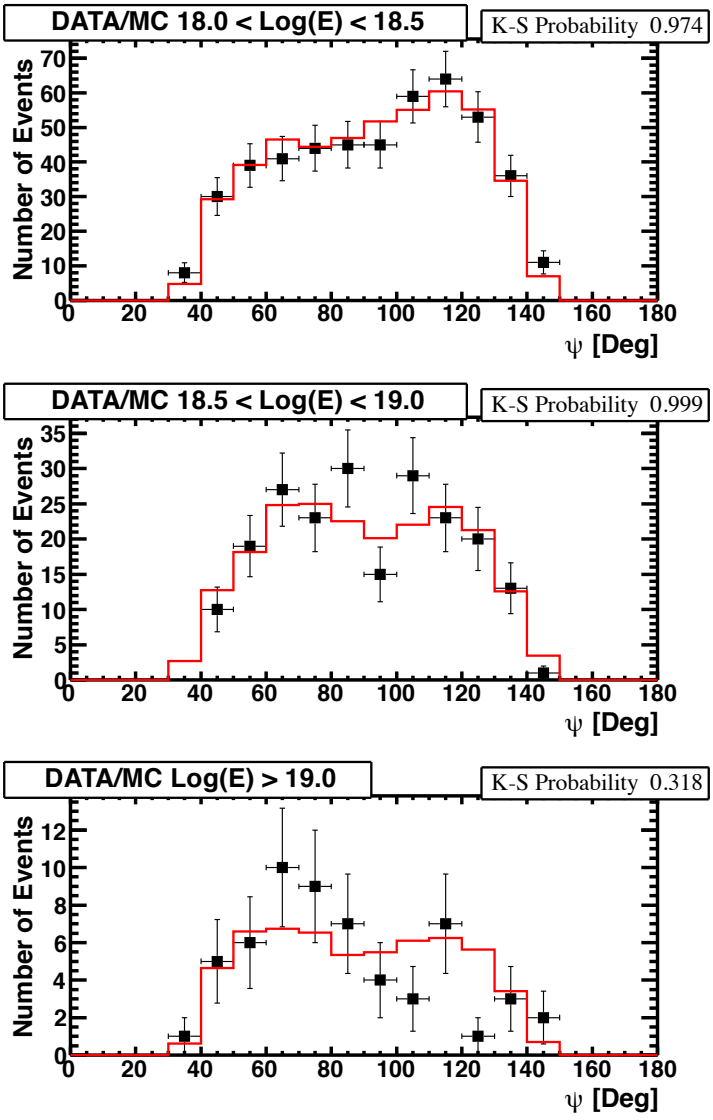


**Figure 4.17**. Data-MC comparison: the Middle Drum hybrid in-plane angle ($\psi$) is shown in three energy ranges: top to bottom, $10^{18.0} < \mathrm{E} < 10^{18.5}$ eV, $10^{18.5} < \mathrm{E} < 10^{19.0}$ eV, and $\mathrm{E} > 10^{19.0}$ eV, respectively, to show the evolution of this parameter with energy. The distribution of measurements is shown for the data (black points with error bars) and MC (red histogram). The MC has been normalized to the area of the data in these plots. This figure shows that the data and MC agreement for this parameter are not dependent on energy.

MC shown in Figure 4.13 is well reproduced in all energy ranges.

Figures 4.18, 4.19, and 4.20 show Data/MC comparisons for the impact parameter ($R_P$), zenith angle ($\theta$) and azimuthal angle ($\phi$) for three energy ranges. Again, the agreement between data and MC is consistently excellent in all three ranges in these plots.

Figures 4.21 and 4.22 show the reconstructed x and y coordinates of the shower core on the ground. The consistency here is important because several of the hybrid quality cuts are dependent on these values as discussed in Section 6.1. Good agreement between data and MC for these plots shows that these cuts affect the data and MC in the same way. Figures 4.23 and 4.24 show the same parameters broken up into the three energy ranges. Agreement between data and MC is also outstanding in all three plots.

Finally, in addition to making comparisons about geometry, considerations of the optics and electronics are also made. Figures 4.25 and 4.26 show the Data/MC comparison for the number of photoelectrons per degree of shower track. This is an important parameter to study because it depends on understanding the optics and threshold of the electronics. The threshold for initiating a sample-and-hold digitization is varied actively over time to maintain a single-tube trigger ratio of 200 Hz. For this reason, the amount of ambient background light determines the running threshold. Those thresholds are set and recorded once per minute. For the initial pass through the MD monocular analysis, we used the average threshold from the HiRes-1 detector for the simulation. A clear discrepancy was seen in these particular plots. However, it was clear that the recorded thresholds for the electronics at Middle Drum during good weather observation periods were 20% lower than for the same electronics at HiRes [38]. This is indicative of a lower level of background light. The MC threshold was therefore adjusted to match the new running conditions. The agreement shown between data and MC in the number of photoelectrons per degree in the current version of Figure 4.25 demonstrates that the threshold level and triggering of the detector are being simulated accurately after the adjustment was made.

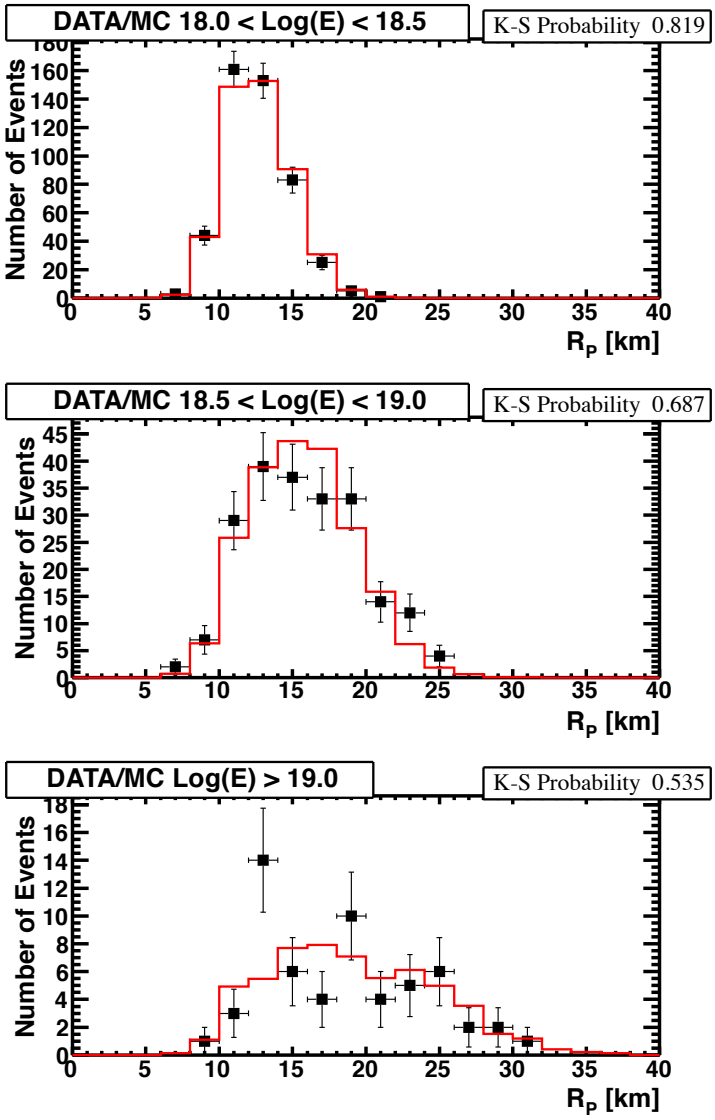


**Figure 4.18**. Data-MC comparison: the Middle Drum hybrid impact parameter ($R_P$) is shown in three energy ranges: top to bottom, $10^{18.0} < \mathrm{E} < 10^{18.5}$ eV, $10^{18.5} < \mathrm{E} < 10^{19.0}$ eV, and $\mathrm{E} > 10^{19.0}$ eV, respectively, to show the evolution of this parameter with energy. The distribution of measurements is shown for the data (black points with error bars) and MC (red histogram). The MC has been normalized to the area of the data in these plots. This figure shows that the data and MC agreement for this parameter are not dependent on energy.

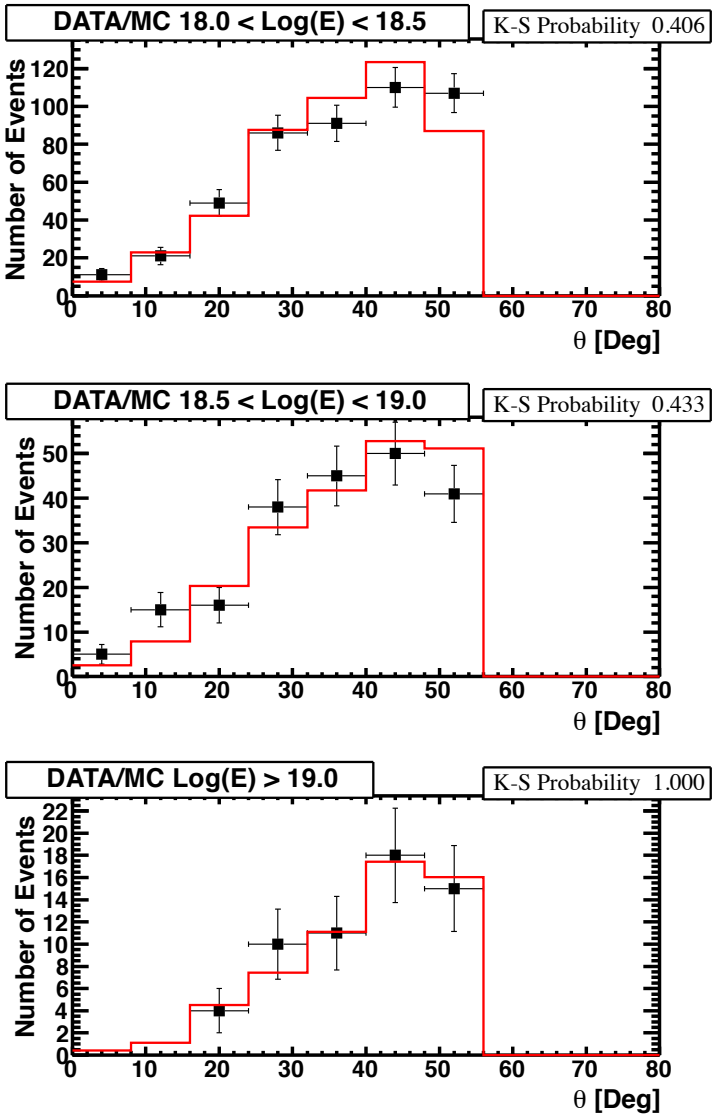


**Figure 4.19**. Data-MC comparison: the Middle Drum hybrid zenith angle ($\theta$) is shown in three energy ranges: top to bottom, $10^{18.0} < \mathrm{E} < 10^{18.5}$ eV, $10^{18.5} < \mathrm{E} < 10^{19.0}$ eV, and $\mathrm{E} > 10^{19.0}$ eV, respectively, to show the evolution of this parameter with energy. The distribution of measurements is shown for the data (black points with error bars) and MC (red histogram). The MC has been normalized to the area of the data in these plots. This figure shows that the data and MC agreement for this parameter are not dependent on energy.

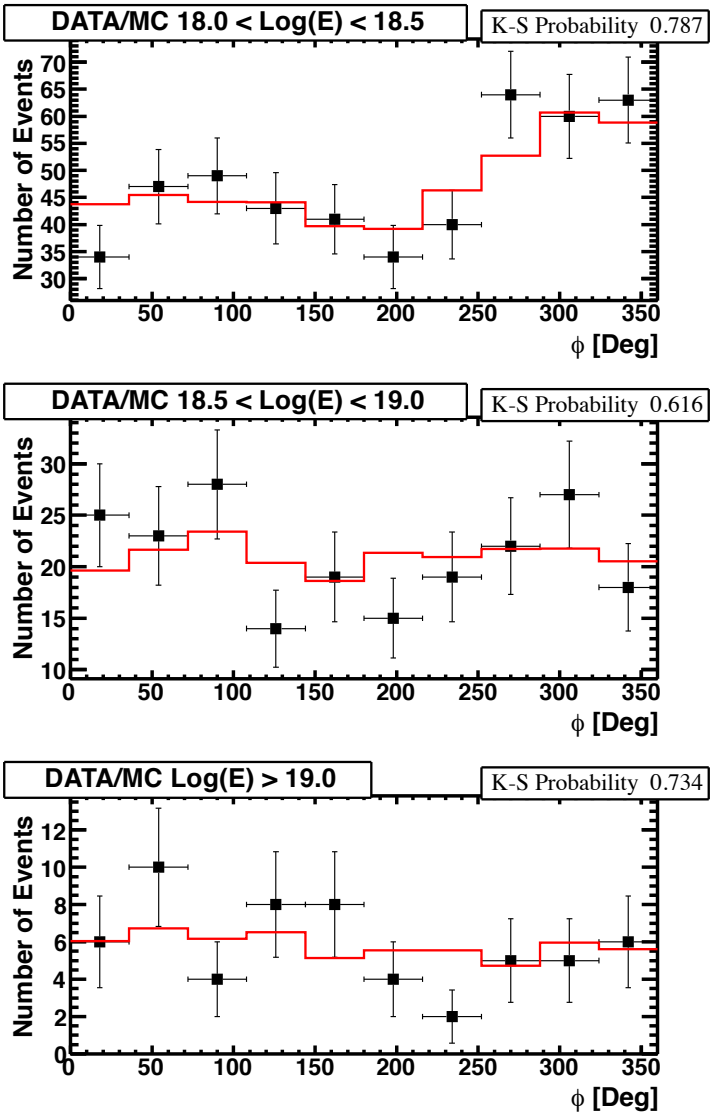


**Figure 4.20**. Data-MC comparison: the Middle Drum hybrid azimuthal angle ($\phi$) is shown in three energy ranges: top to bottom, $10^{18.0} < \mathrm{E} < 10^{18.5}$ eV, $10^{18.5} < \mathrm{E} < 10^{19.0}$ eV, and $\mathrm{E} > 10^{19.0}$ eV, respectively, to show the evolution of this parameter with energy. The distribution of measurements is shown for the data (black points with error bars) and MC (red histogram). The MC has been normalized to the area of the data in these plots. This figure shows that the data and MC agreement for this parameter are not dependent on energy.

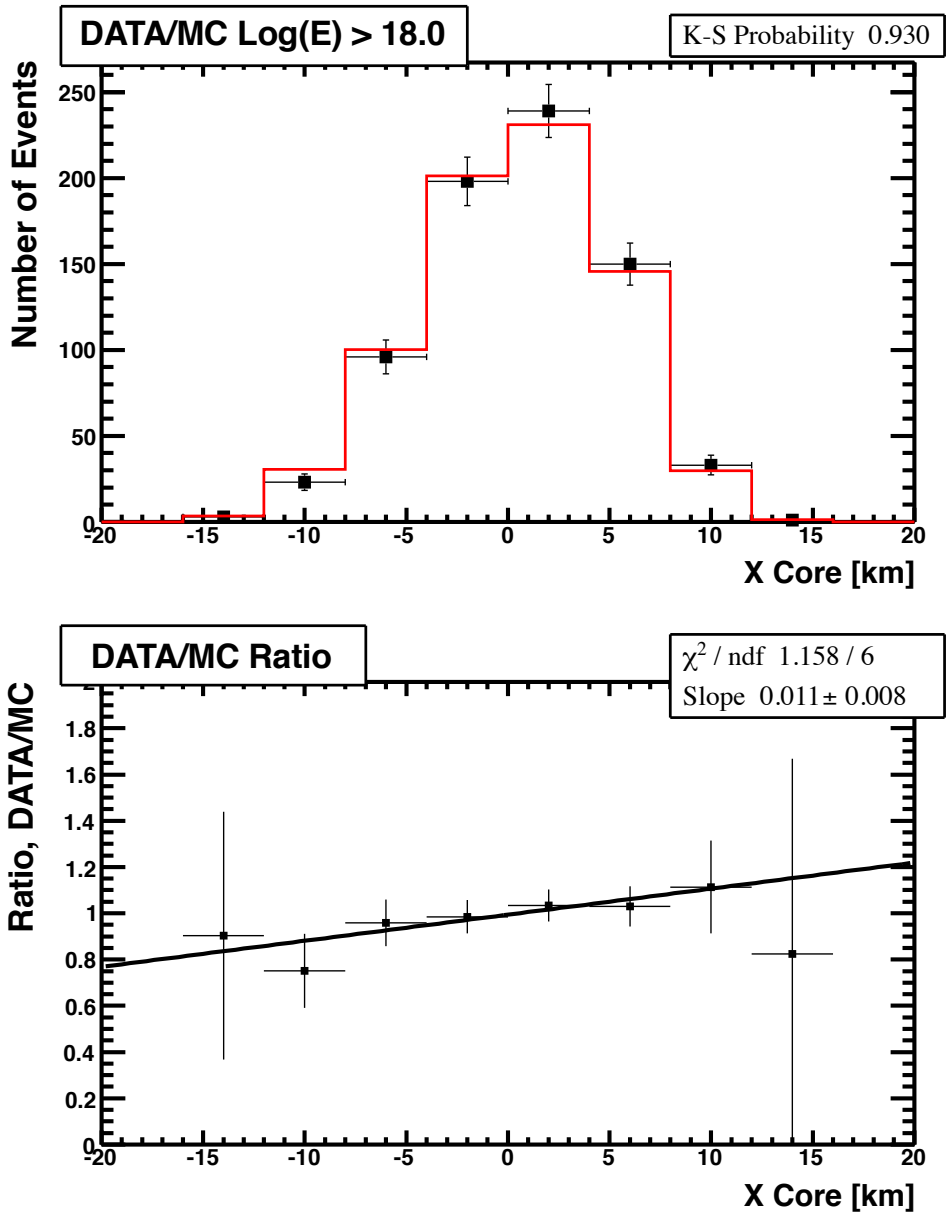


**Figure 4.21**. Data-MC comparison: the Middle Drum hybrid location of the east-west ("X") coordinate of the shower core is calculated with respect to the Central Laser Facility (CLF). Above: the distribution of measurements is shown for the data (black points with error bars) and MC (red histogram). The MC has been normalized to the area of the data in this plot. Below: the ratio of the data to the MC. The line is a linear fit to the points. It is flat with a ratio of 1 at just over 1 $\sigma$, indicating good agreement.

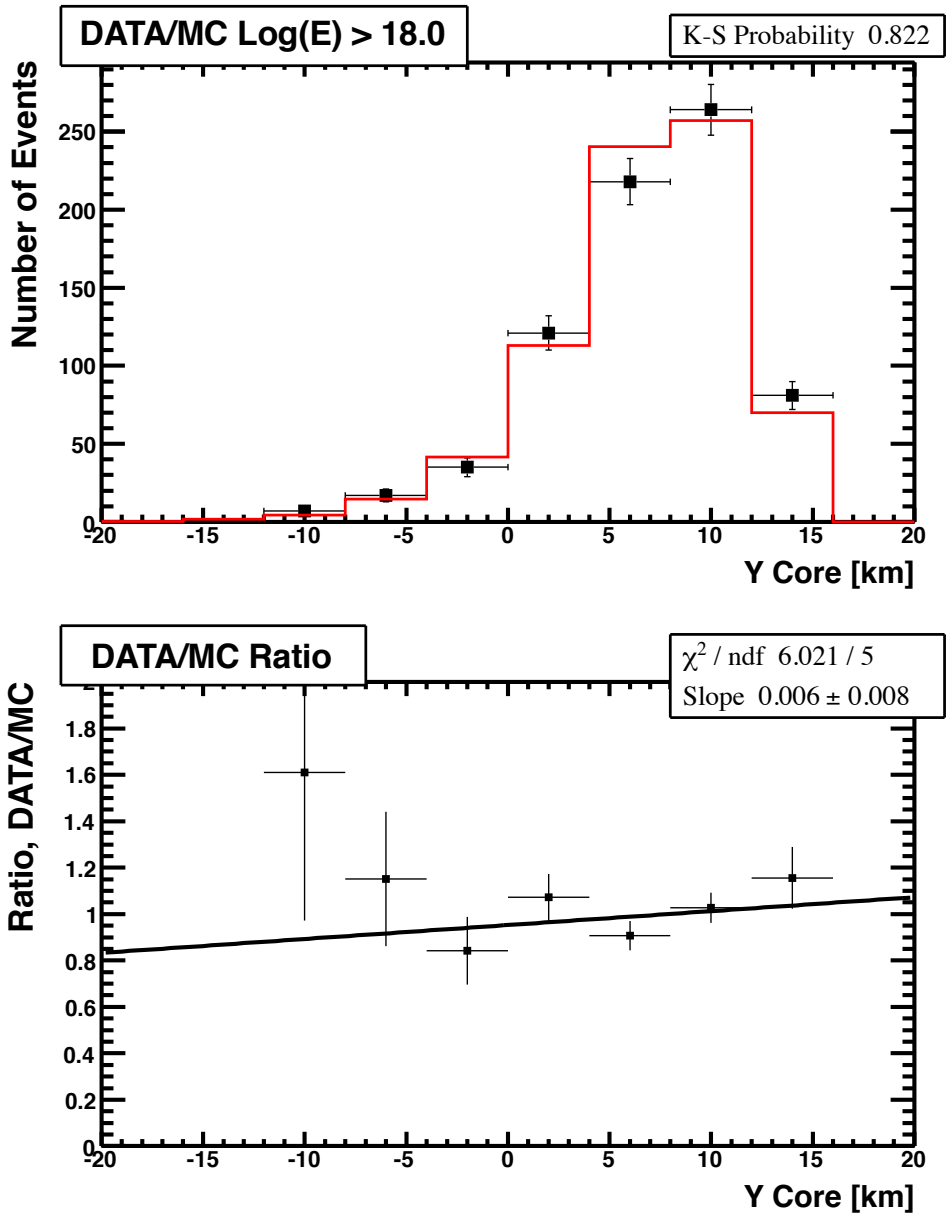


**Figure 4.22**. Data-MC comparison: the Middle Drum hybrid location of the north-south ("Y") coordinate of the shower core is calculated with respect to the Central Laser Facility (CLF). Above: the distribution of measurements is shown for the data (black points with error bars) and MC (red histogram). The MC has been normalized to the area of the data in this plot. Below: the ratio of the data to the MC. The line is a linear fit to the points. It is flat with a ratio of 1 within uncertainties, indicating very good agreement.

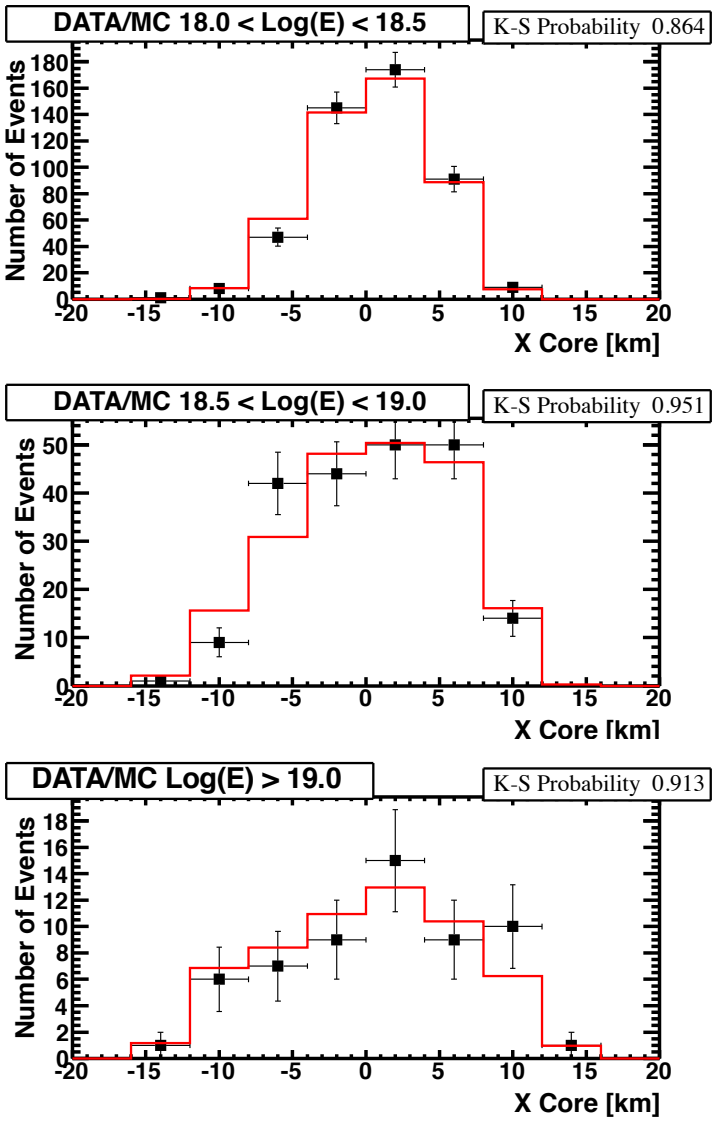


**Figure 4.23**. Data-MC comparison: Middle Drum hybrid calculated location of the east-west ("X") coordinate of the shower core with respect to the Central Laser Facility (CLF), is shown in three energy ranges: top to bottom, $10^{18.0} < E < 10^{18.5}$ eV, $10^{18.5} < E < 10^{19.0}$ eV, and $E > 10^{19.0}$ eV, respectively, to show the evolution of this parameter with energy. The distribution of measurements is shown for the data (black points with error bars) and MC (red histogram). The MC has been normalized to the area of the data in these plots. This figure shows that the data and MC agreement for this parameter are not dependent on energy.

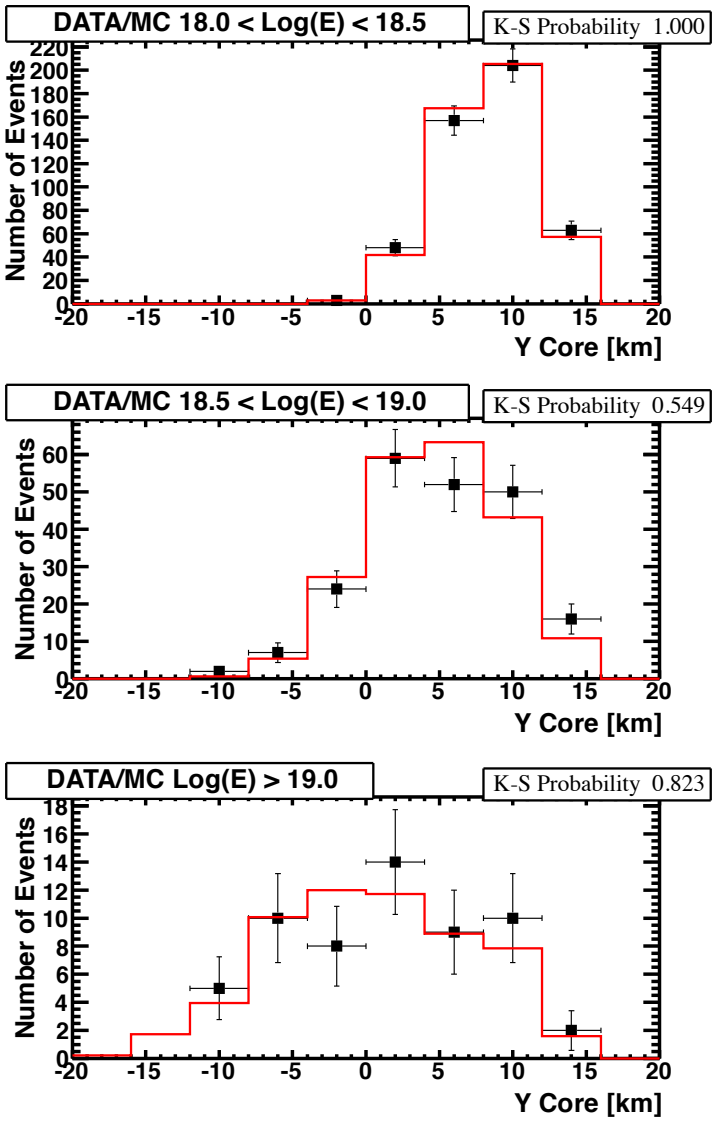


**Figure 4.24**. Data-MC comparison: Middle Drum hybrid calculated location of the north-south ("Y") coordinate of the shower core with respect to the Central Laser Facility (CLF) is shown in three energy ranges: top to bottom, $10^{18.0} < \mathrm{E} < 10^{18.5}$ eV, $10^{18.5} < \mathrm{E} < 10^{19.0}$ eV, and $\mathrm{E} > 10^{19.0}$ eV, respectively, to show the evolution of this parameter with energy. The distribution of measurements is shown for the data (black points with error bars) and MC (red histogram). The MC has been normalized to the area of the data in these plots. This figure shows that the data and MC agreement for this parameter are not dependent on energy.

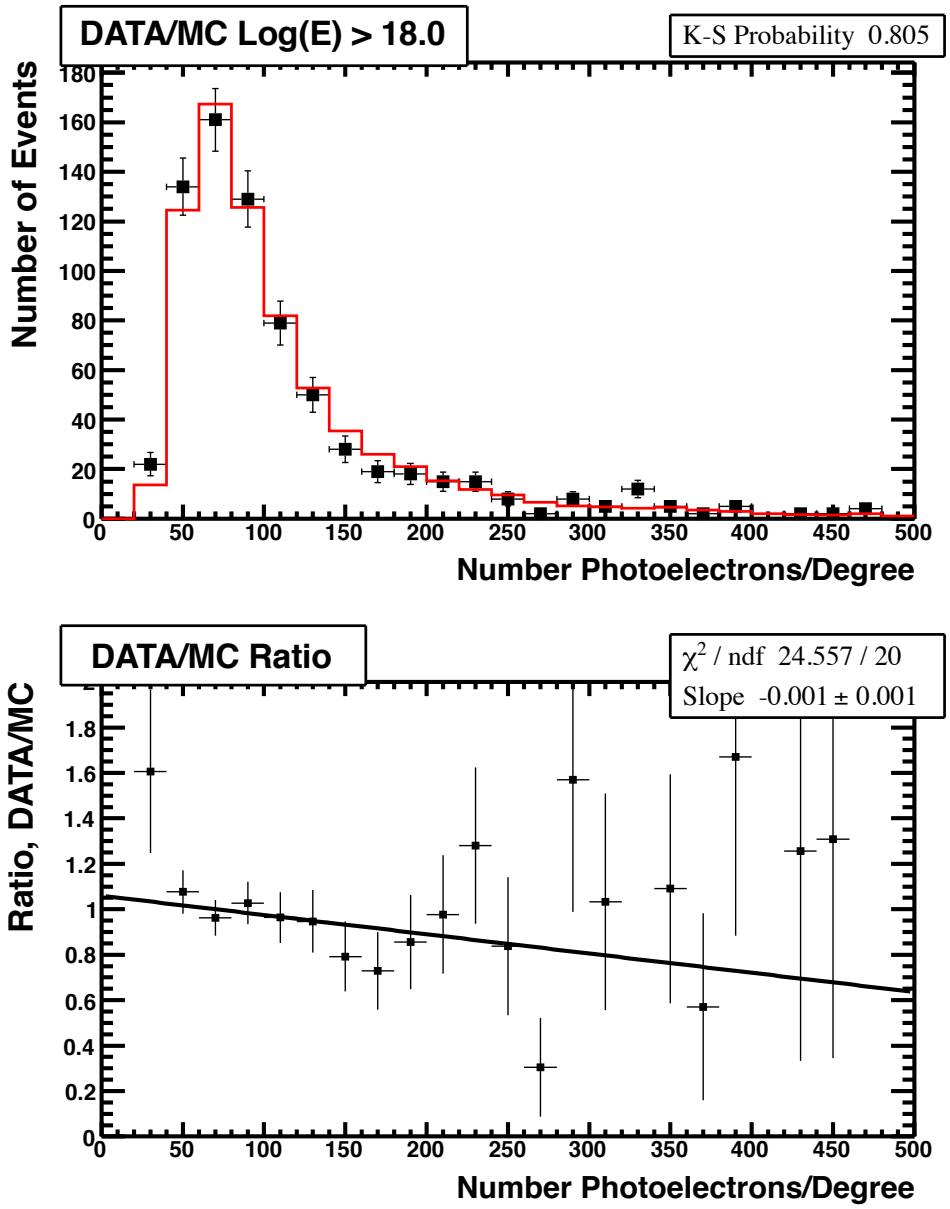


**Figure 4.25**. Data-MC comparison: Middle Drum hybrid number of photoelectrons is shown per degree of track length. Above: the distribution of measurements is shown for the data (black points with error bars) and MC (red histogram). The MC has been normalized to the area of the data in this plot. Below: the ratio of the data to the MC. The line is a linear fit to the points. It is flat with a ratio of 1 within uncertainties, indicating very good agreement.

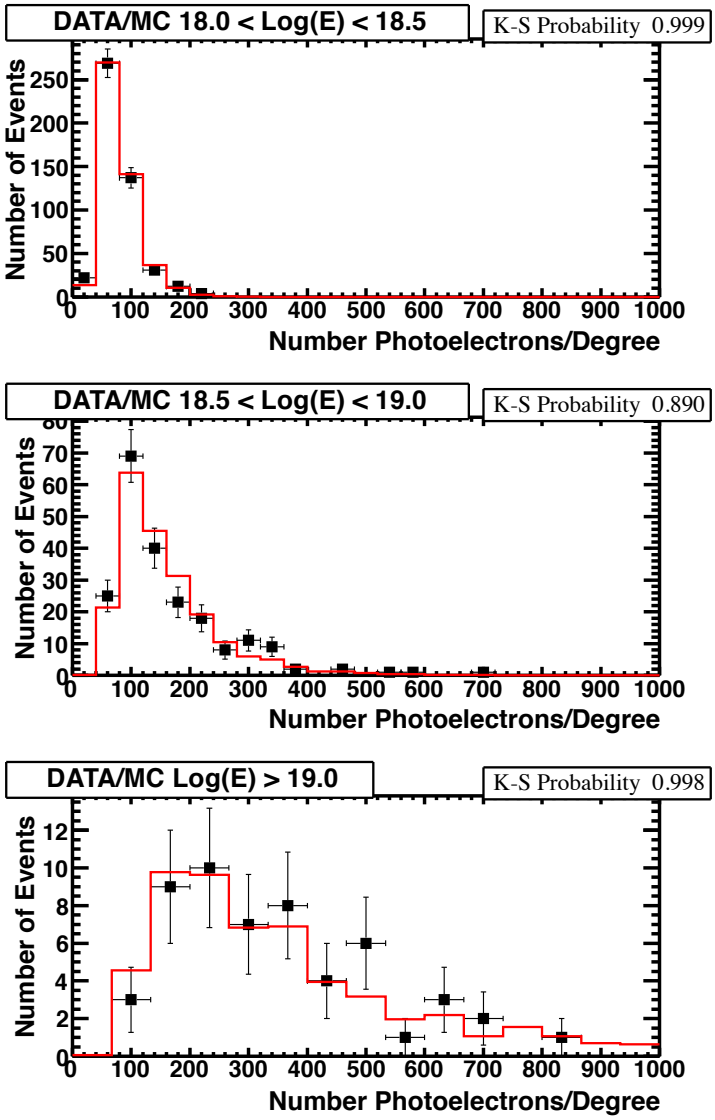


**Figure 4.26**. Data-MC comparison: Middle Drum hybrid number of photoelectrons per degree of track length is shown in three energy ranges: top to bottom, $10^{18.0} < \mathrm{E} < 10^{18.5}$ eV, $10^{18.5} < \mathrm{E} < 10^{19.0}$ eV, and $\mathrm{E} > 10^{19.0}$ eV, respectively, to show the evolution of this parameter with energy. The distribution of measurements is shown for the data (black points with error bars) and MC (red histogram). The MC has been normalized to the area of the data in these plots. This figure shows that the data and MC agreement for this parameter are not dependent on energy.

# CHAPTER 5

# EVENT RECONSTRUCTION

The hybrid reconstruction pairs up coincident MD and SD events using a time-matching program described in Section 5.4. The hybrid analysis takes advantage of improved geometric reconstruction by adding the SD constraints to the fitting. This, in turn, provides an improved energy measurement and a more reliable spectrum measurement than either the monocular SD or MD measurements (see Section 4.2.2). The SD monocular reconstruction programs are run prior to the hybrid analysis. Reconstruction of the SD information provides an accurate measurement of the shower core position which is then used to constrain the hybrid reconstruction. Therefore, The MD data are also passed through pre-reconstruction event selection identical to that of the monocular analysis before MD-SD time matching. In this chapter, I will describe the necessary SD and MD monocular reconstruction programs, along with the hybrid analysis programs used to create the MD hybrid event set.

## 5.1 Data Format

The TA group has established a collaboration-wide standard format. It is called Data Summary Tape (DST). All the raw and processed data are stored in "banks." A bank is an object containing both the structure and the methods needed to access the data. Each DST bank stores an array of variables. The individual processing of the hybrid events (SD and MD reconstruction) begins in exactly the same way as the monocular processing. The following list summarizes the analysis programs and banks used in the hybrid analysis. The processing sequence is described in detail in the subsequent sections.

- SD Pass0: Parses the raw SD data. The "rusdraw" bank stores the signal information.
- SD Pass1: Finds events using pattern recognition and does a preliminary fit for geometry. The "rufptn" bank stores the event information, while the "rusdgeom" bank stores the fit geometry information.

- SD Pass2: Uses the Lateral Distribution Function (LDF) to fit the shower geometry. The new geometry values are stored in the "rufldf" bank. This marks the end of the SD monocular processing. This information is then fed into the hybrid analysis.

- MD Pass0: Parses the raw MD data. The "hraw1" bank is created to hold signal information.

- MD Pass1: Converts the signals to number of photoelectrons and times. The "hraw1" bank is updated to include this information, and the "hbar" bank is created to store calibration information for this event.

- STPS2: Finds events using pattern recognition. A Rayleigh filter is used to cut random coincidences. The output of the pattern recognition program is stored in the "stps2" bank.

- STPLN: Fits events for the Shower Detector Plane (SDP). The SDP information is stored in the "stpln" bank.

- HRLSR: Finds and removes events that appear to be artificial in origin (i.e. lasers). Events are only removed at this step, and no additional information is stored.

- tmatch: Takes the timing information from the "rusdraw" bank and the "hraw1" bank and matches them. The output is a list of matched events containing both SD and MD banks.

- hbpass4: The first hybrid analysis step. Information from the "rufldf" bank as well as the "stpln" bank is used to fit a hybrid geometry. The output of the geometry fit is stored in the "hctim" bank.

- STPFL: Fits the shower profile and calculates the shower energy using the hybrid geometry. The "stpfl" bank stores the profile and energy information.

- MC Events: Contain extra banks to differentiate them from real data events. The extra banks contain "cheat" information, the original MC generated parameters for the event. The SD MC bank is the "rusdmc" bank, and the MD MC bank is the "mc04" bank.

## 5.2 SD Reconstruction

The SD raw data contains trigger and waveform information from particles passing through the scintillator and producing light that is detected by the PMTs. The SD reconstruction determines the geometry and energy of the events by using these signals. This process involves three processing programs: Pass0, Pass1 and Pass2.

The Pass0 program parses the raw data. It scans the FADC traces and finds the time of the signal. Figure 5.1 shows the PMT waveforms from SD counter 0408 for the event observed on 9/19/2009 at 08:45:52 UTC. All of the reconstruction plots to follow in this chapter will display different aspects of this same event. Pass0 also calibrates the signal using a 1 MIP (Minimum Ionizing Particle) and VEM (Vertical Equivalent Muon) calibration described in Section 3.1.4. In this trace, the pulse height was determined to be 1.11 VEM/m$^2$, and the trigger time for this counter was 36.14 $\mu$s after the first triggered counter.

Pass1 takes all of the information from the triggered events (a minimum of 3 adjacent counters, each with more than 3 MIPs is required to form a trigger) (see Section 3.1.4) and fits the geometry of the shower. First, the program determines which counters are part of the actual event, and which detectors were only written out due to electronic noise and stray muons. This is done by only including counters which are considered contiguous in both space and time. Counters that are within $\sqrt{2}\times$ the counter spacing are considered contiguous in space, thus including counters on the diagonal. Two counters with a time difference (divided by the speed of light) less than or equal to their spacing are considered contiguous in time. Counters that don't fit this pattern recognition criteria are removed as electronic noise or random muons.

Next, using the assumption that shower particles travel at the speed of light, the program finds the shower track vector using the trigger times of each SD in the event. Figure 5.2 shows a schematic of the shower front [28]. The variables shown are useful for determining the geometry of the shower. The program minimizes the $\chi^2$ in equation 5.1, while varying the parameters $T_0$, $R_x$, $R_y$, $\theta$, and $\phi$, to be described within the context of the equation.

$$\chi^2_{geom} = \sum_{i=0}^{N} \frac{(t_i - t_i^F)^2}{\sigma_{t_i}^2} + \frac{\|\mathbf{R} - \mathbf{R}_{COG}\|^2}{\sigma^2_{\mathbf{R}_{COG}}} \tag{5.1}$$

In the equation, $\mathbf{R}$ represents the position of the shower core on the ground. $\mathbf{R}_{COG}$ represents the core position as calculated by the Center Of Gravity (GOG) calculation. It is calculated using the pulse heights of the signals from each triggered detector and is

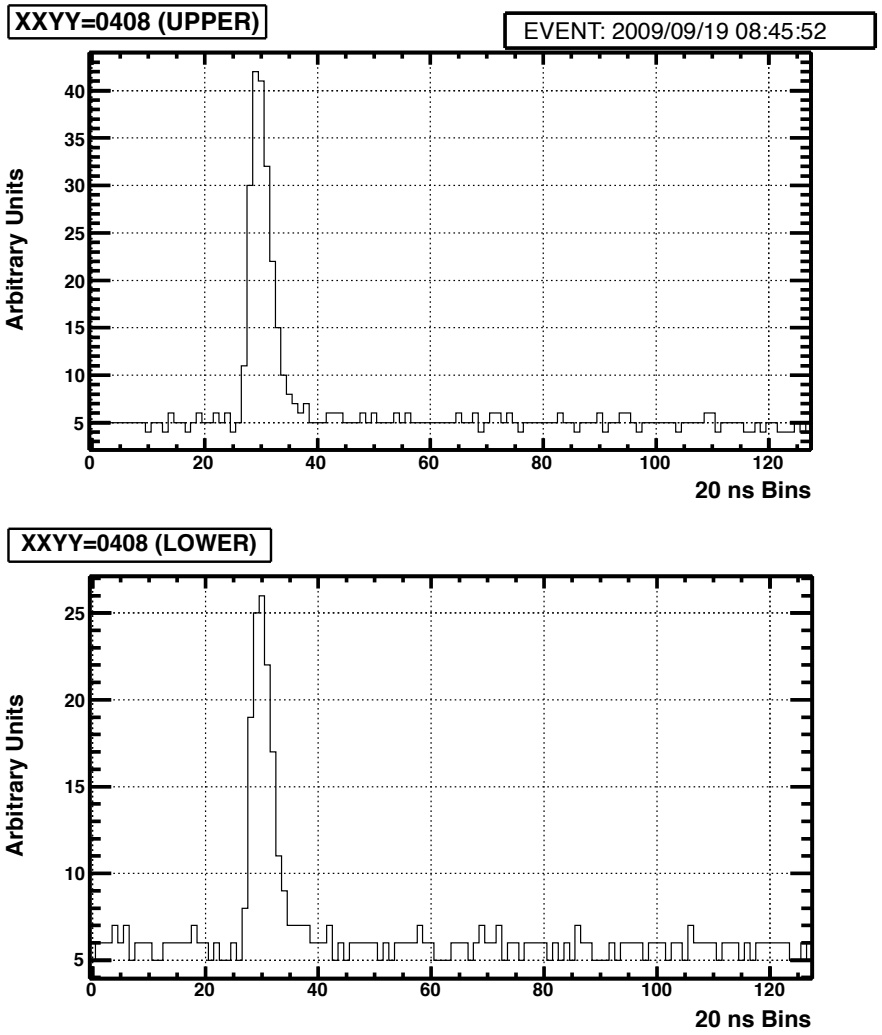


**Figure 5.1**. FADC signal waveforms are shown from the upper (above) and lower (below) layers of scintillator in detector 408 for event 2009/09/19 08:45:52 UTC. The SD Pass0 program parses the signal and calibrates it using 1 MIP and VEM calibrations. The pulse height for this signal is calibrated to 1.11 VEM/$m^2$.

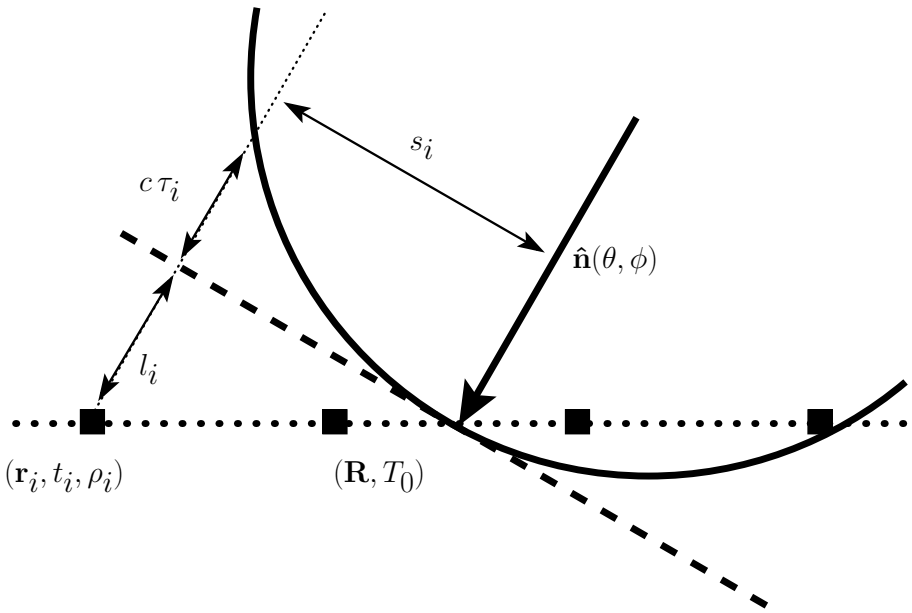


**Figure 5.2**. A schematic of the shower front is shown as it hits the SD array. A unit vector in the direction of the shower axis is represented by $\hat{\mathbf{n}}(\theta, \phi)$, $\mathbf{R}$ is the position where the shower core crosses the SD plane, and $T_0$ is the time that the shower core hits the SD plane. For a given counter, $i$, $\mathbf{r}_i$ is the position of the counter, $t_i$ is the time it registers a signal, and $\rho_i$ is the pulse height per unit area of the signal (VEM/m$^2$). The lateral distance of counter $i$ from the shower axis is $s_i$, and $l_i$ is the distance along the propagation axis from the shower core. The delay of the shower front due to the curvature of the shower is represented by c$\tau_i$.

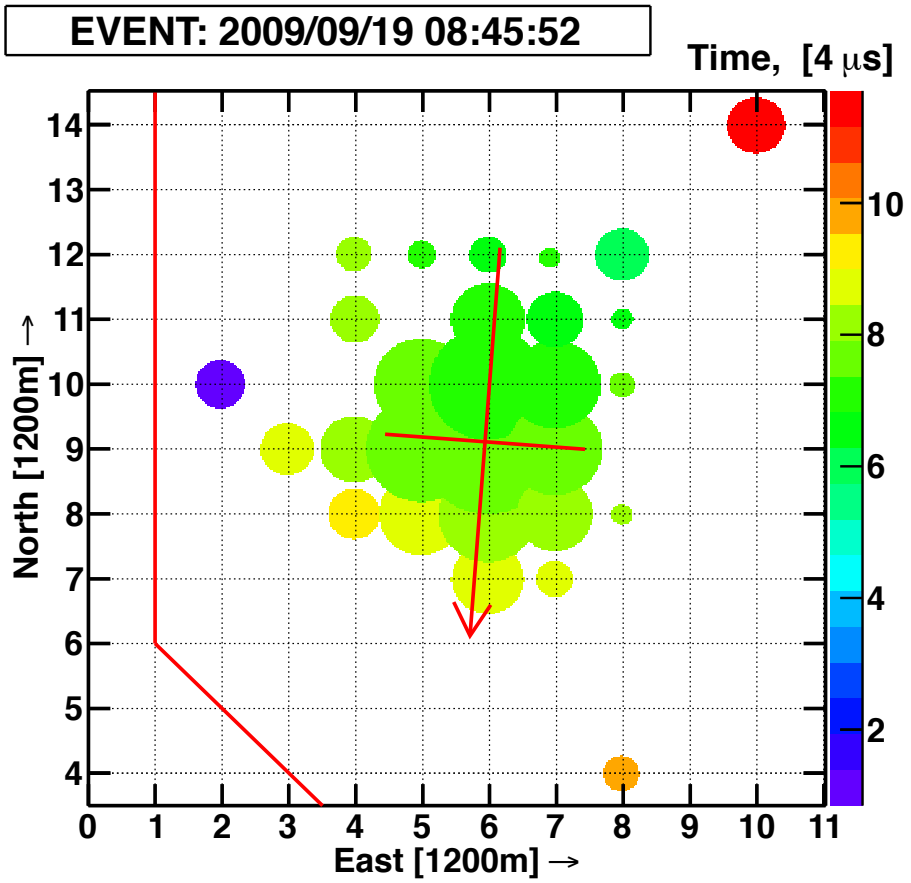


**Figure 5.3**. SD event display: the Center Of Gravity (COG) core position is shown where the arrow crosses the line for event 2009/09/19 08:45:52. The COG core is calculated using only the pulse heights of the signals from triggered SDs. The direction of the arrow is determined by studying the pulse heights of the elliptical footprint of the shower on the ground and effectively finding the semimajor axis of the ellipse. The COG core position is the starting point for the SD timing fit and lateral distribution fit, and the uncertainty in the COG shower core, $\sigma_{\mathbf{R}_{COG}}$, is calculated as 170 m. Note that the triggered counters which are not contiguous (e.g., 0210, 0804, and 1014) are removed from the event in the SD Pass1 program.

used as the starting point for the SD core calculation. Figure 5.3 shows the COG core reconstruction with the geometric direction arrow for the event observed on 9/19/2009 at 8:45:52 UTC.

The timing fit function, $t_i^F$, and uncertainty in the timing, $\sigma_{t_i}$, for counter $i$ in equation 5.1 are defined by equations 5.2 and 5.3.

$$t^F = T_0 + \frac{l}{c} + \tau \tag{5.2}$$

$$\sigma_t = \sqrt{\sigma_e^2 + \sigma_\tau^2} \tag{5.3}$$

Here, $\tau$ represents the time delay of the shower front to counter $i$, $c$ is the speed of light, and $T_0$ is the time when the shower core hits the SD plane. The uncertainty, $\sigma_t$, is defined by the uncertainties in both the time delay, $\sigma_\tau$, and the electronics timing, $\sigma_e$ (20 ns). Finally, $l$ is defined as the distance along the propagation axis from the shower core to counter $i$, defined by equation 5.4,

$$l = (\mathbf{r} - \mathbf{R}) \cdot \hat{\mathbf{n}}(\theta, \phi)\,, \tag{5.4}$$

where $\mathbf{R}$ is the position of the shower core on the ground with respect to the CLF, $\mathbf{r}$ is the position of counter $i$ on the ground and $\hat{\mathbf{n}}(\theta, \phi)$ is the unit vector in the direction of the shower core, as a function of zenith ($\theta$) and azimuthal ($\phi$) angles. The time delay function, $\tau$, is modeled as a modified Linsley time delay function [31]. Equations 5.5 and 5.6 give the time delay function and its uncertainty used in this analysis.

$$\tau = a\left(1 - \frac{l}{12 \times 10^3 m}\right)^{1.05}\left(1.0 + \frac{s}{30m}\right)^{1.35}\rho^{-0.5} \tag{5.5}$$

$$\sigma_\tau = \left(1.56 \times 10^{-3}\right)\left(1.0 - \frac{l}{12 \times 10^3 m}\right)^{1.05}\left(1.0 + \frac{s}{30m}\right)^{1.5}\rho^{-0.3} \tag{5.6}$$

In these equations, $s$ is the lateral distance of counter $i$ from the shower core, and $\rho$ is the pulse height per unit area of the signal (VEM/m$^2$). Note that the factor $1 - \frac{l}{12\times10^3}^{1.05}$ has been included as an added curvature factor which was determined after some preliminary data analysis [28]. All the numbers were calculated from preliminary fitting to the data. The curvature parameter, $a$, is allowed to vary in the fit, along with the parameters $T_0$, $R_x$, $R_y$, $\theta$, and $\phi$. Figure 5.4 shows the timing fit for the event observed on 09/19/2009 at 08:45:52 UTC.

Pass2 is the final reconstruction step for the SD events. The triggered counters are fit to a Lateral Distribution Function (LDF). This program uses the same function that was used

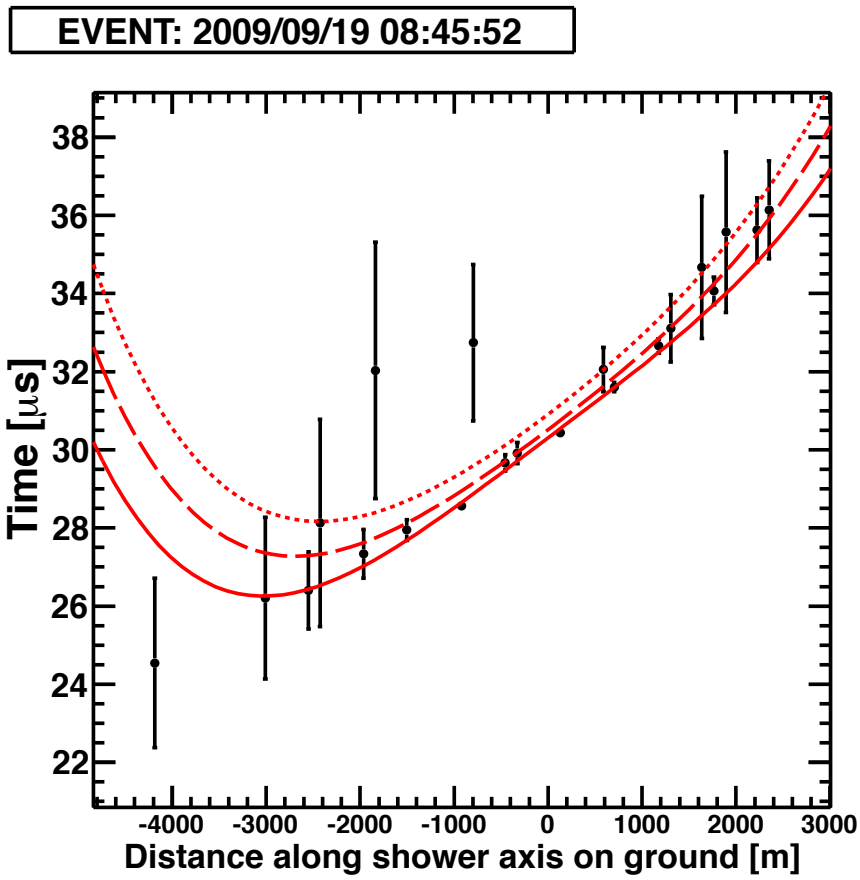


**Figure 5.4**. The SD timing fit shown for event 2009/09/19 08:45:52: the time of counter hit is plotted as a function of distance along the projection of the shower axis on the ground. The curves represent the timing fit to the data. The solid line is the fit expectation from counters that lie along the axis projected on the ground. The dashed and dotted lines are fit expectation times for counters that lie 1 km and 2 km away, respectively, from the axis projected on the ground.

by the AGASA experiment [42, 28] to minimize the $\chi^2$ in equation 5.7 [28]. The parameters being varied in the equation are $R_x$, $R_y$, and $A$.

$$\chi^2_{LDF} = \sum_{i=0}^{N} \frac{(\rho_i - \rho_i^F)^2}{\sigma_{\rho_i}} + \frac{\|\mathbf{R} - \mathbf{R}_{COG}\|^2}{\sigma^2_{\mathbf{R}_{COG}}} \tag{5.7}$$

The second term of equation 5.7 is the same as in equation 5.1, and $\rho_i^F$ represents the density of particles collected by counter $i$ at at distances perpendicular to the shower axis. The empirical form of this function is given in equation 5.8, and the zenith angle dependence is given in equation 5.9.

$$\rho(s) = A\left(\frac{s}{r_M}\right)^{-1.2}\left(1+\frac{s}{r_M}\right)^{-(\eta(\theta)-1.2)}\left(1+\left[\frac{s}{1000}\right]^2\right)^{-0.6} \tag{5.8}$$

$$\eta(\theta) = 3.97 - 1.79[sec(\theta) - 1] \tag{5.9}$$

In both of these equations, $s$ represents the perpendicular distance from the shower core, $r_M$ represents the Moliere multiple scattering unit (91.6 m), and $\theta$ represents the zenith angle. $A$ is a scaling factor. Again, the numbers were calculated using preliminary data fits. The uncertainty in the LDF is given in equation 5.10 [42].

$$\sigma_\rho = \sqrt{0.56\rho + 6.3 \times 10^{-3}\rho^2} \tag{5.10}$$

Recall that the parameters being varied are $R_x$, $R_y$, and $A$. The parameters $s$ and $\theta$ are set to the values calculated in the timing fit, and are not varied in this minimization.

Using the result of the LDF geometry fit, the density of particles at a lateral distance perpendicular to the shower core can be extrapolated at any point. Figure 5.5 shows the result of this fit for the shower observed on 9/19/2009 at 8:45:52 UTC. The distance ~800 m from the shower core has been determined in previous studies to be a stable indicator of shower energy for this size detector (3 $m^2$) and counter separation (1.2 km) [28]. The density of particles at this point is called S800. Figure 5.6 shows the same event display as Figure 5.3; however, a second (red) arrow has been added showing the direction of the shower calculated using the timing fit from Figure 5.4. The position of the shower core is at the intersection of the red arrow and the perpendicular line.

Once S800 is found, an energy table is used to determine the energy. In this method, many showers with different energies and geometries are generated to find the one which gives signals in the detector which most closely resemble the actual data event. Figure 5.7 shows a graphical representation of the table that is generated using a separate set of

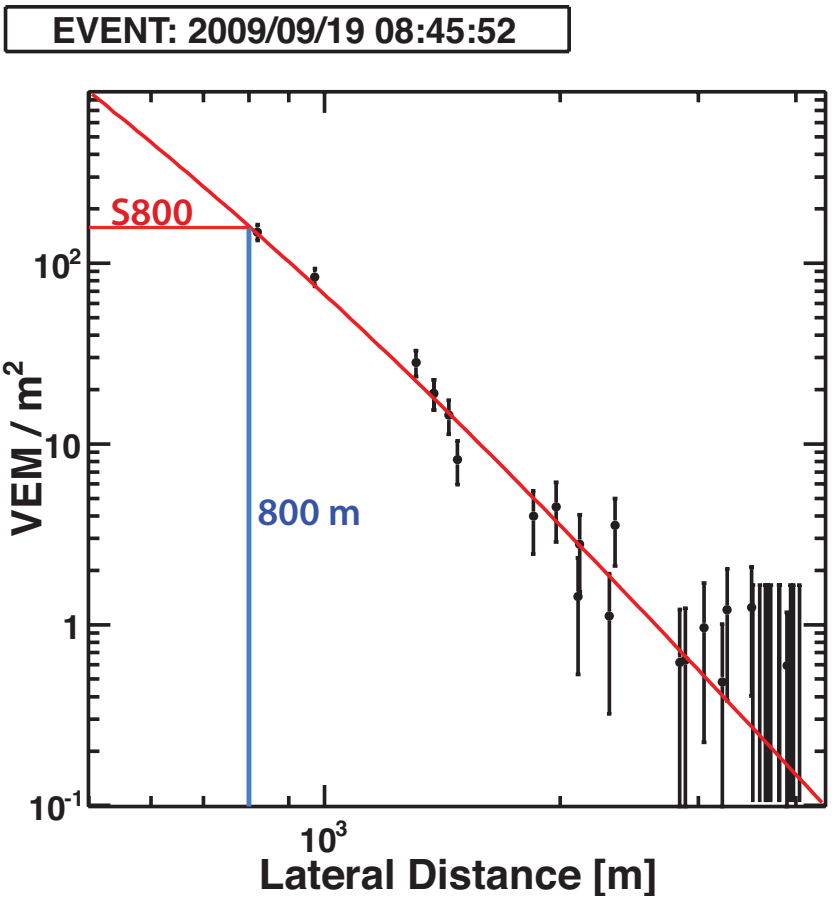


**Figure 5.5**. The fit to the Lateral Distribution Function (LDF): the pulse height (VEM/m$^2$) is plotted as a function of the lateral distance from the shower axis for event 2009/09/19 08:45:52. The estimated signal size , S800, (from the LDF fit) at a distance of 800 m from the shower core is used to determine the energy of the primary particle.

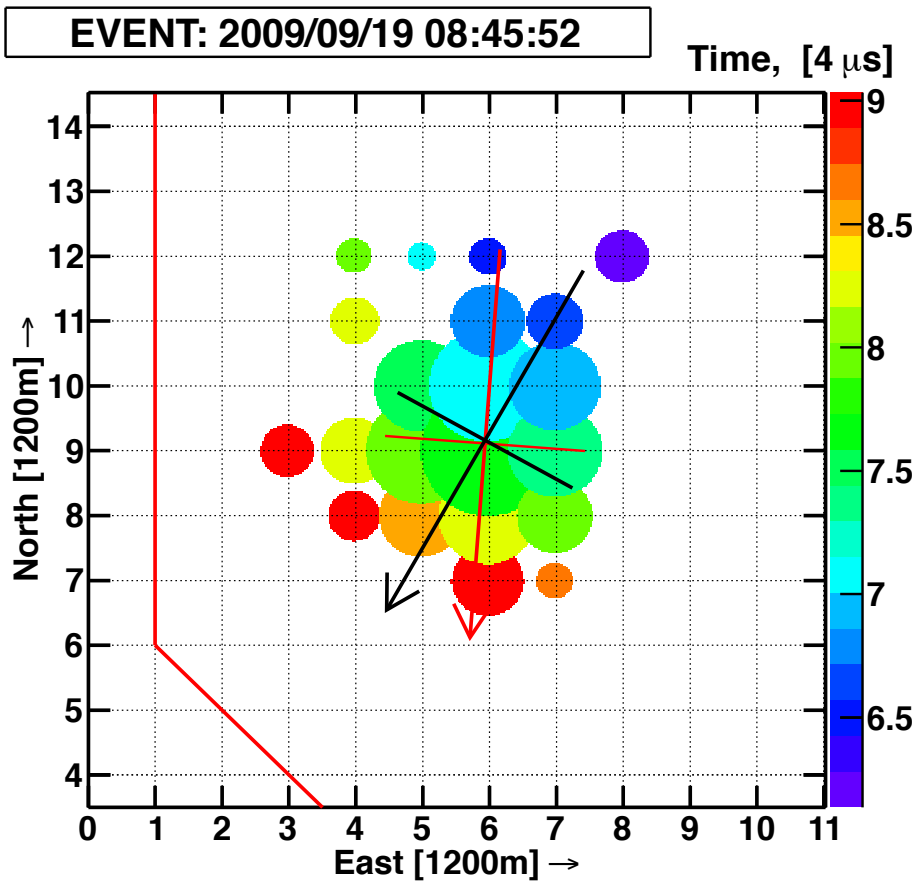


**Figure 5.6**. SD event display: the Center Of Gravity (COG) core position is shown where the red arrow crosses the (red) line, and the arrow points in the initial direction calculated using the COG. The black arrow shows the result of the timing fit for the shower core (where the black arrow crosses the black line). This is the event display for event 2009/09/19 08:45:52.

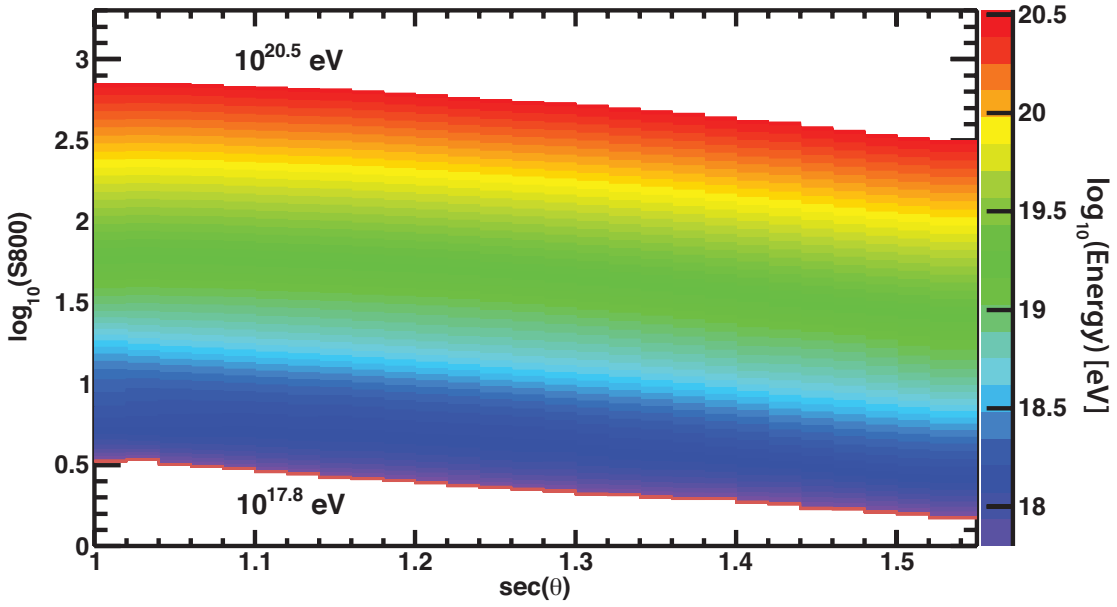


**Figure 5.7**. The SD energy table: the S800 value (in log scale) is plotted as a function of the secant of the zenith angle. The energy for the SD events is found using this table with the calculated values for S800 and zenith angle.

simulated showers to correlate the initial energy of the shower given a particular value for S800 and zenith angle [28]. Detailed information about these programs can be found in the PhD thesis of D. Ivanov [28].

## 5.3 MD Reconstruction

The Middle Drum raw data consist of a list of QDC counts from the PMTs as well as the timing information from the TDCs. Calibration banks are generated each run night storing data from calibration processes (described in Section 3.3). The data are then reconstructed using the "UTAFD" programs. These programs were originally written for the HiRes experiment [11] and have been modified for the Telescope Array geometry. The "UTAFD" programs were written for analyzing data in monocular mode. Therefore some programs exist that are not used in the hybrid analysis; these will not be described here. The programs used by my hybrid analysis are Pass0, Pass1, STPS2, STPLN, and HRLSR. The STPFL program from the "UTAFD" programs is also used in hybrid mode to calculate the energy. Because it has not been used this way before, it will be described with the hybrid analysis in Section 5.4.

The Pass0 program is the event builder. This means it matches the triggered events from individual telescopes using GPS time-stamps. The data from the telescopes are then compared, and telescope events that occur within 100 $\mu$s of each other are combined into a single site event. This is done offline, unlike most high energy physics experiments.

The Pass1 program converts the TDC values into microseconds relative to the GPS time-stamp. Each triggered PMT is given a time relative to the "telescope level trigger" time (see Section 3.1.3). The QDC values are converted into photoelectrons as described in Section 3.3. Pass1 also uses millisecond timing to remove the 1 Hz UVLED signals as well as signals from the CLF that is fired every 30 minutes (see Section 3.3).

The STPS2 program determines the probability that each event is a true cosmic ray event. Specifically, it determines the probability that the event was triggered by noise using a Rayleigh filter. Each pair of neighboring tubes is examined and a unit vector is drawn from the earlier tube to the later one. A Rayleigh vector describes the sum of all such segments. If the event is due to noise, the length of the Rayleigh vector will be short, while for a real cosmic ray event it will be long.

If the Rayleigh vector is produced by random coincidences, its length can be approximated by the isotropic 2D "random-walk" formula given by equation 5.11.

$$p(r) = \frac{r}{\sigma^2} exp\left[-\frac{r^2}{2\sigma^2}\right] \tag{5.11}$$

Here, r is the length of the Rayleigh vector after $N$ steps, and $N$ is the number of adjacent pairs with tube spacial separation $< 1.5^\circ$ and time separation $< 14$ ns [11]. The probability that the event is a noise event (e.g., triggered by a random process) is found by integrating equation 5.11. The result is given in equation 5.12.

$$Prob(r > R) = exp\left[-\frac{R^2}{2\sigma^2}\right] \tag{5.12}$$

Here, $Prob(r > R)$ is the probability that a vector of length R is generated randomly. The value $plog$, found by taking $-log_{10}(Prob)$, is defined in equation 5.13.

$$plog = \frac{R^2}{Nln10} \tag{5.13}$$

Note that here, $\sigma^2$ has been replaced with $N/2$. Events with a $plog$ value $> 2$ (corresponding to a 1% or less probability that the event was generated randomly), are flagged as good events, which are saved for further analysis.

The Rayleigh vector also determines the approximate direction of the event (e.g., up, horizontal, or down). Events are flagged as horizontal if they are within $\pm$ 20° of horizontal.

Events that do not travel downward (directed more than 20° below horizontal) are excluded from this analysis.

The STPLN program is then used to calculate the Shower Detector Plane (SDP), using the pointing directions of the PMTs. The SDP is treated as a line source, as shown in Figure 5.8. The SDP is fit using $\chi^2$ minimization for equation 5.14.

$$\chi^2 = \sum_i \frac{(\hat{\mathbf{n}} \cdot \hat{\mathbf{n}}_\mathbf{i})^2 \cdot w_i}{\sigma_i^2} \tag{5.14}$$

In this equation, $\hat{\mathbf{n}}$ represents the SDP normal vector, and $\hat{\mathbf{n}}_\mathbf{i}$ is the viewing direction of triggered tube $i$. The number of photoelectrons seen by tube $i$ is $w_i$ . This weighting effectively treats each photoelectron as a separate data point. For each tube, $\sigma_i^2$, or the angular uncertainty, is set to 1° because this is the viewing angle of an individual PMT and we can not determine where on the face of the PMT a photon hit it.

Once the SDP is found, noise tubes are identified and removed from the fit, see Figure 5.9. This is done using an iterative procedure. Each tube is plotted in time as a function of its angle within the SDP. These are fit to a quadratic function of the angle. The program calculates an RMS value for deviation from the plane in angle and time for each tube. If the tube has a value $> 3$ RMS from the time-angle plane, it is removed. This process is repeated until no more tubes are be removed. Note that the quadratic fit here is different from the fit done later in the hybrid reconstruction, Section 5.4.

Finally, the HRLSR program was developed to remove laser events which were previously removed by hand. This program looks for events that are similar in time, core location, and amount of light seen, with a goal of removing those events that are from artificial sources. A set of events are removed if they have all of the following properties:

- Consecutive events occur within nine seconds of each other.
- The events have three or more "good" tubes in common.
- The number of photoelectron values for the top six tubes for each event are within 30% of each other.
- The repetitive events have plane normal vectors within 10° of each other.

The MD reconstruction "UTAFD" programs were developed by T. AbuZayyad based on the TA programs established by D. Rodriguez, and are described in detail in [38] and [11].

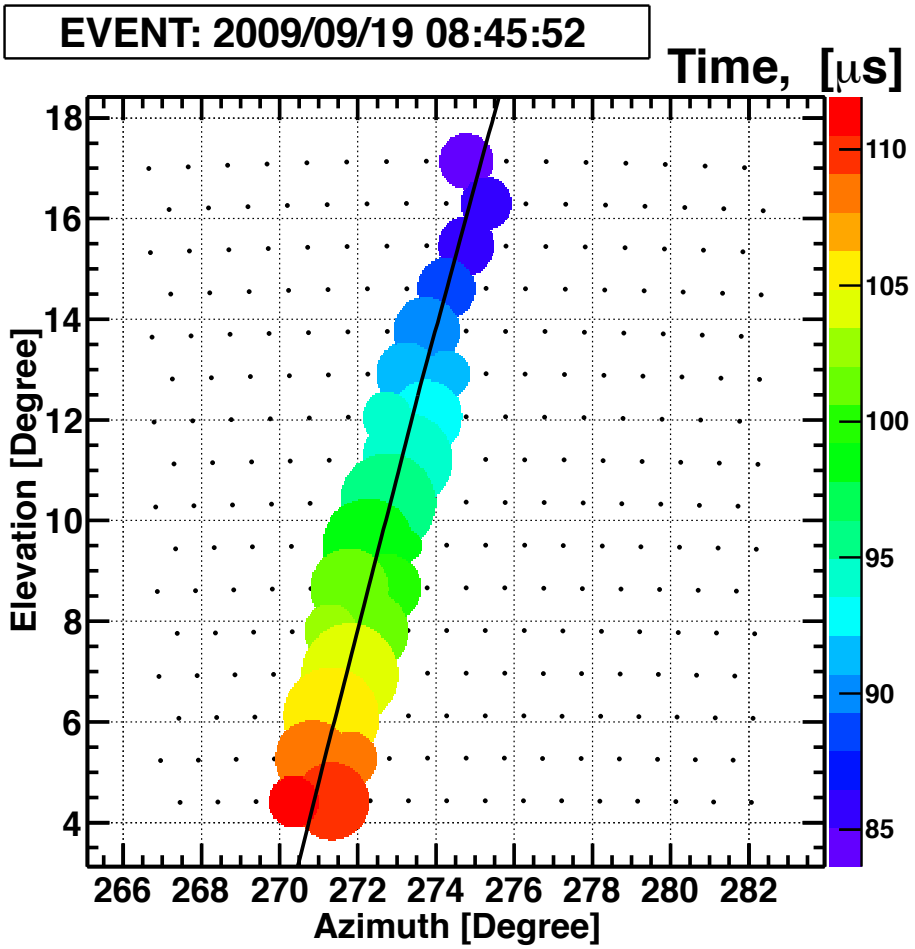


**Figure 5.8**. Middle Drum event display for event 2009/09/19 08:45:52: it shows the Shower Detector Plane (SDP) fit to the PMTs. For each PMT, the size of the circle indicates the signal size, while the color of the circle represents the timing with respect to the other tubes. The black line represents the fit to the projection of the Shower Detector Plane (SDP).

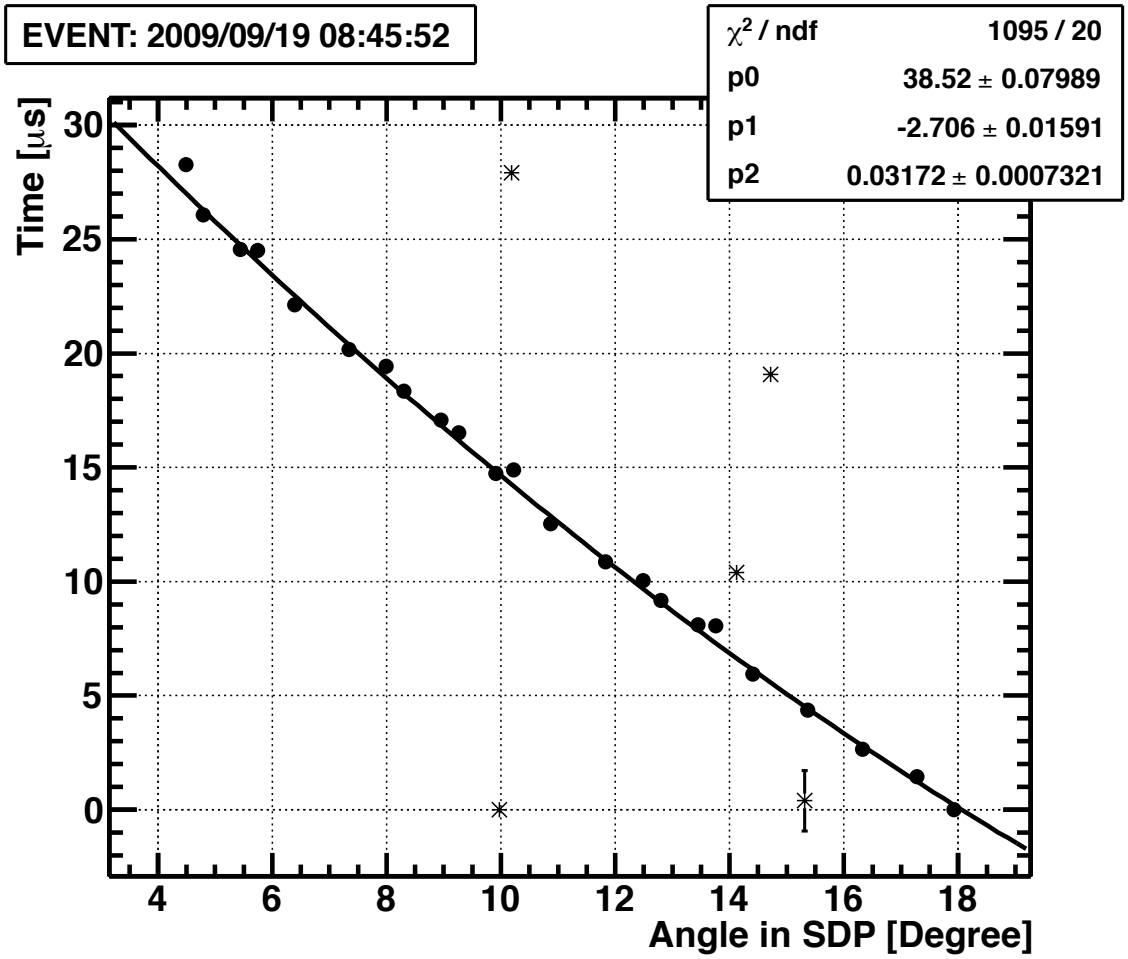


**Figure 5.9**. MD timing vs. angle plot for event 2009/09/19 08:45:52: the time of the PMTs is plotted as a function of their elevation angle within the Shower Detector Plane (SDP). The tubes are fit to a quadratic function, and those which deviate too far from the fit are removed. The curve shows the final fit after the noise tubes (indicated by stars) have been removed.

## 5.4 Hybrid Reconstruction

As described in the previous sections, the SD and MD parts of the hybrid events are reconstructed separately through the Surface Detector Pass2 and the Middle Drum HRLSR reconstruction programs. In order to combine the two sets of information into one hybrid event set, a time matching program compares timing information of each event from the two sets. The time that the shower core crosses the Surface Detector plane is calculated for each set. This time is compared, and events that are within 2 $\mu$s of each other are considered matched. A matched event is then combined into a single common event, and a hybrid event list is generated.

Once a combined set has been created, the events are processed using the information from both detectors in my hybrid analysis program, hbpass4. Equation 5.15 shows the $\chi^2$ equation that is minimized in order to determine the best combined geometry. The equation takes into account (1) the Fluorescence Detector timing, (2) the Surface Detector timing, and (3) the position of the core of the shower as it hits the ground as determined by the Surface Detector, including uncertainties.

$$\chi^2 = \chi^2_{MD_{Timing}} + \chi^2_{SD_{Timing}} + \chi^2_{Core} \tag{5.15}$$

The timing of the fluorescence and surface detectors is summarized by comparing timing with pointing direction. Figure 5.10 shows the "in-plane" view of the shower detector plane. Using equation 5.16, Middle Drum PMT trigger times can be related to their pointing direction. Equation 5.15 is then minimized using equation 5.17.

$$t_i = T_{Rp} + \frac{R_P}{c} tan\left(\frac{\pi - \psi - \chi_i}{2}\right) \tag{5.16}$$

$$\chi^2_{MD_{Timing}} = \sum_i \frac{1}{\sigma_i^2}\left\{t_i - \left(T_{Rp} + \frac{R_P}{c} tan\left(\frac{\pi - \psi - \chi_i}{2}\right)\right)\right\} \tag{5.17}$$

In both equations, $t_i$ represents the triggered time of tube $i$, and $T_{Rp}$ represents the time that the shower reaches the impact parameter ($R_P$). The angle of the shower track within the SDP is represented by $\psi$, and $\chi_i$ is the tube viewing angle within the SDP.

Figure 5.11 shows an example Timing vs. Angle plot of an event observed using the Middle Drum telescopes. The fit curve is calculated from equation 5.16 and $\chi^2$ minimization is used to determine the in-plane angle ($\psi$), impact parameter ($R_P$), and time at $R_P$ ($T_{Rp}$).

Figure 5.12 shows the result of the Hybrid Timing vs. Angle analysis. While Figure 5.11 shows only the MD points, the hybrid plot, Figure 5.12, has been significantly extended

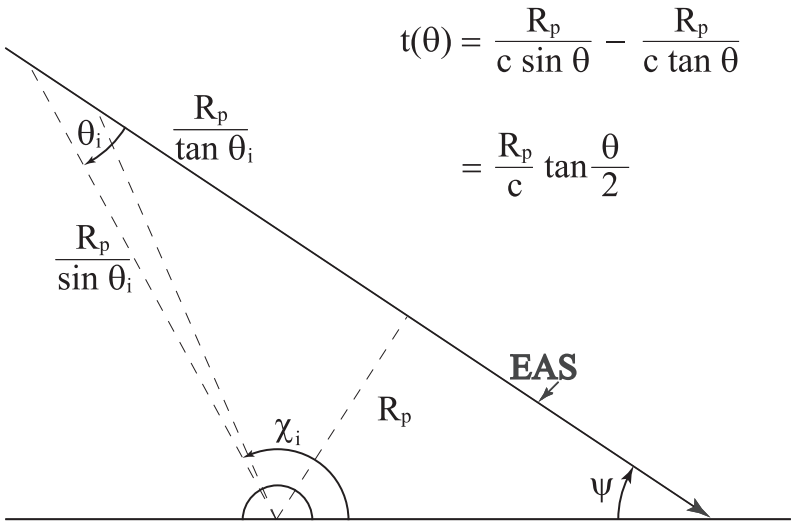


**Figure 5.10**. Diagram indicating the geometry of the shower within the SDP and parameter names: the diagram shows how the PMT trigger time is related to a given pointing angle within the SDP.

using the information from the Surface Detectors. Each triggered surface detector is treated as a virtual PMT located at the Middle Drum detector. Equation 5.18 shows how the trigger time is adjusted for the SD points.

$$t_{SD} = t_{SD_{Trig}} + \frac{SD_{Dist}}{c} \tag{5.18}$$

Here, $t_{SD}$ is the time that a virtual tube at Middle Drum that images the position of the counter would trigger, while $t_{SD_{Trig}}$ is the actual trigger time of the counter. $SD_{Dist}$ is the distance from the counter to MD, and $c$ is the speed of light. Equation 5.19 shows how the SDs are added to the $\chi^2$ calculation in equation 5.15.

$$\chi^2_{SD_{Timing}} = \sum_i \frac{1}{\sigma_i^2} \left\{ t_i - \left( T_{Rp} + \frac{R_P}{c} tan \left( \frac{\pi - \psi - \chi_i}{2} \right) \right) \right\} \tag{5.19}$$

Note that the equation is the same as equation 5.17. The difference is that the observed time, $t_i$, is calculated for each SD counter. The signals registered by the SDs arrive later than those registered by the PMTs at the MD detector because the SDs are sampling the shower on the ground while the light then takes time to get from that point to the telescope. Therefore, as shown in Figure 5.12, all of the SD points are plotted at later times. By adding the SD counters to the calculation, I add to the total number of "PMTs" in the $\chi^2$ minimization (equation 5.19) and, more importantly, extend the range in time

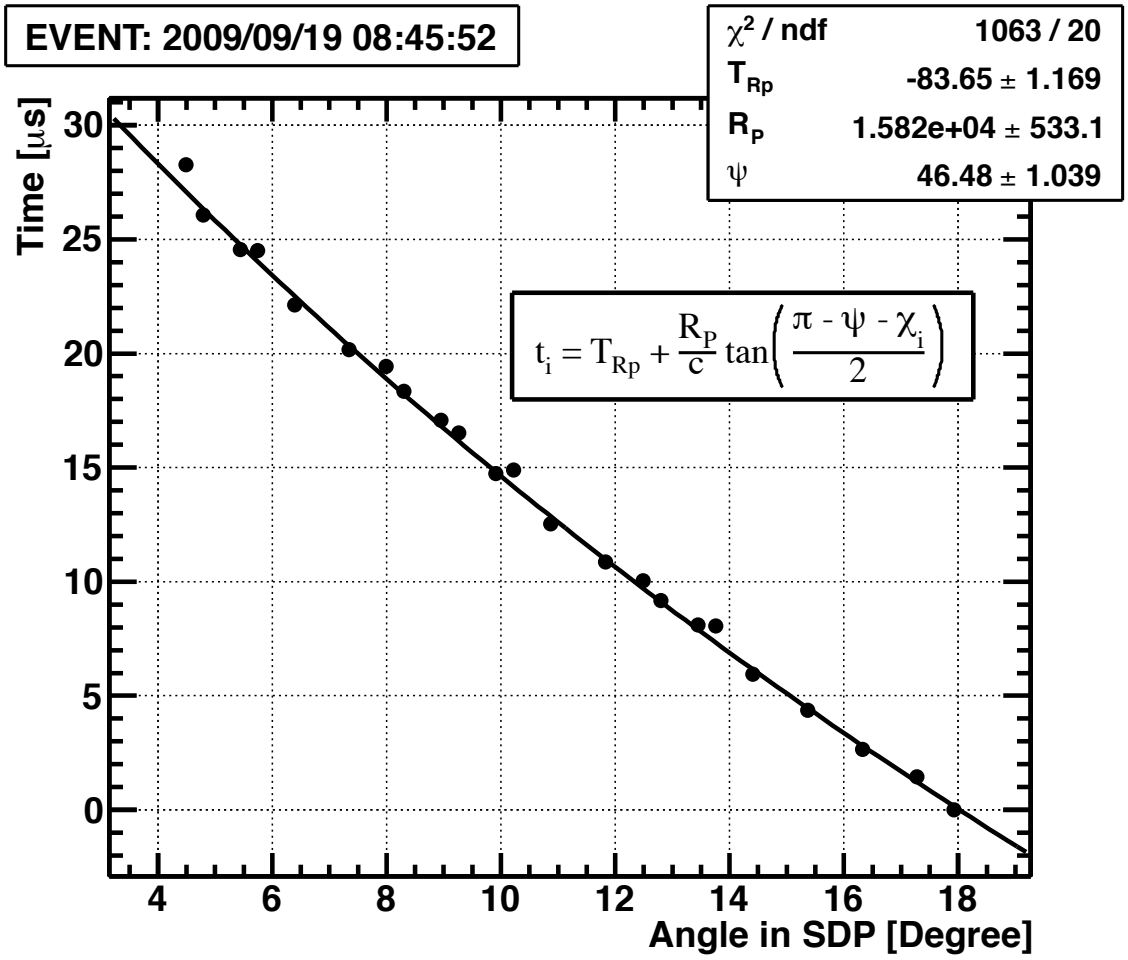


**Figure 5.11**. Timing vs angle plot for event 2009/09/19 08:45:52, observed by the PMTs at the Middle Drum fluorescence detector site: the angle of the observed signal along the SDP is plotted with respect to the time information of the signal. Fitting the curvature provides the timing and impact parameter, which combined with the SDP, give the pointing information of the primary cosmic ray.

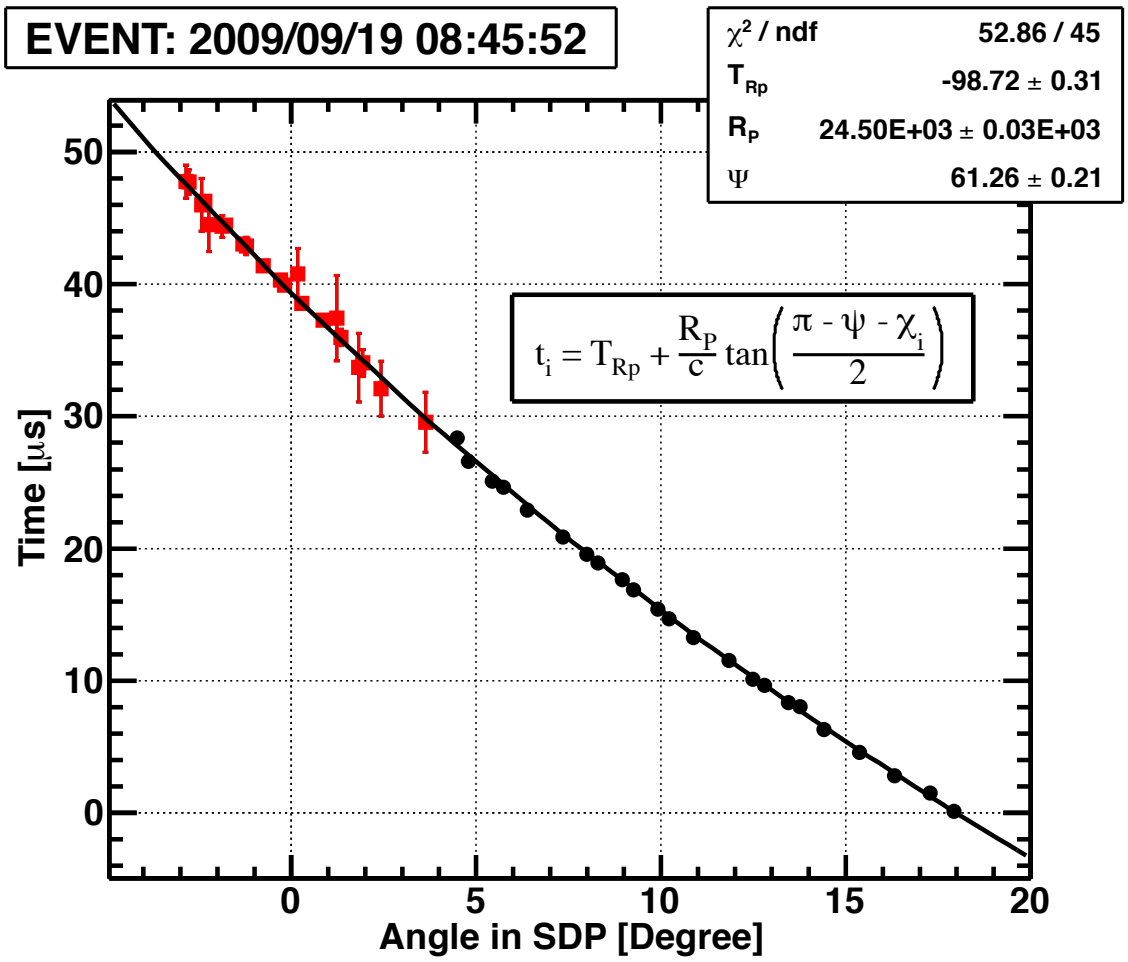


**Figure 5.12**. Timing vs angle plot for event 2009/09/19 08:45:52: it is extended using information from Surface Detectors. Virtual PMTs are created using information from the SD counters (red squares) which have been added to the information from the MD PMTs (black circles). In comparison with Figure 5.11, the curvature is more obvious, and the $\chi^2$ value is significantly better here.

and angle, which in turn produces a more accurate calculation of the parameters. Note that in comparison with Figure 5.11, the curvature in Figure 5.12 is more obvious, and the $\chi^2/dof$ is improved.

The $\chi^2_{Core}$ piece of equation 5.15 is the core constraint of the hybrid analysis. Equation 5.20 shows the minimization to determine the x and y coordinates.

$$\chi^2_{Core} = \sum_{1}^{2} \frac{\|\mathbf{R}_i - \mathbf{R}_{COG}\|^2}{\sigma^2_{\mathbf{R}_{COG}}} \tag{5.20}$$

Here, $\mathbf{R}_i$ represents the reconstructed core position from the Surface Detector Center Of Gravity, $COG$, while $\mathbf{R}_i$ represents the trial parameters. Note that $i = 1$ corresponds to the x-coordinate and $i = 2$ corresponds to the y-coordinate. The $\sigma^2_{\mathbf{R}_{COG}}$ is equal to 170 m, as in Section 5.2.

The hybrid analysis varies the five parameters ($\psi$, $\theta$, $R_P$, $R_x$, and $R_y$) incrementally and minimizes the full $\chi^2$ of equation 5.15 simultaneously. The result of this fitting is the hybrid geometry reconstruction of the UHECR showers.

## 5.5 Energy Reconstruction

The hybrid analysis uses the same energy reconstruction program as the Middle Drum monocular processing, called the STPFL program. It uses an inverse Monte Carlo technique for calculating the shower energy. In order to do this, however, it must first generate a profile of the shower. Using the calculated hybrid geometry, the program converts the viewing angle of each "good" tube (taken from the "stpln" bank) into a shower depth, in g/cm$^2$. The atmospheric profile used to calculate the slant depth is described in Section 3.3.2.1. The result is shown in Figure 5.13. The signal size, or number of photoelectrons seen by each tube is plotted as a function of depth. The amount of light seen from fluorescence is shown, in addition to the light generated due to Rayleigh scattering, aerosols, direct scintillation light and Cherenkov light.

The hybrid energy reconstruction procedure works as follows: the shower track geometry values stored in the "hctim" bank are fixed. These values, combined with a set of input parameters for the shower profile and energy are used to calculate the detector response for comparison with observation. A $\chi^2$ is calculated for this set of input parameters. Then the input parameters are adjusted until the $\chi^2$ value is minimized.

In inverse Monte Carlo, the fluctuations are removed. The MC showers are parametrically calculated using Poisson statistics rather than thrown and saved. The input parameters

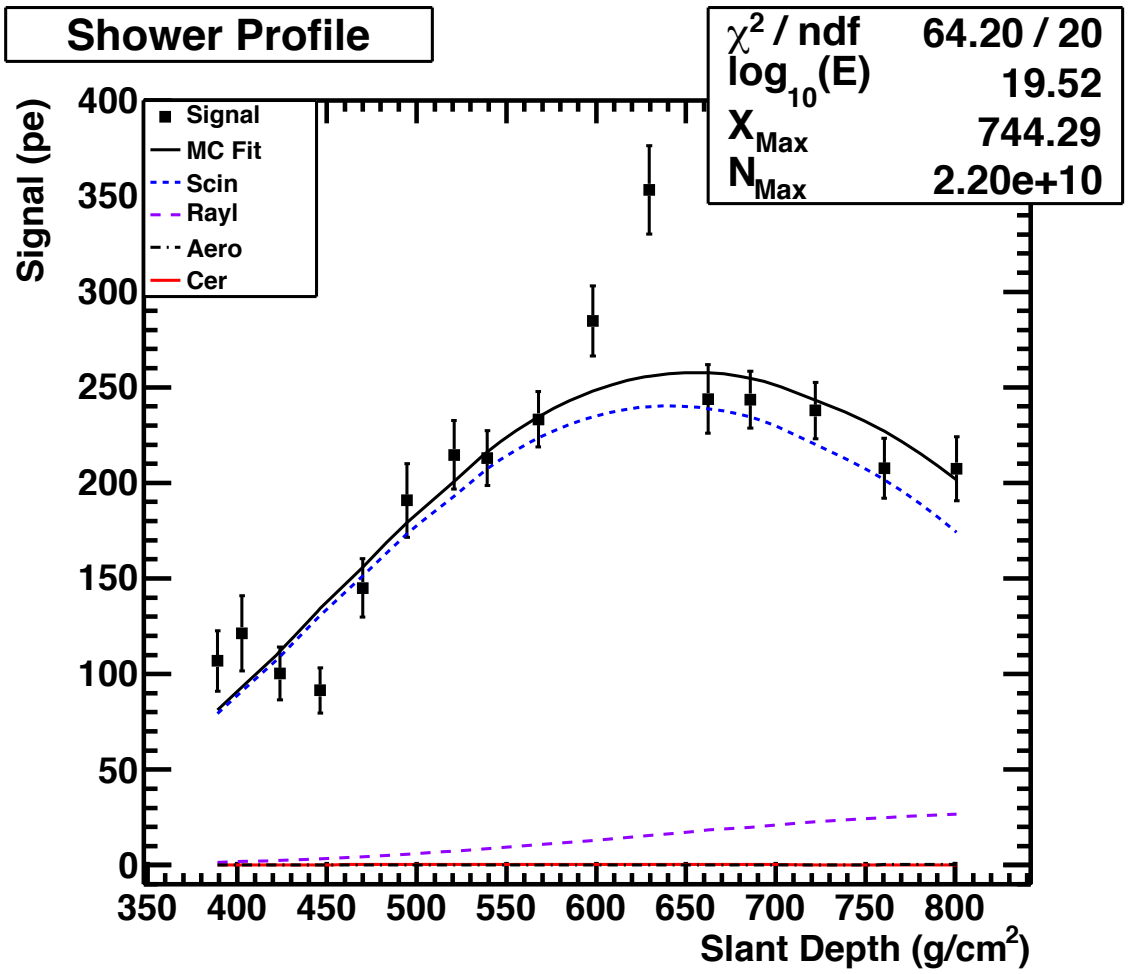


**Figure 5.13**. The profile plot for hybrid event 2009/09/19 08:45:52: the signal size is plotted as a function of slant depth in the shower. The black points are "good" tubes from the MD data. The points are fit to the Gaisser-Hillas function (equation 4.1). The amount of light generated due to Rayleigh scattering, Aerosols, Cherenkov light, and direct Scintillation light are also shown.

for the profile of the calculated shower are taken from the Gaisser-Hillas function, (equation 4.1),

$$N_e\left(x\right) = N_{max} \times \left[\frac{x - X_0}{X_{max} - X_0}\right]^{\frac{X_{max}-X_0}{\lambda}} exp\left(\frac{X_{max} - x}{\lambda}\right),$$

specifically, $x_0$, $X_{max}$, $N_{max}$, and $\lambda$. The values of $x_0$ and $\lambda$ are fixed to 40 g/cm$^2$and 70 g/cm$^2$, respectively, while, $X_{max}$ and $N_{max}$ are allowed to vary. The $\chi^2$ function for the profile is given given by equation 5.21.

$$\chi^2_{Profile} = \sum_i \frac{1}{\sigma_i^2}\left(S_i^{(m)} - S_i^{(p)}\right)^2 \tag{5.21}$$

Here, $S_i^{(m)}$ represents the measured tube signal, while $S_i^{(p)}$ is the predicted tube signal calculated from the input shower. The minimized $\chi^2$ value gives the Monte Carlo generated shower that best matches the observed shower. The energy of the Monte Carlo shower is then stored as the calculated hybrid energy of the real shower.

As this reconstruction was performed in the same way for all events in the data set, it is instructive to show a representative sample of events. The Appendix contains the important graphical representations of an event for each of the top 11 highest energy events in the MD Hybrid data. These plots include the MD event display, the SD event display, the hybrid timing vs. angle plot, and the profile plot.

# CHAPTER 6

# DATA AND ENERGY SPECTRUM RESULTS

## 6.1 Middle Drum Hybrid Event Selection

The first step to running any of the Middle Drum (MD) reconstruction programs described in Section 5.3, is to apply an initial weather cut to the data. Light from cosmic ray showers that develop through clouds can either be obscured or exaggerated by scattering with water droplets, making the reconstruction of the shower track very difficult, if not entirely impossible. Therefore, this analysis excludes data that were taken on nights when clouds were present in the directions that the Middle Drum (MD) telescopes point, namely, South and East. The events were also excluded if the overhead cloud cover was greater than 50%. The allowed WEAT codes are presented in Table 6.1 [38]. Details about WEAT codes are in Section 3.3.2.

Additional cuts were made on the data using the resolution plots (see Section 4.2.2) to improve the quality of the reconstruction. As shown in Section 4.2.3, the simulated showers are a good representation of the data. Below is a list of quality cuts that were made on the data, based on a study of the simulated showers.

1. Failmode: Events that failed the profile reconstruction are removed from the set (see Section 5.5).

2. Zenith angle $> 56^{\circ}$: The Monte Carlo does not simulate showers with zenith angle greater than $60^{\circ}$, and therefore, no determinations can be made about them. Due to overflow, events close to $60^{\circ}$ are also difficult to analyze.

3. Hybrid/Surface Detector Core Position (difference >1200 m): The core location of the shower at the ground is used to determine if the MD event and the SD event are the same event, so that only true hybrid events are kept.

4. Border Cut (>100 m): The border cut uses the hybrid core location to determine how close the shower falls to the edge of the surface detector array. Showers with

**Table 6.1**. A table of allowed WEAT code combinations: events that occur during times when these criteria are not met are cut from the data set.

| East | South | Overhead |
|---|---|---|
| 0 | 0 | 0 |
| 0 | 0 | 1 |
| 0 | 0 | 2 |
| 0 | 1 | 0 |
| 0 | 1 | 1 |
| 0 | 1 | 2 |
| 1 | 0 | 0 |
| 1 | 0 | 1 |
| 1 | 0 | 2 |
| 1 | 1 | 0 |
| 1 | 1 | 1 |

calculated core locations that fall at, or outside, the border of the array are difficult to reconstruct due to the missing information that may be out of range of the surface detectors. Therefore, showers that fall within 100 m of the border are removed.

5. Tracklength <8.0°: Events with shorter track lengths have less information, and therefore provide a less accurate reconstruction.

6. $X_{max}$ "Bracketed": Events which reconstruct with the depth of the shower maximum, or $X_{max}$ outside of the field of view of the detector camera are removed. The energy and composition are reconstructed more accurately if $X_{max}$ is seen.

## 6.2 Middle Drum Hybrid Aperture and Exposure Calculations

The energy spectrum refers to the differential flux of cosmic rays, and is calculated by taking the number of data events per energy bin and dividing by the exposure and energy interval for that bin, defined by equation 6.1.

$$J(E) = \frac{N(E)}{A\Omega(E) \times \Delta t \times \Delta E} \tag{6.1}$$

$N(E)$ refers to the number of reconstructed events in an energy bin, $A\Omega$ is the calculated aperture in the energy bin, $\Delta t$ is the hybrid detector on-time, and $\Delta E$ is the energy interval covered by the bin.

The exposure is calculated by taking the aperture per energy bin and multiplying by the on-time for the detector. The SD array collects data 24 hours a day. Taking into account the detectors in the array that are not working periodically, the array has better than 99.5% on-time. Therefore, the main contribution to the on-time calculation for this analysis comes from the fluorescence telescopes. The MD detector only operates on clear, moonless nights, with a minimum of three hours of dark time. After taking this and weather cuts into account, the MD detector duty cycle is ∼9%. The integrated on-time hours are shown in Figure 6.1. The on-time hours in the figure show an approximation based on the total number of telescope hours divided by the number of telescopes (14). Each telescope has a calculated on-time of >98% with respect to the whole site, making an average in this way a reasonable representation of the on-time per telescope.

Table 6.2 shows the bin-by-bin aperture calculation for the proton Monte Carlo set, described in Section 4.2. Simulated events are thrown such that the core of the shower intersects with the SD plane within a circle of radius 25 km centered at the Central Laser Facility (CLF), which is the geometric center of the three telescope stations (see Figure 4.4). The solid angle, $\Omega_0$, is defined by equation 6.2. Equation 6.3 represents the "thrown" aperture and is defined by the area of the circle multiplied by the solid angle. The calculated aperture for the spectrum is given in equation 6.4.

$$\Omega_0 = 2\pi \int_0^{\theta_{max}} sin\theta cos\theta d\theta = \pi sin^2\theta_{max} \tag{6.2}$$

$$A_0\Omega_0 = \pi^2 R^2 sin^2\theta_{max} \tag{6.3}$$

$$A\Omega = A_0\Omega_0 \frac{N_{Reconstructed}}{N_{Thrown}} \tag{6.4}$$

Here, $R$ is the radius of the circle (25 km), $\theta_{max}$ is 60° (The maximum zenith angle thrown in the simulated showers), $N_{Reconstructed}$ represents the number of Monte Carlo events that reconstruct and pass cuts, and $N_{Thrown}$ represents the number of events that were thrown (generated) in the set.

The aperture is calculated for each bin of $1/10^{th}$ energy decade by multiplying it by the ratio of successfully reconstructed events to the number of thrown events. Figure 6.2 shows the calculated aperture as a function of energy for the MD detector assuming proton

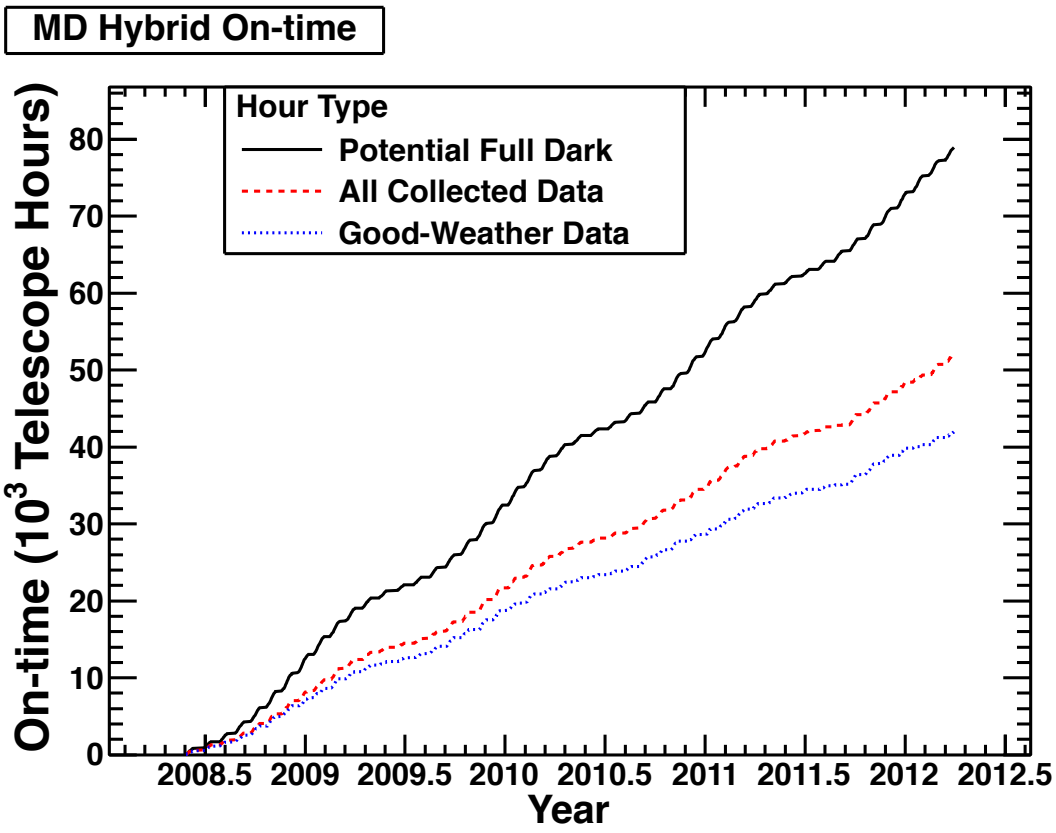


**Figure 6.1**. Middle Drum hybrid on-time: the solid line indicates an integration of all hours when there is no sun and no moon. However, we only collect data on nights with a minimum of three hours with no sun and no moon. Furthermore, if the weather is really bad, such as raining or lightning, no data are taken. The dashed line indicates the integrated data collected. After cuts are made for clouds, the dotted line indicates good weather data.

**Table 6.2**. Aperture calculation for showers initiated by proton primary particles: the number of events thrown and reconstructed are given for each energy bin, as well as the calculated aperture.

| Energy Bin Center $\log_{10}$(E) eV | # Events Thrown | # Events Reconstructed | Aperture $\log_{10}(A\Omega)$ $m^2$ |
|---|---|---|---|
| 17.65 | 3665546 | 3 | 3.85 |
| 17.75 | 5014172 | 34 | 5.12 |
| 17.85 | 2992583 | 181 | 6.07 |
| 17.95 | 1786624 | 520 | 6.76 |
| 18.05 | 1065814 | 905 | 7.22 |
| 18.15 | 634899 | 1436 | 7.65 |
| 18.25 | 378793 | 1605 | 7.92 |
| 18.35 | 225568 | 1441 | 8.10 |
| 18.45 | 134395 | 1189 | 8.24 |
| 18.55 | 80128 | 973 | 8.38 |
| 18.65 | 47646 | 709 | 8.46 |
| 18.75 | 28345 | 563 | 8.54 |
| 18.85 | 16897 | 448 | 8.63 |
| 18.95 | 10227 | 332 | 8.68 |
| 19.05 | 6624 | 238 | 8.72 |
| 19.15 | 4369 | 168 | 8.75 |
| 19.25 | 2875 | 134 | 8.83 |
| 19.35 | 1878 | 68 | 8.72 |
| 19.45 | 1237 | 62 | 8.87 |
| 19.55 | 827 | 47 | 8.91 |
| 19.65 | 543 | 29 | 8.89 |
| 19.75 | 350 | 23 | 8.96 |
| 19.85 | 243 | 14 | 8.96 |
| 19.95 | 154 | 4 | 8.58 |
| 20.05 | 105 | 2 | 8.49 |
| 20.15 | 64 | 1 | 8.36 |
| 20.25 | 44 | 3 | 9.01 |

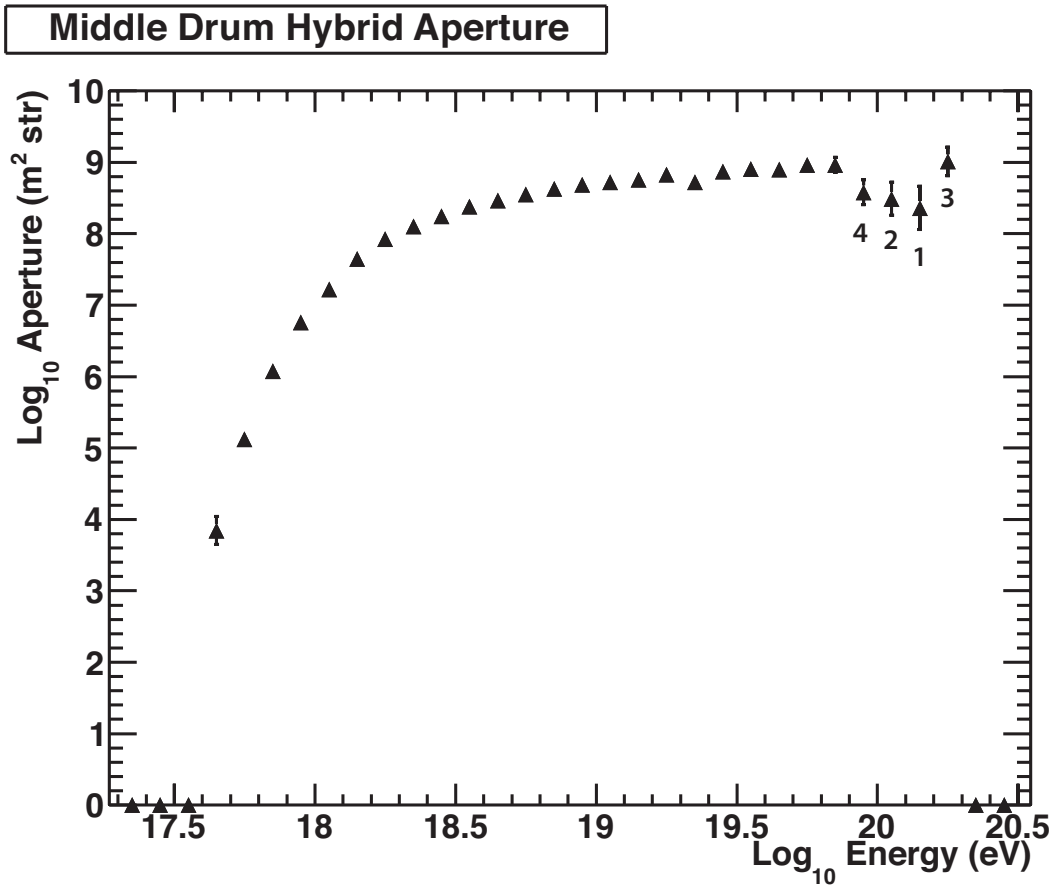


**Figure 6.2**. Middle Drum hybrid aperture for simulated showers initiated by a proton primary: It ramps up with energy and flattens out at about $10^{8.5}$ m$^2$ steradians. The numbers below the data points indicate the number of reconstructed Monte Carlo events in those bins.

primaries. This aperture is used for the final spectrum calculation because independent analyses indicate that the initial cosmic ray particles are light, or proton-like (see Chapter 7). The exposure for each energy bin is then calculated by multiplying the aperture in each bin by the number of on-time seconds for the detector (see Figure 6.1).

### 6.2.1 Reconstruction Bias Correction

Any bias in the energy reconstruction of the Monte Carlo must be accounted for in the data. In this context, bias refers to a systematic shift in the reconstructed energy of an event from its true energy, as observed in the Monte Carlo data set. There are many possible reasons for a small bias in this result, including an inexact assumption of the shower speed. Figure 6.3 shows the mean energy reconstruction bias as a function of energy. In the lower energy range, the bias is clearly larger than in the higher energy range. A two line fit was done to account for this difference. A constant energy reconstruction bias of +4.4% was calculated in the range of energy between $10^{18.0}$ to $10^{18.5}$ eV, and a constant bias of +2.8% in the range of energy greater than $10^{18.5}$ eV. Before the spectrum is calculated, a correction for these biases is applied. For events which reconstruct with energies $< 10^{18.5}$ eV, the reconstructed energy is multiplied by a factor of 0.956 to account for the 4.4% bias (the solid line in the figure). For events which reconstruct with energies $\geq 10^{18.5}$ eV, the reconstructed energy is multiplied by a factor of 0.972 to account for the 2.8% bias (the dashed line in the figure). The corrected energies are used in the final spectrum calculation.

### 6.2.2 Ratio Correction

Section 4.2.1 described the energy scale difference between the CORSIKA energies and the Fluorescence Detector (FD) energies. In this section, the initial attempt at accounting for this problem is examined. Figure 6.4a shows the trigger aperture of SDs using the CORSIKA energies compared to the FD energies. As expected, the aperture curve, and in particular, the threshold rise, is shifted to lower energies. The ratio, $R_{corr}$, of the apertures is shown in Figure 6.4b. Note that in the lowest energy bins after cuts ($10^{18.45}$ eV), the aperture grows by $\sim$25% due to the Corsika/FD energy correction.

A preliminary study used the ratio, $R_{corr}$ to see how the trigger threshold affected the hybrid spectrum. The hybrid aperture for each energy bin was corrected using equation 6.5.

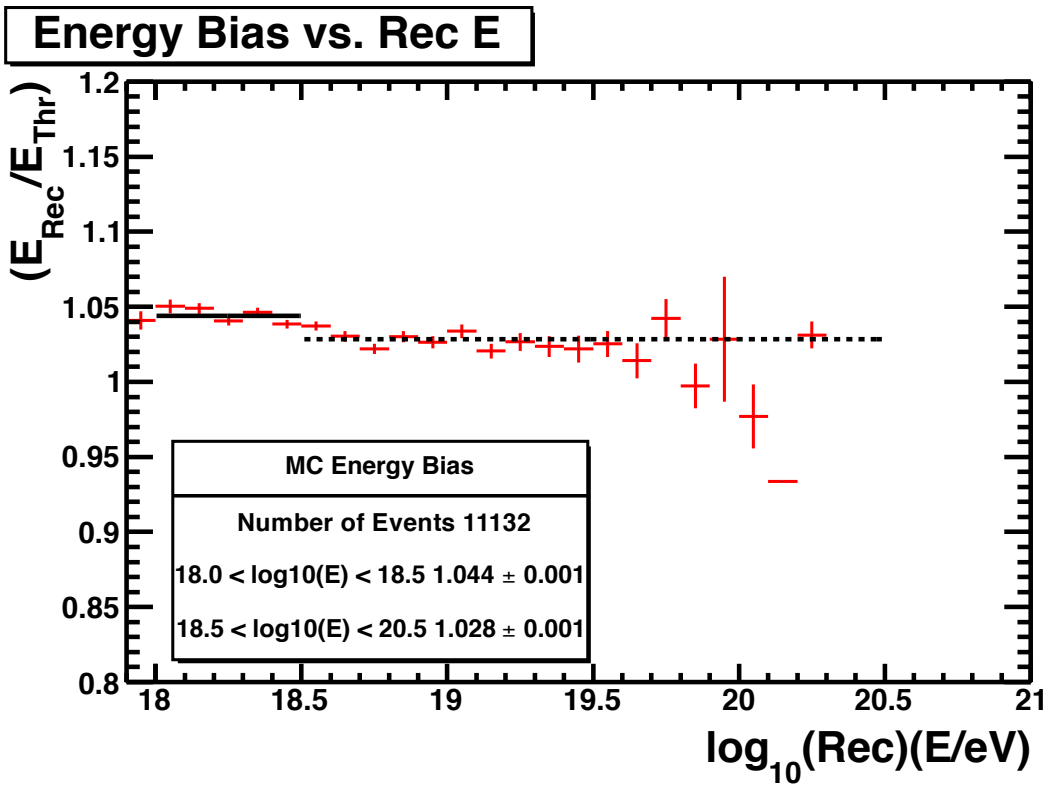


**Figure 6.3**. Mean energy reconstruction bias as a function of energy: above $10^{18.0}$ eV, the hybrid energy resolution is very good. The solid line shows a fit to the bias for $10^{18.0} <$ E $< 10^{18.5}$ eV, while the dashed line shows a fit to the bias for E $> 10^{18.5}$ eV. Two bias constants of +4.4% and +2.8%, respectively, were determined by the fits.

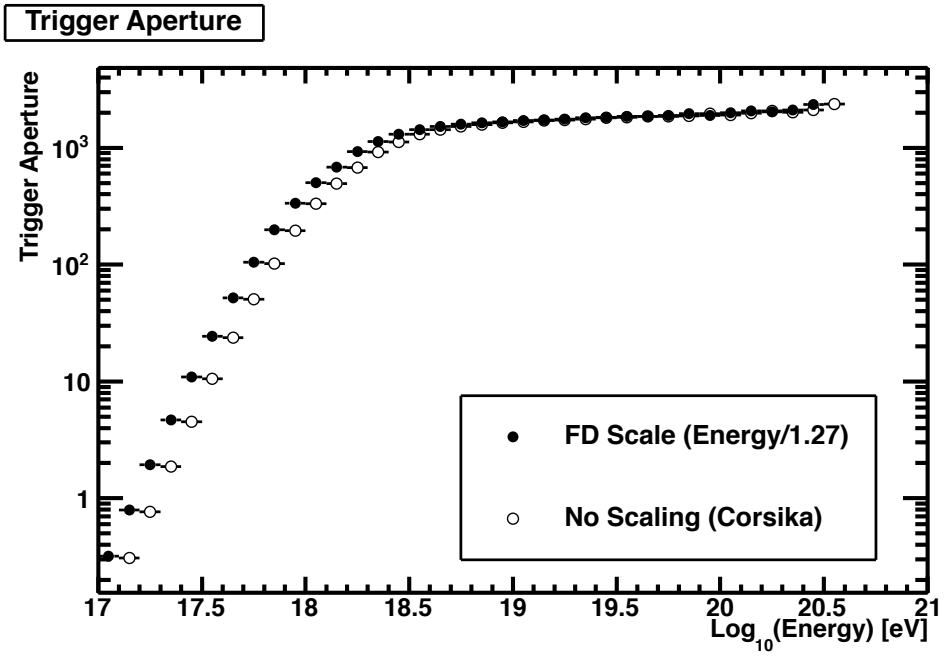


(a)

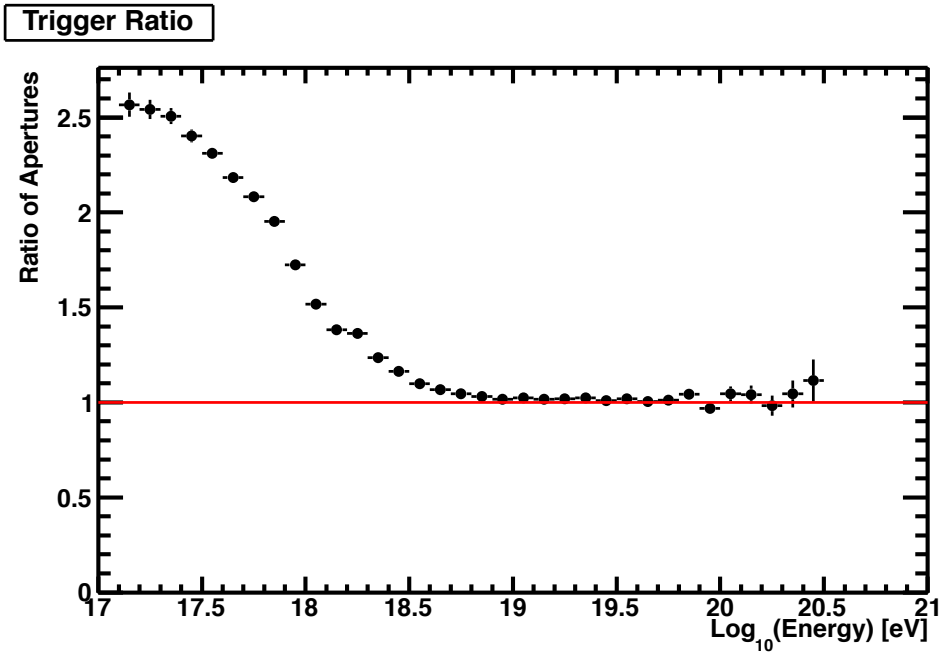


(b)

**Figure 6.4**. Shown is the aperture from the CORSIKA energy compared with the Fluorescence Detector (FD) energy. In (a), the apertures are shown separately, and the increase in aperture in the lower bins is expected because the fluorescence energy is 27% lower than the CORSIKA energy. Shown in (b) is the ratio of the apertures from the CORSIKA energy to the FD energy.

$$A\Omega = \pi^2 R^2 sin^2\theta_{max} \frac{N_{Reconstructed}}{N_{Thrown}} \times R_{corr} \tag{6.5}$$

Again, the $R_{corr}$ is the number taken from Figure 6.4b. Figure 6.5 shows the change in the aperture using this modification compared with the aperture using no modification, as well as the new aperture calculated after throwing a new Monte Carlo set, described in Section 4.2.1. Note that the ratio corrected aperture and that from the new Monte Carlo are in excellent agreement, whereas a discernible difference is seen in the uncorrected points (squares).

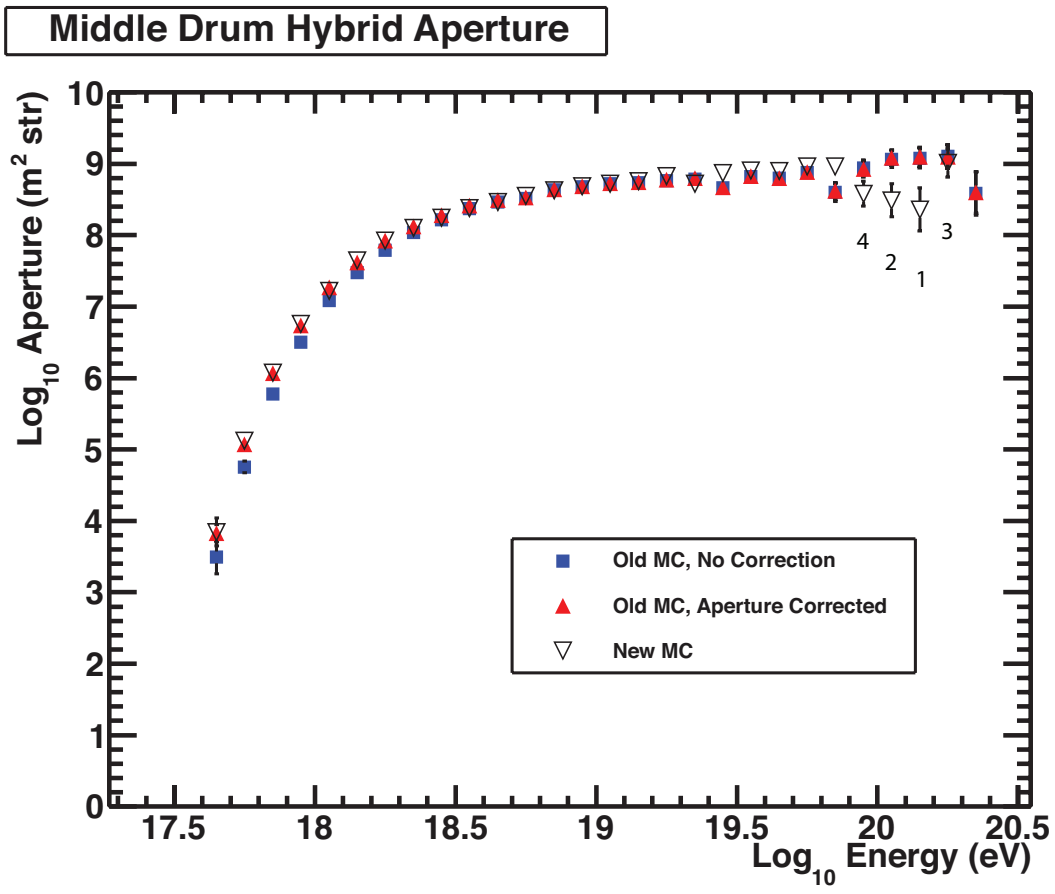


**Figure 6.5**. The Middle Drum hybrid aperture: shown are the apertures from the proton Monte Carlo (MC) set using no correction, the ratio correction to the aperture, and a new MC set with the trigger efficiency folded in. Note that the ratio corrected aperture agrees very well with the new MC set. The numbers below the bins indicate the number of reconstructed events in the new MC set. Before the new MC set was thrown, the ratio corrected aperture was used to generate the hybrid energy spectrum at an intermediate stage. The final spectrum for this analysis was calculated using the new MC.

## 6.3 Result

The Middle Drum hybrid energy spectrum was calculated using three years of data, between May 11, 2008 (Surface Detector turn on) and July 9, 2011. There were 1282 triggered events in the data set. After all the cuts were applied, the final data set has 731 events with reconstructed energies above $10^{18}$ eV. The final spectrum for this analysis has a lower boundary at $10^{18.4}$ eV and includes 349 events. The raw energy distribution of these events is summarized in Table 6.3 and is also shown in Figure 6.6. Note that the highest energy event has a reconstructed energy of $1.32\times10^{20}$ eV. This event was not used in the Surface Detector monocular spectrum because it reconstructed with a zenith angle of 55.7°, and events with zenith angle >45° were cut from the analysis due to poor SD reconstruction of these events.

Figure 6.7 shows the differential flux versus energy for the Middle Drum hybrid events. Due to the geometric limitations of collecting data in hybrid mode, the statistics for this spectrum are relatively small. However, the systematics and resolutions are the best in the Telescope Array experiment (see Section 4.2.2). As described in detail in Chapter 5, much of the code sets used to reconstruct these data were used in previous experiments, and have been in continuous use for 15 years. Combining these stable programs with the new hybrid technique provided me with proven reliability in my result.

The MD hybrid analysis plays an important role in connecting the measurements of the High Resolution Fly's Eye (HiRes) experiment to the Telescope Array experiment. The MD monocular spectrum [10] provided the retrograde link between the TA and HiRes spectra, and my hybrid analysis takes this link a step further by creating a direct connection between the Middle Drum detector and the Surface Detector array. For this purpose, comparisons with other TA analyses are discussed in the next section.

### 6.3.1 Comparison with other Telescope Array Analyses

The MD monocular spectrum has been shown to agree with the HiRes spectrum [38]. The MD monocular spectrum was created using the exact same reconstruction as the HiRes data. In particular, the energy deposited by an Extensive Air Shower (EAS) was calculated using simulation studies done by M. Hillas in [26, 27]. The two spectra are in good agreement. After the HiRes spectra were published, however, a new study was done by F. Nerling, to calculate the same parameters more accurately using CORSIKA [35] simulations. Both the Pierre Auger Observatory (PAO) and the Telescope Array FD

**Table 6.3**. The number of data events per energy bin, after cuts, used in the spectrum calculation are given.

| Energy Bin Center $log_{10}$ (E) eV | # Data Events |
|---|---|
| 18.45 | 86 |
| 18.55 | 63 |
| 18.65 | 48 |
| 18.75 | 32 |
| 18.85 | 35 |
| 18.95 | 27 |
| 19.05 | 24 |
| 19.15 | 9 |
| 19.25 | 10 |
| 19.35 | 8 |
| 19.45 | 3 |
| 19.55 | 2 |
| 19.65 | 0 |
| 19.75 | 1 |
| 19.85 | 0 |
| 19.95 | 0 |
| 20.05 | 0 |
| 20.15 | 1 |

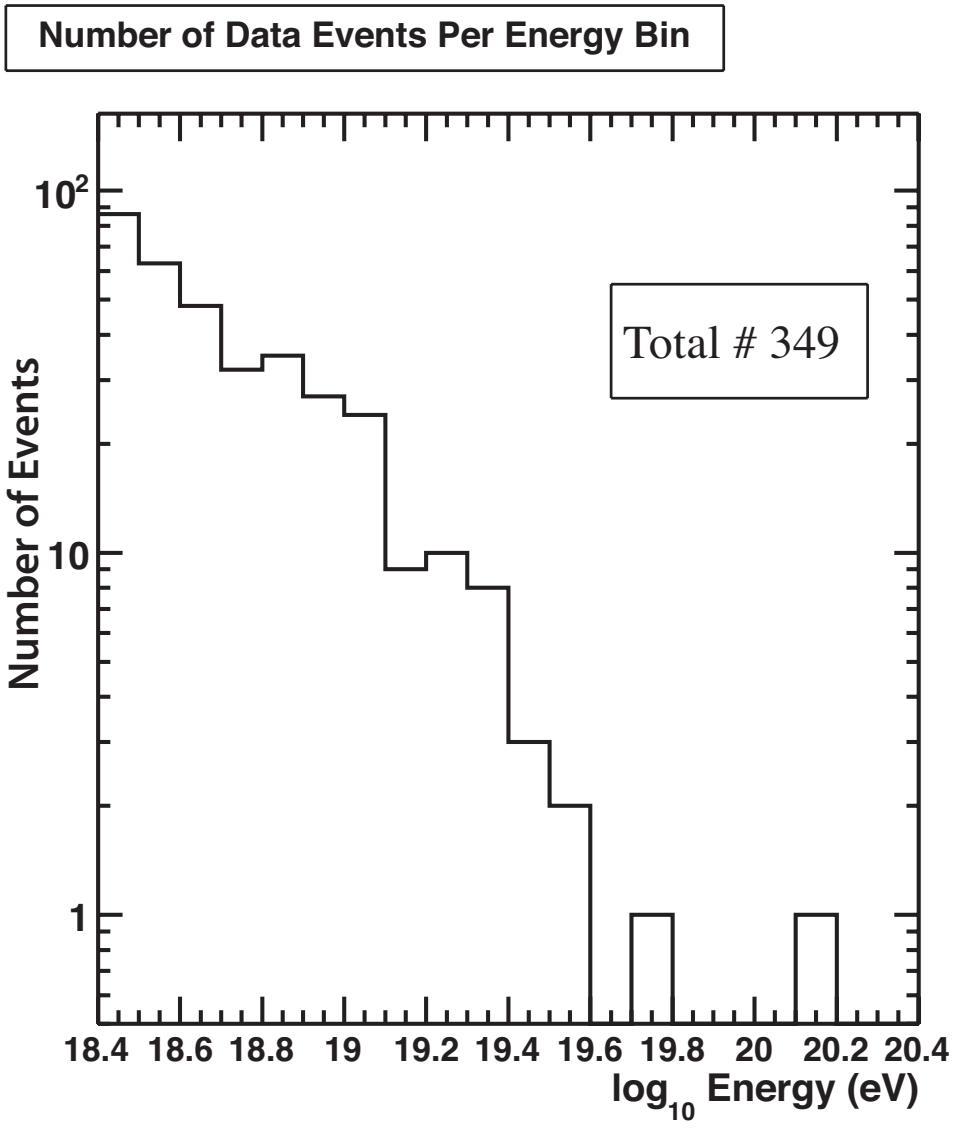


**Figure 6.6**. The raw energy distribution of events passing all quality cuts observed in hybrid mode by the Middle Drum telescope site: the events are binned in energy and total 349 that were used for the MD hybrid spectrum.

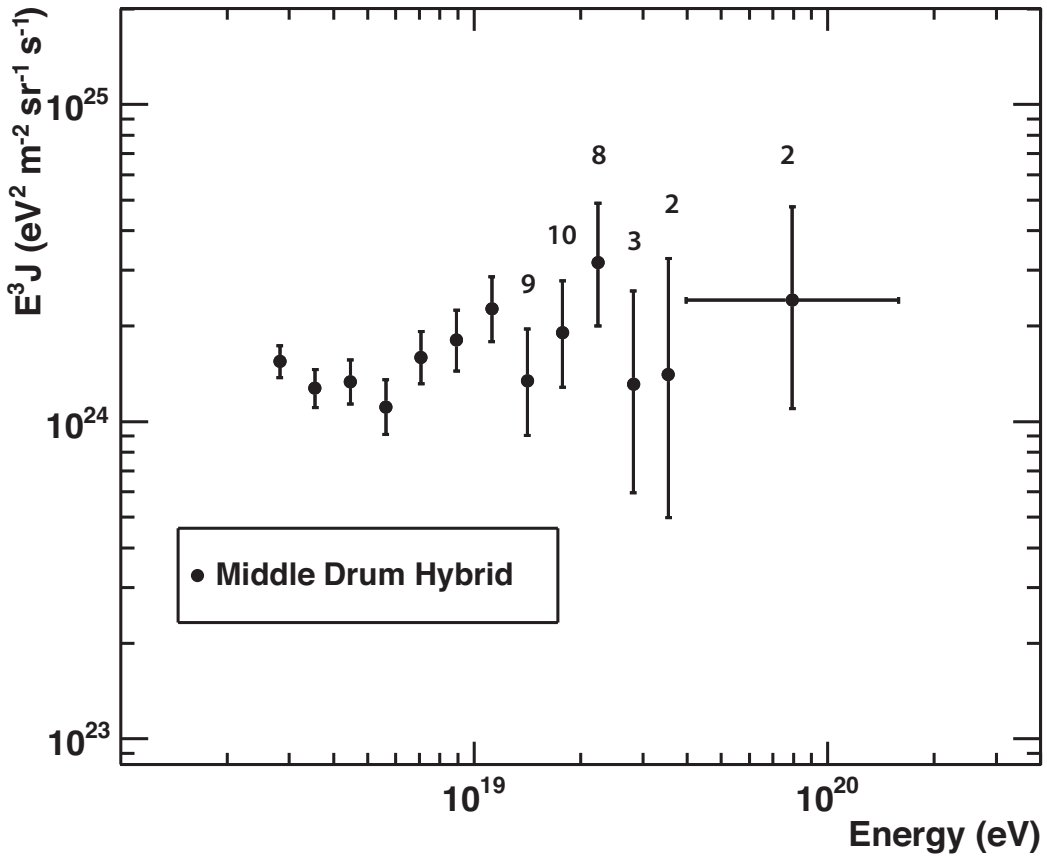


**Figure 6.7**. Middle Drum hybrid energy spectrum: shown is the differential flux of ultra high energy cosmic rays versus energy. The flux has been multiplied by a factor of $E^3$ to take out the steep slope of the overall spectrum and better show the fine structure. The numbers above the data points indicate the number of observed events in those bins. Note that the top six energy bins in Figure 6.7 have been combined due to small statistics. Only two events were observed in hybrid mode with energies $> 10^{19.6}$ eV.

analyses are now using the new parametrizations. My hybrid analysis also uses the new formulas.

An event-by-event study was performed on the MD monocular spectrum data calculated using the Hillas formulas in comparison with my hybrid analysis (using the Nerling formulas) to assess any bias created when changing the energy deposition method. Figure 6.8 shows each event plotted as the MD hybrid reconstructed energy vs MD monocular Hillas reconstructed energy. The solid line in the figure is the fit to the data, while the dashed line is the 1:1 line. The two lines are nearly indistinguishable, indicating that there is negligible bias in the difference in the event energies. Furthermore, Figure 6.9 shows a histogram of the log ratio of the MD monocular Hillas reconstructed energy over the MD hybrid reconstructed energy. Again, no bias is seen.

Figure 6.10 shows the comparison between the MD monocular spectrum using the Hillas formulas and my MD hybrid analysis, along with the HiRes-1 and -2 spectra. Note that there are three points in the low end of the spectrum which differ significantly between my hybrid analysis and the MD monocular spectra which dominate the $\chi^2$ calculation. Even so, the spectra are in reasonable agreement. This allows for a direct comparison between my hybrid Nerling reconstruction and the Hillas reconstruction in the HiRes spectra. As shown in the figure, my MD hybrid spectrum agrees with both of the HiRes spectra. And in fact, in the $10^{18.5} - 10^{18.7}$ eV range, my hybrid spectrum agrees better with HiRes than the Middle Drum monocular analysis.

The next step in linking the HiRes spectrum to the Telescope Array is a comparison between the Middle Drum hybrid energy spectrum and the TA Surface Detector. This is shown in Figure 6.11. They are in good agreement, and establish a starting point for comparison with TA spectra as the experiment moves forward.

For each comparison, a $\chi^2$ test was performed to see how well the spectra agree. The results of the comparison of my hybrid analysis with other spectra are summarized in Table 6.4 as well as on each plot. Note that a $\chi^2$ test is only appropriate when the number of events per bin is $\geq 7$. As shown in Table 6.3, the number of events per bin in the hybrid analysis drops below this limit in bins at energies $\log_{10}(E) \geq 19.4$ eV. The $\chi^2$ test was performed twice for each comparison: once using only those bins at energies $\log_{10}(E) < 19.4$ eV, and once including the two bins above that threshold. Each * in the table indicates a calculation performed including the extra two bins.

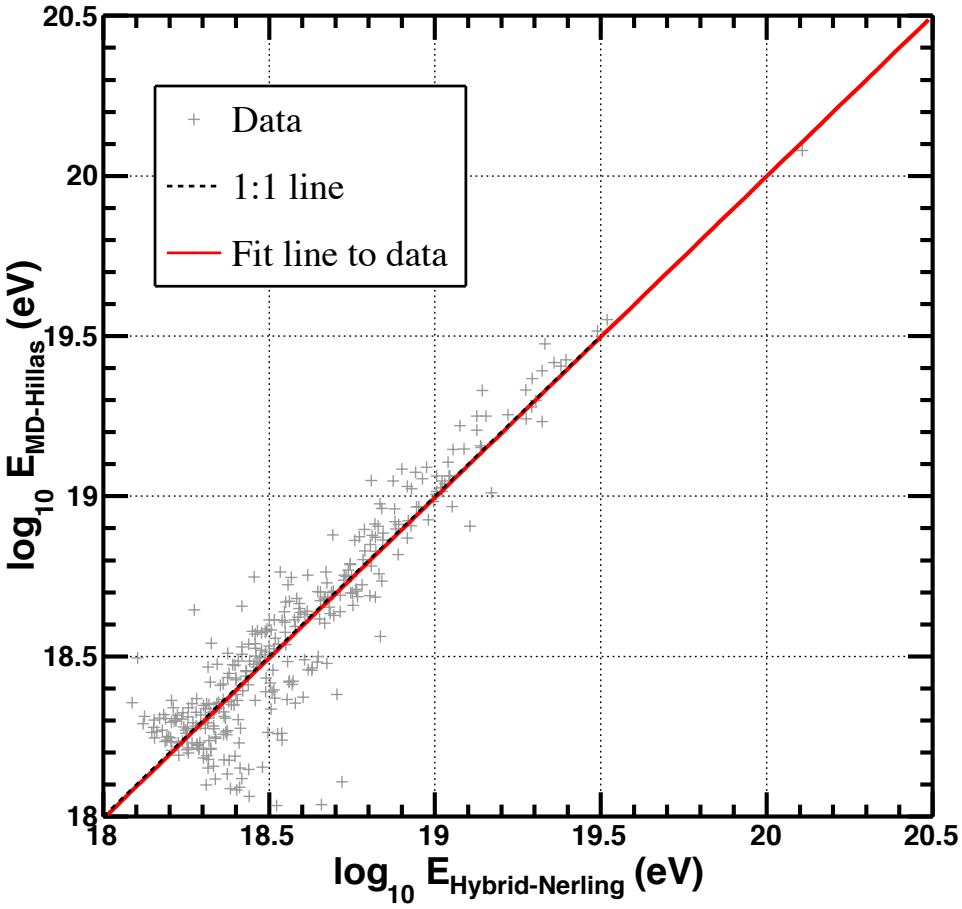


**Figure 6.8**. A scatter plot showing the an event-by-event comparison of data events reconstructed by the Middle Drum hybrid Nerling analysis (X-axis), and the Middle Drum monocular Hillas analysis (Y-axis). The solid line is a fit to the data, while the dashed line indicates the 1:1 line.

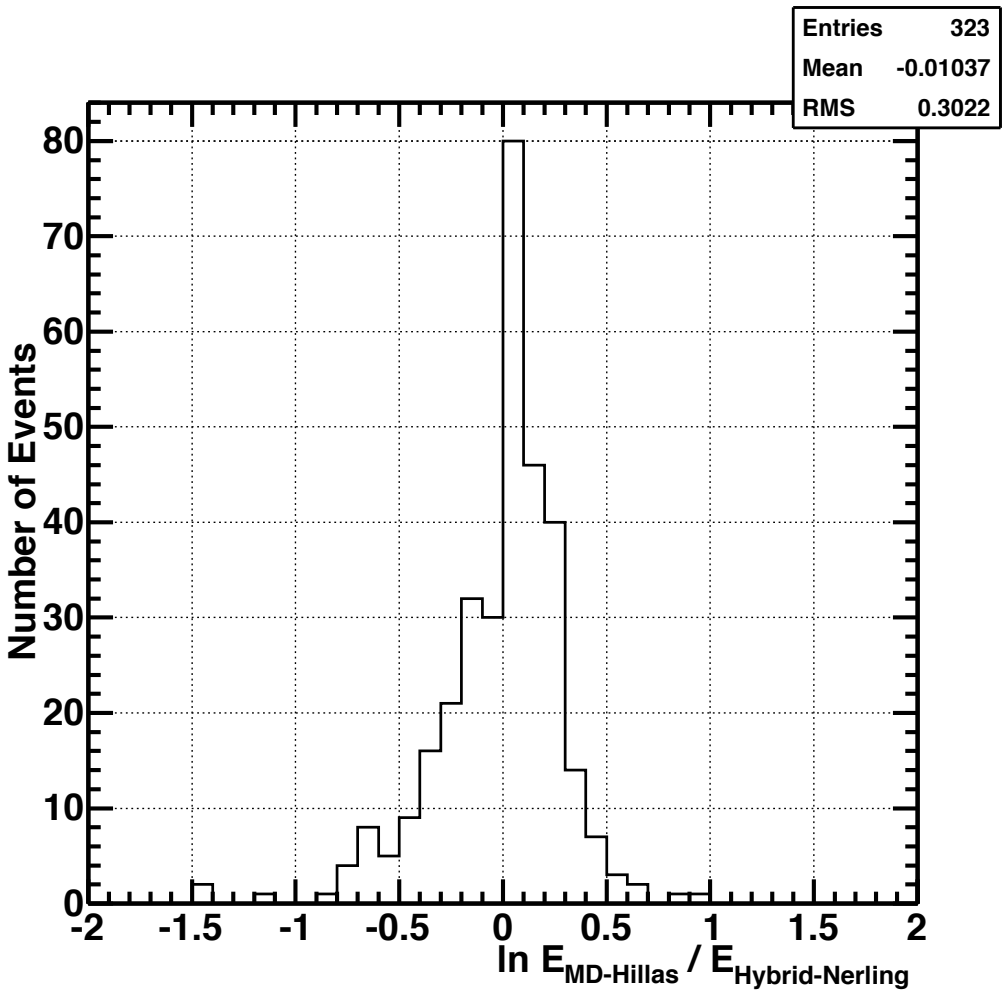


**Figure 6.9**. A histogram of the log ratio of the energies of events reconstructed by the Middle Drum monocular Hillas analysis versus the Middle Drum hybrid analysis: the width in this histogram is dominated by the resolution in the MD monocular reconstruction.

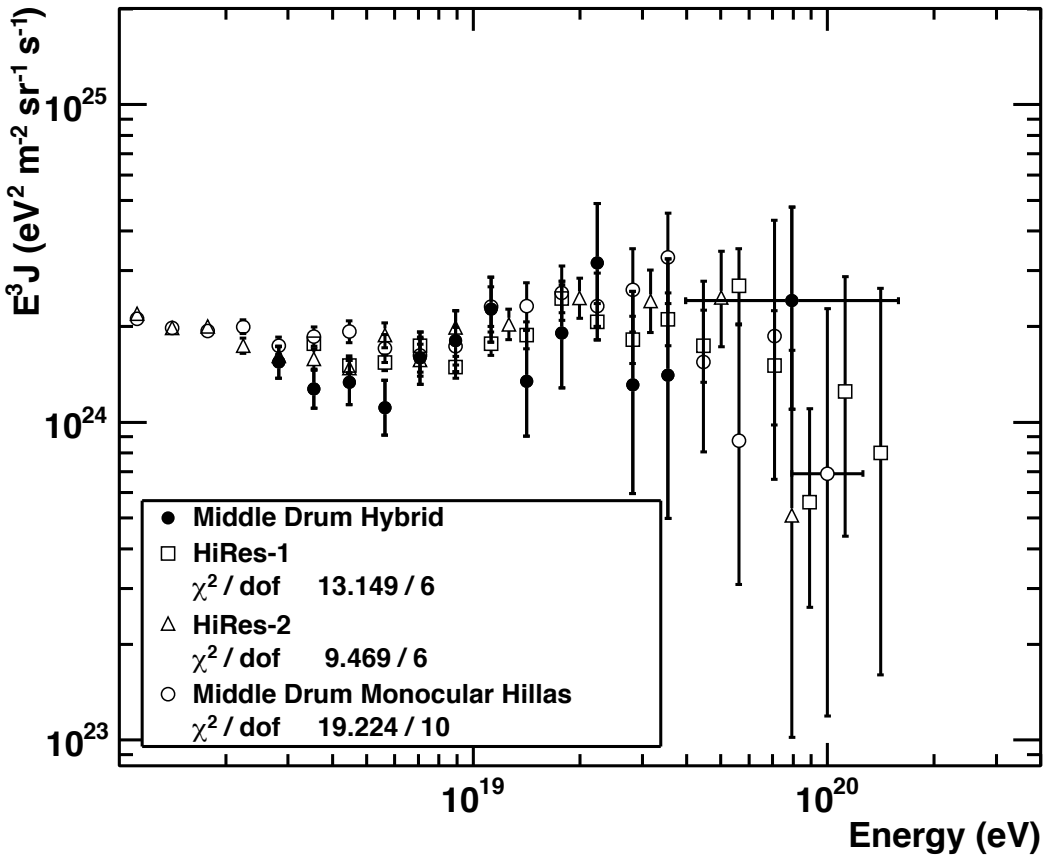


**Figure 6.10**. The Middle Drum hybrid energy spectrum (closed circles) compared with the spectrum measured by the Middle Drum detector in monocular mode, using the Hillas reconstruction (open circles), as well as the spectra measured by the HiRes-1 (open squares) and HiRes-2 (open triangles) detectors. The results of a $\chi^2$ comparison between the MD hybrid spectrum and each of the other spectra are shown in the plot.

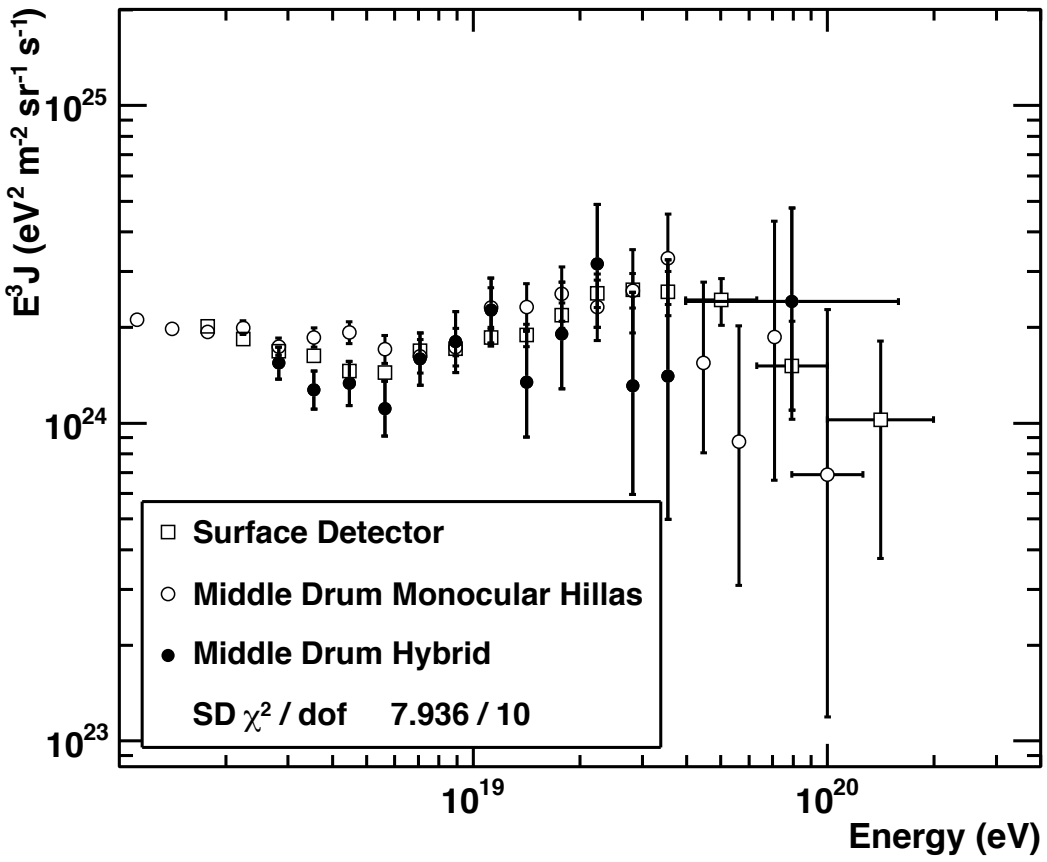


**Figure 6.11**. The Middle Drum hybrid spectrum (closed circles) compared with the spectrum measured by the surface array (open squares): the MD monocular spectrum is shown for reference. The results of a $\chi^2$ comparison between the MD hybrid spectrum and the SD spectrum is shown on the plot.

**Table 6.4**. A summary of the results of a $\chi^2$ test performed to compare four analyses with the Middle Drum hybrid analysis is given. Two comparisons were performed for each analysis: one using only bins with energy $\log_{10}(E) < 19.4$ eV, and one including the two bins above that. A * indicates comparisons with data which included the two higher bins.

| Data | Lower (E) bound $\log_{10}(E)$ eV | Upper (E) bound $\log_{10}(E)$ eV | $\chi^2$ | # Degrees of Freedom |
|---|---|---|---|---|
| MD Mono | 18.4 | 19.4 | 6.019 | 10 |
| MD Mono* | 18.4 | 19.6 | 7.479 | 12 |
| SD Mono | 18.4 | 19.4 | 7.936 | 10 |
| SD Mono* | 18.4 | 19.6 | 9.322 | 12 |
| HiRes-1 | 18.5 | 19.4 | 13.149 | 9 |
| HiRes-1* | 18.5 | 19.6 | 13.438 | 11 |
| HiRes-2 | 18.4 | 19.0 | 9.469 | 6 |

# CHAPTER 7

# COMPOSITION RESULT

## 7.1 Introduction

The composition of Ultra High Energy Cosmic Ray (UHECR) particles is a subject of heated debate within the community. As discussed in Chapter 2, The High Resolution Fly's Eye Experiment (HiRes) and the Pierre Auger Observatory (PAO) have come to diverging conclusions regarding composition at the highest energies. Although the data selection described in Chapter 6 optimized the set for an energy spectrum analysis, the improved accuracy of the shower reconstruction in hybrid mode makes this analysis well-suited for a composition study. A more detailed analysis with data selection optimized for composition is anticipated from future work by the collaboration.

## 7.2 $X_{max}$ Studies

The low flux, as well as the highly penetrating nature of UHECR makes it unfeasible to study them by direct detection. Because of the large event-to-event fluctuation inherent in air shower production, the fluorescence detection technique is unable to determine the mass of any individual primary cosmic ray. Instead, the characteristics of longitudinal development of events are used to give a statistical measure of the composition. Specifically, the distribution of events are used to distinguish between showers produced by light, proton-like particles, and those produced by heavy particles, such as iron nuclei. The most important parameter in studying these trends is $X_{max}$, the slant depth of the point in the shower where the number of charged particles reaches a maximum, see equation 7.1.

$$X = \int_{\text{top of atmosphere}} \rho \, \mathrm{d}s \tag{7.1}$$

Here, $X$ is the slant depth at a given point in the shower, $\rho$ is the atmospheric density, and $s$ is height in the atmosphere. Using this equation, $X_{max}$ can be calculated by integrating from the top of the atmosphere to the shower maximum.

The $X_{max}$ parameter helps distinguish between light, proton-like and heavy, iron-like showers in two ways: (1) $<X_{max}>$, the average $X_{max}$ value: proton-induced showers tend

to penetrate further into the atmosphere and develop later, resulting in a larger $<X_{max}>$ value, than iron-induced showers of the same energy. They tend to interact sooner, and produce a much larger multiplicity of secondaries on the first interaction, resulting in a smaller $<X_{max}>$ value. The $<X_{max}>$ from the data is compared to a set of Monte Carlo (MC) using proton and a set using iron nuclei to determine which set best describes the data. (2) The distribution of the $X_{max}$ value: proton-induced showers fluctuate more, and have a smaller multiplicity of particles when making a first interaction with the atmosphere. This results in a wider distribution of $X_{max}$ values, while iron-like showers interact immediately, resulting in a narrower distribution.

The two most important composition measurements for UHECR have come from the High Resolution Fly's Eye (HiRes) experiment and the Pierre Auger Observatory (PAO). Recent composition results from these experiments are shown here for comparison with this analysis. Figure 7.1 shows the final HiRes composition measurement [5]. The figure shows that the data closely resembles the proton MC, which is also consistent with the previous results from HiRes, shown in Chapter 2. Figure 7.2 shows the width of the distribution of the $X_{max}$ value in the data compared to the same parameter in proton and iron induced MC sets [5]. The data is again consistent with the proton induced MC set.

The most recent PAO composition measurement is shown in Figure 7.3 [6]. The data in this figure start light/protonic at $\sim 10^{18}$ eV through $\sim 5 \times 10^{18}$ eV then trend toward a heavier primary particle at the highest energies. This result is also consistent with the previous PAO result, shown in Chapter 2. Figure 7.4 shows the RMS values for the width of the data distribution in comparison with proton and iron induced Monte Carlo [6]. Note that the RMS value in this figure is smaller at the higher energies, which is indicative of showers induced by heavier nuclei.

We note that while a small RMS value is more consistent with a heavy composition, such as iron, a mixed composition (some light particles, some heavy) should result in an RMS value that is larger than even the proton RMS alone. This is because combining distributions with different means would result in a wider distribution than either original width. In addition, a detection of the GZK cut-off implies that particles at the highest energies must be proton, as the interaction with the CMB which causes the cut-off is a proton interaction.

Furthermore, the most recent anisotropy measurement from the PAO claims a correlation with Active Galactic Nuclei (AGNs) at the highest energies [8]. This correlation assumes

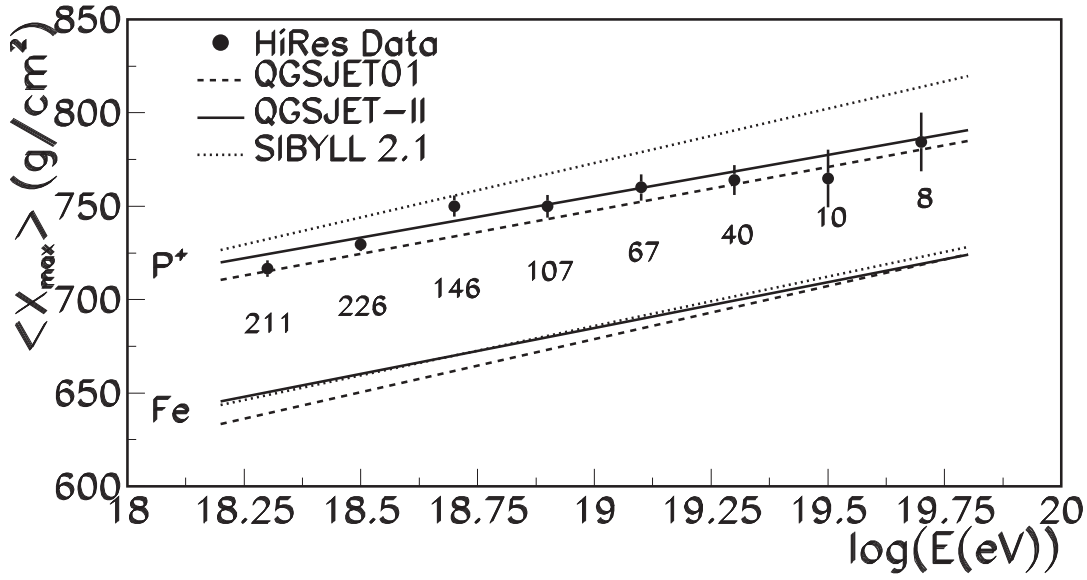


**Figure 7.1**. The HiRes stereo composition result: the $<X_{max}>$ value as a function of energy is plotted (filled circles) with several "rails" which represent different shower models for proton (top) and iron (bottom) showers. A clear agreement with the proton models is shown at energies $> 10^{18.25}$ eV. Copyright (2010) by the American Physical Society http://prl.aps.org/abstract/PRL/v104/i16/e161101.

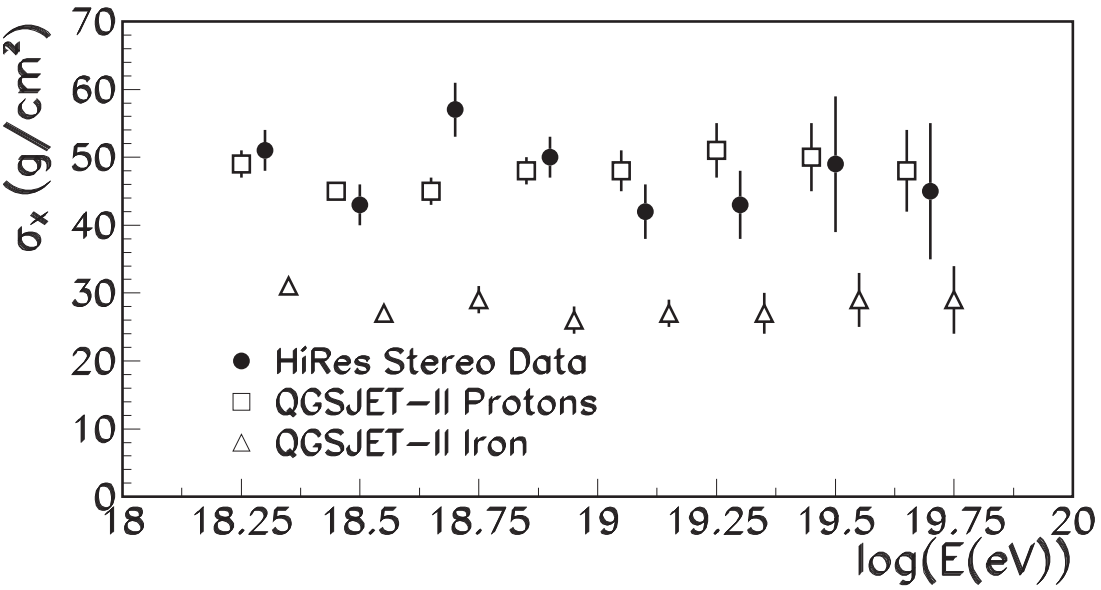


**Figure 7.2**. HiRes stereo composition result: the $X_{max}$ distribution width, $\sigma$, is plotted as a function of energy. The HiRes stereo data is compared with proton and iron data. The data is again consistent with a proton composition of cosmic rays at energies $> 10^{18.25}$ eV. Copyright (2010) by the American Physical Society http://prl.aps.org/abstract/PRL/v104/i16/e161101.

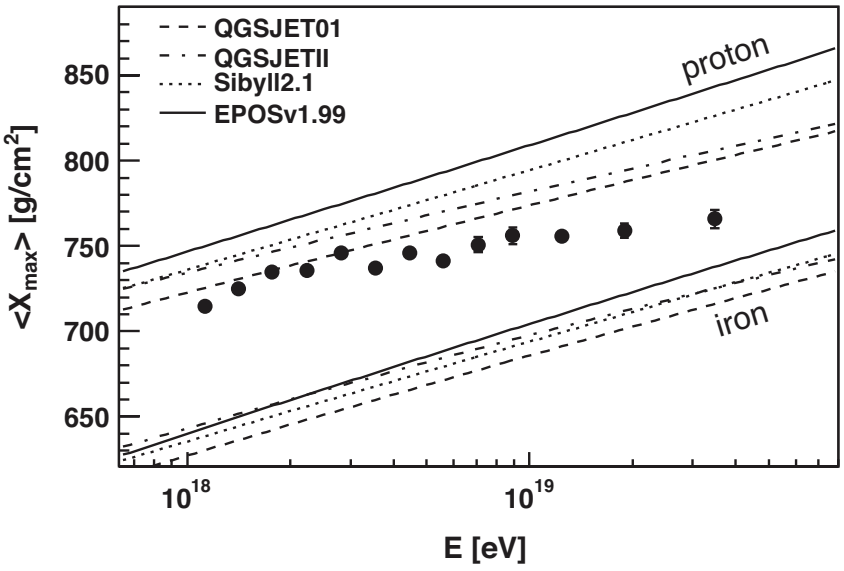


**Figure 7.3**. PAO hybrid composition result: the $<X_{max}>$ value as a function of energy is plotted with several "rails" which represent different shower models for proton (top) and iron (bottom) showers. The data starts light/protonic around $10^{18}$ eV, and then indicates a transition to heavier composition from $5\times10^{18}$ to $3\times10^{19}$ eV. Copyright (2010) by the American Physical Society http://prl.aps.org/abstract/PRL/v104/i9/e091101.

that the UHECRs are light, since heavier nuclei would be bent in the galactic/extragalactic magnetic fields. The overall picture created by the PAO is therefore self-inconsistent.

The hybrid analysis in this dissertation only includes events in which the shower maximum is within the field of view of the Middle Drum detector, the same selection cuts used in the HiRes stereo study. This means that the profile fit will be more accurate, including a more accurate measurement of shower maximum, $X_{max}$, and reconstruction of the energy. For this analysis, a data set ranging from May 11, 2008 to Sep 7, 2011 was used. Using only events which pass cuts (see Chapter 6), and have energies $\geq 10^{18.0}$ eV, the set contains 743 events. The proton induced MC shower set used for this study was produced for the energy spectrum calculation and was described in Chapter 4. However, as an iron nuclei-induced MC shower set was also required, it will be described here.

## 7.3 Iron Monte Carlo Set

Composition studies from TA require the use of a Monte Carlo (MC) set thrown with iron nuclei to supplement the proton set. The iron MC set was thrown in the same manner as the proton MC. The only difference is the primary particle (see Chapter 4 for details).

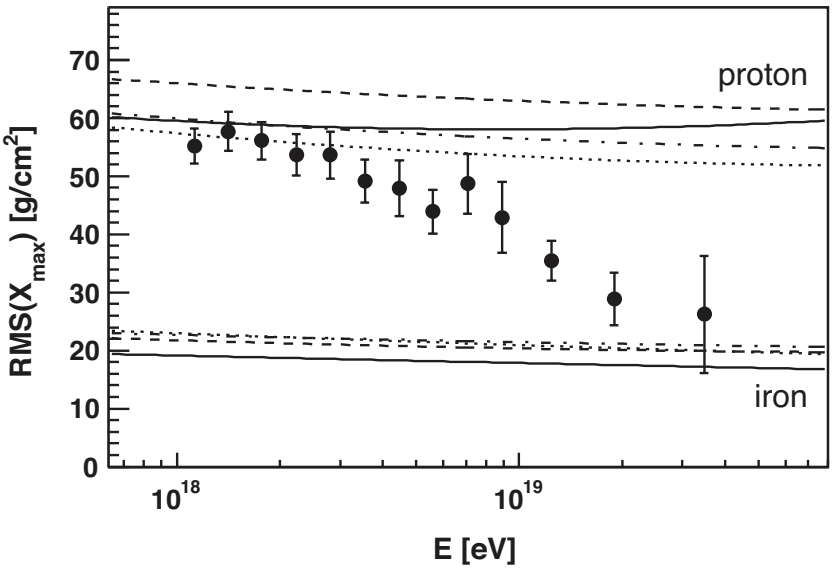


**Figure 7.4**. PAO hybrid composition result: the $X_{max}$ distribution width, RMS, is plotted as a function of energy. The "rails" again represent different shower models. The composition again appears to transition from light to heavy. Copyright (2010) by the American Physical Society http://prl.aps.org/abstract/PRL/v104/i9/e091101.

Figures 7.5a and 7.5b show the resolutions, or difference between thrown and reconstructed values in the MC. Note that they are comparable to the proton resolutions. Figures 7.6 and 7.7 show the data/MC comparisons for the impact parameter ($R_P$) of the iron MC set. Figures 7.8 and 7.9 show the data/MC comparisons for the zenith angle ($\Theta$) for the iron MC set. The results of a Kolmogorov-Smirnov (K-S) test are shown for each comparison, and indicate that in all cases, the data in fact agree rather poorly with the iron MC.

## 7.4 Composition Results

This analysis uses the MC iron set described in the previous section and the MC proton set that was described in Section 4.2. The proton Monte Carlo set triggered 18,447 events in hybrid mode. After quality cuts, 11,761 events remained. The iron Monte Carlo set triggered 25,523 events in hybrid mode. With cuts, 18,202 events were kept. Figures 7.10a and 7.10b show the $X_{max}$ distribution for the proton and iron Monte Carlo sets, respectively. The mean $X_{max}$ value for the proton set is 741.7 g/cm$^2$, significantly higher than the mean of the iron set, 678.8 g/cm$^2$. Note that the mean $X_{max}$ for the proton data is deeper and that the width of the proton distribution is significantly wider. Furthermore, there is significant overlap between the two distributions. These two factors make event-by-event

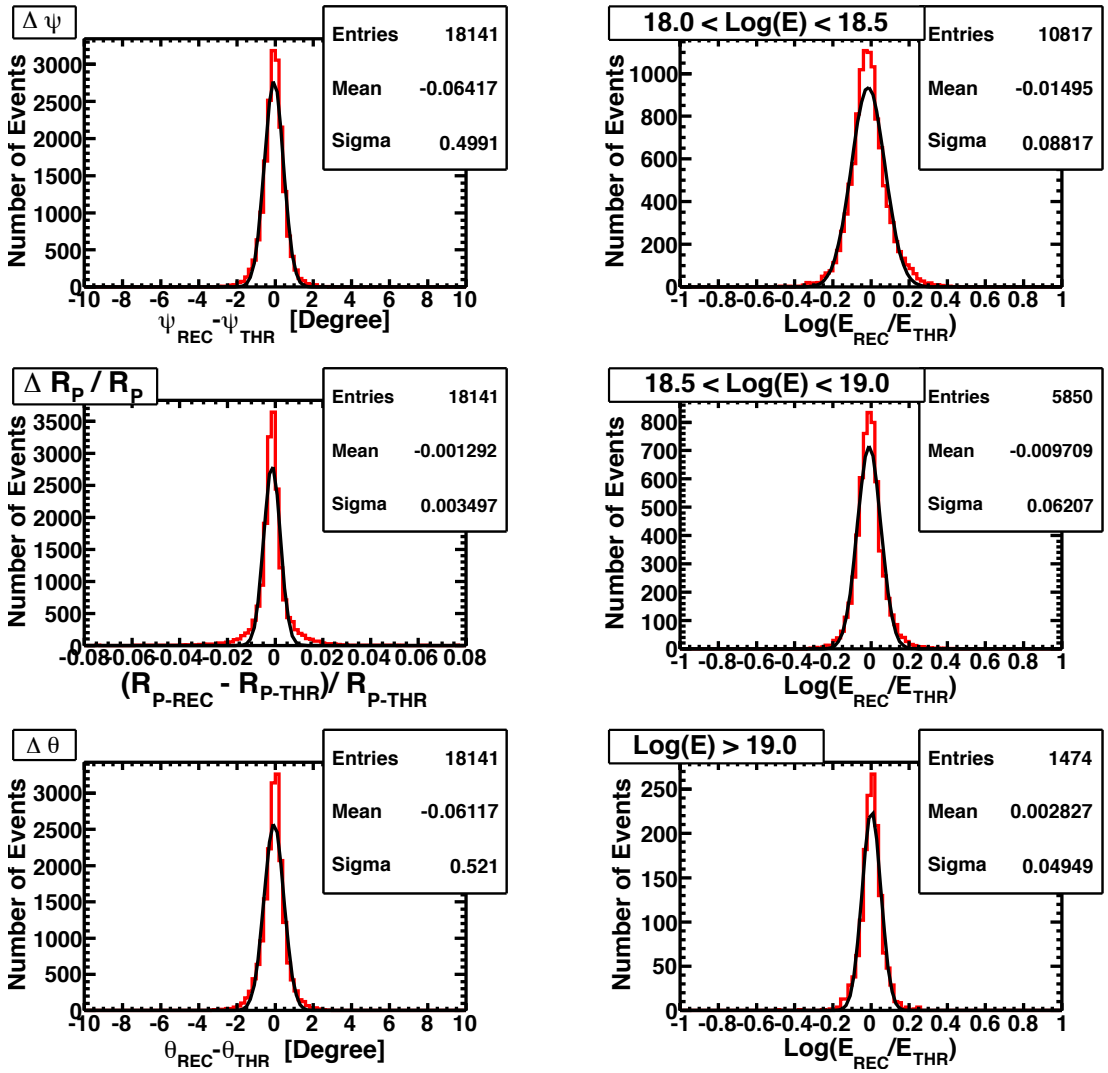


(a) (b)

**Figure 7.5**. Resolution plots are shown for the iron Monte Carlo geometry and energy resolutions. (a) geometry resolutions: Middle Drum hybrid in-plane angle ($\Psi$), (top), impact parameter ($R_P$), (middle), and zenith angle ($\Theta$) (bottom). The (red) histogram shows the difference between the reconstructed and thrown values for each event, or in the case of the impact parameter, the normalized difference. The black line is a Gaussian fit to the histogram. (b) energy resolutions: Events broken up into energy ranges: $10^{18}$ < E < $10^{18.5}$ eV (top), $10^{18.5}$ < E < $10^{19.0}$ eV (middle), and E > $10^{19.0}$ eV (bottom). The histogram (red) shows the log of the ratio of the reconstructed and thrown energy for each event set. The black line is a Gaussian fit to the histogram.

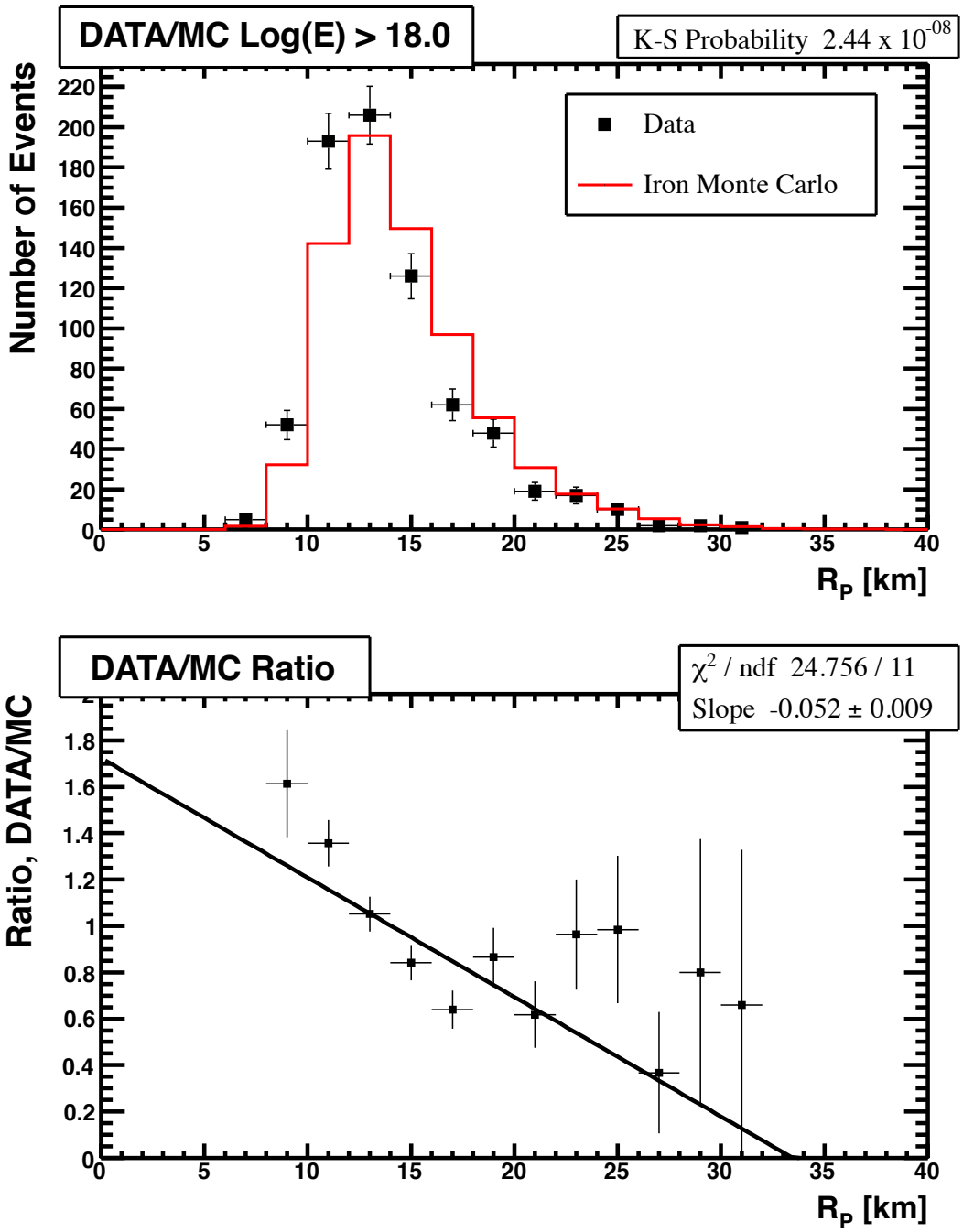


**Figure 7.6**. Data/iron MC comparison: shown is the comparison for the Middle Drum hybrid impact parameter ($R_P$). Above: The distribution of measurements is shown for the data (black points with error bars) and Monte Carlo (MC) (histogram). The MC has been normalized to the area of the data. Below: the ratio of the data to the MC. The line is a linear fit to the points. The K-S value here indicates that the data and MC are in poor agreement.

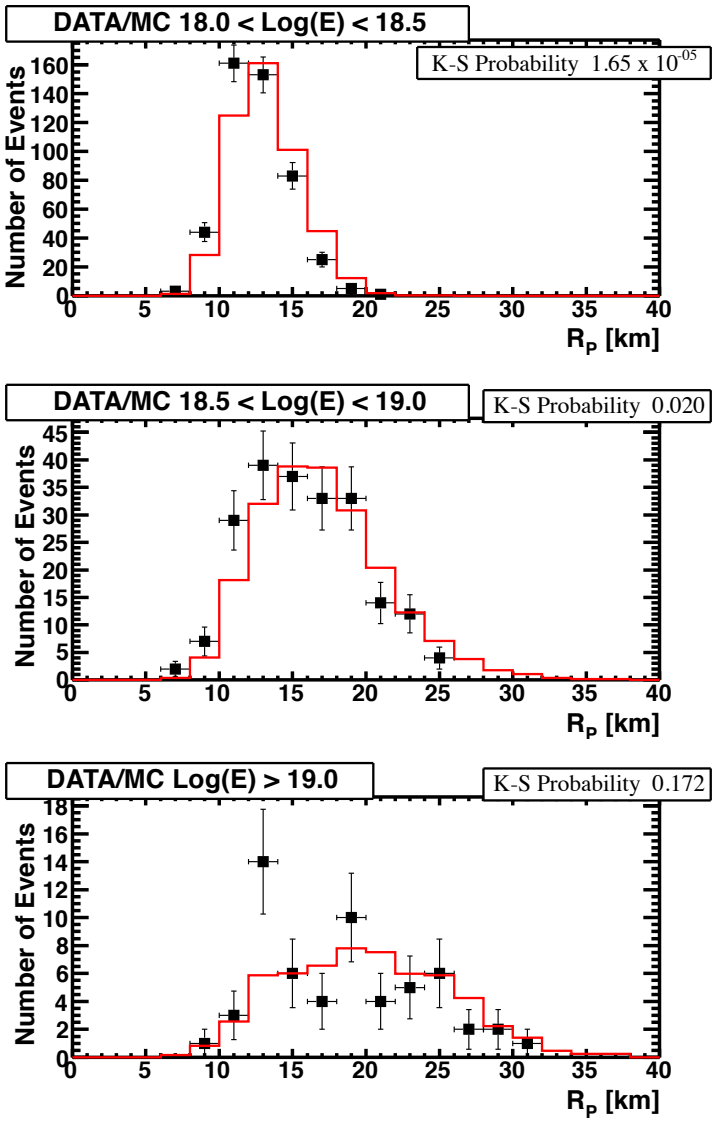


**Figure 7.7**. Data/iron MC comparison: Middle Drum hybrid impact parameter ($R_P$) is shown in three energy ranges: top to bottom, $10^{18.0}$ < E < $10^{18.5}$ eV, $10^{18.5}$ < E < $10^{19.0}$ eV, and E > $10^{19.0}$ eV, respectively, to show the evolution of this parameter with energy. The distribution of measurements is shown for the data (black points with error bars) and Monte Carlo (MC) (histogram). The MC has been normalized to the area of the data in these plots. Again, the K-S values indicate poor agreement in the lower energy ranges. In the highest energy range, while it appears that the data and MC agree more closely, the statistics here are poor.

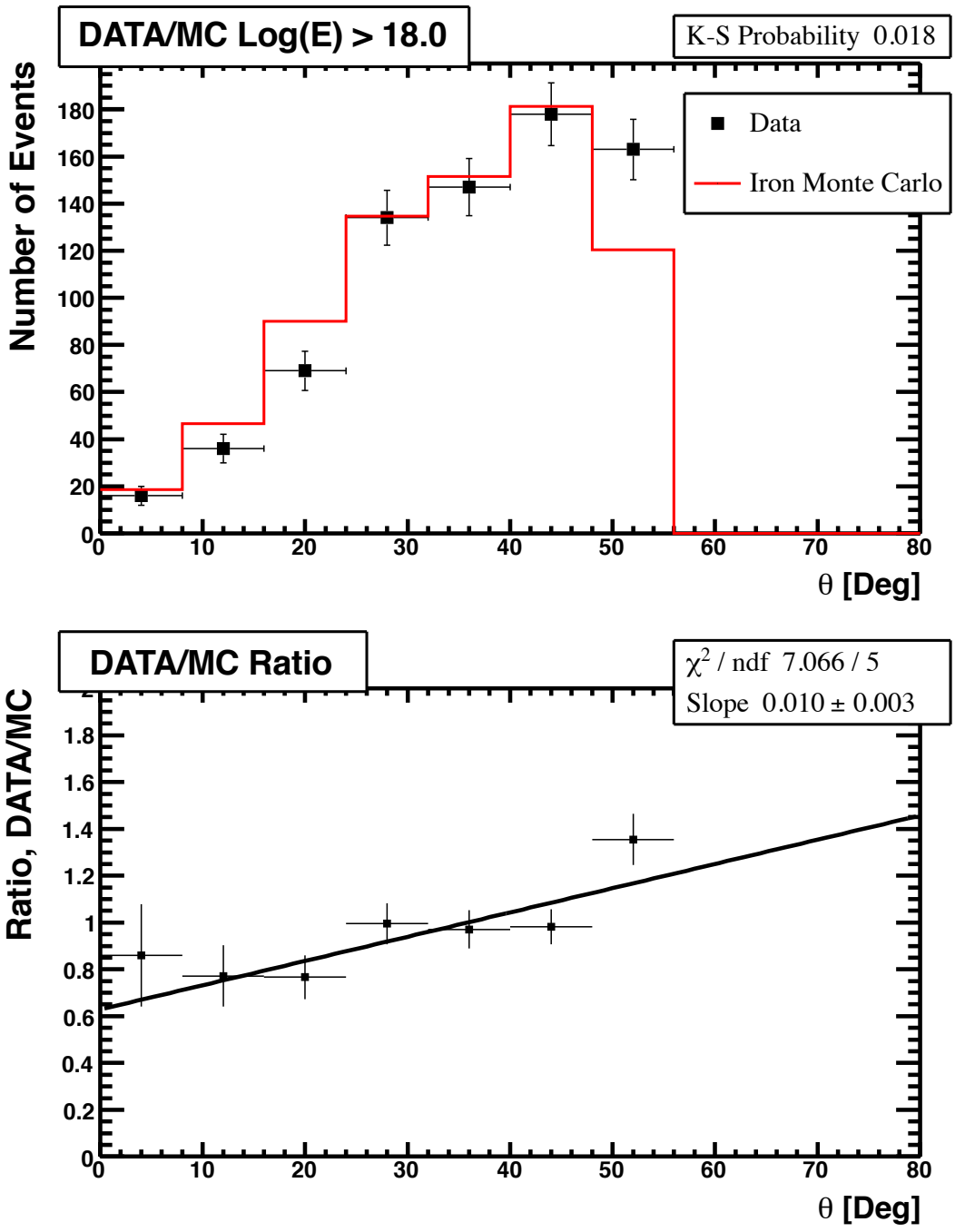


**Figure 7.8**. Data/iron MC comparison: shown is the comparison for the Middle Drum hybrid zenith angle ($\theta$). Above: The distribution of measurements is shown for the data (black points with error bars) and Monte Carlo (MC) (histogram). The MC has been normalized to the area of the data. Below: the ratio of the data to the MC. The line is a linear fit to the points.The K-S value here indicates that the data and MC are in poor agreement.

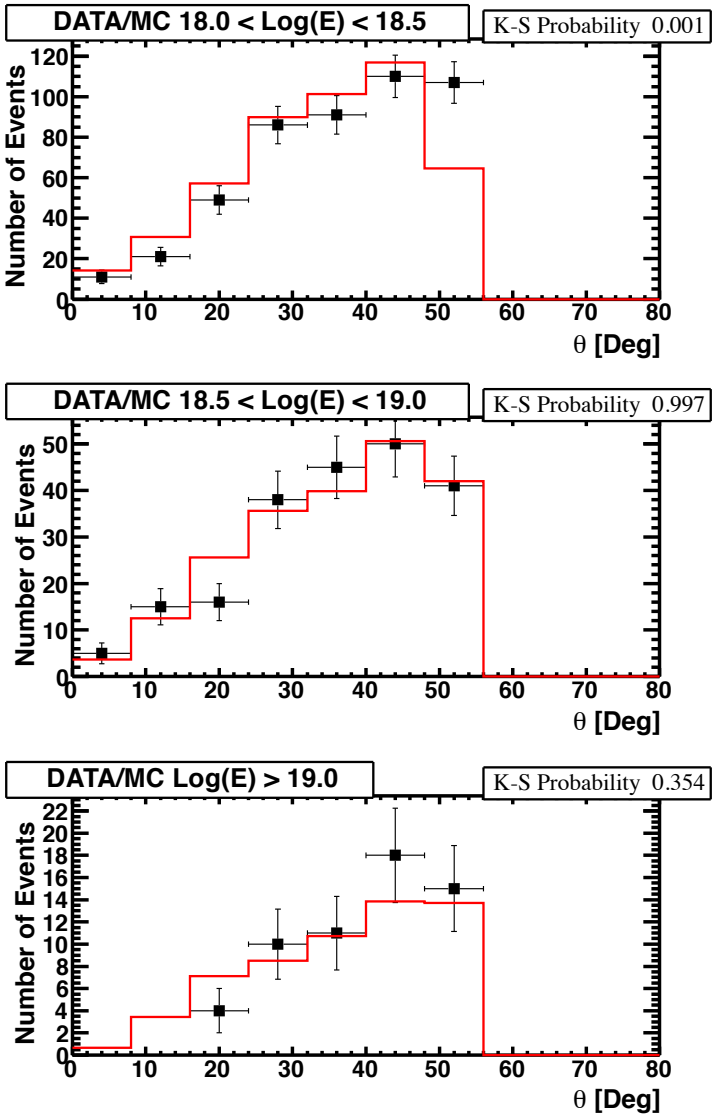


**Figure 7.9**. Data/iron MC comparison: Middle Drum hybrid zenith angle ($\Theta$) is shown in three energy ranges: top to bottom, $10^{18.0} < E < 10^{18.5}$ eV, $10^{18.5} < E < 10^{19.0}$ eV, and $E > 10^{19.0}$ eV, respectively, to show the evolution of this parameter with energy. The distribution of measurements is shown for the data (black points with error bars) and Monte Carlo (MC) (histogram). The MC has been normalized to the area of the data in these plots. In the upper two energy ranges, the data and MC appear to be in agreement, indicating that the lowest energy range is dominating the overall value.

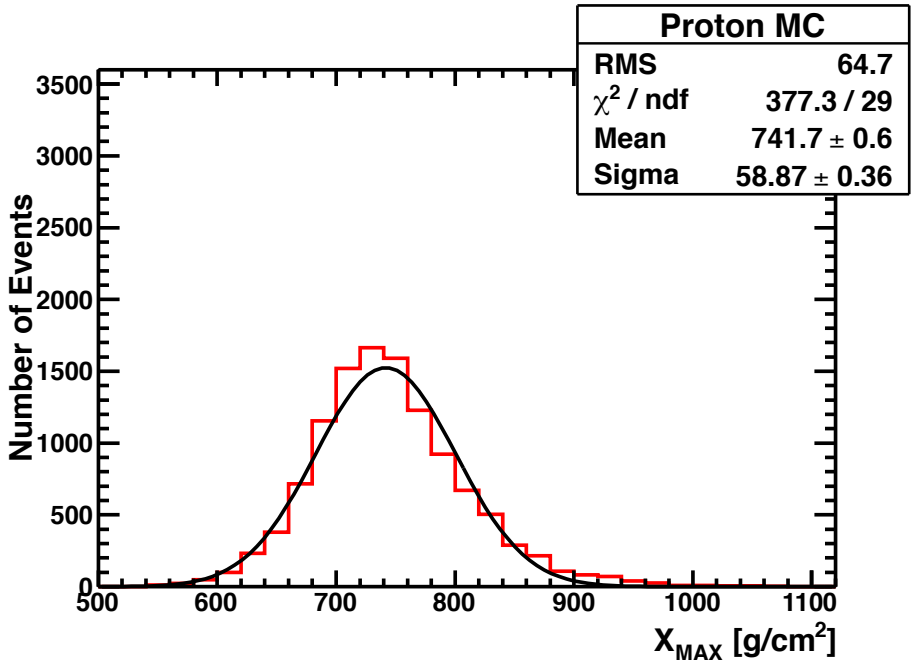


(a)

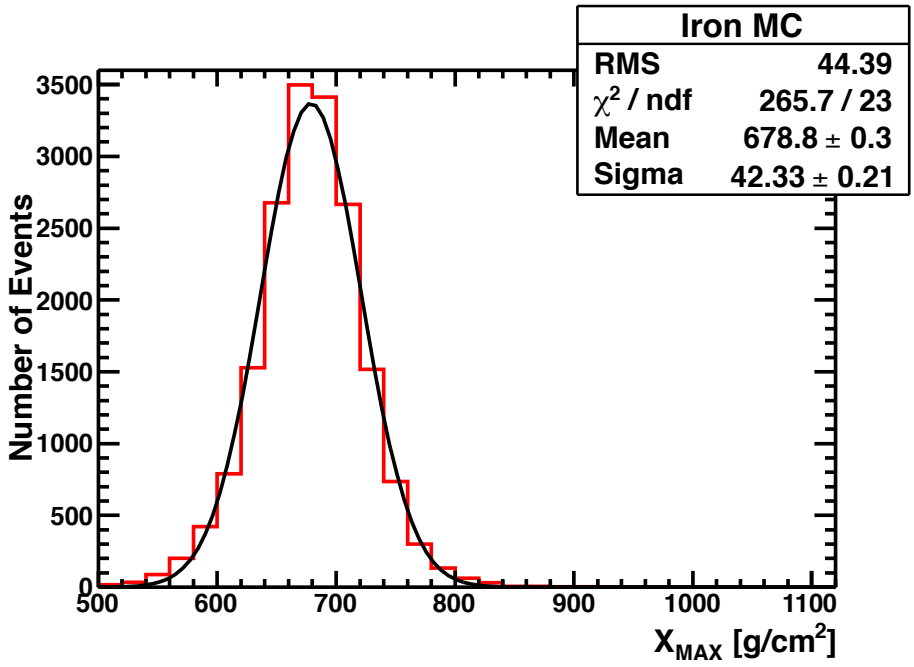


(b)

**Figure 7.10**. The distribution of the shower maximum for (a) the proton Monte Carlo set, and (b) the iron Monte Carlo set, are shown, each fit to a gaussian. These distributions show all events with energies, E $>10^{18}$ eV. Note that the mean $X_{max}$ for the proton data is deeper and that the width of the proton distribution is significantly wider. Also note that there is significant overlap between the two distributions, thus making an event-by-event identification impossible.

composition identification impossible.

Figures 7.11a and 7.11b show the reconstructed $X_{max}$ resolution for the proton and iron Monte Carlo, respectively. The resolution for the proton set is 32.9 g/cm$^2$, with a bias is -2.98 g/cm$^2$. The resolution for the iron set is comparable, with a width of 29.8 g/cm$^2$and a bias of +5.47 g/cm$^2$. The reconstruction bias is significantly lower than the resolution in both cases. Therefore, no correction was made to either the data or the MC.

Figures 7.12a and 7.12b show scatter plots of $X_{max}$ values as a function of their energy dependance for the proton and iron Monte Carlo, respectively. The points with error bars represent the $<X_{max}>$ and RMS of the data scatter points in each energy bin. The line is a fit to the $<X_{max}>$ values. The slope of the line, or elongation rate, is 32.9 g/cm$^2$/ energy decade for the proton, and a little steeper, 42.7 g/cm$^2$/ energy decade for iron. The measured elongation rate takes into account the detector and reconstruction bias that is included in the Monte Carlo, and therefore does not represent the true elongation rate of cosmic ray particles.

Figures 7.13a and 7.13b show the overall data/Monte Carlo comparison of the $X_{max}$ distribution for the proton and iron Monte Carlo, respectively. The mean $X_{max}$ value for the data set is 733.2 g/cm$^2$. The K-S probabilities are shown for each pair of distributions. Note that the proton distribution has a much higher probability than the iron distribution, though the K-S value is still quite low. This might be explained by looking at figure7.14a which breaks up the proton MC and data into three energy ranges. In particular, the lowest energy range (between $10^{18.0}$ and $10^{18.5}$) has the lowest K-S probability, which dominates the overall distribution. This might indicate that the data are likely to be heavy, or contain a mixed composition in this energy range. Figure 7.14b also shows the iron data/Monte Carlo comparison broken up into three energy ranges. In all energy ranges, the K-S fit indicates that the data is not consistent with iron primaries. The parameters in the data and both Monte Carlo sets are summarized in Table 7.1.

Figure 7.15 shows a scatter plot of the data $X_{max}$ values as a function of their energy compared with the proton and iron Monte Carlo. The data points are binned by $\log_{10}(E)$ to show the energy dependence in the $X_{max}$ average value. The proton and iron "rails" are taken from plots 7.12a and 7.12b, indicating the $<X_{max}>$ values of showers thrown as protons or iron nuclei. The data clearly agree more closely with the proton rail than the iron rail. Recall that the proton and iron MC sets have used the same reconstruction programs as well as the same cuts as the data set (see Section 6.1).

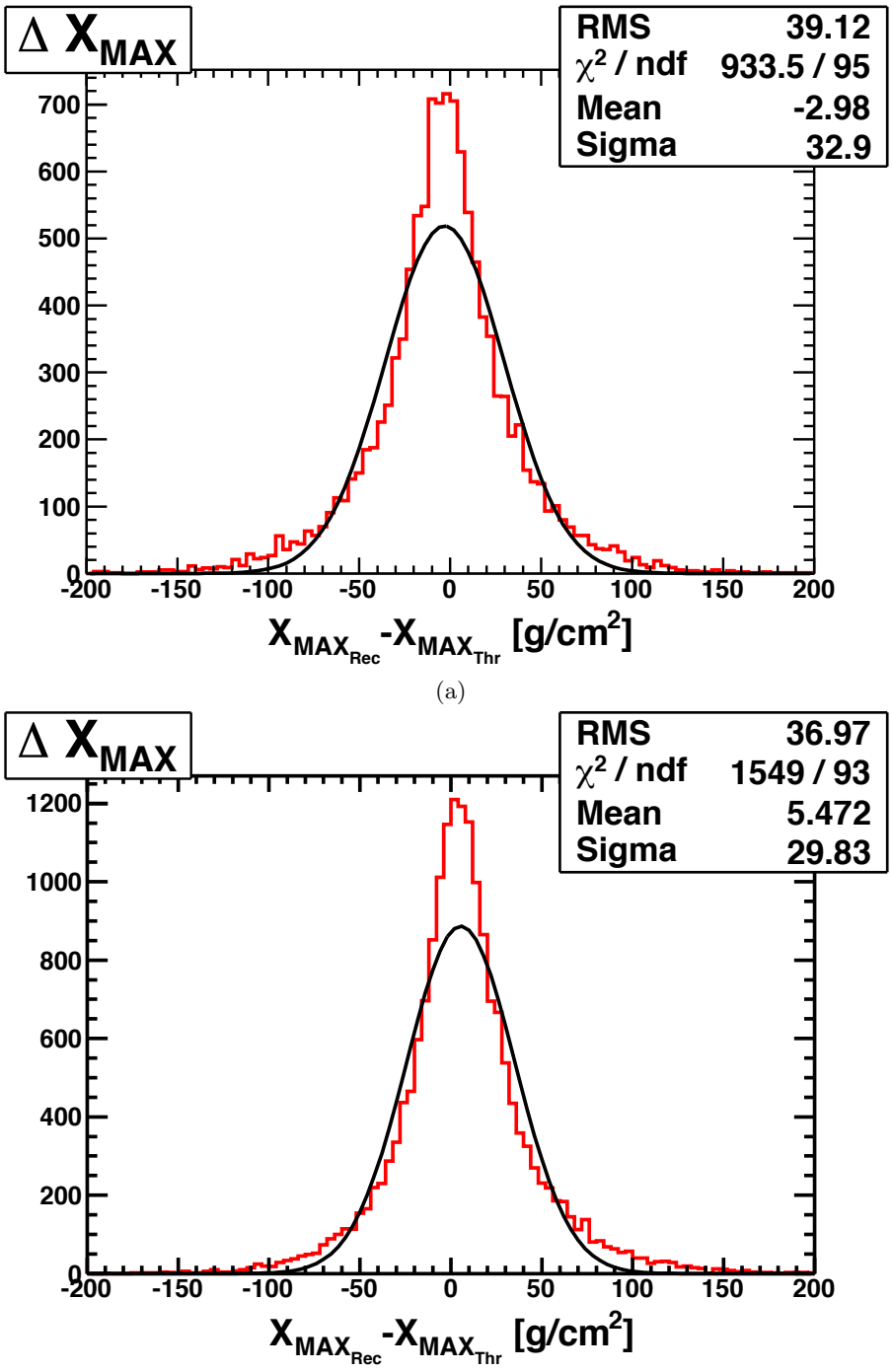


(a)

(b)

**Figure 7.11**. The MD hybrid $X_{max}$ resolution for the Monte Carlo sets: shown is the difference between the reconstructed $X_{max}$ values and the thrown $X_{max}$ values for (a) proton, and (b) iron induced showers, fit to a gaussian.

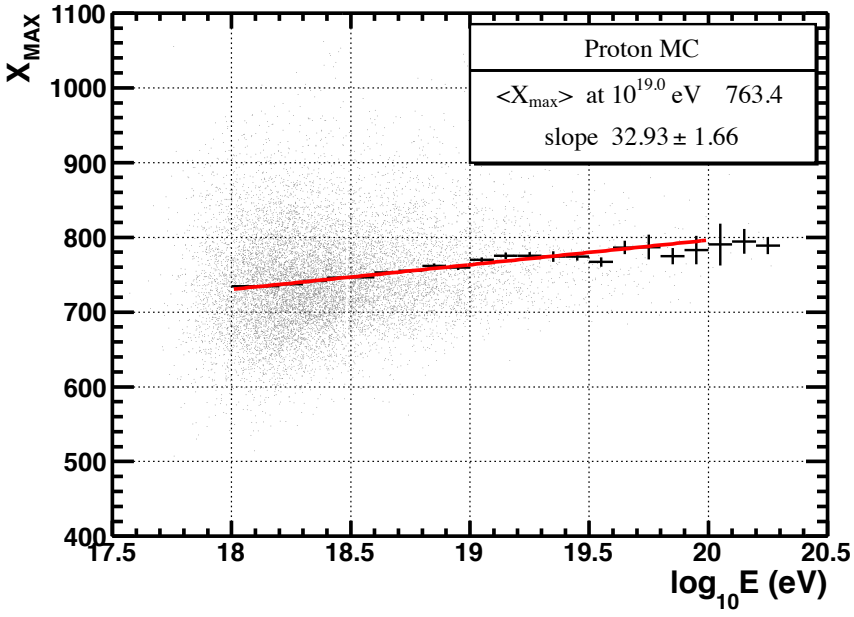


(a)

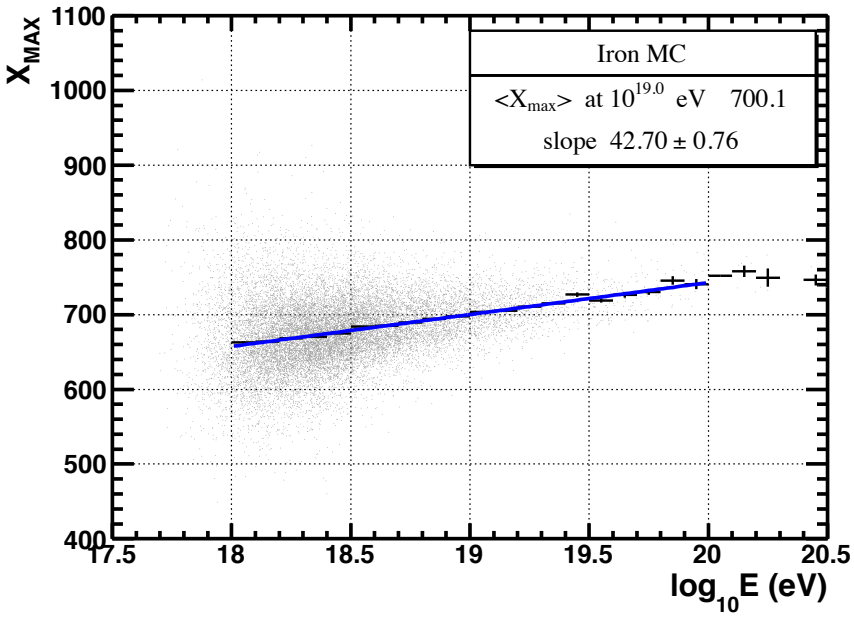


(b)

**Figure 7.12**. Middle Drum hybrid $X_{max}$ distribution scatter plot: the $<X_{max}>$ values are plotted as a function of energy. The solid line is the fit to the $<X_{max}>$ values. (a) proton and (b) iron induced Monte Carlo are shown along with the apparent elongation rate, or slope, of the fit.

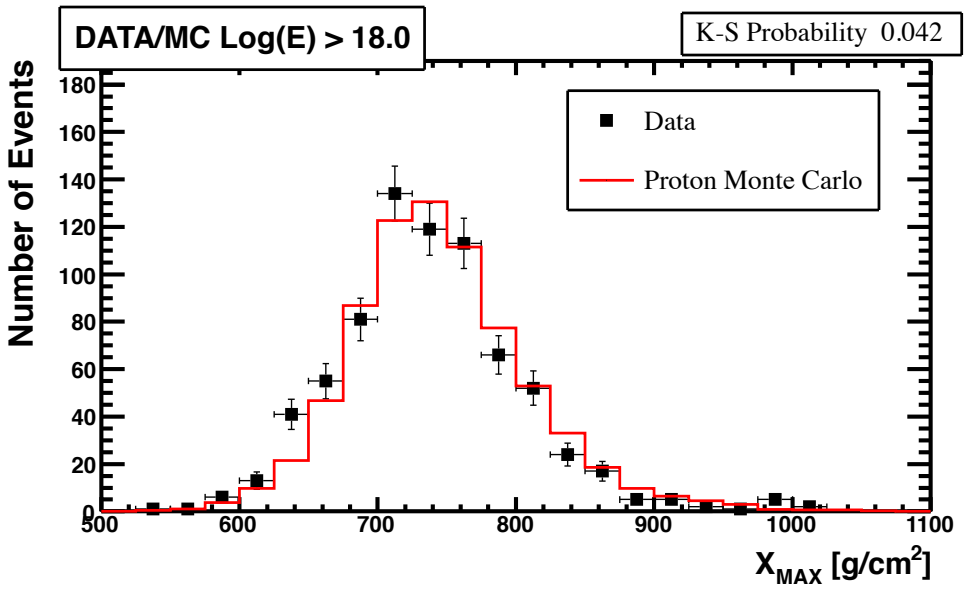


(a)

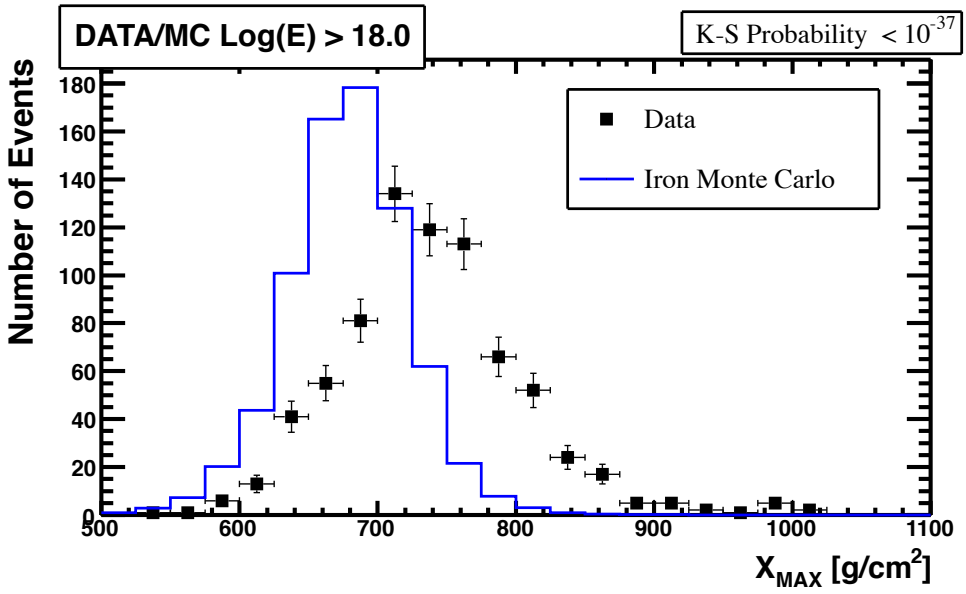


(b)

**Figure 7.13**. The data/MC comparisons of the shower maximum ($X_{max}$): the distribution of measurements is shown for the data (black points with error bars) with (a) the proton Monte Carlo (MC), and (b), the iron MC (histograms). The MC has been normalized to the area of the data. The K-S Probability for the iron MC is listed as $< 10^{-37}$ to indicate the single precision limit on the significance of this number, meaning that the value of the must be smaller than $10^{-37}$.

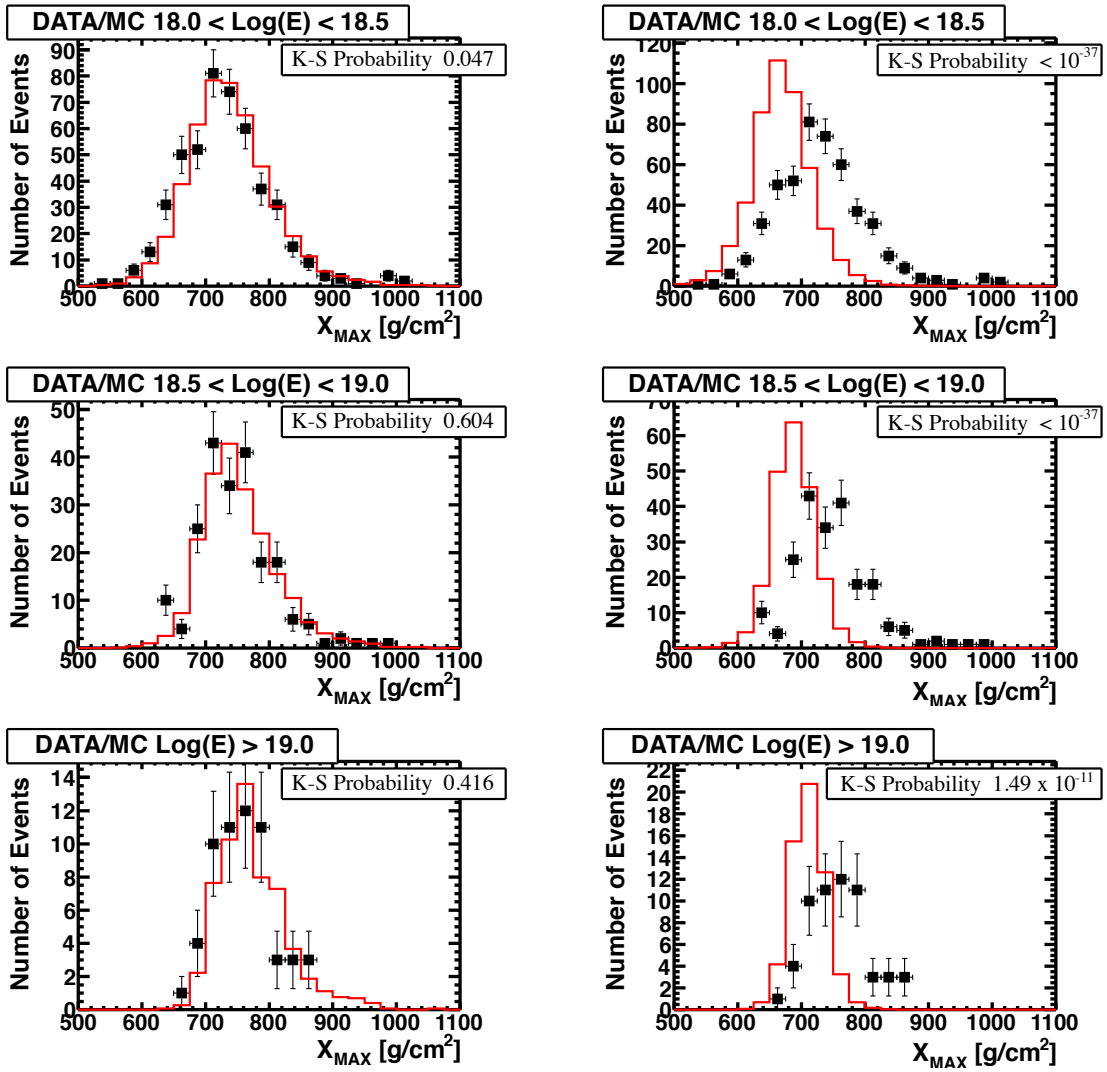


(a) (b)

**Figure 7.14**. The data/MC comparison of the shower maximum ($X_{max}$) is plotted broken up into 3 energy ranges: top to bottom, $10^{18.0} < \mathrm{E} < 10^{18.5}$ eV, $10^{18.5} < \mathrm{E} < 10^{19.0}$ eV, and $\mathrm{E} > 10^{19.0}$ eV, respectively, to show the evolution $X_{max}$ with energy. The distribution of measurements is shown for the data (black points with error bars) with (a) proton Monte Carlo (MC), and (b) iron MC (histograms). The MC has been normalized to the area of the data in these plots. The K-S values, as well as a visual check indicate that the data in all three energy ranges looks more like protons than iron.

**Table 7.1**. The composition parameters are given for the data, proton MC, and iron MC. Note that in the highest energy bin, there are only two events, which may account for the consistency with both the proton and iron distributions.

| Set | $<X_{max}>$ | $RMS_{<X_{max}>}$ | $X_{max}$ $\sigma$ | $X_{max}$ Resolution |
|---|---|---|---|---|
| Data | 733.2 | 66.4 | 59.61 | $N/A$ |
| Proton | 741.7 | 64.5 | 58.9 | 32.9 |
| Iron | 678.8 | 44.3 | 42.32 | 29.8 |

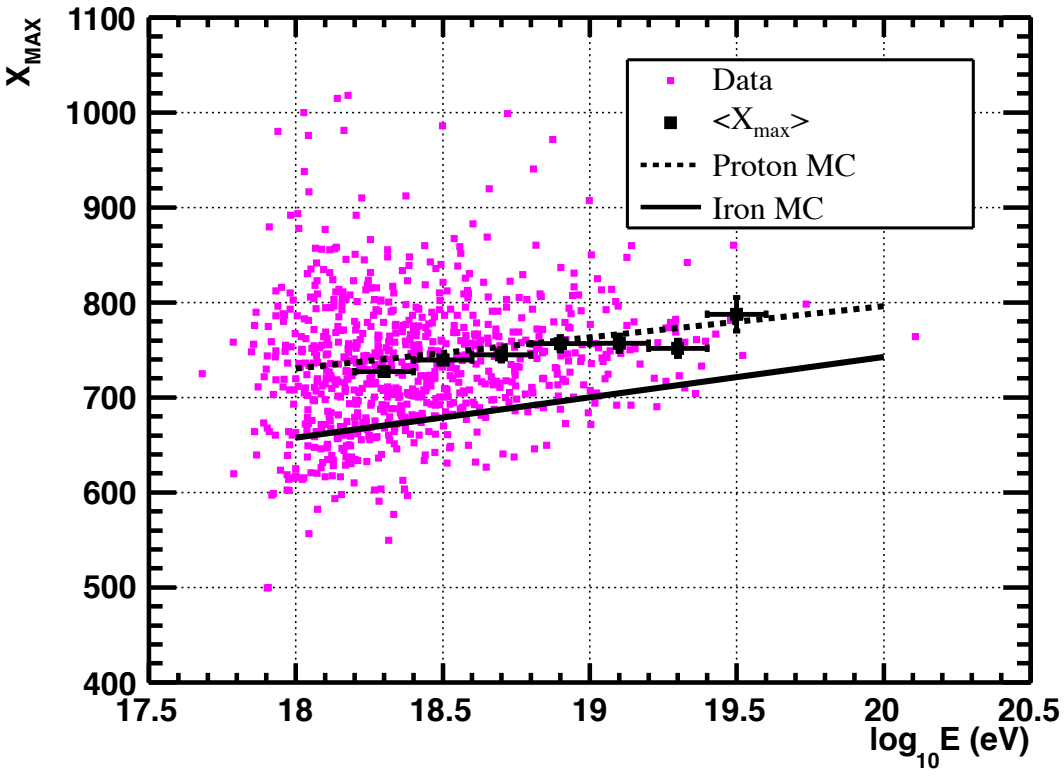


**Figure 7.15**. Middle Drum hybrid composition result: the $<X_{max}>$ values for each data event are plotted as a function of energy overlaid with the proton and iron "rails". The light pink points are a scatter plot of the $X_{max}$ of the real data as a function of energy. The black data points with error bars represent the $<X_{max}>$ values binned by energy. The red dotted "rail" is the fitted line to the proton MC set $<X_{max}>$ values (from Figure 7.12a), while the blue solid "rail" is the fitted line to the iron MC $<X_{max}>$ values

While an overall look at the $X_{max}$ distributions can give some insight into the composition of the primary particles in the data, it does not give a complete picture. The cosmic ray particle composition is energy dependent; recall that in the energy range from $10^{8.0}$ to $10^{18.5}$ eV, the data $X_{max}$ distribution does not agree particularly well with either the iron MC or proton MC. Therefore, a study of how this distribution evolves with energy is suitable, and the distributions of the $X_{max}$ parameter for the data compared to both MC sets are are examined in smaller energy ranges.

Figures 7.16 - 7.24 show the distributions in energy ranges in $2/10^{th}$ energy decadal bins. Note that in the very first energy bin (Figure 7.16, in the range from $10^{18.0}$ to $10^{18.2}$ eV), the data does not agree well with either set. This may indicate a mixed composition of particles in this bin. However, by the second bin (Figure 7.17), the data agrees well with the proton distribution. For each energy bin beyond the first, lowest energy bin, the data is in good agreement with the proton MC. The K-S values for each pair of distributions are shown on each plot, as well as summarized in Table 7.2. Using these values, a K-S plot is shown in Figure 7.25 comparing the values for the data-proton comparison with the values from the data-iron comparison. The line for the K-S probability at 0.05 is also shown. Values above this line are generally assumed to indicate good agreement. Again, the proton comparisons are in much better agreement than the iron comparisons. Note that although the highest energy bin is the only one that is not inconsistent with iron, it contains only two events, causing us to lose the ability to discern. Collecting additional data will allow us to extend this measurement to higher energies.

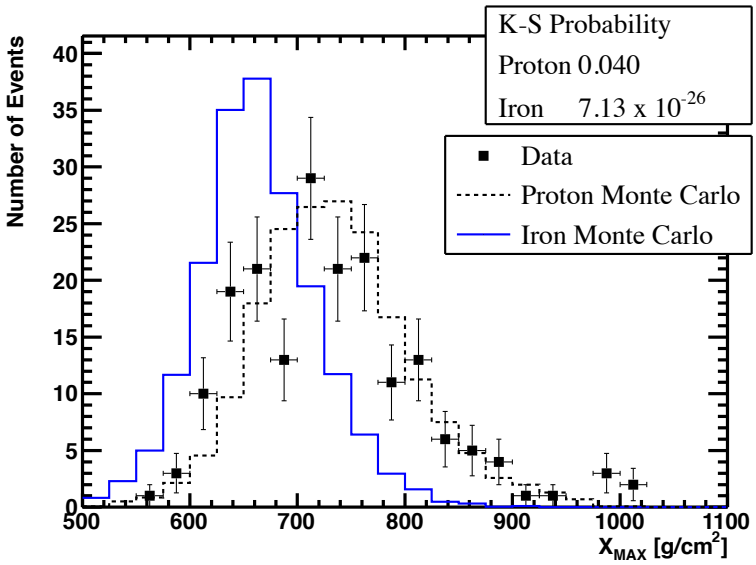


**Figure 7.16**. The $X_{max}$ distributions from the data (black points), proton MC (dotted histogram), and iron MC (solid histogram): energy range = $18.0 \leq Log_{10}(E) < 18.2$ eV.

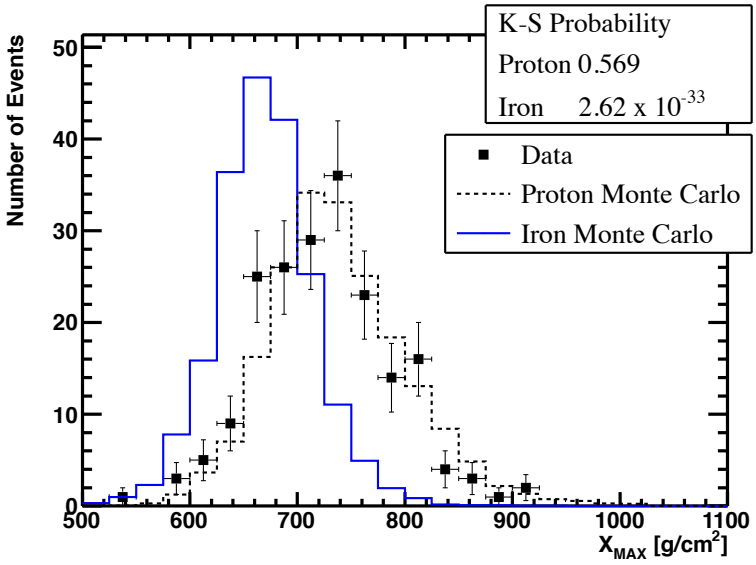


**Figure 7.17**. The $X_{max}$ distributions from the data (black points), proton MC (dotted histogram), and iron MC (solid histogram): energy range = $18.2 \leq Log_{10}(E) < 18.4$ eV.

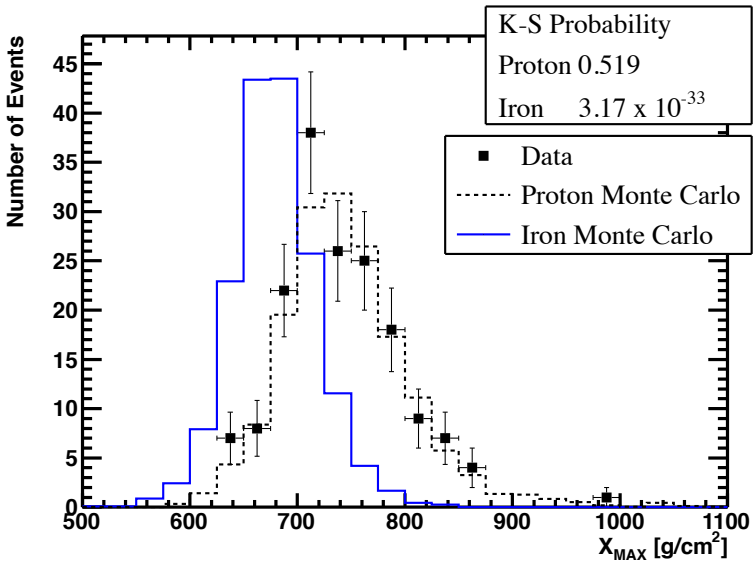


**Figure 7.18**. The $X_{max}$ distributions from the data (black points), proton MC (dotted histogram), and iron MC (solid histogram): energy range = $18.4 \leq Log_{10}(E) < 18.6$ eV.

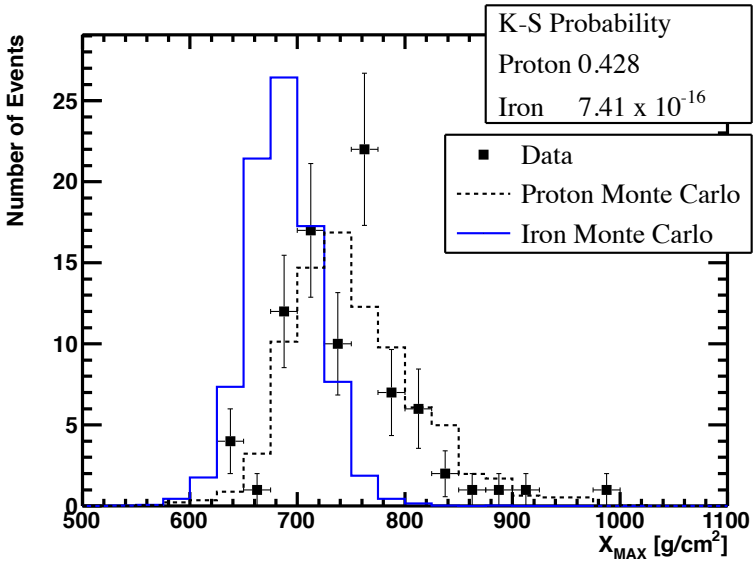


**Figure 7.19**. The $X_{max}$ distributions from the data (black points), proton MC (dotted histogram), and iron MC (solid histogram): energy range = $18.6 \leq Log_{10}(E) < 18.8$ eV.

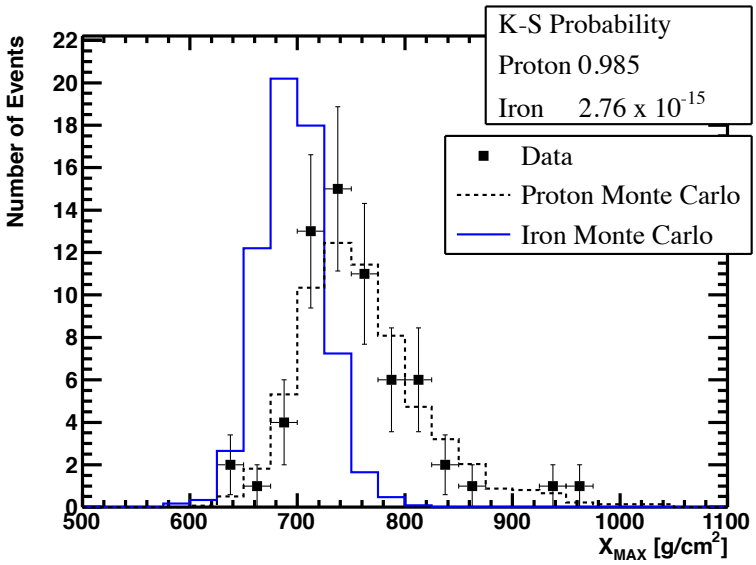


**Figure 7.20**. The $X_{max}$ distributions from the data (black points), proton MC (dotted histogram), and iron MC (solid histogram): energy range = $18.8 \leq Log_{10}(E) < 19.0$ eV.

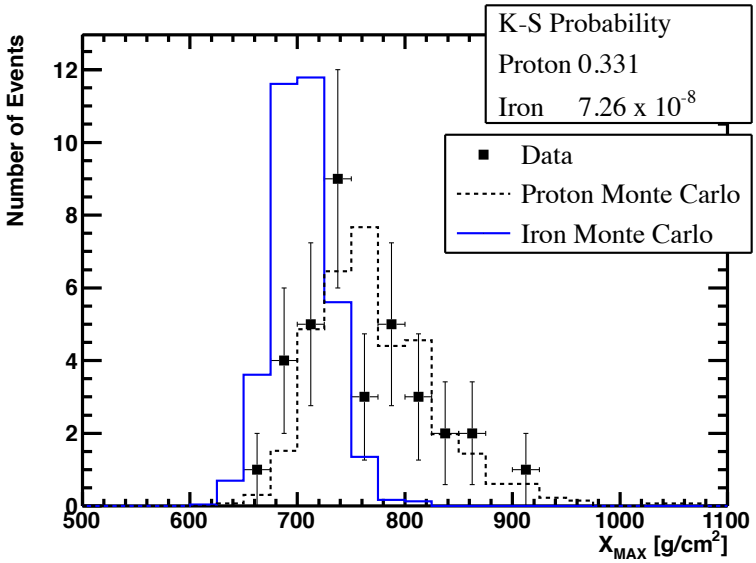


**Figure 7.21**. The $X_{max}$ distributions from the data (black points), proton MC (dotted histogram), and iron MC (solid histogram): energy range = $19.0 \leq Log_{10}(E) < 19.2$ eV.

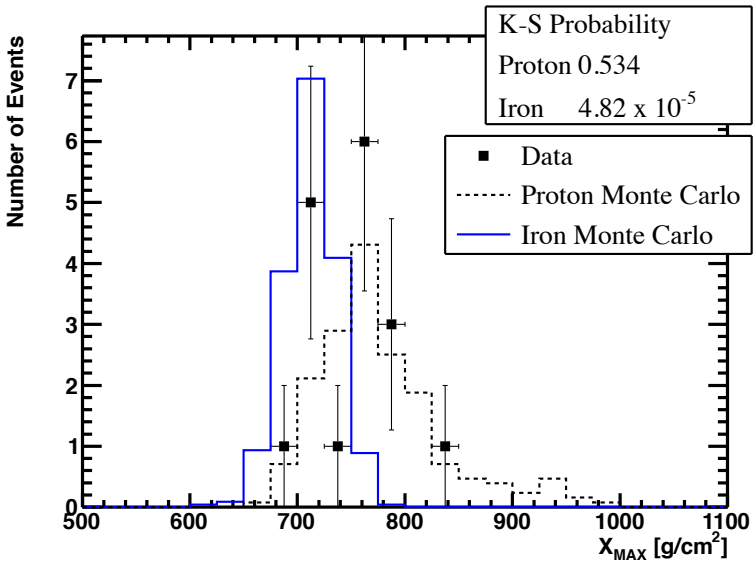


**Figure 7.22**. The $X_{max}$ distributions from the data (black points), proton MC (dotted histogram), and iron MC (solid histogram): energy range = $19.2 \leq Log_{10}(E) < 19.4$ eV.

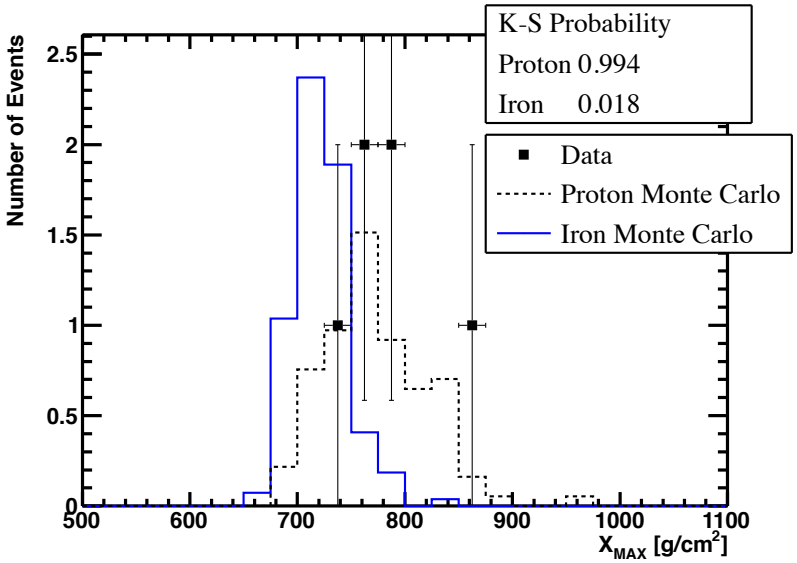


**Figure 7.23**. The $X_{max}$ distributions from the data (black points), proton MC (dotted histogram), and iron MC (solid histogram): energy range = $19.4 \leq Log_{10}(E) < 19.6$ eV.

**Table 7.2**. A summary of the K-S tests performed to compare the MD hybrid data to the proton and iron Monte Carlo sets for the $X_{max}$ parameter is given.

| Figure | Lower (E) bound $log_{10}(E)$ eV | Upper (E) bound $log_{10}(E)$ eV | Proton K-S Probability | Iron K-S Probability |
|---|---|---|---|---|
| 7.16 | 18.0 | 18.2 | 0.040 | 7.13 x $10^{-26}$ |
| 7.17 | 18.2 | 18.4 | 0.569 | 2.62 x $10^{-33}$ |
| 7.18 | 18.4 | 18.6 | 0.519 | 3.17 x $10^{-33}$ |
| 7.19 | 18.6 | 18.8 | 0.428 | 7.41 x $10^{-16}$ |
| 7.20 | 18.8 | 19.0 | 0.985 | 2.76 x $10^{-15}$ |
| 7.21 | 19.0 | 19.2 | 0.331 | 7.26 x $10^{-8}$ |
| 7.22 | 19.2 | 19.4 | 0.534 | 4.82 x $10^{-5}$ |
| 7.23 | 19.4 | 19.6 | 0.994 | 0.018 |
| 7.24 | 19.6 | 20.2 | 0.977 | 0.216 |

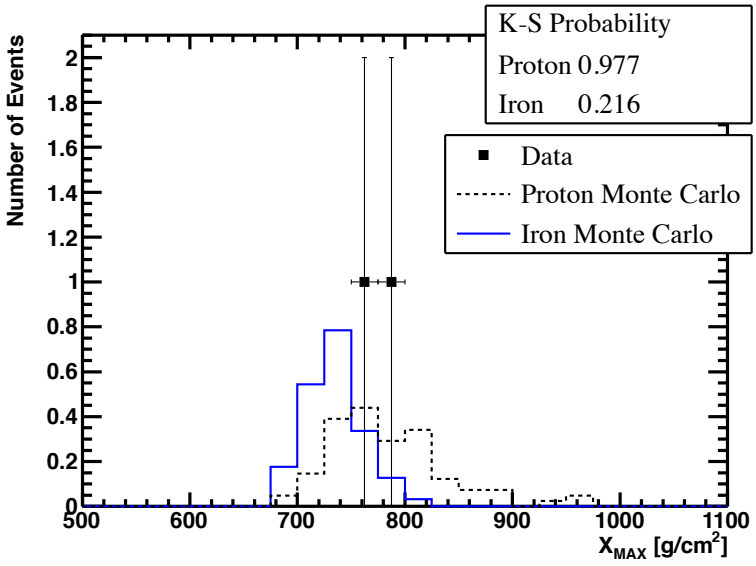


**Figure 7.24**. The $X_{max}$ distributions from the data (black points), proton MC (dotted histogram), and iron MC (solid histogram): energy range = $Log_{10}(E) > 19.6$ eV. All energy bins above $Log_{10}(E) = 19.6$ eV have been combined so that the two highest energy events are in one bin.

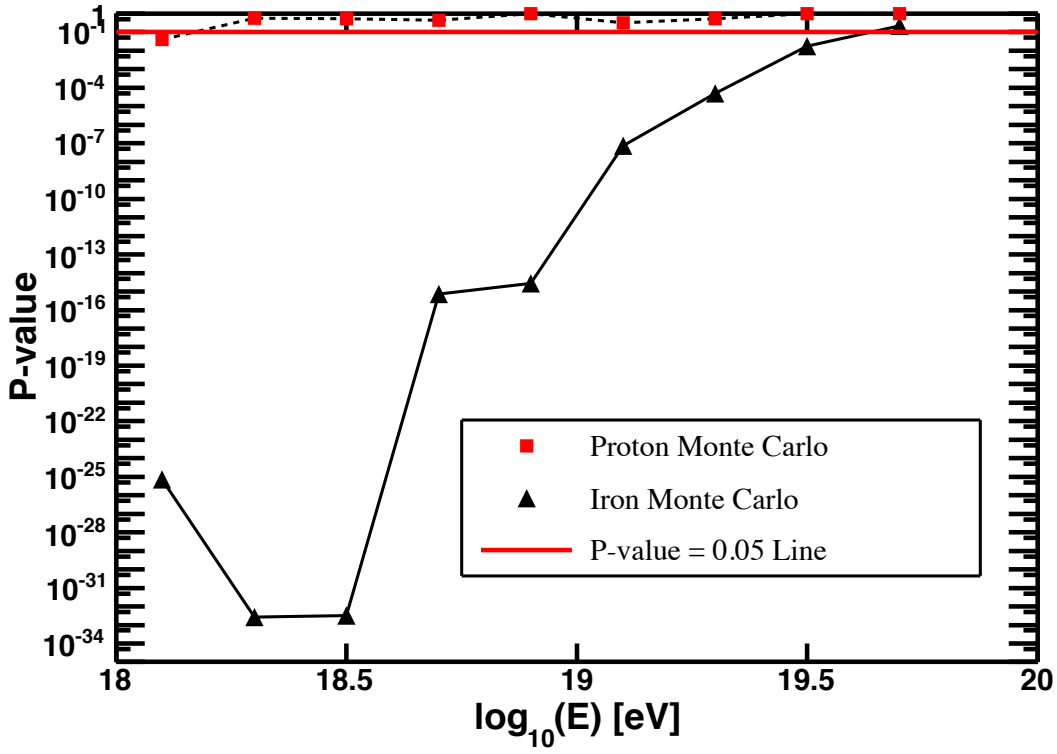


**Figure 7.25**. The K-S values for the data-proton MC comparisons are plotted with the K-S values for the data-iron MC comparisons. The line for P = 0.05 is also drawn for comparison; values above this line are considered to indicate good agreement. There is good agreement with protons over the full energy range. The data are inconsistent with iron until the highest energy bin, in which the statistics are limited.

# CHAPTER 8

# SUMMARY

The work in this dissertation is focused on studying the energy spectrum and composition of Ultra High Energy Cosmic Rays (UHECRs) (Energy, E $>10^{18}$ eV). The Telescope Array experiment was designed to answer questions about the sources, acceleration mechanisms, and propagation of UHECRs. The energy spectrum and composition measurements are independent, and taken together can help build a consistent picture of the physics of these particles.

An overview of the recent results in the energy spectrum and composition measurements in the field is given in Chapter 2. These results leave many unanswered questions, motivating the new measurements discussed here, as well as placing it within the proper context. Notably, the Pierre Auger Observatory (PAO) is the only other experiment in the field that is currently taking data. The recent results from the PAO are not self-consistent. They have published an energy spectrum measurement of the GZK cut-off which indicates a proton interaction (see Figure 2.13), but at the same time their composition measurements show that the particles at the highest energies are not protons (see figures 7.3 and 7.4). Furthermore, the anisotropy measurement from the PAO suggests a correlation between UHECRs and nearby Active Galactic Nuclei (AGN) [8]. Their conclusion is predicated on the assumption that the magnetic fields do not bend the particles significantly from their trajectory, which is only true for light particles.

The Telescope Array (TA) is a hybrid detector that uses refurbished fluorescence telescopes from the High Resolution Fly's Eye (HiRes) experiment [4] at its Middle Drum (MD) site, in order to provide a link back to that experiment. It also uses Surface Detectors (SD) built using the same design as those used in the Akeno Giant Air Shower Array (AGASA) [42], providing a similar link to that experiment. Energy spectrum measurements had previously been made using the Middle Drum detector in monocular mode, and had been compared to HiRes [38]. The work in this dissertation, however, is the first measurement done in hybrid mode using the Middle Drum detector, providing the next step in linking

the overall TA experiment back to HiRes. TA began operation in hybrid mode in May, 2008. A detailed description of the hardware and electronics of both the Middle Drum fluorescence telescopes and the surface scintillator detectors is provided in Chapter 3. Detailed simulations, described in Chapter 4 were performed in order to calculate an aperture and verify the reconstruction programs which were described in Chapter 5.

The Middle Drum Hybrid data set is perhaps the cleanest set in the entire Telescope Array experiment. Ironically, this is because the Surface Detector is far away ($\sim$10 km) from the Middle Drum detector compared to the other fluorescence detectors in the experiment. Furthermore, the geometry and energy resolutions are some of the best in the field. The graphical representations of the top 11 highest energy events are shown in the Appendix. The plots show the event displays from the MD detector, the SD detector, the geometry fit of the timing vs angle plot (Section 5.4), and the profile fit to the data (Section 5.5). The highest energy event has a reconstructed energy of $1.32\times10^{20}$ eV. The high quality of the data is evidenced by these top events.

The first hybrid energy spectrum measurement using the Middle Drum detector in conjunction with the surface detector is presented in Chapter 6, Figure 6.7. The results are compared with the same measurement performed by the Middle Drum detector in monocular mode, as well as the HiRes results in Figure 6.10. Good agreement is shown between all the spectra. A comparison between the MD Hybrid spectrum the SD in monocular mode is shown in Figure 6.11, also with good agreement. The agreement with the SD links the MD detector, and therefore HiRes, to the rest of the TA experiment.

Finally, the preliminary composition results using the MD Hybrid detector are shown in Chapter 7. The average $X_{max}$ parameter per energy bin calculated from the data is compared with the same values from simulated cosmic ray showers generated by protons and iron nuclei in Figure 7.15. The MD Hybrid data set clearly agrees more closely with the proton simulated data. Furthermore, the distribution of the $X_{max}$ parameter from the data set is compared with distributions from the simulated sets. This is done over the whole energy range in Figure 7.13, and broken up in to smaller energy bins in figures 7.16 - 7.24. Aside from the lowest energy bin, where the data appears to agree with neither simulated set well, all the figures show clear agreement with the proton set and clear disagreement with the iron set. Finally, a Kolmogorov-Smirnov test was performed for each comparison and the results are shown in Figure 7.25. Again, the data agree much better with the proton simulated data.

In conclusion, the Middle Drum Hybrid energy spectrum and composition measurements agree with and confirm the HiRes spectra and composition results, that the highest energy particles are protons. These results are self-consistent. Finally, my results agree with the PAO energy spectrum measurement in shape, though the normalizations are different. My composition results disagree with the PAO composition measurement.

# APPENDIX

# TOP ELEVEN HIGHEST ENERGY EVENTS

The Middle Drum hybrid data set is perhaps the cleanest set in the entire Telescope Array experiment. The geometry and energy resolutions are also some of the best in the field. This high quality data set is used to prepare some graphical representations of the highest energy events. The top 11 events are shown because the $10^{th}$ and $11^{th}$ events have nearly identical energies, making it arbitrary to include one and not the other.

Figure A.1 shows the hybrid event display for the highest energy event. This event was observed in hybrid mode on August 12, 2010 at 7:30:33 Universal Time Coordinated (UTC). In the figure, the Middle Drum (MD) detector is represented by a star, and the intersections of the grid indicate counters in the Surface Detector (SD) array. Each SD that saw a signal in the time window is indicated with colored circles, where the color represents the timing (see Section 5.2). The broken black line shows the intersection between the Shower Detector Plane (SDP) from Middle Drum and the SD plane (see Section 5.3). The calculated core position of the event is shown where the arrow crosses the solid black line, and the direction of the arrow indicates the direction of the Extensive Air Shower (EAS). Note that the x and y axes are in units of SD counters, and the position of the event in the array can be easily determined from these numbers. For the remaining 10 events, only a zoomed in display of this plot will be shown, but the position in the array can be inferred from the information on the plot.

Figure A.2 gives a comprehensive graphical look at the highest energy event. Figure A.2a shows the event display from the Middle Drum detector. The points represent pixels or PMTs, and the size of the circles are proportional to the signal size in each pixel, while the color again represents the timing. The black line is a fit to the MD SDP. Figure A.2b shows the zoomed in picture of the SD event display. The red line represents the SD array border, while the intersections of the gridline are SD counters. Again, the circle sizes are proportional to the signal size in each counter, while the color represents timing. The

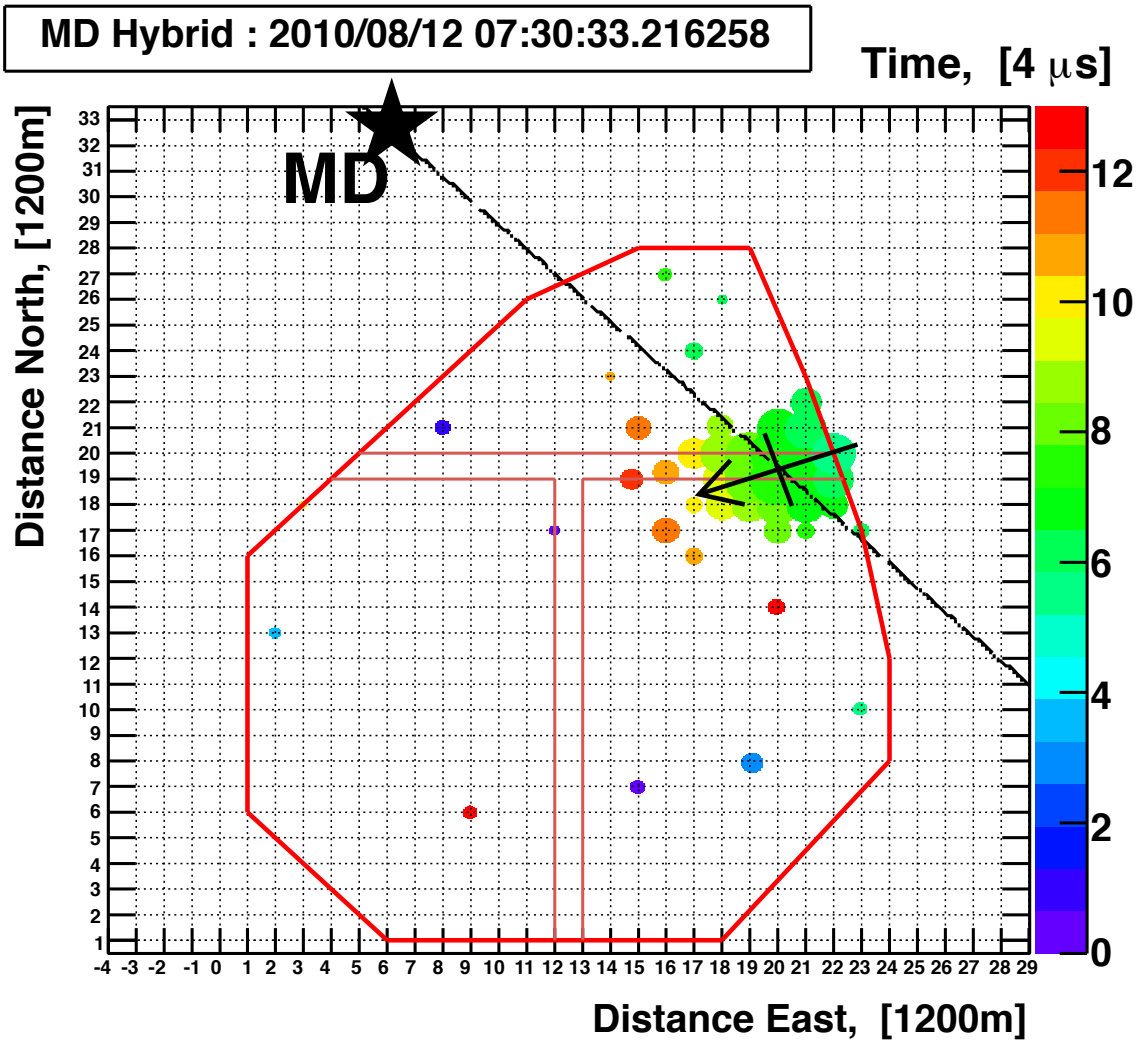


**Figure A.1**. A MD Hybrid event display: shown is the highest energy event in the data set. The star is the MD detector, while intersections of the grid lines are the SD counters. The size of the signal from each SD counter is represented by the size of the colored circles, while their color indicates the timing. The calculated core position of the shower is shown where the black arrow crosses the small black line, and the direction of the shower is given by the direction of the arrow. The intersection between the calculated MD shower detector plane and the SD plane is given by the broken black line.

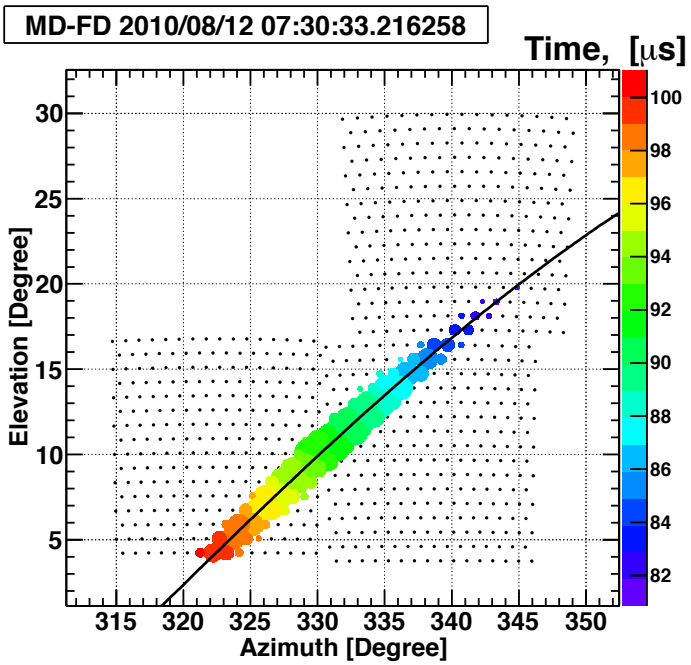


(a)

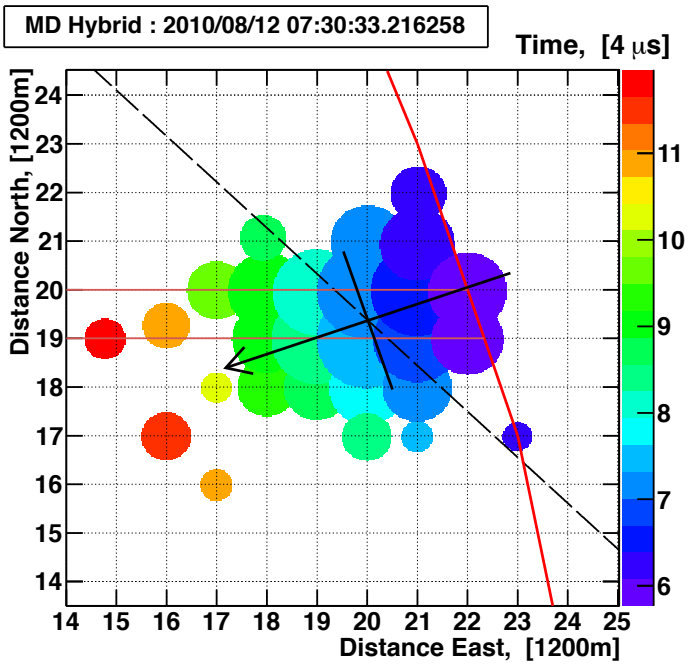


(b)

**Figure A.2**. The highest energy event in the Middle Drum hybrid data set: it was recorded on 08/12/2010 at 7:30:33 UTC. Shown are (a) the Middle Drum event display, and (b) the Surface Detector event display.

broken black line shows the fit to the SDP here as well. The arrow points in the calculated direction of the cosmic ray EAS, and it crosses the smaller, solid black line at the calculated position of the shower core on the ground.

Figure A.2c shows the timing vs. angle fit, or geometry calculation for the highest energy event. The black points are timing signals from the MD PMTs which the red points represent virtual "PMTs" located at MD that view the part of the shower detected by the SD. Each red point represents one SD. The geometry from the EAS is shown on the plot: $T_{Rp}$ is the time that the EAS reached its point of closest approach to MD, $R_P$ is the distance of closest approach, and $\Psi$ is the angle of the EAS in the SDP.

Figure A.2d is the profile fit for the energy of this event. The black points indicate data from the PMTs at MD, and the solid curve is a fit to this data. The other curves represent different contributions to the overall signal: light from direct scintillation, Rayleigh scattering, interactions with aerosols, and Cherenkov radiation. The signal size is plotted as a function of atmospheric depth of the EAS and the depth at the shower maximum, or $X_{max}$ is one of the fit results. It is important to note that the calculated $X_{max}$ value for an event will not coincide with the peak of this distribution. This is because as an EAS generates light, the light is attenuated at a rate of $1/\text{distance}^2$. Therefore, depending on the geometry of the shower, the brightest part of the shower that is observed by the detector is not in general the part with the most particles. Figures A.3 - A.12 give the same comprehensive look at each of the remaining ten events.

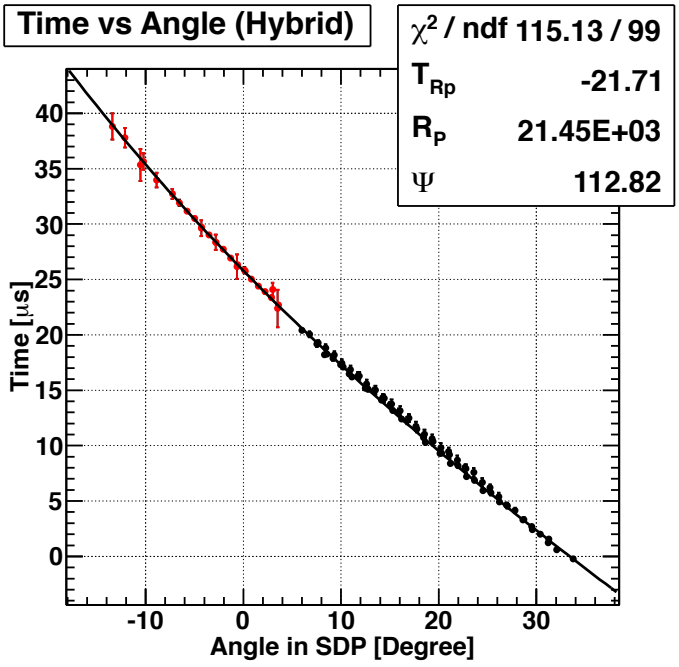


(c)

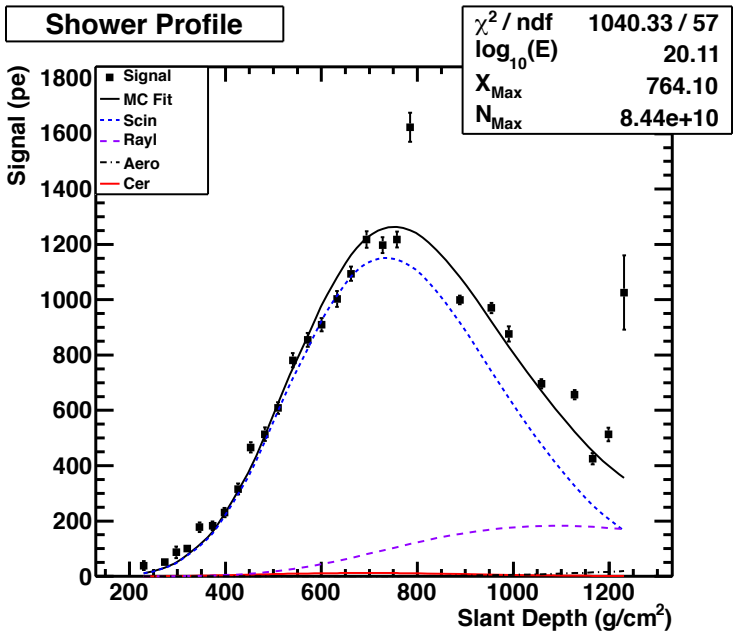


(d)

**Figure A.2**. Continuation of the highest energy event in the Middle Drum hybrid data set: shown are (c) the timing vs. angle plot for the geometry reconstruction, and (d) the plot of the shower profile (signal as a function of atmospheric depth).

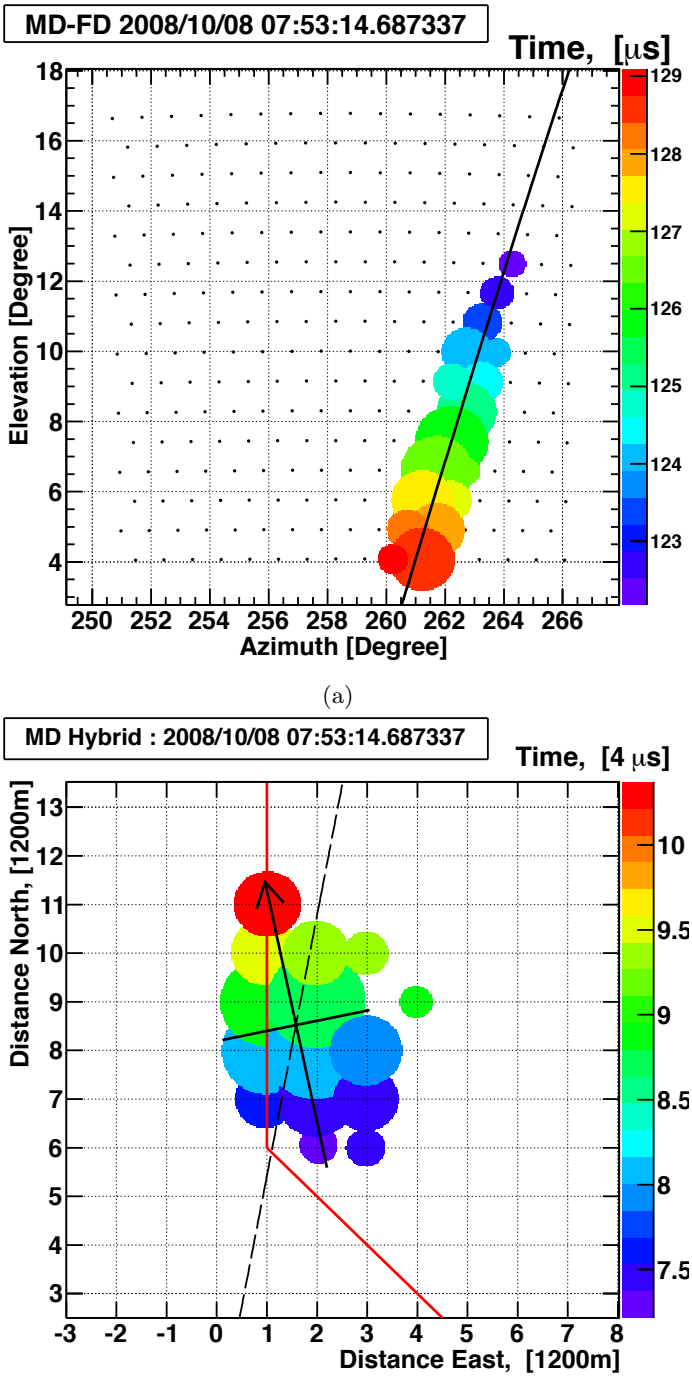


**Figure A.3**. The second highest energy event in the Middle Drum hybrid data set: it was recorded on 10/08/2008 at 7:53:14 UTC. Shown are (a) the Middle Drum event display, and (b) the Surface Detector event display.

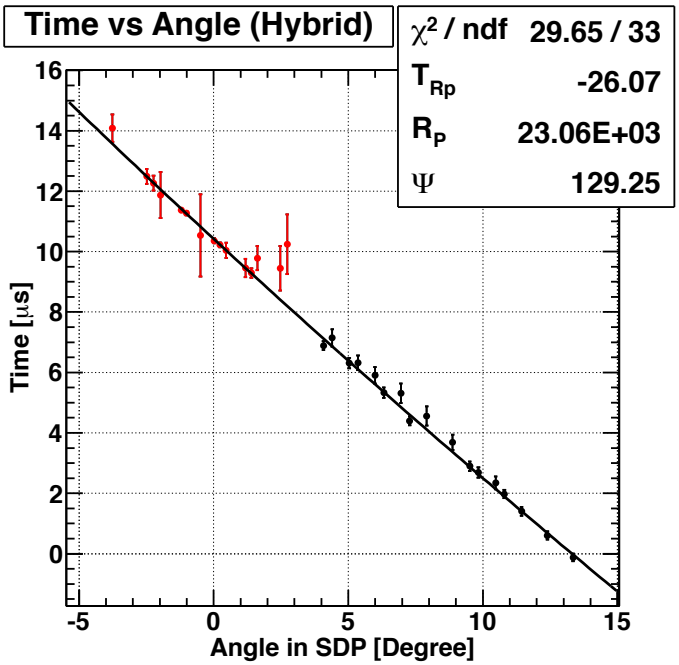


(c)

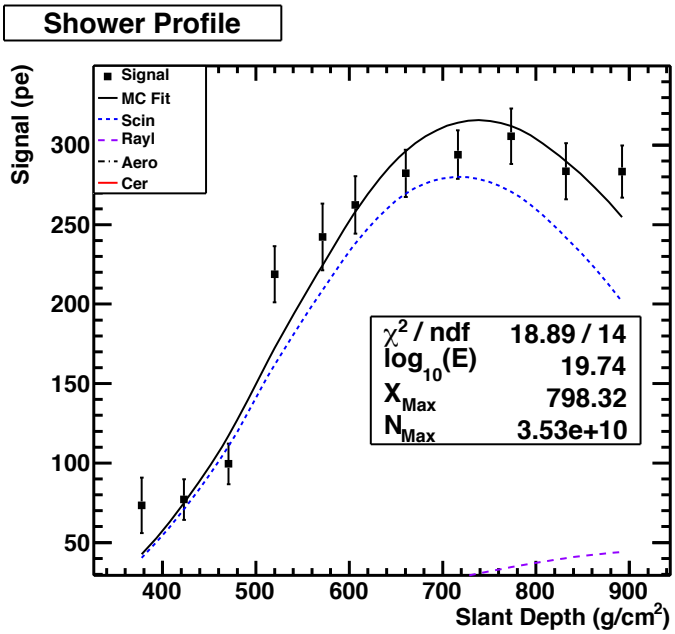


(d)

**Figure A.3**. Continuation of the second highest energy event in the Middle Drum hybrid data set: it was recorded on 10/08/2008 at 7:53:14 UTC. Shown are (c) the timing vs. angle plot for the geometry reconstruction, and (d) the plot of the shower profile (signal as a function of atmospheric depth).

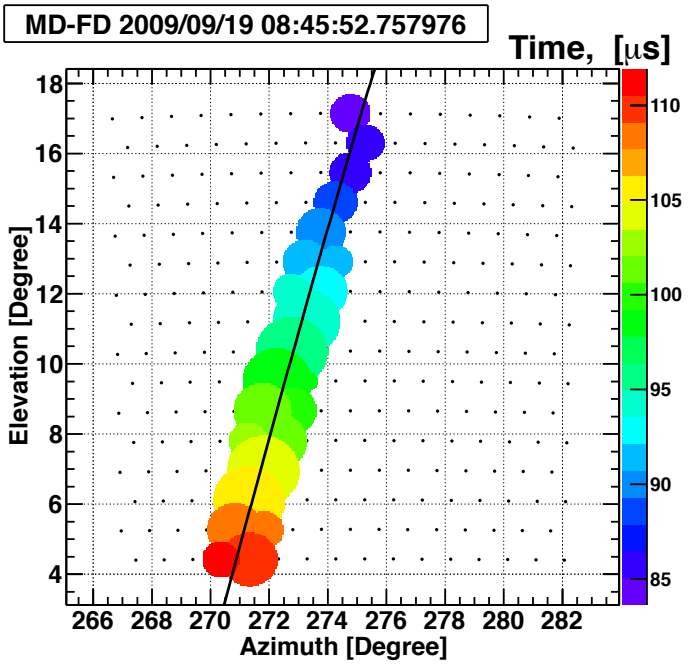


(a)

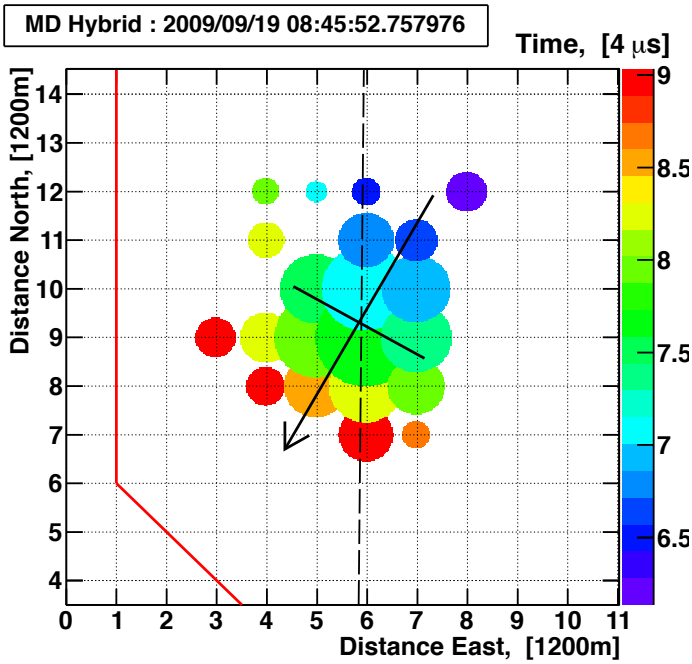


(b)

**Figure A.4**. The third highest energy event in the Middle Drum hybrid data set: it was recorded on 09/19/2009 at 8:45:52 UTC. Shown are (a) the Middle Drum event display, and (b) the Surface Detector event display.

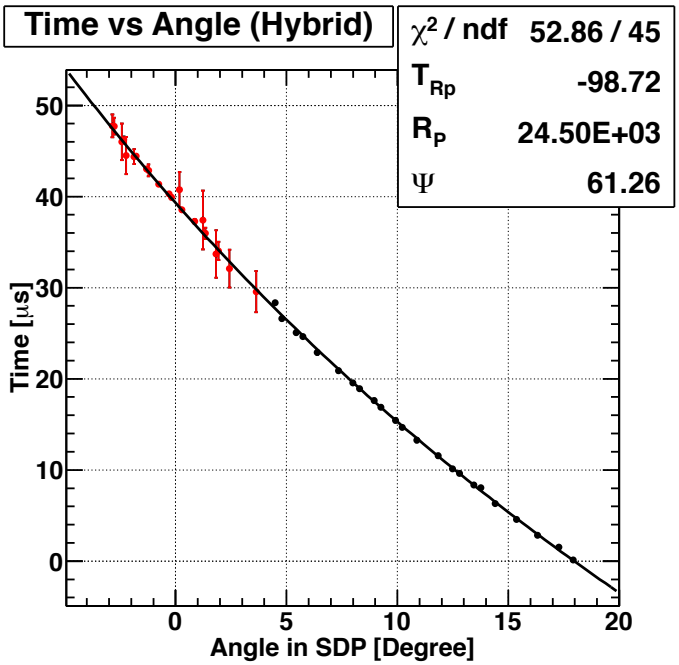


(c)

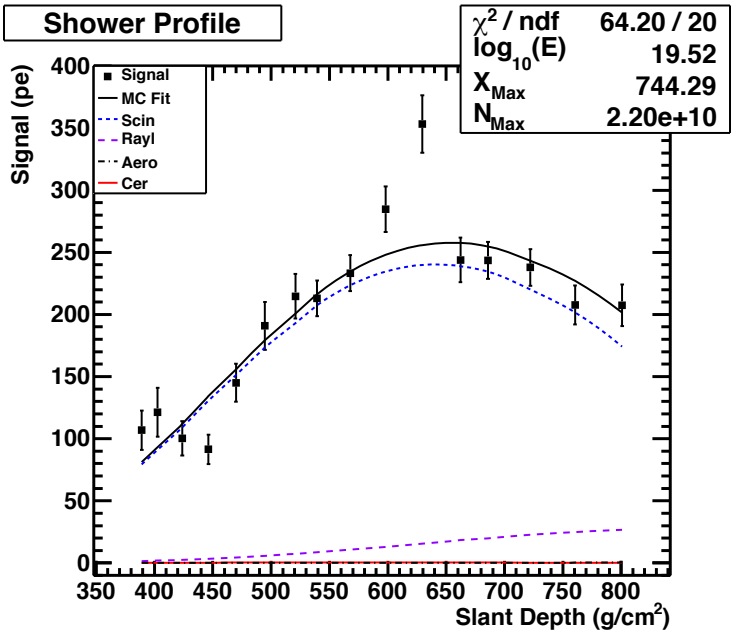


(d)

**Figure A.4**. Continuation of the third highest energy event in the Middle Drum hybrid data set: it was recorded on 09/19/2009 at 8:45:52 UTC. Shown are (c) the timing vs. angle plot for the geometry reconstruction, and (d) the plot of the shower profile (signal as a function of atmospheric depth).

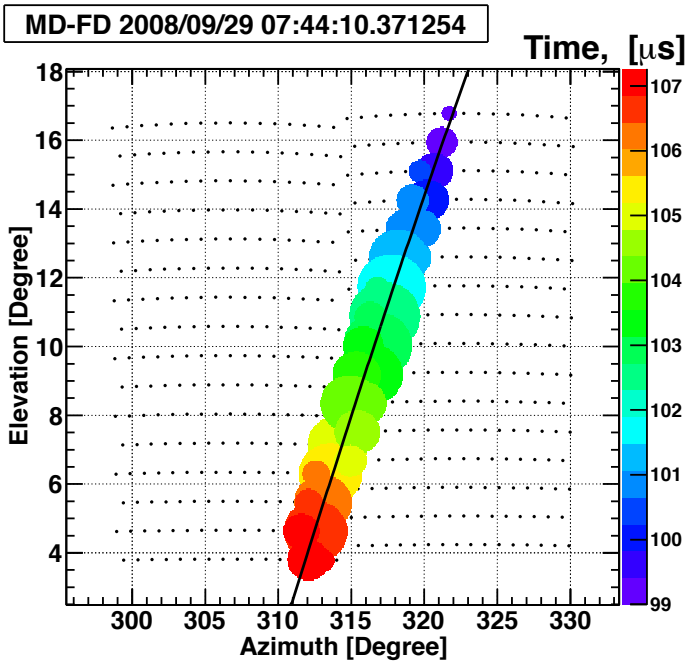


(a)

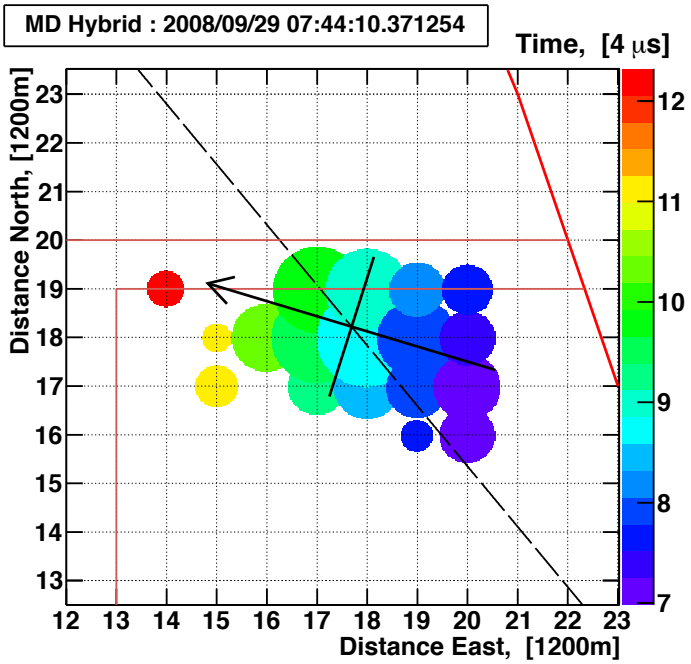


(b)

**Figure A.5**. The fourth highest energy event in the Middle Drum hybrid data set: it was recorded on 09/29/2008 at 7:44:10 UTC. Shown are (a) the Middle Drum event display, and (b) the Surface Detector event display.

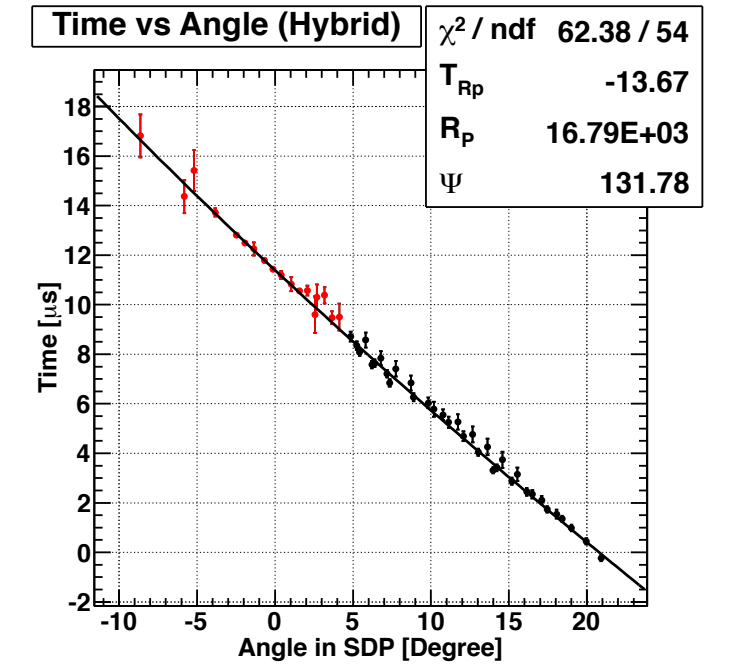


(c)

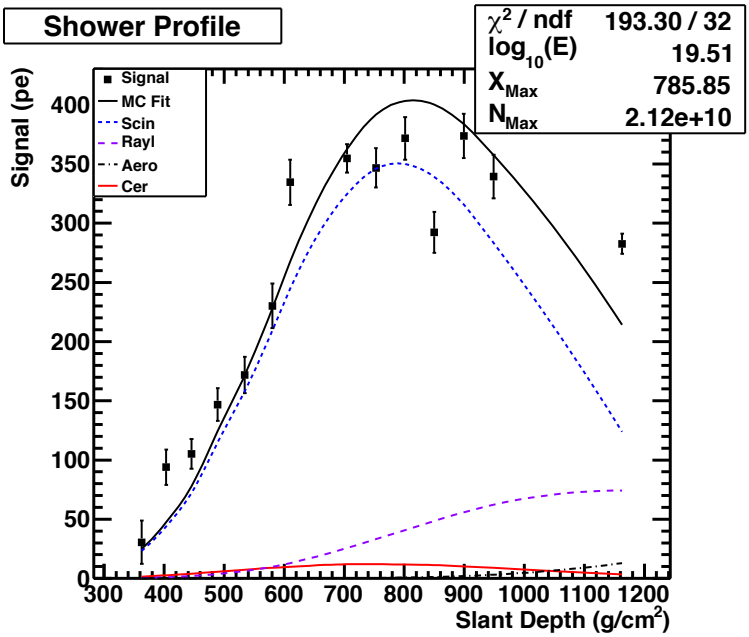


(d)

**Figure A.5**. Continuation of the fourth highest energy event in the Middle Drum hybrid data set: it was recorded on 09/29/2008 at 7:44:10 UTC. Shown are (c) the timing vs. angle plot for the geometry reconstruction, and (d) the plot of the shower profile (signal as a function of atmospheric depth).

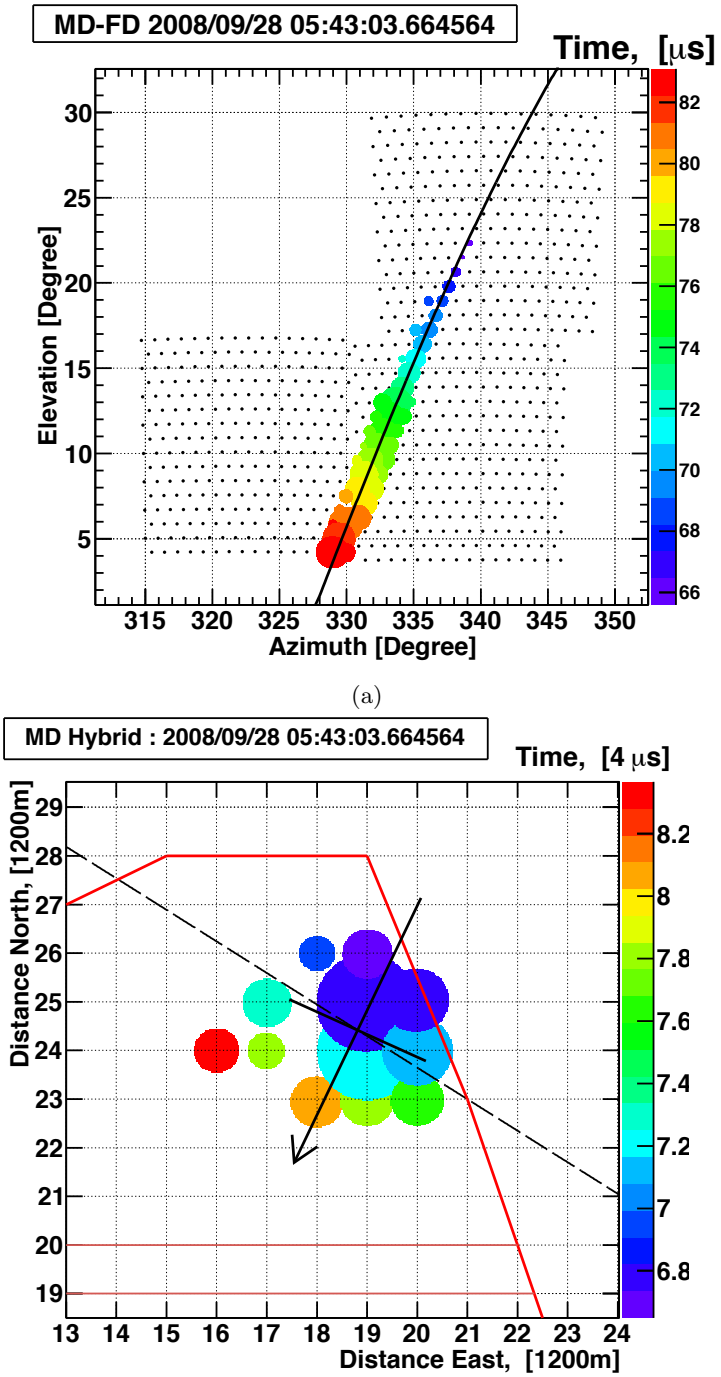


(a)

(b)

**Figure A.6**. The fifth highest energy event in the Middle Drum hybrid data set: it was recorded on 9/28/2008 at 5:43:03 UTC. Shown are (a) the Middle Drum event display, and (b) the Surface Detector event display.

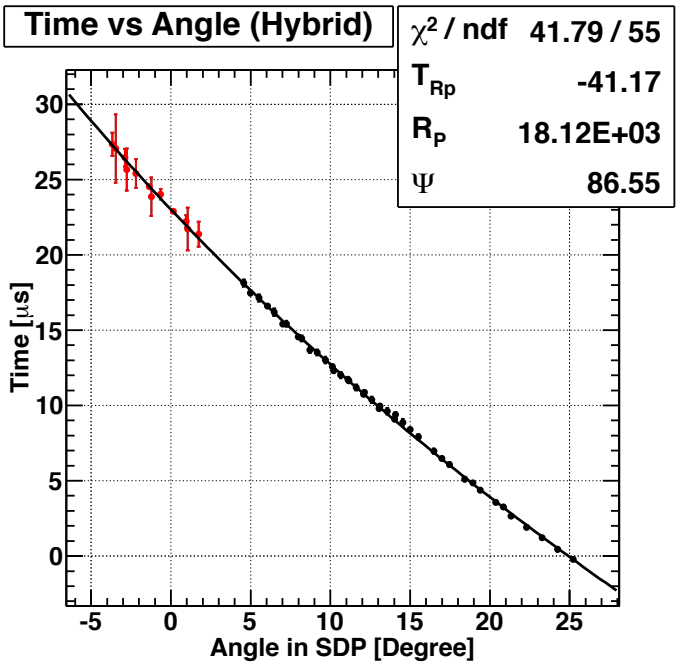


(c)

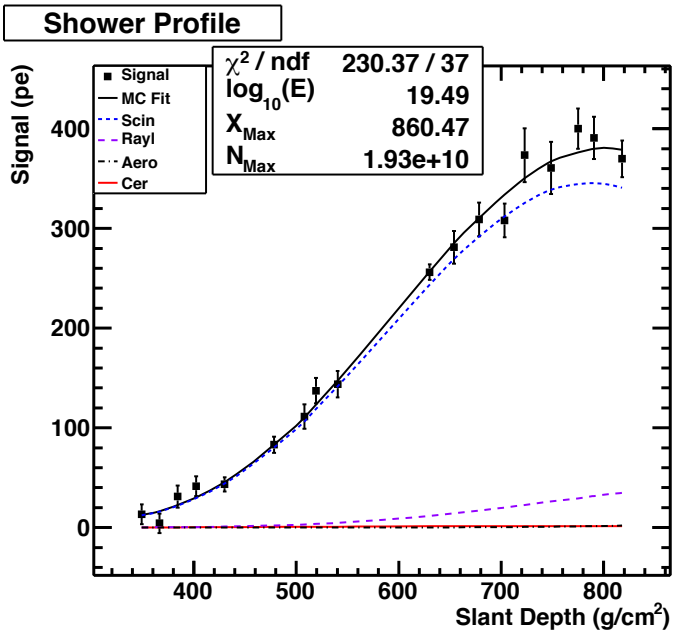


(d)

**Figure A.6**. Continuation of the fifth highest energy event in the Middle Drum hybrid data set: it was recorded on 9/28/2008 at 5:43:03 UTC. Shown are (c) the timing vs. angle plot for the geometry reconstruction, and (d) the plot of the shower profile (signal as a function of atmospheric depth).

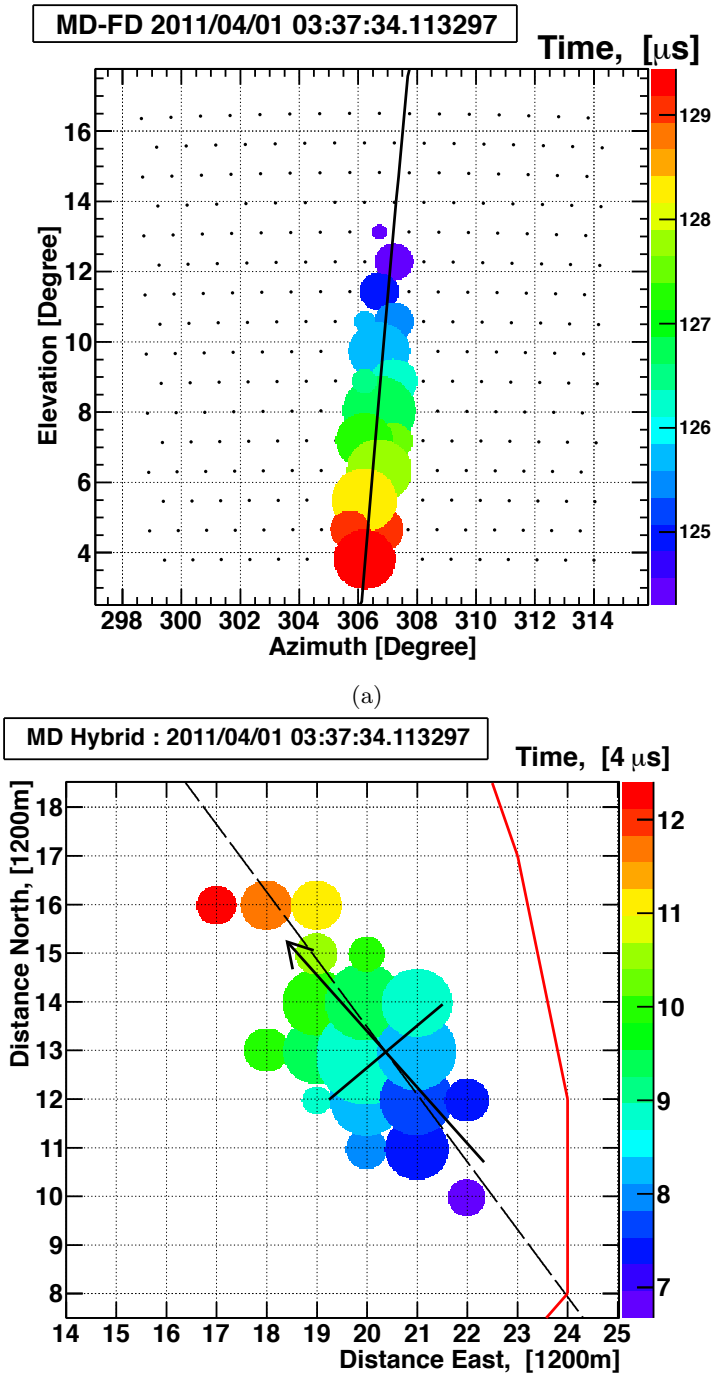


(a)

(b)

**Figure A.7**. The sixth highest energy event in the Middle Drum hybrid data set: it was recorded on 4/01/2011 at 3:37:34 UTC. Shown are (a) the Middle Drum event display, and (b) the Surface Detector event display.

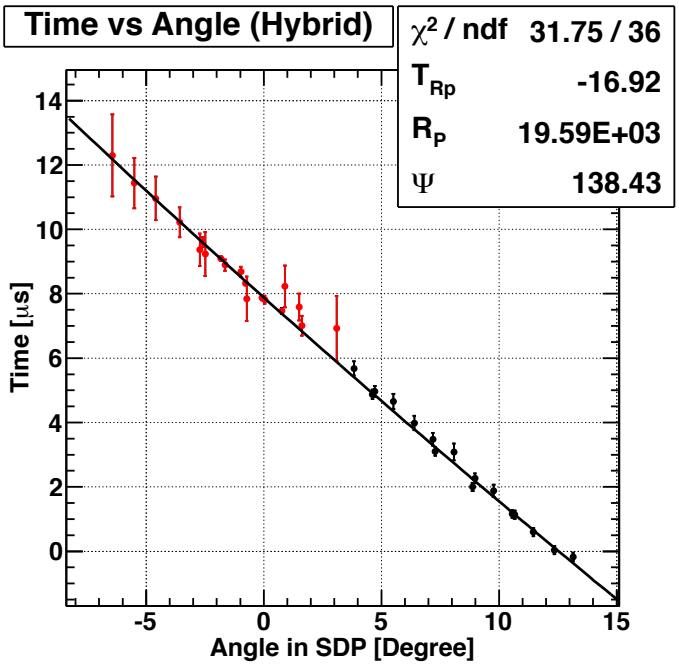


(c)

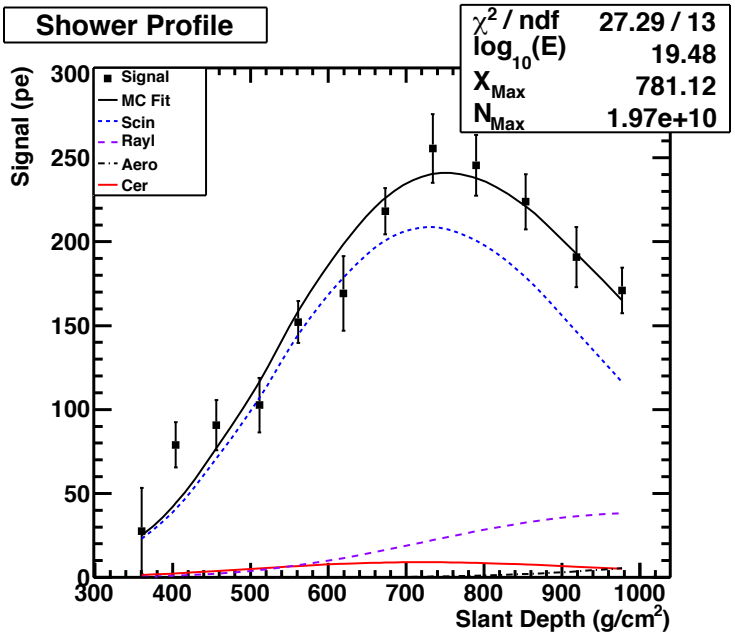


(d)

**Figure A.7**. Continuation of the sixth highest energy event in the Middle Drum hybrid data set: it was recorded on 4/01/2011 at 3:37:34 UTC. Shown are (c) the timing vs. angle plot for the geometry reconstruction, and (d) the plot of the shower profile (signal as a function of atmospheric depth).

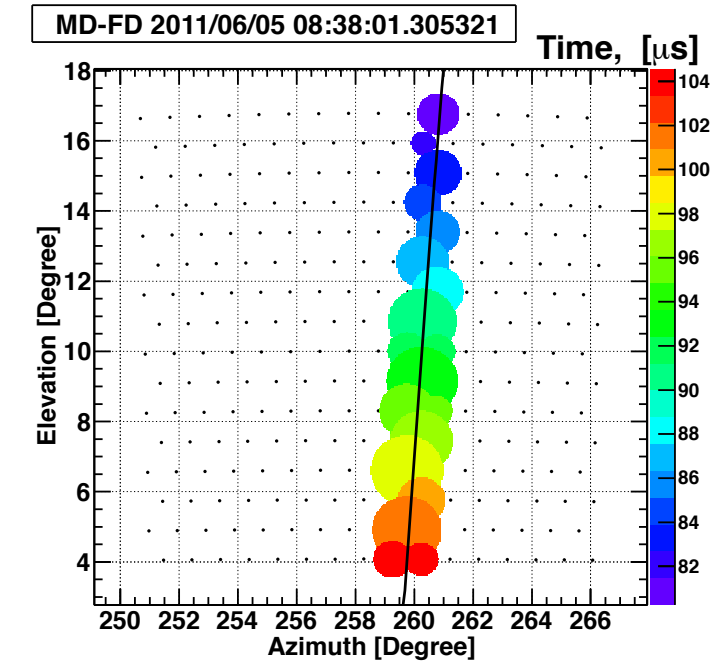


(a)

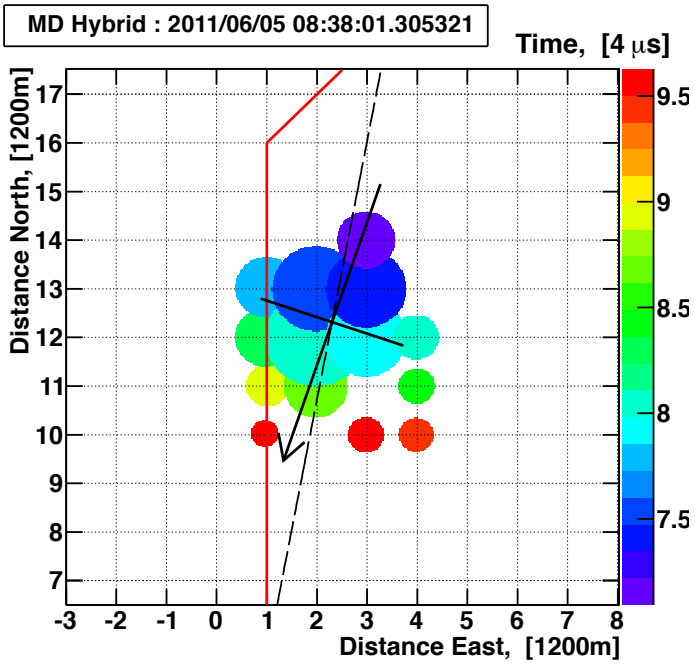


(b)

**Figure A.8**. The seventh highest energy event in the Middle Drum hybrid data set: it was recorded on 6/05/2011 at 8:38:01 UTC. Shown are (a) the Middle Drum event display, and (b) the Surface Detector event display.

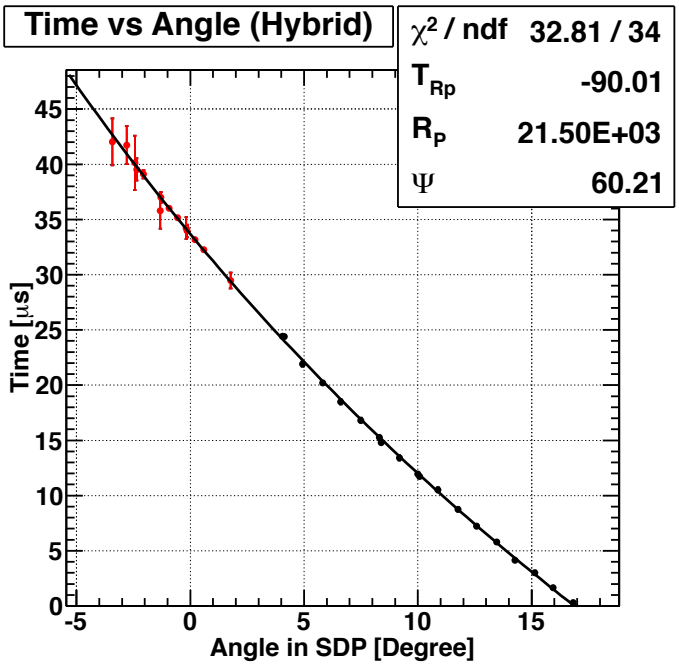


(c)

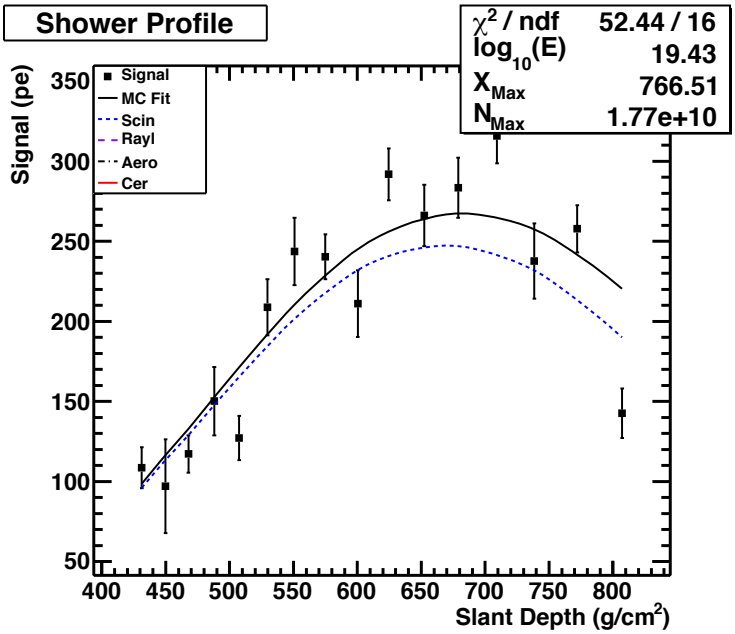


(d)

**Figure A.8**. Continuation of the seventh highest energy event in the Middle Drum hybrid data set: it was recorded on 6/05/2011 at 8:38:01 UTC. Shown are (c) the timing vs. angle plot for the geometry reconstruction, and (d) the plot of the shower profile (signal as a function of atmospheric depth).

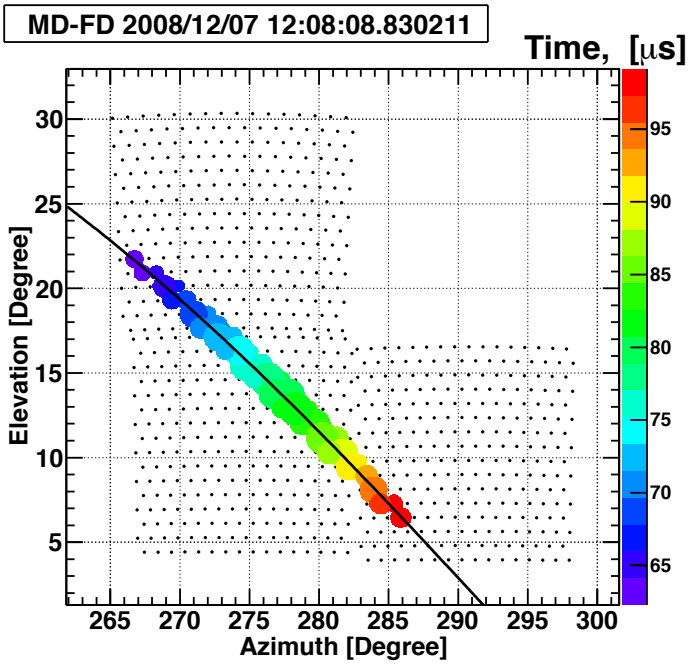


(a)

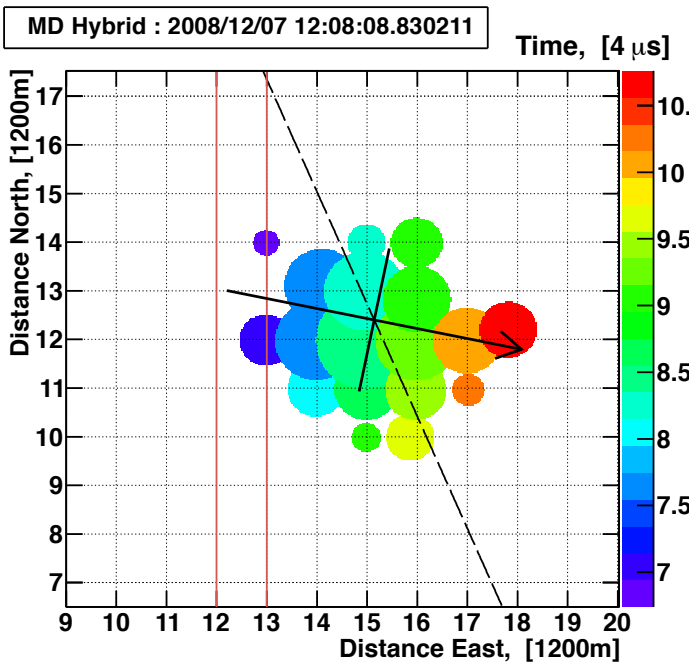


(b)

**Figure A.9**. The eighth highest energy event in the Middle Drum hybrid data set: it was recorded on 12/07/2008 at 12:08:08 UTC. Shown are (a) the Middle Drum event display, and (b) the Surface Detector event display.

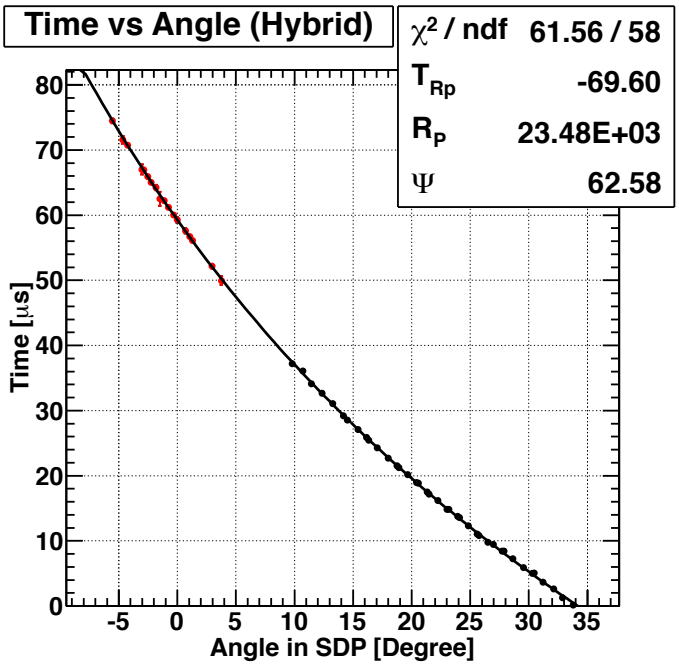


(c)

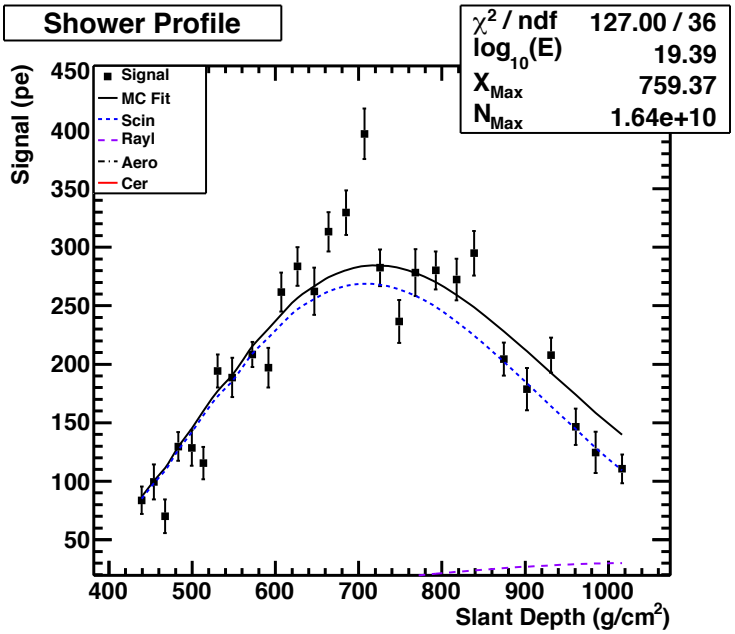


(d)

**Figure A.9**. Continuation of the eighth highest energy event in the Middle Drum hybrid data set: it was recorded on 12/07/2008 at 12:08:08 UTC. Shown are (c) the timing vs. angle plot for the geometry reconstruction, and (d) the plot of the shower profile (signal as a function of atmospheric depth).

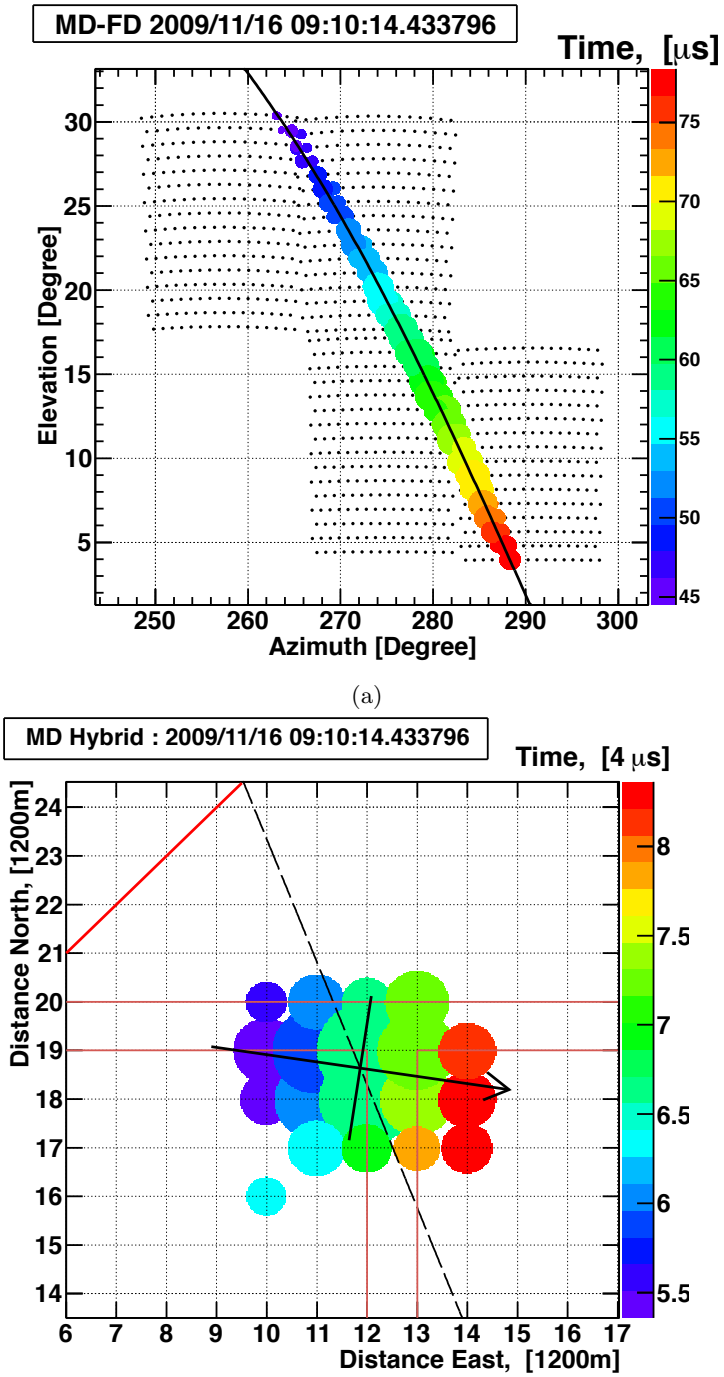


(a)

(b)

**Figure A.10**. The ninth highest energy event in the Middle Drum hybrid data set: it was recorded on 11/16/2009 at 9:10:14 UTC. Shown are (a) the Middle Drum event display, and (b) the Surface Detector event display.

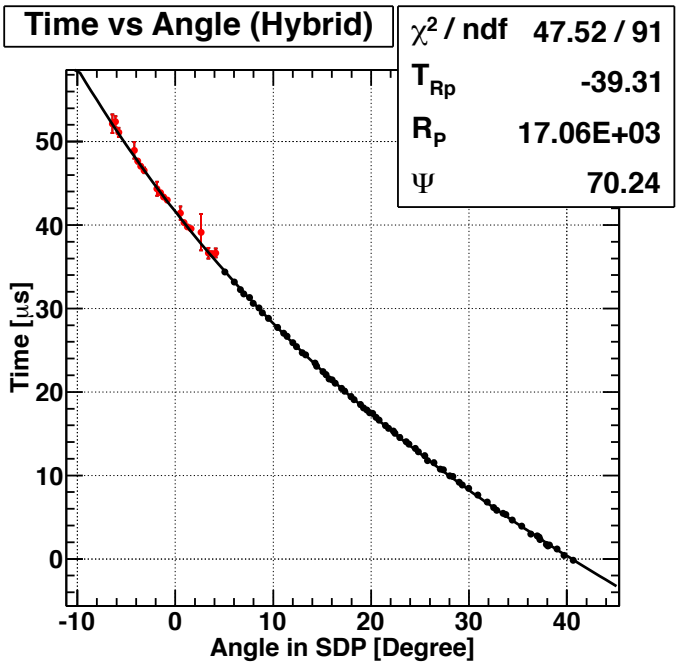


(c)

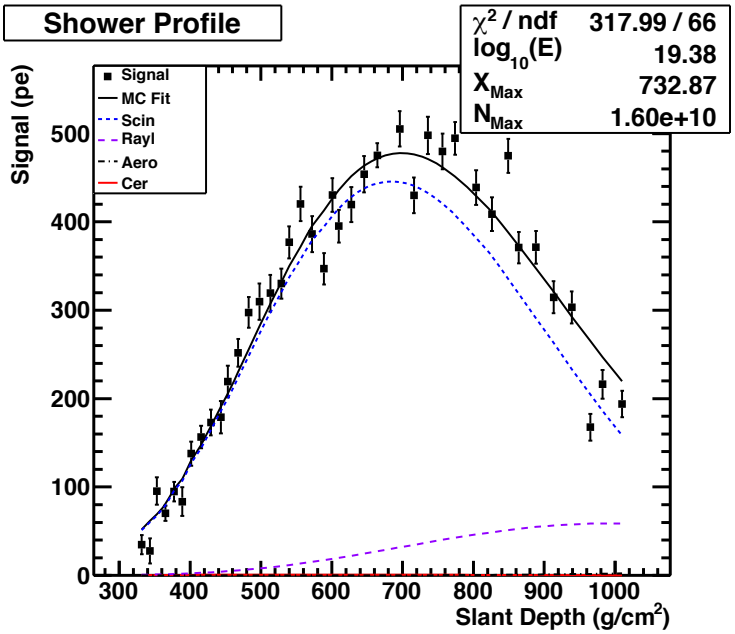


(d)

**Figure A.10**. Continuation of the ninth highest energy event in the Middle Drum hybrid data set: it was recorded on 11/16/2009 at 9:10:14 UTC. Shown are (c) the timing vs. angle plot for the geometry reconstruction, and (d) the plot of the shower profile (signal as a function of atmospheric depth).

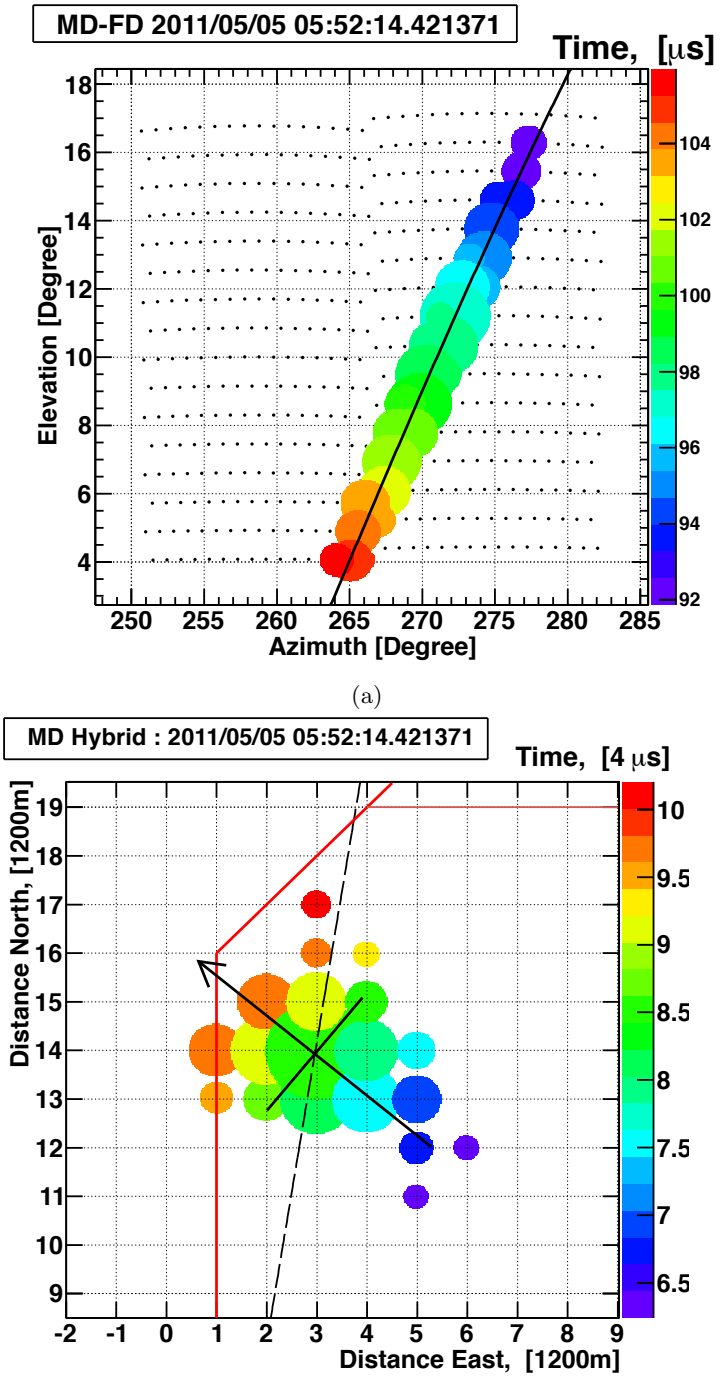


(a)

(b)

**Figure A.11**. The tenth highest energy event in the Middle Drum hybrid data set: it was recorded on 5/05/2011 at 5:52:14 UTC. Shown are (a) the Middle Drum event display, and (b) the Surface Detector event display.

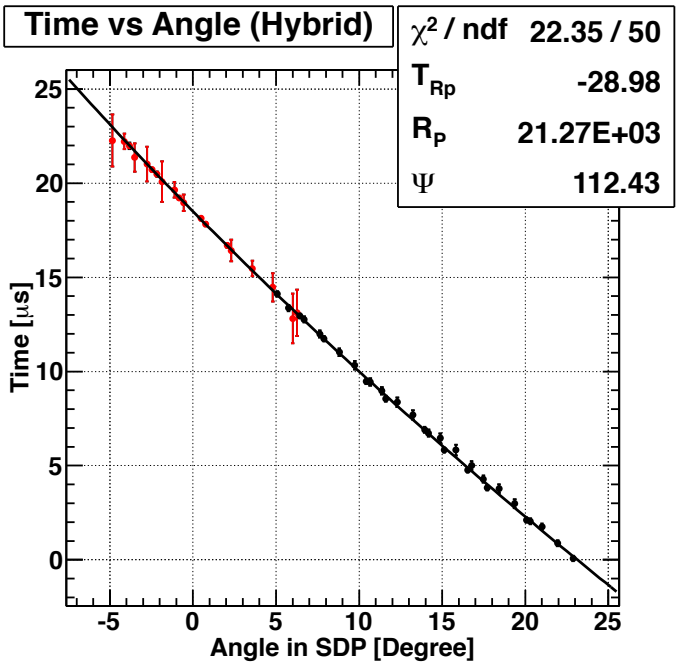


(c)

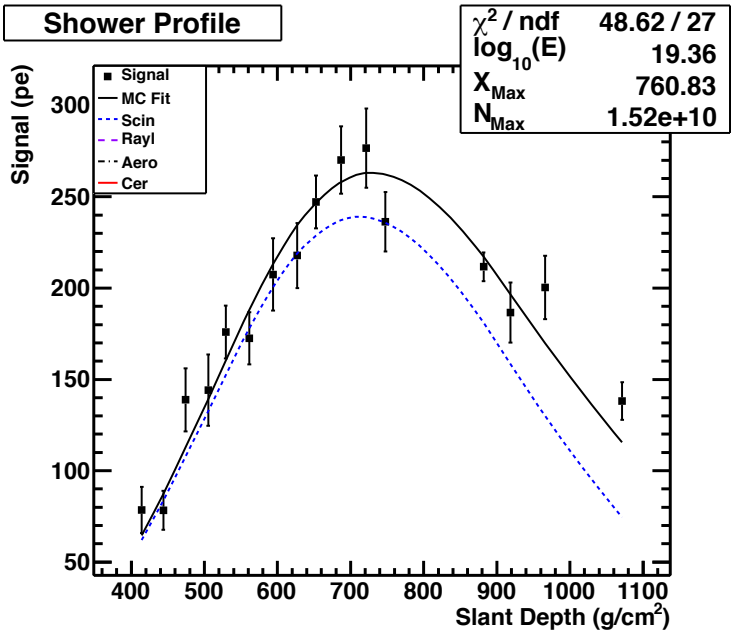


(d)

**Figure A.11**. Continuation of the tenth highest energy event in the Middle Drum hybrid data set: it was recorded on 5/05/2011 at 5:52:14 UTC. Shown are (c) the timing vs. angle plot for the geometry reconstruction, and (d) the plot of the shower profile (signal as a function of atmospheric depth).

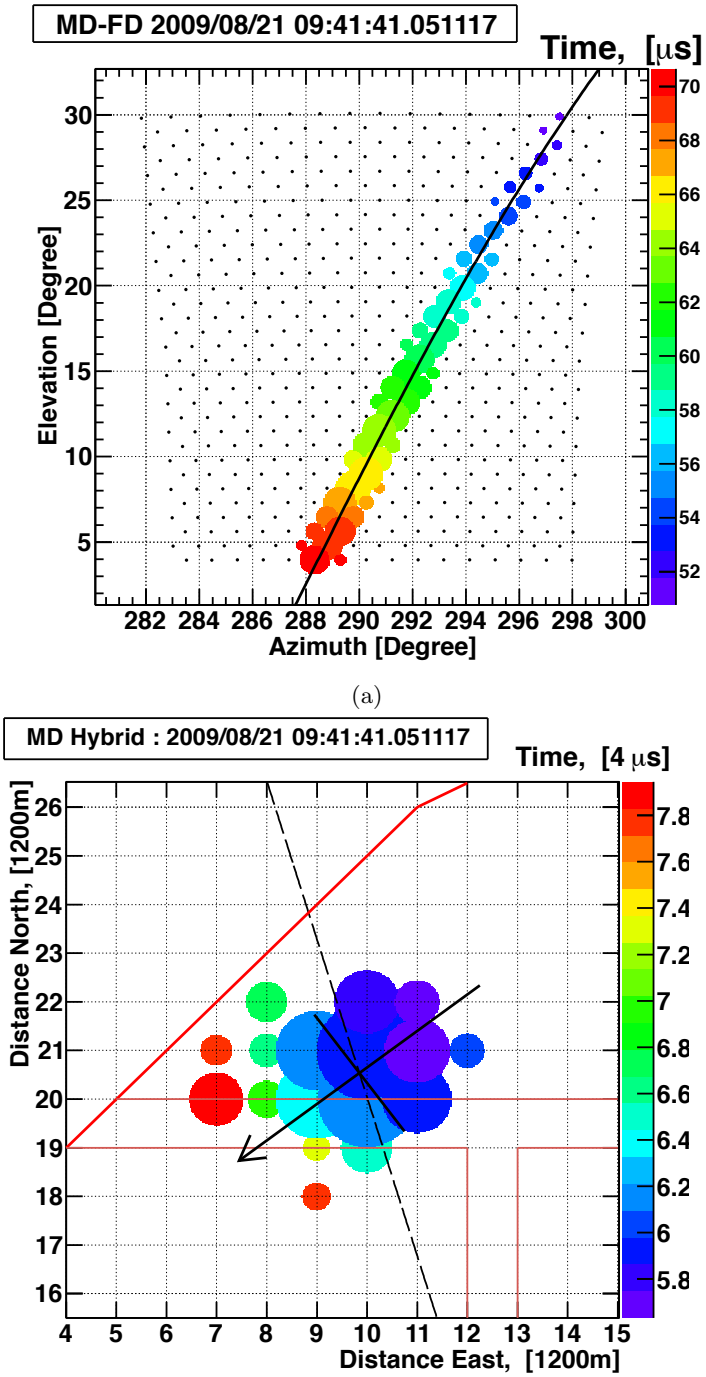


(a)

(b)

**Figure A.12**. The eleventh highest energy event in the Middle Drum hybrid data set: it was recorded on 8/21/2009 at 9:41:41 UTC. Shown are (a) the Middle Drum event display, and (b) the Surface Detector event display.

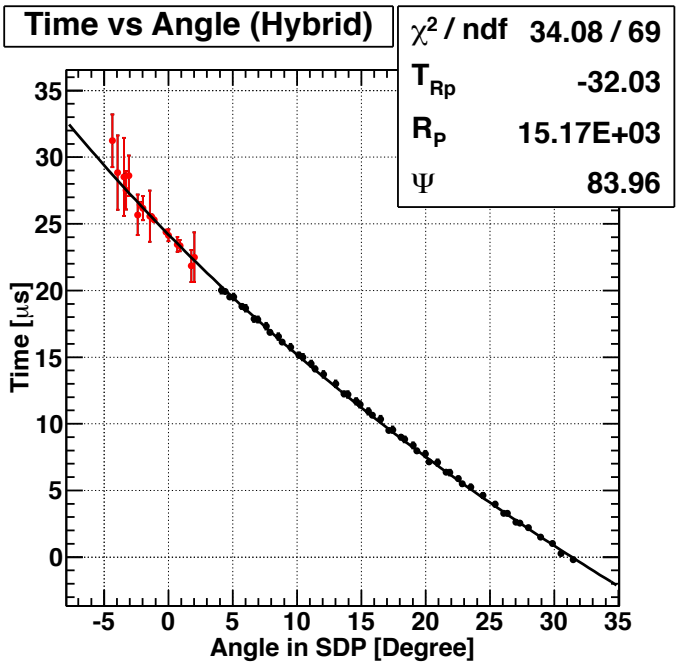


(c)

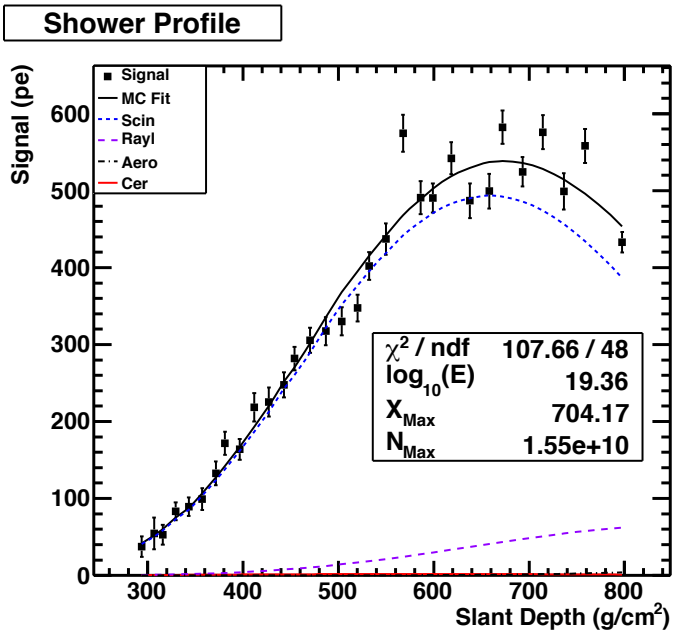


(d)

**Figure A.12**. Continuation of the eleventh highest energy event in the Middle Drum hybrid data set: it was recorded on 8/21/2009 at 9:41:41 UTC. Shown are (c) the timing vs. angle plot for the geometry reconstruction, and (d) the plot of the shower profile (signal as a function of atmospheric depth).

# REFERENCES


[1] Abbasi, R., et al. 2006, Astroparticle Physics, 25, 74

[2] Abbasi, R., et al. 2009, Astroparticle Physics, 32, 53

[3] Abbasi, R. U., et al. 2005, The Astrophysical Journal, 622, 910

[4] Abbasi, R. U., et al. 2007, Physical Review Letters, 100, 4

[5] Abbasi, R. U., et al. 2010, Physical Review Letters, 104, 161101

[6] Abraham, J., et al. 2010, Physical Review Letters, 104, 091101

[7] Abraham, J., et al. 2010, Physics Letters B, 685, 239

[8] Abreu, P., et al. 2010, Astroparticle Physics, 34, 314

[9] Abu-Zayyad, T., et al. 2001, The Astrophysical Journal, 557, 686

[10] Abu-Zayyad, T., et al. 2012, Astroparticle Physics, 39-40, 109

[11] AbuZayyad, T. Z. 2000, PhD thesis, University of Utah

[12] Allison, J., et al. 2006, IEEE Transactions on Nuclear Science, 53, 270

[13] Auger, P., Ehrenfest, P., Maze, R., Daudin, J., & Fréon, R. 1939, Reviews of Modern Physics, 11, 288

[14] Battistoni, G., et al. 2008, Nuclear Physics B - Proceedings Supplements, 175-176, 88

[15] Belz, J., Cao, Z., Chen, P., Field, C., & Huntemeyer, P. 2002, Fluorescence in Air from Showers (FLASH), Tech. rep., Stanford University

[16] Bird, D., et al. 1993, Physical Review Letters, 71, 3401

[17] Bird, D. J., et al. 1995, The Astrophysical Journal, 441, 144

[18] Bunner, A. N. 1967, PhD thesis, Cornell University

[19] Elterman, L. 1968, Environmental Research Papers, 285, 1

[20] Fukushima, M., et al. 2006, ICRR Annual Report, Tech. Rep. April 2006, Institute for Cosmic Ray Research, University of Tokyo

[21] Gaisser, T. K. 1991, Cosmic Rays and Particle Physics (Cambridge University Press), 296

[22] Greisen, K. 1966, Physical Review Letters, 16, 748

[23] Hanlon, W. F. 2008, PhD thesis, University of Utah

[24] Heck, D., Knapp, J., Capdevielle, J. N., Schatz, G., & Thouw, T. 1998, Forschungszentrum Karlsruhe, FZKA 6019, 1

[25] Hess, V. 1912, Physikalische Zeitschrift, 13, 1084

[26] Hillas, A. M. 1982, Journal of Physics G: Nuclear Physics, 8, 1461

[27] Hillas, A. M. 1982, Journal of Physics G: Nuclear Physics, 8, 1475

[28] Ivanov, D. 2012, PhD thesis, Rutgers, the State University of New Jersey

[29] Jones, B. F., et al. 2001, in Proceedings of the 27th International Cosmic Ray Conference, ed. W. Droege, H. Kunow, & M. Scholer (Berlin, Germany: Copernicus Gesellschaft), 641–644

[30] Kakimoto, F., Loh, E., Nagano, M., Okuno, H., Teshima, M., & Ueno, S. 1996, Nuclear Instruments and Methods in Physics Research Section A: Accelerators, Spectrometers, Detectors and Associated Equipment, 372, 527

[31] Linsley, J. 1985, In NASA. Goddard Space Flight Center 19th International Cosmic Ray Conference, 7, 359

[32] Luo, S. M. 1992, PhD thesis, University of Utah

[33] National Oceanic and Atmospheric Administration, National Aeronautics and Space Administration, & United States Air Force. 1976, U.S. Standard Atmosphere, 1976, Tech. rep., National Oceanic and Atmospheric Administration

[34] Nelson, W. R., Hirayama, H., & Rogers, D. W. 1985, The EGS4 Code System, Tech. Rep. SLAC-265, Standford Linear Accelerator Center

[35] Nerling, F., Blümer, J., Engel, R., & Risse, M. 2006, Astroparticle Physics, 24, 421

[36] Ostapchenko, S. 2004, Nuclear Physics B - Proceedings Supplements, 151, 143

[37] Reil, K., et al. 2004, SLAC Publication

[38] Rodriguez, D. C. 2011, PhD thesis, University of Utah

[39] Sokolsky, P. 2004, Introduction to Ultrahigh Energy Cosmic Ray Physics (Westview Press), 1–208

[40] Stokes, B., Cady, R., Ivanov, D., Matthews, J., & Thomson, G. 2012, Astroparticle Physics, 35, 759

[41] Takeda, M., et al. 1998, Physical Review Letters, 81, 1163

[42] Takeda, M., et al. 2002, Astroparticle Physics, 19, 447

[43] Tomida, T., et al. 2011, Nuclear Instruments and Methods in Physics Research Section A: Accelerators, Spectrometers, Detectors and Associated Equipment, 654, 653

[44] Unger, M., et al. 2007, in Proceedings of the 30th International Cosmic Ray Conference, ed. R. Caballero, J. C. D'Olivo, G. Medina-Tanco, L. Nellen, F. A. Sanchez, & J. F. Valdes-Galicia, Vol. 4 (Mexico City, Mexico: Universidad Nacional Autonoma de Mexico), 373–376

[45] Wilson, C. 1901, Proceedings of the Royal Society of London, 68, 151

[46] Zatsepin, G. T., & Kuz'min, V. A. 1966, Journal of Experimental and Theoretical Physics Letters, 4, 78